Dynamic coupling between passive and active complex fluids in curved geometries

Martina Clairand

PSL UNIVERSITÉ PARIS

THÈSE DE DOCTORAT
DE L'UNIVERSITÉ PSL

Préparée à l'ESPCI Paris

Dynamic coupling between passive and active complex fluids in curved geometries

Couplage dynamique entre fluides passifs et actifs complexes dans des géométries courbes

Soutenue par
Martina Clairand
Le 16 décembre 2021

École doctorale n°564
Physique en Île-de-France

Spécialité
Physique

Composition du jury :

Benoit LADOUX DR, Université de Paris, CNRS	*Président*
Julia YEOMANS Pr, Université d'Oxford	*Rapporteure*
Miha RAVNIK A.Pr, Université de Ljubljana	*Rapporteur*
Corinna MAAß A.Pr, Universié de Twente	*Examinatrice*
André ESTEVEZ-TORRES DR, Sorbonne Université, CNRS	*Examinateur*
Teresa LOPEZ-LEON CR, ESPCI Paris, CNRS	*Directrice de thèse*
Jordi IGNES-MULLOL A.Pr, Université de Barcelone	*Co-directeur de thèse*

ESPCI PARIS | PSL

ACKNOWLEDGMENTS

I wish to express my sincere acknowledgements to Julia Yeomans and Miha Ravnik for the careful revision and evaluation of my thesis manuscript. I would also like to extend my gratitude to André Estevez, Corinna Maass and Benoit Ladoux for accepting to examine this work.
I'd like to thank the European Union's Horizon 2020 research and innovation program, for funding this work under the Marie Sklodowska-Curie grant agreement No 754387.

Countless people have supported my efforts during the past three years. First, I would like to express my deepest gratitude to my supervisors Teresa Lopez-Leon and Jordi Ignes-Mullol, whose invaluable patience and guidance made my research both productive and enjoyable. Teresa, even though these last years were eventful, in both good and bad ways, you have never stopped supporting me, and giving me helpful advice on our regular zoom meetings and in the lab, with always great enthusiasm shining from your face. I highly appreciate the confidence and trust you have placed in me, as well as the many times you provided constructive discussions on my experiments and meticulous feedbacks on my writings, regardless of the time of day or even night. I was also profoundly impressed by how you managed to do so many things, sometimes in areas beyond science, to make this world a better place. Thank you!

Jordi, although we didn't get much time to know each other better, because of the geographical distance, you have contributed to make the last years, and specially the months I've spent at the UB, some of the most enriching episodes of my academic and professional life. Not only because I deepened my knowledge on active nematics but also because I learned from you how to adapt entire experimental setups with whatever was at hand. Your technical skills, ingenuity and teachings played a significant role in the achievement of my research and have become a great source of inspiration for my post–PhD life.

I would also like to extend my gratitude to Francesc Sagués, who made me feel as if I had three advisors rather than two. Your availability and critical thinking combined with your friendly and passionate personality were essential for the continuous improvement of my results and writings.

From time to time throughout this journey, I felt I was making no progress or that the outcomes of my work were not the ones I expected. In those moments it was comforting to know that I could count on the support of my colleagues. The first of them was Jérôme-*the active nematics charmer*-Hardoüin, with whom I conducted part of the research on active ellipsoids and entangled emulsions. Your inexhaustible source of ideas and contagious optimism motivated me to never give up and to try a new strategy every time

an experiment failed. I will never forget your striking ability to prepare samples with a clockmaking precision neither the many critical times you came to my aid, with the best attitude, when I faced a problem.

On the other side of the Ocean, I had the chance to collaborate with de Pablo's group from the University of Chicago, especially with Ali Mozaffari. Ali, even if we've never met in person, working with you remotely was really productive and pleasant. Despite your busy schedule and our different time zones, you always found a slot to discuss our projects. The charisma and self-confidence you transmitted behind the screen were very reassuring and helped me to confront all the challenges and concerns I had regarding our different projects.

My performance in the lab would not have been the same without the presence of Claire Dorée, with whom we constantly shared precious information about scientific protocols as well as delicious "goûtés" and anecdotes of our touristic "escapades" in the kitchen. Your exhaustive investigations and conclusions influenced in a great manner the understanding of my own work, just as your enthusiasm and serenity did with my mood in the stressful moments.

I am also extremely thankful to Guillaume Durey and Martyna Goral for their kindness and the valuable time they devoted to teaching me all I know on the microfluidic fabrication of double-emulsions. I would like to extend my gratitude to Kevin Phan for his availability and assistance in the micro-fabrication techniques I performed at the IPGG. I would also like to dedicate a special mention to Charlotte de Blois, Aurélie Lloret, Alice Billon and Meng Shi for their prompt assistance whenever I had a technical issue.

In the short time I spent in Barcelona, I had the chance to meet fabulous lab mates that helped me in so many ways that I don't even know where (or with whom) to start, but let's try. One of the first memories that comes to my mind is that of Berta, frequently keeping an eye on my work from over my shoulder and asking with an enthusiastic tone about the advancement of my research. Although this is just an anecdote, it summarizes well the many times you helped me with Java codes, experiments, shipments, or even on personal matters. Regarding the last point, I will never forget your hospitality, the Catalan words you taught me, the donuts on my birthday and the "villancicos" performance.

The next souvenir I have is that of the restless efforts of Ignasi to catch a vesicle to the beat of music. Thank you Igni for sharing your knowledge on electroformation with me and supporting my alternative (although unsuccessful) approaches for fabricating nematic vesicles. I hope one day you will achieve what I didn't manage to, and if not, you can always try to join the reggaeton industry, a brilliant future awaits you there.

I was also really fortunate to meet Anna, who was always willing to help me whenever I faced a technical problem, especially regarding the placement of the fluorescence cubes. I've learned a lot from you, including the fascinating history of Cataluña and the hidden sites and secrets of Barcelona. You deserve a big "merci".

Last but not least, I would like to thank Ramon, who kept me company during the long working days and advised me about the dangers of leaving the UB at night. I hope you will make good use of the microfluidic systems I left for you.

Back to Paris, the amazing ambience at Gulliver contributed to make my days unforgettable. It was a great pleasure to share the office with Kamel, Guillaume, Samuel, and recently with Coline and Rocio. Each of you found a personal way to fill the atmosphere

with great enthusiasm and good vibes: Kamel with his passion for soccer, Samuel with his dancing skills, Coline with her talent at the “tir à l’arbalète” and in chess, and Rocio for her amazing conversation and empathy. On the other side of the door, I also found many other people to be grateful to: Vincent for his multiple invitations to play soccer, Antoine for the weekend picnics, Jérémy for the chess breaks, just to give a few examples. There are plenty of people that I have not mentioned here, but that have also made my way through the lab very enjoyable. Thank you all for caring and sharing with me so many beautiful moments such as the Gulliver Olympics and trips, the laser games, the lunch breaks, the summer schools, and the “soirées”.

At the ESPCI, I frequently found support from my colleagues and the team of UPto.Paris. I wish to recognize Rositsa Yancheva, Virginie Cardoso and Alexandra Marynets for their fabulous work and the close follow-up that enhanced my experience in Paris. I extend my thanks to my colleagues and friends from the different calls, with whom we frequently shared our international experiences as well as our concerns and motivations in life, over a drink.

Striking a balance with life outside of the lab corridors would not have been easy without my friends. First, I would like to thank Carlos, my bachata sensei, for the wonderful moments of dancing and fun we had in Paris and in Barcelona as well as for his valuable advice regarding the PhD and the professional life. My gratitude is also dedicated to the AMARUN people with whom we organized regular meetings, including animated discussions and meals. I am also extremely thankful with Magda, Makis and Liss, my partners in crime, always fleeing from justice and finding a time slot to meet each other. My words of thanks also go to Andilu, Cuñis, Tochi, Edgar and the ”Salachines” who, despite being far away, always found ways to encourage me. One of the hardest times I faced during these last years was the covid crisis. If I managed to overcome this rude episode, it was, in part, thanks to Rodrigo, my “parcerito”, who helped me to see things with the right perspective due to his immeasurable generosity and optimism. The greatest debt of gratitude however, is owed to Majo and Yadi, my legal guardians, in whom I found not only extraordinary friends but also a family in Paris. Gracias ladies!

Lastly, my warm and heartfelt thanks go to my family, who selflessly motivated me to explore new directions to find my own way in life. The culmination of this dissertation is the unfailing proof of your encouragements and unconditional love.

CONTENTS

INTRODUCTION

This thesis summarizes the results obtained during the three years that I spent as a Ph.D. student in the Gulliver laboratory, at ESPCI, from September 2018 to November 2021, under the supervision of Teresa Lopez-Leon (ESPCI). The experiments were co-supervised by Jordi Ignés-Mullol from the SOC&SAM group in the department of Material Science and Physical Chemistry of the University of Barcelona where I spent four months from September 2019 to January 2020. The present introduction provides the motivation of this work and the outline of the manuscript.

Nature provides a fascinating variety of dynamic networks, where out-of-equilibrium units coordinate themselves to make the system perform complex functions. A remarkable example can be found in cells, where an intricate dynamical network of filamentous polymers and regulatory proteins ensures a multitude of vital functions, such as cellular division or motion. How the structure and dynamics of the network depends on the environment is a crucial question. Answering this question is not only important to understand biological process, but also to design new bio-inspired materials, such as autonomous micro-machines or soft robots.

A new class of synthetic active material, called the active nematic (AN), provides a model system to address these questions. Such a system has been obtained from the condensation of microtubules (MTs) and kinesin motor proteins at the interface between an aqueous suspension and an oil. The main peculiarity of such a two-dimensional material is that it conciliates nematic order with chaotic persistent flows. On the one hand, the aggregation of MTs at the interface induces the formation elongated bundles, the active units of this system, which self-align to develop long range orientational order, as in a typical nematic liquid crystal. On the other hand, as a result of the activity, this alignment is continually disrupted by the spontaneous generation/annihilation of topological defects, leading to chaotic large-scale flows. Under the shadow of this apparent chaos, the active nematic hides the often ignored, yet crucial, ability to adapt to the environment where it resides. Imposing geometrical constraints or damping textures to the active nematic can force it to reorganize its turbulent flows and to develop regular dynamics, prospecting the functioning of primitive, bio-inspired micro-machines.

Remarkable effects arise when the active nematic is condensed to a liquid crystalline interface, featuring viscous anisotropy, rather than an oil. The rheological properties of the passive liquid crystal enforce preferential flow directions, resulting in controlled dynamics at a large organizational level. Letting the interface bend in the third dimension brings new tools to control active flows, for instance by imposing curvature gradients to the director field. Fascinating oscillatory behaviors arise when confining the active nematic to the surface of a spherical droplet, which becomes a colloidal clock with tunable frequency. In this thesis, we build on this context to develop an innovative experimental platform where to study the coupling between active nematics and passive liquid crystals on curved geometries. Our work brings three main novelties with respect to previous

studies. First, we experimentally investigate the role of Gaussian curvature and we show that it is a crucial parameter for coding the defect emplacements and thereby the trajectories of the active flows. The second major innovation resides on how we traduce micro-activity into macro-movement across the active/passive coupling. Finally, we exploit the binding capabilities of topological defects to build larger active structures, where AN droplets are connected by topological networks. These last results are the first step towards the development of the field of "active nematic colloids".

In chapter one, we provide the theoretical framework and main concepts required for the understanding of this manuscript. We review some fundamental properties of liquid crystals and extend the framework to explain the physics behind a second class of material: the active nematics. We also introduce the physical mechanisms that inspired the design of the experimental platforms detailed in chapters 3 and 4. This includes the explanation of some fundamental principles, such as the Brownian motion or the active transport of passive particles, as well as the mechanisms ruling inter-particle interaction and colloidal assembly in liquid crystals.

In chapter two, we describe the different materials and experimental methods employed for the fabrication of hybrid active/passive structures. We begin by the procedure of synthesis of the active material: an in vitro active gel, fabricated using recipes from our collaborators and the literature. Some elements of the active gel were directly synthesized by members of specialized teams such as the BioNMR and the SOC&SAM groups at the University of Barcelona (UB). We also describe the acquisition techniques and some custom image analysis programs developed with the occasional help from Jérôme Hardoüin, a PhD student from the UB. Finally, we explain the different experimental techniques used for the production and manipulation of micro-droplets. The assembly and operation of capillary microfluidic devices were taught by Martyna Goral and Guillaume Durey from Gulliver at ESPCI, while photolitography for PDMS molds preparation was assisted by Kevin Phan at the Institut Pierre Gilles de Gennes (IPGG). The experimental setup for producing the assemblies in chapter 4 benefited from a collaboration with Uros Tkalec from the University of Ljubljana and Jérôme Hardoüin.

In the third chapter, we study the dynamics of active nematics confined to the surface of ellipsoidal smectic droplets. We describe two emerging states, with quadrupolar and dipolar symmetry, respectively, in which the system regularly oscillate between a rotational and translational state. By combining experiments and numerical simulations, we shed light on the mechanisms underlining these intriguing dynamics. Finally, we extend the experimental studies to other non-spherical geometries. Experiments were mainly performed in Gulliver lab at ESPCI. Simulations were carried out by Ali Mozaffari and Rui Zhang under the supervision of Juan de Pablo at the Unversity of Chicago.

In Chapter four, we explored the coupling between active/passive liquid crystals in a configuration that is the inverse from the previous one, i.e active aqueous droplets embedded in a passive liquid crystal. In the first part of the chapter, we study single active droplets, which are able to perform self-directed motion in the dispersing liquid crystal medium. In the second part of the chapter, we analyse the oscillatory behavior of complex assemblies, where AN droplets are bounded together via different kinds of topological loops and knots.

In Chapter five, we present the main conclusions and future perspectives on the different topics.

This work has received funding from the European Union's Horizon 2020 research and innovation program, under the Marie Sklodowska-Curie grant agreement No 754387.

CHAPTER

ONE

THEORETICAL FRAMEWORK

1.1 Liquid crystals

1.1.1 Liquid crystals: an unconventional state of matter

In condensed matter physics, the distinction between crystalline and liquid phases is governed by the degree and type of molecular ordering. In liquids, molecules only possess short-range order, so that they diffuse in random directions, allowing them to flow. On the other hand, crystalline solids have both long-range positional and orientational order, since molecules are constrained to occupy specific sites in a lattice[1]. An intermediate state, which exhibits long-range orientational order, and occasionally, partial positional order, also exists in nature. Liquid crystals (LCs) are mesophases that share some hydrodynamic properties with conventional liquids and some anisotropic physical attributes with crystals. To meet simultaneously these criteria, the liquid crystal molecules, usually called mesogens, display high shape-asymmetry, meaning that they are either long and rigid (calamitic), disc-shaped (discotic) or conical (bowlic).

Liquid crystals are usually classified in two main categories: lyotropic and thermotropic. In lyotropic liquid crystals, the mesogens, which are usually amphiphilic molecules, are dispersed in a solvent, and phase transitions from the disordered state to more ordered states are triggered by an increase in the mesogen concentration. For example, after exceeding a critical concentration, amphiphilic molecules such as soaps or phospholipids assemble together in ordered structures, including micellar crystalline phases or lamellar phases[1]. Lyotropic phases are ubiquitous in living matter: they appear in biopolymers, biological membranes or DNA.

On the other hand, in thermotropic LCs, molecular ordering does not depend on concentration but rather on temperature variations, meaning that thermodynamically stable mesophases will appear either upon heating or cooling the system. At high temperatures, for instance, the axes of the thermotropic liquid crystal molecules point in random directions, leading to an isotropic phase. By cooling down, the mesogens align their long axis along a unique direction, named the director $\mathbf{n}$. The resulting phase is called the nematic phase and features long-range orientational order, but no positional order. Additionally, the introduction of certain amount of chiral molecules to the nematic phase leads to an interesting twisted arrangement, known as the cholesteric phase.

When cooling the system further, lateral interactions between mesogens facilitate the nucleation of a complex layered structure known as the smectic phase[2]. In this state,

mesogens maintain the general orientational order of nematics, while they additionally organize themselves into equidistant layers, displaying positional order in one dimension. Depending on the orientation of the molecules with respect to the layer, smectic LCs are further classified in several subcategories. In the simplest case, the director is perpendicular to the layers, leading to a smectic-A (SmA) phase, while in a closely related state, called smectic-C (SmC), the director is tilted with respect to the layer normal.

More sophisticated arrangements arise from other types of molecular shape. Commonly, molecules with a discotic structure induce polar packing along an axis, leading to the formation of columns that align parallel to each other in the nematic phase. At larger concentrations, the columns arrange themselves in a crystalline network, the columnar phase, displaying positional ordering in two dimensions. Another example of a complex liquid crystalline phase is provided by bowl-like mesogens, which are able to embed their cones into one another to form polar columns displaying ferroelectric properties[3].

The easiest way to recognize a thermotropic liquid crystal from a conventional liquid is to induce a temperature change and look at any aspect variation. Under a critical temperature, named the *clearing point*, liquid crystals have a milky appearance due to the director fluctuations corresponding either to the nematic or smectic phase. Above this threshold, the isotropic state is attained and the liquid crystal becomes transparent, just as ordinary liquids. At the molecular level, calamitic mesogens share common structural features that enhance molecular ordering: they combine a stiff core, such as aromatic cycles, with flexible aliphatic tails, which define the long axis of the molecule. The most commonly studied type of thermotropic liquid crystals belongs to the family of cyanobiphenyls. These synthetic compounds contain two aromatic cores in between a cyano group and an aliphatic chain of variable size. Naturally, the length of the aliphatic chain dictates the type of mesophase accessible at room temperature. For instance, $4' - pentyl - 4 - cyanobiphenyl$ (5CB), one of the most popular liquid crystals in research labs and in the industry of displays, exhibits a nematic phase at room temperature ($T_N = 18.2 - 35.3$ °C); while $4 - octyl - 4 - cyanobiphenyl$ (8CB), containing 3 more $-CH_2$ groups, displays a smectic phase under the same temperature conditions (T_{SmA} =21.4 – 33.4 °C). Most cyanobiphenyls have a nematic phase for a large range around room temperature, excellent chemical stability, a low viscosity and prominent electrical and optical properties[2].

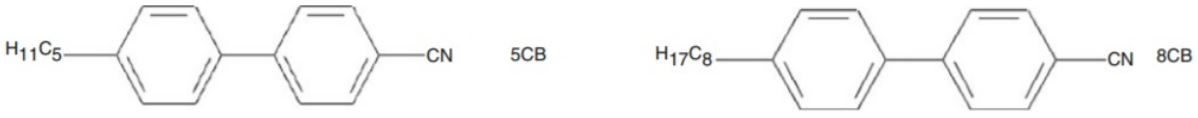

Figure 1.1: Chemical structure of 5CB and 8CB nematogens. Adapted from[4]

Although most of the concepts addressed in this thesis apply to both lyotropic and thermotropic liquid crystals with mesogens of varying shape, in the following sections, we will focus on thermotropic nematic liquid crystals whose mesogens are calamitic. This is the simplest way to introduce the basic principles and main characteristics of liquid crystals, which will be exploited experimentally in this research work. Special emphasis will be also given to structures in the smectic phase, which will be used in Chapter 3.

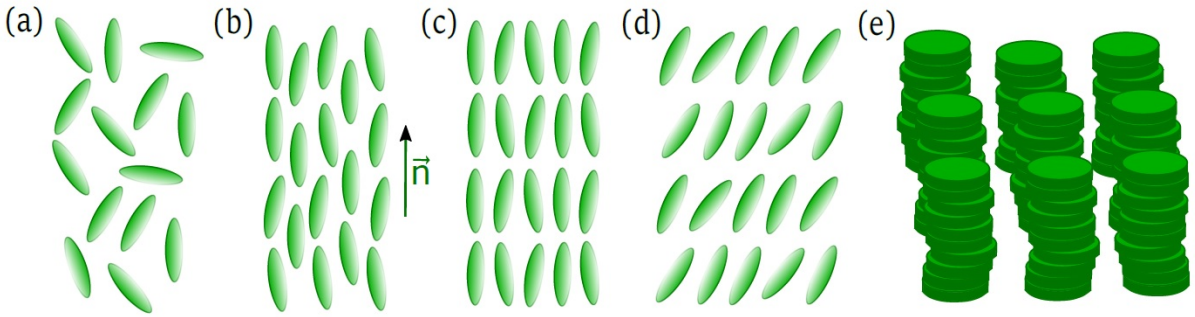

Figure 1.2: Molecular arrangements in liquid crystalline phases: (a) Isotropic, (b)nematic, (c) Smectic A and (d) Smectic-C mesophases. (e) Columnar phase for discotic molecules.

1.1.2 Order and symmetry

The most fundamental parameter describing liquid crystalline phases is the order parameter, which quantifies the orientational order of the anisotropic molecules. As mentioned in the previous section, all molecules in an ordinary nematic phase have at equilibrium the same average orientation, parallel to a unit vector **n** called the director. They are said to display long range orientational order, which implies that only molecular rotations around the n axis and π-rotations around any axis perpendicular to n are allowed by symmetry[1]. If we consider the representation in Fig. 1.2 (b), we can imagine, for instance, that turning the molecules upside-down leads to the same arrangement, where **n** ≡ -**n** due to inversion symmetry.

If we pay further attention to the individual rod-shaped molecules, we will notice that they are slightly deviated from the director **n**. Let's consider that the LC molecules are oriented along a unit vector **u**, defined by its polar angles θ and ϕ see Fig. 1.3). The nematic vector **n** is taken as the z-axis of the (x, y, z) frame.

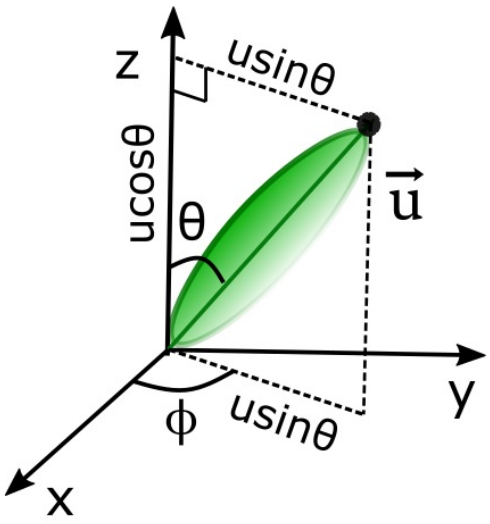

Figure 1.3: Parametrization of the molecular orientation in a nematic liquid crystal in three dimensions.

The fluctuations around **n** or the degree of alignment can be described by a distribution function $f(\theta, \phi)d\omega$ associated to the probability of finding the molecular axis in an angle $d\omega = sin\theta d\theta d\phi$ around **n**. In uniaxial nematics, where all molecules lye parallel

to the director, the intrinsic cylindrical symmetry of the nematic phase around $\mathbf{n}$ makes $f(\theta, \phi)$ independent of ϕ. Consequently, the distribution function can be written as $f(\theta)$, whose evolution is represented in Fig. 1.4. The amount of orientational order can be formally measured by the first moment of the distribution function named the scalar order parameter S:

$$S = \int_0^{\pi} f(\theta)(3cos^2\theta - 1)/2sin\theta d\theta, \tag{1.1}$$

leading to:

$$S = \langle (3cos^2\theta - 1)/2 \rangle \tag{1.2}$$

where $\theta = arccos(\mathbf{u} \cdot \mathbf{n})$ is the angle that the long axis of the molecule makes with the director. Averaging this function conveniently leads to values between -1/2 and 1, where $S = 1$ denotes a perfect alignment along $\mathbf{n}$, and $S = 0$ corresponds to a completely disordered isotropic phase. Alternatively, when $S = -1/2$, $f(\theta)$ reaches a minimal value of $\pi/2$ indicating that the molecules prefer to sit perpendicular to $\mathbf{n}$.

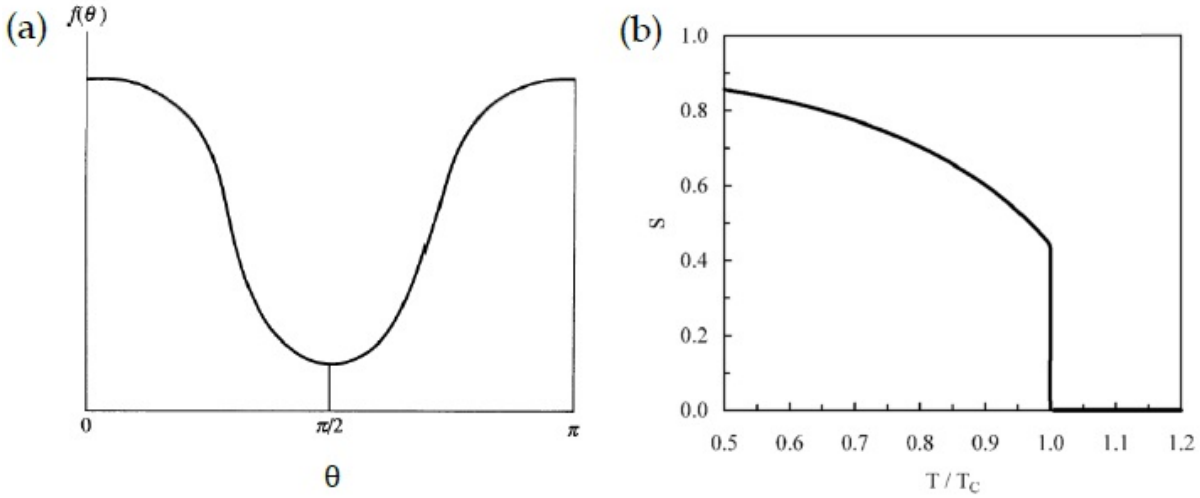

Figure 1.4: Evolution of the distribution function $f(\theta)$ and the scalar order parameter of a system of rods in a nematic phase. (a) $f(\theta)$ is large around θ=0 or π and S=1 i.e when molecules are parallel to $\mathbf{n}$. Conversely $f(\theta)$ is small close to $\theta = \pi/2$ corresponding to a molecular alignment perpendicular to $\mathbf{n}$. (b) The scalar order parameter S decreases with temperature. When reaching the clearing point, S becomes null and the liquid crystal transits toward the isotropic phase. Adapted from[5]

The order parameter is highly sensitive to the temperature of the sample and for instance, the average molecular orientation along $\mathbf{n}$ in a high-temperature isotropic liquid differs from that of a nematic mesophase. To quantify these variations in a three-dimensional field, we should construct a single uniaxial tensor $\mathbf{Q}$ that takes into account the average molecular orientation of the molecules along the vectors $\mathbf{u}$, and the identity matrix $\mathbf{I}$:

$$\mathbf{Q} = \langle \mathbf{u}_i \otimes \mathbf{u}_j - \frac{1}{3}\mathbf{I}_{ij} \rangle \tag{1.3}$$

In the isotropic phase $\mathbf{Q}$ equals zero as $\langle \mathbf{u}_i \cdot \mathbf{u}_j \rangle = \frac{1}{3}\mathbf{I}_{ij}$. Because this tensor is symmetric and traceless, we can diagonalize $\mathbf{Q}$ to find the nematic director $\mathbf{n}$[1]:

$$\mathbf{Q} = S\langle \mathbf{n}_i \otimes \mathbf{n}_j - \frac{1}{3}\mathbf{I}_{ij} \rangle \tag{1.4}$$

Note that this expression is characteristic of uniaxial systems and depends on three independent parameters: the amplitude S, and two of the three components of $\mathbf{n}$. Yet, depending on the nature of the liquid crystals this expression could differ. For instance, in optically biaxial nematics, the definition of the order parameter $\mathbf{Q}$ remains unchanged, but it depends on five independent quantities, which we will not detail here for the sake of simplicity. In this work we will exclusively focus on nematics displaying uniaxial optical properties, for which *eq.* 1.4 holds.

1.1.3 Elastic properties

When a well-aligned nematic configuration is distorted either by external fields or by confining boundaries, different types of restoring torques act on the liquid crystal to bring it back to the aligned, ground state. Typically, any arbitrary deformation can be decomposed into three elementary operations: splay, twist and bend (Fig. 1.5). The energy contribution associated to these elastic distortions in a nematic can be expressed by a quadratic function of the curvature strains, as indicated in the Frank free energy density:

$$f = \frac{1}{2}K_1(\boldsymbol{\nabla}\cdot\mathbf{n})^2 + \frac{1}{K_2}(\mathbf{n}\cdot\boldsymbol{\nabla}\times\mathbf{n})^2 + \frac{1}{2}K_3(\mathbf{n}\times(\boldsymbol{\nabla}\times\mathbf{n}))^2 \tag{1.5}$$

where K_1, K_2 and K_3 represent splay, twist and bend elastic constants, respectively. The magnitude of these constants being very small (of the order of 10 pN), director distortions can be induced very easily and propagate over macroscopic distances, so that they can often be observed optically. In many situations, these constants are assumed to be equal. This is the so called the "one-constant approximation". Since $K_1 = K_2 = K_3 = K$, we can reduce the free-energy density expression to:

$$f = \frac{1}{2}K[(\boldsymbol{\nabla}\cdot\mathbf{n})^2 + \boldsymbol{\nabla}\times\mathbf{n})^2] \tag{1.6}$$

In analogy with conventional mechanics, this formula is reminiscent of the internal energy, for example, of a stretched spring $E = \frac{1}{2}kx^2$, where k is the spring elastic constant.

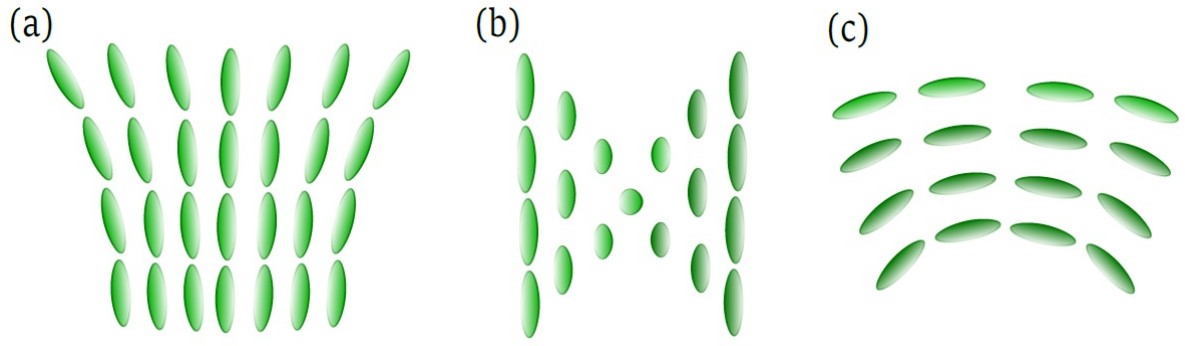

Figure 1.5: Elastic distortions in a nematic liquid crystal: (a) Splay, (b) Twist and (c) Bend.

1.1.4 Surface anchoring

The organisation of many systems is influenced by the properties of the substrate they are in contact with. In epitaxy for example, the orientation of forming layers is defined by the

crystal lattice that supports their growth. In analogy, the presence of a boundary usually impacts the organization of the liquid crystal in contact through the so called molecular anchoring, that is, the preferential orientation of the molecules at the boundary. When a solid (treated plate) or a liquid (immiscible fluid) substrate is placed in contact with a nematic LC, molecules near the surface are distorted from their original position to follow a preferred direction **a**, called the *anchoring direction*[6]. In the simplest case, **a** can assume two main orientations given by a single angle θ measuring the molecular tilt with respect to the normal of the surface (z-axis). When **a** is perpendicular to the surface, i.e. $\theta = 0$, the anchoring is said to be homeotropic (Fig. 1.6 (c)), but when molecules lie on the interface, $\theta = \frac{\pi}{2}$, the anchoring is said to be planar. In certain situations, molecular orientation admits an additional degree of freedom described by the azimuthal angle ϕ, the in-plane orientation of the mesogen units. When ϕ is fixed, the planar configuration is uniform giving rise to nematic order along the ϕ direction (Fig. 1.6(a)). If instead ϕ takes random values, planar anchoring becomes *degenerate* (Fig. 1.6(b)). Conical anchoring occurs when the director is tilted from the substrate and the azimuthal direction is constant and non-null ($0 < \theta < \pi/2$) (Fig. 1.6(d)). As in the planar case, conical anchoring can be uniform ($\phi = constant$) or degenerate (ϕ can vary).

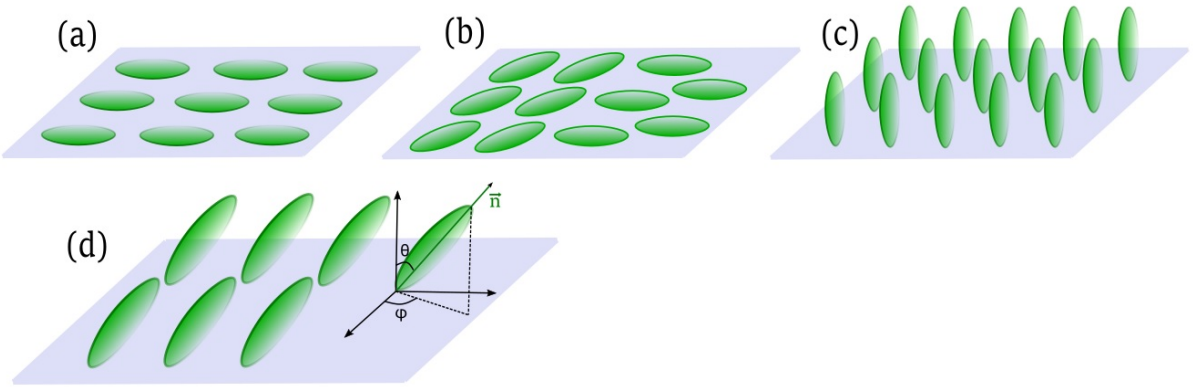

Figure 1.6: Orientation of the nematic director under (a) uniform planar $\theta = \pi/2$ and $\phi = constant$, (b) planar degenerate $\theta = \pi/2$, ϕ random, (c) homeotropic $\theta = 0$ and (d) uniform conical anchoring $0 < \theta < \pi/2$ and $\phi = constant$.

Anchoring effects are typically sensed not only close to the boundary, but also in the bulk. Usually, the mean deviation θ of the molecules at the boundary can be transmitted to the bulk via elastic forces. Far from the surface, an equilibrium field configuration is established due to the balance between the contributions from the boundary and from the bulk mesogens, which tend to reestablish the far-field alignment. In the continuum description of liquid crystals, this balance is expressed by adding a surface term, the *anchoring potential* $f_{anchoring}$, to the local free energy density. In the Rapini-Papoular formalism, the latter is expressed as:

$$f_{anchoring} = \frac{1}{2} W_\theta sin^2(\theta - \theta_0) + \frac{1}{2} W_\phi sin^2(\phi - \phi_0) \tag{1.7}$$

where θ and ϕ are fixed zenithal and azimuthal angles at the interface and θ_0 and ϕ_0 those of the easy axis, i.e of the preferred $\boldsymbol{n}$ direction at the boundary. W_θ and W_ϕ on the other hand, are called anchoring strengths and represent the energy needed for the maximal deviation of $\boldsymbol{n}$ at the surface.

To characterize the anchoring strength, one can simply analyze the $Kleman - de\ Gennes$ extrapolation length $L \sim K/W$, where K is the Frank elastic constant and W is a surface anchoring coefficient. If K dominates over W, L becomes large, and the anchoring is considered weak. On the other hand, for infinitely large W, L becomes zero and the anchoring is said to be strong. A geometrical interpretation of the anchoring extrapolation length is given in Fig. 1.7.

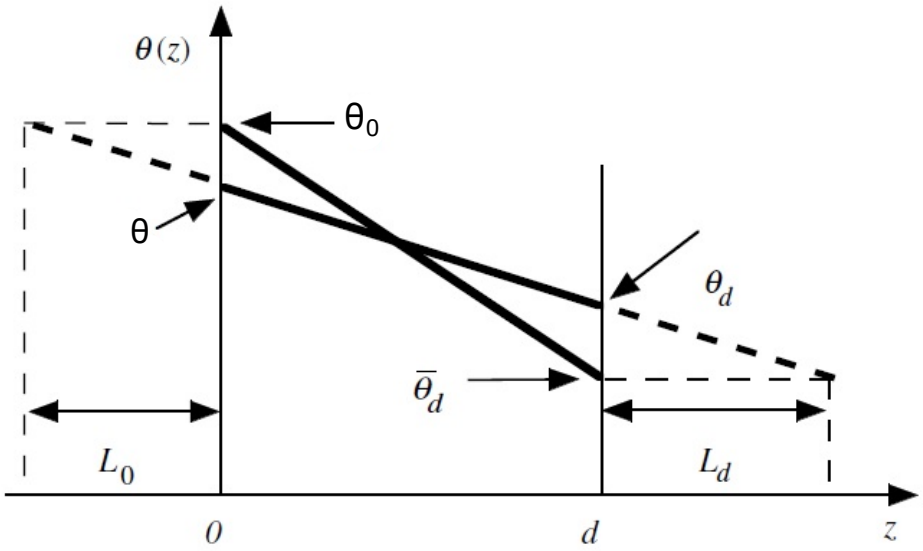

Figure 1.7: Geometrical interpretation of the anchoring extrapolation length. Adapted from[7]

Experimentally, the liquid crystal orientation can be controlled by treating the surface either physically or chemically. For instance, a typical method to get homogeneous planar anchoring on glass slides consists in coating the glass surface with polyvinyl alcohol (PVA) and rubbing it with a velvet along a specific direction. Other strategies, such as silanization or polymer grafting, are used to align the molecules homeotropically using physico-chemical interactions. In fluid interfaces, the anchoring is usually set by the addition of surfactants to the phase in contact with the liquid crystal. To select the surfactant properly, both the nature of the confining phase and the liquid crystal should be taken into consideration. The details of the surface treatments used in our experiments will be provided in section 2.

1.1.5 Topological defects

1.1.5.1 Topological defects in 2D nematics

Topological defects are ubiquitous in many areas of physics, including condensed matter, particle physics or even cosmology. In liquid crystals, defects correspond to regions where the director is ill-defined. In general, they can feature a core where the order is almost non-existent (points or disclination lines), and a far field region of significant strain[8]. Numerous studies regarding topological defects have been performed in two-dimensional liquid crystals, as will be the case in this work. To understand the nature of these singularities, let's assume a plane defined by x and y axes (Fig. 1.8). In this plane, the angle between $\mathbf{n}$ and the x axis is denoted $\phi(x, y)$, so that in the cartesian frame $(\mathbf{i}, \mathbf{j})$,

the director can be read:

$$\mathbf{n} = cos\phi\ \mathbf{i} + sin\phi\ \mathbf{j} \tag{1.8}$$

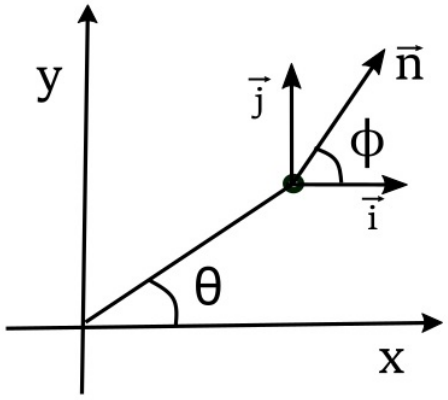

Figure 1.8: Parametrization of the nematic field in two dimensions.

If we consider the one-elastic-constant approximation eq. 1.6, i.e we assume the three elastic constants equal to K, then the Frank-Oseen free energy density can be written as:

$$f = \frac{1}{2}K(\boldsymbol{\nabla}\phi)^2 \tag{1.9}$$

As the free energy around the defect core should be minimal, f is integrated over the xy plane to recover the free energy per unit length:

$$f_L = \frac{1}{2}K \iint (\boldsymbol{\nabla}\phi)^2\, dx\, dy \tag{1.10}$$

which is in turn minimized as $\frac{\delta f_L}{\delta \phi} = 0$, leading to:

$$\boldsymbol{\nabla}^2\phi = 0 \tag{1.11}$$

To solve the above Laplace equation we convert cartesian coordinates (x, y) into polar coordinates (r, θ), i.e $x = rcos(\theta)$ and $y = rsin(\theta)$, and we define the polar angle θ as follows:

$$\theta = arctan\frac{y}{x} \tag{1.12}$$

The general solution to eq. 1.11, corresponding to the director configuration around a point defect takes the form:

$$\phi(\theta) = m\theta + \phi_0 \tag{1.13}$$

This equation indicates that an increment of 2π in θ carries a full $2\pi m$ rotation of the director. Yet, since **n** ≡ **-n**, due to inversion symmetry, a πm variation of $\phi(\theta)$ is sufficient to bring the director to its initial configuration[9]. As a consequence, the strength m, must equal a multiple of $\pm\frac{1}{2}$, giving the following equation for the director field around a point disclination in 2D nematics:

$$\mathbf{n} = cos(m\theta + \phi_0)\ \mathbf{i} + sin(m\theta + \phi_0)\ \mathbf{j} \tag{1.14}$$

where $m = \pm\frac{1}{2}, \pm 1, \pm\frac{3}{2}, \pm 2 \ldots$ $\theta \in [0; 2\pi]$

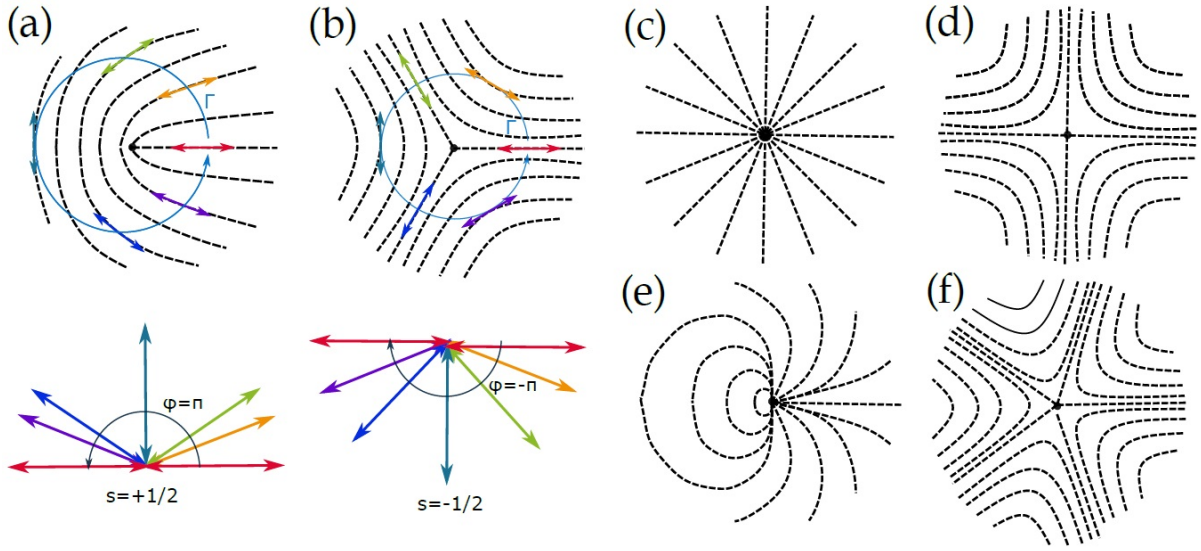

Figure 1.9: Field lines for point defects of charge (a) s =+1/2, (b) s =-1/2, (c) s =+1, (d) s =-1, (e)s=+3/2, (f)s=-3/2. Bottom figures (a) and (b) display the Burger circuit surrounding the defect core. A 2π-rotation along the loop Γ, conducts the director to rotate through an angle of (a) π and b) $-\pi$.

These structures can be sketched by an imaginary closed circuit, named the *Burger circuit*, that maps the field lines around the defect in 2D, as shown in Fig. 1.9.

In this representation, the closed "Burgers" loop Γ, runs counter clock-wise from a starting point M, surrounding the defect over a complete 2π period[10]. By looking at the variation of the director orientation, φ, along Γ, we can estimate the winding number s of the defect via the following integral[11]:

$$s = \frac{1}{2\pi} \oint_{\Gamma} \boldsymbol{\nabla}\varphi \cdot d\mathbf{r} \tag{1.15}$$

In other terms, s refers to the number of times the director experiences a 2π rotation and can be simplified as:

$$s = \frac{\varphi}{2\pi} \tag{1.16}$$

This value can be either positive or negative depending on whether φ rotates clock-wise or counter clock-wise and corresponds to the topological charge of the defect. To further illustrate these equations, let's consider the example in Fig. 1.9 (a). If we represent only a few consecutive director vectors while describing the Γ loop over a 2π period, we will notice that φ takes a value of π. Thus, according to eq. 1.16, $s = +\frac{1}{2}$. Although s can be calculated everywhere around a defect, there is only a specific place on which the charge takes the exact multiple half-integer value. This place corresponds to the defect core. Finally, as the vector $\boldsymbol{\nabla}\phi$ is everywhere tangential and of magnitude $|\boldsymbol{\nabla}\phi| = \frac{m}{r}$, where $r = \sqrt{x^2 + y^2}$, we can replace this term in eq. 1.10 to deduce the final expression of the Frank-Oseen free energy:

$$f = \frac{1}{2} K \frac{m^2}{r} \tag{1.17}$$

By integrating this expression over a distance L, the distortion energy of a 2D disclination or the energy per unit length of a 3D disclination becomes[12]:

$$E = \int_{R_c}^{L} f 2\pi r dr = \pi K m^2 ln(\frac{L}{R_c}) + F_c \tag{1.18}$$

The terms R_c and F_c are respectively the radius and the energy of the disclination core, inside which the distortions are too strong and the order parameter too low to be described by a simple phenomenological theory[1,12]. According to this equation, the energy varies as m^2, making singularities of low topological charge energetically favored. In fact, experimentally only those with $m = \pm 1$ and $m = \pm\frac{1}{2}$ are typically observed.

Defects are typically created after an isotropic-nematic phase transition, and their density decreases as the nematic phase relaxes. Generally this occurs because topological defects increase the free energy of the liquid crystal, since they create distortions in the director field. Consequently, oppositely charged defects tend to annihilate and disappear. Nevertheless, under confinement, liquid crystals might have topological defects in their ground states, due to global topological requirements associated to the confining surface. Although topological defects were initially seen as "imperfections" that could compromise the functioning of LC displays, today we know that they are powerful tools to control material properties, with potential applications for the development of optical devices[13] and metamaterials[14], as well as for the assembly of colloidal crystals into unconventional architectures[15].

1.1.5.2 Line defects in 3D nematics

Sometimes, point defects hide valuable information that cannot be accessed by simple surface observation. Dark spots appearing through crossed polarizers eventually correspond to the termination of disturbances propagating throughout the whole volume. Imagine for example, a nematic inside a circular cylinder treated to impose normal anchoring at the boundaries (Fig. 1.10 (a)). We expect the formation of a radial line that extends all along the axis of the cylinder. This line singularity is termed *dislclination* and can take different topological charges. According to eq. 1.18, energy is minimized when the strength of the defect line splits into pairs of $m = +\frac{1}{2}$ point defects. As a consequence, an integer disclination is unstable and the director is smoothly reoriented along the cylinder axis to relax the distortion. The core of the line eventually vanishes and the only singularities left in the system are point defects pushed away to the top and to the bottom edges of the cylinder. In such case, the disclination is said to "escape in the third dimension"[12] Fig. 1.10 (b).

A more stable type of disclination line is obtained when $\pm 1/2$ point defects extend to the third dimension. Locally, every cross section of the disclination can be described by a central core and a surrounding director field following the configuration of its corresponding two dimensional counterpart, i.e the field around the line can be either parabolic ($+1/2$ defect) or hyperbolic ($-1/2$ defect), see Fig. 1.10 (c-d). In these conformations with half-integers winding numbers, the escape is geometrically impossible, and thus, the line remains stable.

1.1.5.3 Three dimensional defects

The simplest system to study point defects in three dimensions is a soft nematic droplet, obtained by dispersing a liquid crystalline phase into an immiscible fluid, such as water or oil containing different sorts of surfactants. Under strong homeotropic anchoring conditions at the droplet's surface, two types of topological defects are observed, referred to as radial and hyperbolic hedgehog, whose structures are respectively shown in Fig. 1.11 (a) and (c). Each of them is assigned a unit topological charge N, which is the three dimensional extension of the surface charge m. Around a radial hedgehog, the vectorized

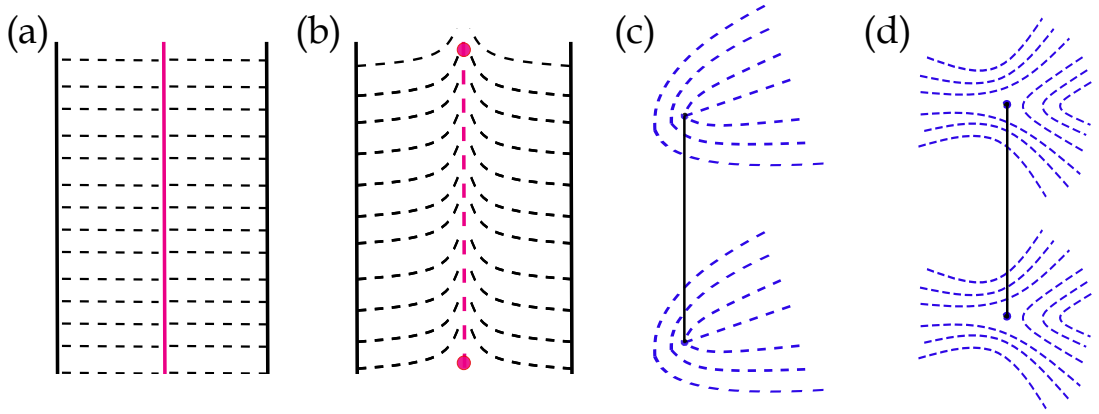

Figure 1.10: Schematic representations of the director field around (a) a disclination of charge s=+1 inside a cylinder with homeotropic anchoring and (b) 1 escaped structure joining two point defects. A stable disclination line can be obtained by extending (c) $s = +1/2$ and (d) $s = -1/2$ defects in the third dimension.

director can point either towards (or away from) the center of the sphere in all directions, resulting in a volume topological charge of magnitude 1, see Fig. 1.11 (a). In the hyperbolic hedgehog, the vectorized director points away from the singularity in two directions of space, and towards it in the other direction (or vice versa), see Fig. 1.11 (c)). Since $+\boldsymbol{n}$ and $-\boldsymbol{n}$ are formally equivalent in nematics, it is not possible to unequivocally establish the sign of N for an isolated hedgehog, since it will depend on the direction of vectorization chosen; however, it is possible to distinguish between two hedgehogs of opposite charge that are connected by the same director field.

Another type of singularity in a bounded nematic are surface point defects, named boojums. They got their name from the poem "The Hunting of the Snark", telling the story of the imaginary creature "boojum" which softly and suddenly vanishes away, just as disclinations do when escaping to form surface point defects[16,17]. In nematic liquid crystals, boojums are reminiscent of one-half hedgehogs and can be described as their projection on the surface in terms of a 2D topological charge s. A typical example is a bipolar nematic droplet with tangential anchoring containing two surface point defects of charge $s = +1$ at the poles.

1.1.6 Defect tailoring through liquid crystal confinement

Topological defects are energetically costly and spontaneously disappear in unconfined stable nematic phases. Interestingly, this is not true when the liquid crystal experiences geometrical frustration due to external constrains such as confining boundaries. A typical case consists of two adjacent plates imposing different anchoring conditions to the liquid crystal in between. Another classical configuration inducing significant frustration in the liquid crystal is obtained by confining the nematic LC between walls that impose degenerate (heterogeneous) planar boundary conditions. In such cases, lines and isolated point defects appear connected by dark brushes under cross polarizers, a texture named the Schlieren texture[19].

Other methods for creating topological defects in a controllable manner include the imposition of surface patterns with chemical gradients[20,21] or the application of specific topographies[22]. Moreover, line defects can also be produced and modified externally by imposing electric or magnetic fields to the liquid crystal[23,24]. Frustration may also

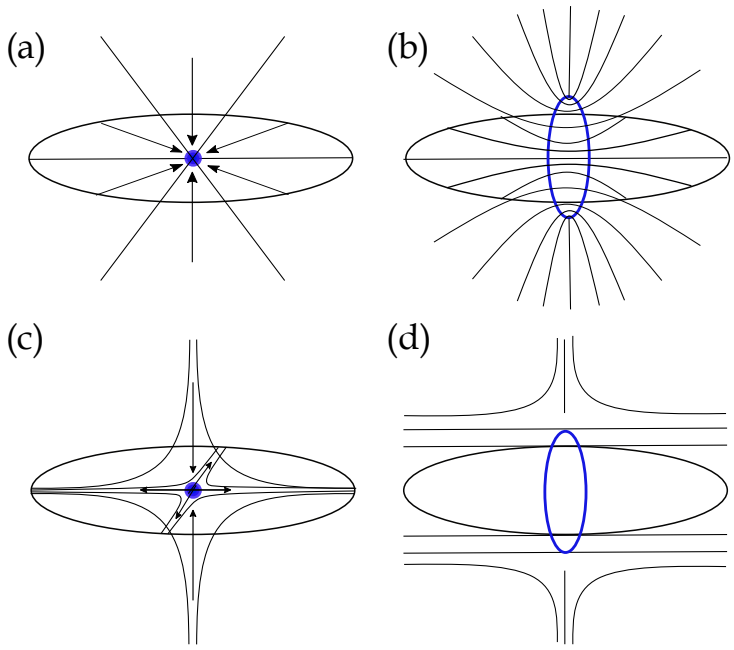

Figure 1.11: Representation of the director field around (a) radial and (c) hyperbolic hedgehogs opening into rings (b-d). Point defects of charge k =+1 (k =−1) turn into disclination loops of charge k =+1/2 (k =−1/2). Adapted from[18].

stem from the addition of small inclusions inside a liquid crystal, which cause localized distortions in the director field. Such systems will be studied in detail in section 4.2. Finally, one of the most robust strategies to stabilize defects and to control their position and number is to tune the geometry and topology of the confining surface. In the next section, we will introduce some basic concepts about geometry, curvature and topology and describe how these parameters can be employed to organize the defects on a liquid crystalline structure in both two and three dimensional spaces.

1.1.6.1 Confinement on curved geometries

1.1.6.1.1 Geometry of surfaces

One way to measure how sharply a curve bends is adjusting circles of different radius at different points of the curve. The radius of the best fitting circle at a given point determines the *curvature* at that point. To better understand this concept, consider a curve ζ in the plane given by $\mathbf{r}(s)$ with s being the arc-length parameter (Fig. 1.12(a)). At particular points M and N on the curve, we can draw two tangents subtending angles ψ and $\psi + \delta\psi$ with the x-axis. The curvature $\kappa(s)$ at the point M can be defined as the rate of change of ψ with respect to the arc length s:

$$\kappa(s) = \frac{\delta\psi}{\delta s} \tag{1.19}$$

If the circumference of the osculating circle of radius R(s) coincides with the arc MN, then the expression becomes:

$$\kappa(s) = \frac{1}{R(s)} \tag{1.20}$$

The curvature can take either positive or negative values depending on whether the osculating circle is above or below the curve as shown in Fig. 1.12(b).

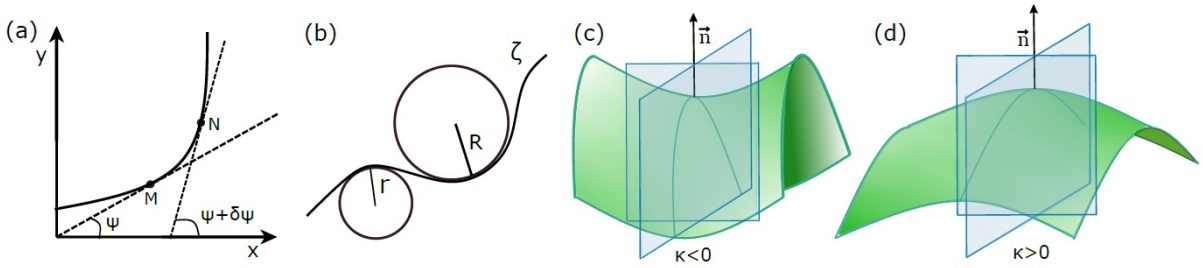

Figure 1.12: (a) Tangents to the curve at M and N are separated by an angular distance $d\psi$. The curvature at the point N is given by the limit of $\frac{\delta\psi}{\delta s}$, when M approaches N; (b) The radii of curvature, R and r are equivalent to the radii of the osculating circles at two given points. The curvature is negative(positive) when the circle is below (above)the curve. (c-d) Examples of Gaussian curvature calculated by multiplying the principal curvatures at the intersection between the surface and the orthogonal planes. In (c) the principal curvatures have different signs, i.e the Gaussian curvature is negative, whereas in (d)both principal curvatures are equal and the Gaussian curvature is positive. Adapted from[25].

In differential geometry, the intrinsic curvature can be interpreted as an extension of the planar case. Imagine a cross section of the surface in Fig. 1.12(c) containing a vector **n** perpendicular to the surface. The curvature of the resulting slice-curve can be calculated in the same manner as above. Now, consider the examples in Fig. 1.12(c) and (d). The maximal (upward) κ_1 and minimal (downward) κ_2 curvatures are called the principal curvatures and they occur in orthogonal directions. In the case of flat surfaces, the radius of curvature is infinite and thus the curvature equals zero everywhere. By combining the two principal curvatures, we can further calculate two important parameters for the geometrical characterization of surfaces: the mean curvature H and the Gaussian curvature κ, which are given by

$$\kappa = k_1 k_2, \tag{1.21}$$

$$H = \frac{k_1 + k_2}{2}. \tag{1.22}$$

Gaussian curvature is said to be bending invariant, since it remains unchanged by such deformation in a region that has not been stretched, shrink or torn. For example, a flat plane ($\kappa = 0$) can be easily rolled into a cylinder, making the principal curvatures change while keeping Gaussian curvature null. Conversely, we cannot cover a sphere ($\kappa = constant$) without stretching the sheet of paper. To match the intrinsic geometry, paper fibers usually form crumples and ridges displaying a wide distribution of local Gaussian curvatures.

1.1.6.1.2 Spherical surface: where geometry meets topology

When trying to wrap a ball with a foil, one quickly encounters the geometric abyss between paper inherent flatness and the sphere natural curvature. During the process one may even notice that crinkles get bigger and bigger. Interestingly, an alternate way to cover the surface of the sphere without wrinkling the foil is to decompose it into domains similar to those displayed at the surface of a soccer ball, i.e both by hexagons and pentagons. But why not only by hexagons? In fact, under positive curvature, hexagons try to close up on themselves reducing the distances between neighbors. As a consequence, some hexagons have to be replaced by pentagons to match the metric

restrictions. In other words, mapping the entire soccer ball with only hexagonal patches is impossible. Formally, this concept can be explained by the Euler characteristic, χ, a topological invariant under smooth transformations of the surface such as twisting and bending:

$$\chi = F - E + V \tag{1.23}$$

where V, E and F are respectively the numbers of vertices, edges and faces of any tessellation of the surface.
According to this formula, the soccer ball needs 12 pentagonal patches interspersed with the hexagonal ones, regardless how inflated the ball is. Now imagine you replace the rigid patches of the soccer ball by stretchable rubber domains. The sphere can thus be deformed into elongated geometries such as an ellipsoid, or a narrow cylinder with caps. Curiously, Descartes and Euler discovered that variations in the shape do not have any effect on χ, and that for surfaces with the topology of the sphere (for instance all polyhedra) $\chi = 2$[25]. For this reason, χ is said to be a topological characteristic. This idea does not only apply to the tessellation of a surface with polygons, but also to the organisation of rods, such as the molecules of a liquid crystal, on the surface. Both the inter-layer separation distance and the alignment along the director $\mathbf{n}$ are preserved, regardless the shape of the surface. The mathematical relation that allows us to bridge the gap between topology and the Gaussian curvature κ of a surface S, is given by the Gauss-Bonnet theorem[18]:

$$\chi = \frac{1}{2\pi} \oint_S \kappa dS = 2(1 - g) \tag{1.24}$$

where the term g designates the genus number and counts the number of holes or handles in the surface. A sphere, has no holes and thus its genus is null and $\chi = 2$. A torus (doughnut shape), on the other hand, has one hole yielding to $\chi = 0$, and so on.
Closed surfaces sharing the same genus (and thus the same χ), such as the sphere and the ellipsoid, are homeomorphic. This means that they can be mapped into one another while keeping their topological properties constant[26].

1.1.6.1.3 Defects and topology

We recently mentioned that wrapping curved geometries with a flat sheet resulted in heterogeneities in the sheet topography, such as wrinkles and ridges. In a general way, this phenomenon arises from the impossibility to conciliate incompatible geometrical requirements. Interestingly, on smooth rounded shapes, geometrical frustration results in the formation of topological defects.

Let's first address this problem in 2D by calling S a closed surface, immersed in a direction field $d : \mathbb{R}^2 \to \mathbb{R}^2$. Singularities occur for a particular position (x, y) when $d(x, y) = 0$. Singular points P_i can be classified by their index around a neighborhood Ω, in a similar fashion as the winding number (eq. 1.15):

$$s_s = \frac{1}{2\pi} \int_{\delta\Omega} \mathbf{n}.d\phi \tag{1.25}$$

In addition, if we design a cycle $\gamma(s)$ equal to the boundary of the neighborhood Ω , we obtain the field of singularities:

$$s_b = \frac{1}{2\pi} \int_{\gamma(s)=\delta\Omega} \kappa dS \tag{1.26}$$

Since S is a surface with boundaries, the total index of singularity, corresponds to the sum of the interior and boundary indices:

$$\sum_{i=1}^{n_s=n_i+n_b} s^i = \sum_{i=1}^{n_i} s_b^i + \sum_{i=1}^{n_b} s_s^i \tag{1.27}$$

where n_i and n_b represent the number of singularities embedded on the surface and on boundaries respectively[27]. Formally, the net topological charge of defects (given by the indices s) on a two dimensional system can be connected to the euler characteristic through the Poincaré-Hopf theorem:

$$\sum_i s^i = \chi \tag{1.28}$$

For instance, imagine a disk where the vector field is forced to orient normal to the boundaries, as in Fig. 1.13 (a). We observe that the tilt angle ϕ_b at the boundaries does not vary while describing the 2π cycle $\gamma(s)$ along the boundary, yielding $s_b = 0$. In the bulk, on the other hand, the director describes a 2π rotation along the same $\gamma(s)$ circuit, representing a contribution of $s_s = +1$ to the topological charge. By adding both indices, we find a global value $s = +1$ matching the Euler characteristic of a disk. In a different configuration, we can imagine the same disk with weak anchoring at its surface, see Fig. 1.13 (b). The alignment in the bulk seems to be constant, so that no topological defects nor associated charges are present. This is compensated at the boundaries, where the director field rotates by 2π along $\gamma(s)$, providing the $s = +1$ charge required by the Poincaré-Hopf theorem. By extending this example to higher dimensions, we find that a nematic sphere under strong homeotropic anchoring hosts a virtual defect of charge $s = +1$ in its center. This is indeed a direct consequence of the Gauss-Bonnet theorem eq. 1.24 which dictates that the sum of the topological charges N of all point defects inside the bounded volume is[17]:

$$\sum_i N^i = \chi/2 \tag{1.29}$$

For a sphere ($\chi = 2$) this leads to a global charge of +1, held by the bulk hedgehog. In the next section, we will see that point defects come in a wide variety of configurations on spherical systems depending on the anchoring conditions imposed to the liquid crystalline molecules as well as on the elastic properties of the liquid crystal.

1.1.7 Elastic multipoles

When a microsphere is embedded in an aligned nematic, it produces local distortions in the director field that typically result in the formation of one or several topological defects linked to the particle. These defects can have different nature and organize themselves around the spherical inclusions just as electrons do at the outermost shells of chemical elements. The local conformation near the particle surface basically depends on three main parameters: The particle size, the anchoring conditions at the particle surface and the elastic properties of the liquid crystalline phase.

The distortion of the director in the neighbourhood of a particle is accounted for by means of the de Gennes–Kleman length $L = K/W$, representing the ratio between the average elastic constant and the anchoring coefficient (see section 1.1.4). In principle, if the inclusion does not cause any deviation of the liquid crystal orientation and the director

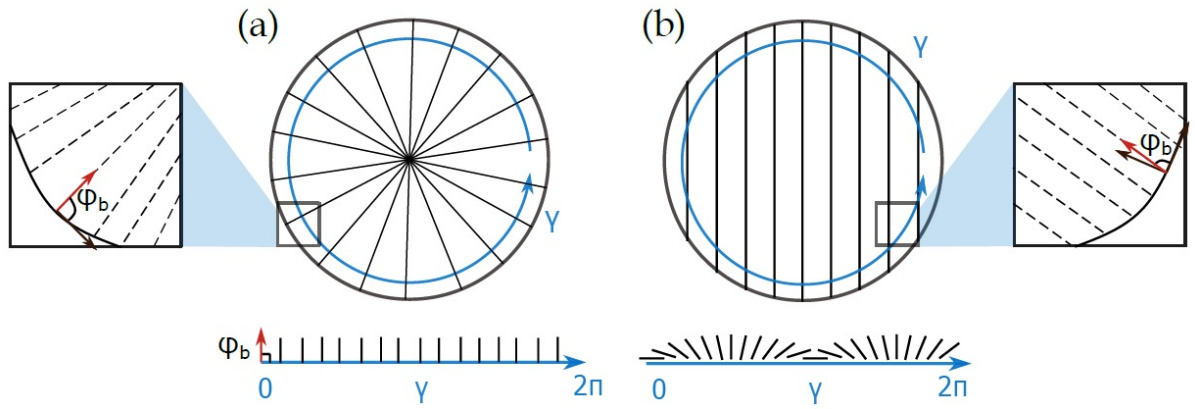

Figure 1.13: Evolution of the orientation field at the boundaries of a disk. (a) For normal director orientation the angle ϕ_b is constant all along the 2π γ loop, so that no charge is generated at the boundaries. Only the bulk contributes with a $s_s = +1$ charge. (b) When the director is uniformly aligned, ϕ_b varies from 0 to 2π along γ, resulting in a $s_b = +1$ topological charge at the boundaries. Adapted from[28]

remains uniform everywhere, the energy penalty takes the form of the anchoring energy (integrated over the surface of the particle) and scales as $F_{anch} \sim WR^2$. Conversely, if the director deviates at the vicinity of the particle according to the anchoring conditions, the elastic energy of the distortion scales mostly linearly with R as $F_{elastic} \sim KR$. In practice, the final conformation arises from the balance between both anchoring and elastic energies and is strongly dependent of the particle radius R. Therefore, for small particles $R << K/W$, the surrounding director field remains uniform, while for large particles $R >> K/W$, the surface anchoring dominates and the director deviates in the neighborhood of the particle[29]. The distortion becomes more important with the particle size, leading to different types of defects depending on the anchoring cues at the particle surface. In the following sections, we will describe different kinds of defect configurations emerging upon the incorporation of spherical inclusions in an anisotropic liquid crystal.

Dipolar structures: Particles with Hedgehogs

Dipole-like structures typically appear when the spherical inclusion imposes normal molecular anchoring on the nematic LC. Topological defects appear in the form of a hyperbolic hedgehog and of a radial hedgehog of charge $q = 1$ to conserve the topological charge of the whole system. In experiments by Poulin et al.[30], where spherical droplets were disperesed in a nematic, only the negatively charged defects were visible, since radial hedgehogs reside in the center of the particles, they are virtual.

Under crossed polarizers, the radial hedgehog at the center of the aqueous droplet features a characteristic optical texture, known as the Maltese cross, consisting in a dark four-armed star extending over the particle, see Fig. 1.14 (a). Hyperbolic hedgehogs, in turn, produce an optical texture consisting of a distorted star in the region connecting droplet pairs, see Fig. 1.14 (b). Because the droplet chains are stable, the hedgehogs sitting between the droplets are thought to play the role of topological and energy barriers that prevent the spontaneous collapse of the droplets. The separation distance between a droplet and the hedgehog increases with the droplet size. Furthermore, the droplet and its associated hedgehog behave as an elastic dipole that aligns with the field. The chain formation results, thus, from the long-range anisotropic interaction between droplets[30].

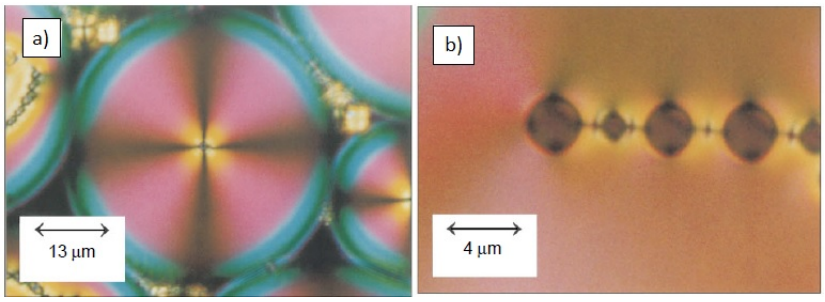

Figure 1.14: Aqueous droplets embedded in a 5CB liquid crystal observed by polarized light microscopy. (a) A radial hedgehog is created inside the droplet due to the homeotropic anchoring imposed at its surface. (b) Hyperbolic hedgehogs appear at the vicinity of each droplet and display a star shape under cross polarizers. Extracted from[30]

Quadrupolar structures and Saturn ring defects

So far we have considered point defects lying either inside or next to the spherical particles. Yet, other significant defect conformations, minimizing the Frank free energy, can be also observed. As initially predicted numerically by E.M. Terentyev[31] and later proved experimentally by H. Stark[32], the hyperbolic hedgehog can be transformed into a singular $-1/2$ loop encircling the particle at the equator under the action of a magnetic field. In this transformation the point defect represented in Fig. 1.15 (c) is opened into a ring, properly called *Saturn ring* (Fig. 1.15 (d)), that preserves the $q = -1$ charge of the hyperbolic hedgehog in three-dimensions. Similarly, a radial hedgehog can be smoothly transformed into a positively charged disclination ring, see Fig. 1.11 (a),(b).
Detailed theoretical and experimental analysis further demonstrated that without an external field (magnetic or electric[33]) the dipole is energetically favored over the metastable quadrupole. Saturn Ring defects can however emerge in three additional scenarios: when the normal surface anchoring is weak[34], when confining the particle to a thin planar liquid crystal film[35], and when decreasing the diameter of the microsphere[36]. In particular, when the anchoring strength is lowered below a critical value, the ring shrinks to sit at the surface of the particle, rather than at a finite distance from the surface. This Saturn-ring configuration is the second one of quadrupolar symmetry (Fig. 1.15 bottom).

Hexadecapolar structures: Coexistence of point defects and Saturn rings

Unlike atoms with filled s-, p- and d- orbitals, which can be found in nature or created artificially by human manipulation, elements holding full -g shells, are still unknown. Interestingly, this latter structure shares symmetry with hexadecapolar nematic colloids. Such symmetry arises from the superposition of two quadrupoles and it is usually obtained by imposing conically degenerate boundary conditions at the particle embedded in the nematic field. This results in the simultaneous apparition of two point defects at the poles (boojums) and a Saturn ring disclination around the equator of the particle, as shown in Fig. 1.16. This structure has a quadrupolar elastic moment, but when connected with another particle of identical characteristics, the overall system displays a strong hexadecapolar moment[37]. The sketches and the micro-graphs of single and composite hexadecapoles are presented in Fig. 1.16.

Under polarized light, hexadecapoles display eight bright lobes separated by eight dark lobes at the periphery of the colloid, each of them corresponding to an angular sector of inter-particle interaction. Whether these regions are attractive or repulsive,

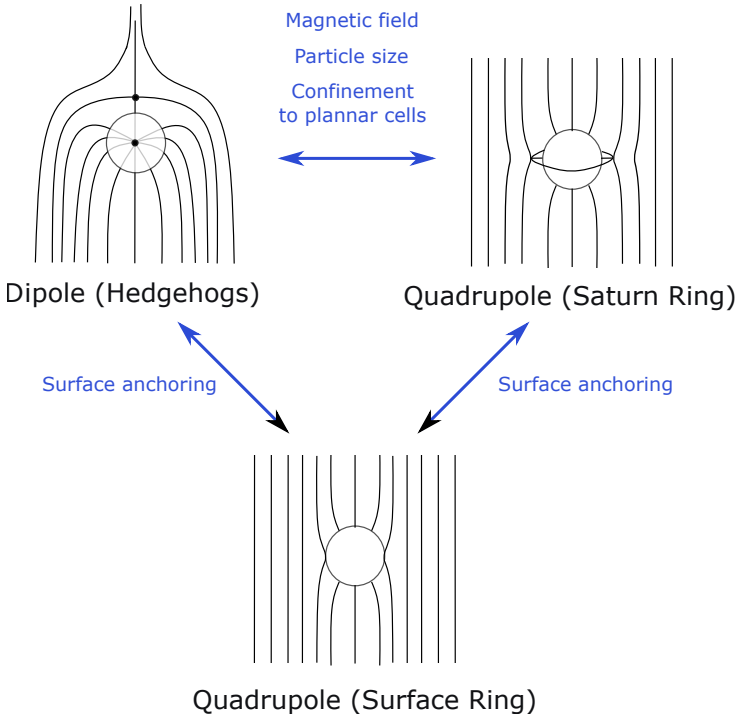

Figure 1.15: Director field around a spherical inclusion with homeotropic anchoring at its surface. Inside an uniformly aligned nematic liquid crystal, three configurations are possible: (i) the dipole consists of two hedgehogs, one virtual (radial) and one residing in the continuous medium (hyperbolic); (ii) the Saturn-ring is a -1/2 disclination loop surrounding the particle at the equator; and (iii) the surface-ring configuration. Conformations can be switched from one to another by varying several parameters. Adapted from[32].

the interaction occurs basically along radial directions[38]. As a consequence of the rich energetic landscape surrounding hexadecapolar systems, the angular positioning between building elements can be controlled in order to create of a vast spectrum of two and three-dimensional crystal lattices. Recent advances on this topic will be presented in section 1.1.8.

1.1.8 Colloidal assemblies in liquid crystals

Colloidal organization in liquid crystals results essentially from two distinct processes: i) elastic interactions between the particles induced by the liquid crystal and ii) the action of external forces.

The first mechanism is observed when dispersing colloidal particles in a thin liquid crystal layer confined between two glass plates. One can rapidly notice that the particles spontaneously arrange into structures that feature a certain degree of local order. Naturally, one can think that the aggregation process results from the combination of Van der Waals forces and repulsive forces, including steric ones; however, unlike suspensions in isotropic fluids, the interactions between nematic colloids are much stronger, of the order of $1000k_BT$. The reason is that the interactions between nematic colloids have an elastic origin, as explained in section 1.1.7, they result from the distortion induced by the particles in the liquid-crystal. Because nematic liquid crystals display long-range orientational ordering, the elastic distortions between the embedded particles are also of long range and propagate through distances far away from the microsphere.

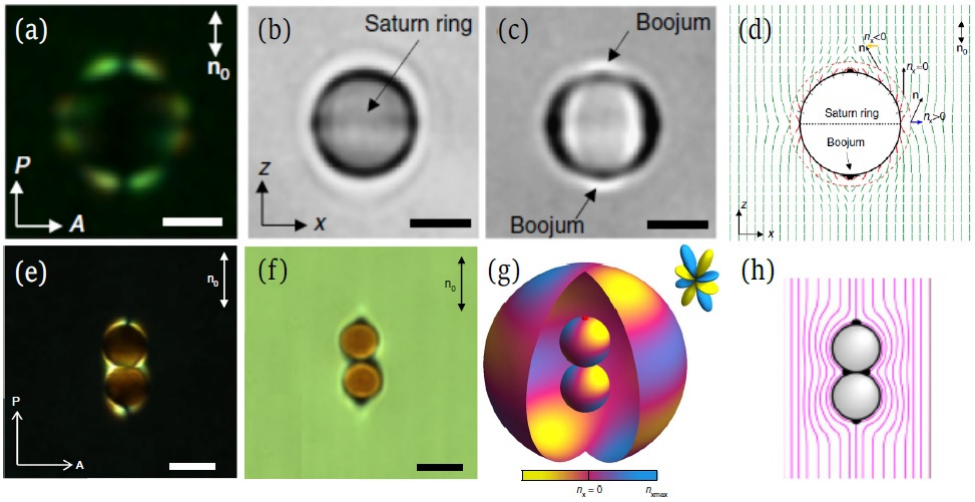

Figure 1.16: Elastic hexadecapoles induced by a colloidal particle. Optical micrographs obtained by (a,e) polarized light and (b, c, f) bright field microscopy. Particles exhibiting conically degenerate anchoring conditions at their surface develop two surface point defects and a Saturn ring loop around the equator. (g) Color-coded diagram of the x-component of n(r) shows that an hexadecapolar moment can be obtaining by assembling two quadrupolar monomers together. (d,h) Director field configuration around an hexadecapolar structure. Extracted from[39] and[37]

Imagine two colloidal particles, each of them surrounded by a distorted field extending over several particle diameters. When the two particles are close to each other, their distorted regions overlap causing either attractive or repulsive interactions. If the distortions induced by the two particles match, the colloids will approach and remain close together. Otherwise, the overlap will increase energy, making them repel from each other. The force resulting from the overlap of the deformed regions originated by different particles is referred to as *structural force* and in nematic systems it is anisotropic. When particles are far from each other, none of these effects are observed since the overlap is non-existent or negligible.

When colloidal particles are immersed in a planar nematic cell, they usually form linear or kinked structures oriented at specific angles with respect to the far-field director. The first configuration (linear chains) is well exemplified by the experiments by Poulin et al[30], described in section 1.1.7. They dispersed water droplets in a nematic pentylcyanobiphenyl (5CB) liquid crystal, with a small amount of surfactant to impose normal anchoring at the droplet surface, and they confined the dispersion between uniformly aligned planar plates. Under these conditions, a radial hedgehog, sitting in the center of the droplet, and its hyperbolic counterpart, placed in the LC near the particle, create a local director field connecting the radial director field produced by the droplet with the planar far field. In analogy with electrostatics and the multipole expansion[40], this pattern corresponds to that of a conducting sphere with charge Q in an external electric field E. When two droplets are dispersed in the planar nematic cell, they act as elastic dipoles, feeling an attractive inter-particle interaction. Experimentally, one can see that when particles are separated, they slowly approach each other. However, as their separation distance decreases, they accelerate, achieving the maximal speed when they reach each other. Between neighboring droplets, the hyperbolic hedgehog provides a repulsive short-range barrier that prevents them from being in contact. These observations were further analyzed numerically by Brochard and de Gennes[41] and experimentally by Kreuzer et al.[42] in nematic liquid crystals containing magnetic and silica nanoparticles, respectively.

They demonstrated that, as two particle approach, with their elastic dipoles parallel and colinear, the total free energy of the system decreases.

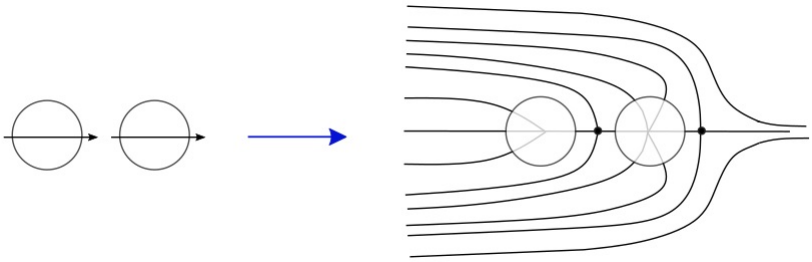

Figure 1.17: Colinear interaction between two particles embedded in a nematic liquid crystal. The director field reorganizes around the chain of dipolar inclusions.

This dipole-dipole interaction leads to the spontaneous formation of linear chains, whose length depends on the number of particles and on their relative location. Remember that due to the anisotropy of the pair interactions (Fig. 1.17), only particles whose surrounding field is aligned with the director and points towards the same direction would participate on such topological "ferroelectric" chaining.

Other type of linear structures are produced by nematic colloids with different symmetry, such as quadrupoles or hexadecapoles. Isolated quadrupoles feature two surface boojums located at the poles of the microsphere or a Saturn ring defect encircling the particle equator. The first conformation arises when imposing tangential alignment at the surface of the sphere. Under such conditions, elastic interactions will make them form chains tilted 30° on average with respect to the far-field alignment. Similar to dipolar interactions, quadrupoles revealed a strong angular anisotropy in their interaction force as shown in the experiments by Kotar et al.[43] and in the theoretical works by Ruhwandl and Terentjev[44]. Saturn ring defects, on the other hand, can be observed on particles imposing homeotropic molecular anchoring on the nematic liquid crystal. When comparing the interaction forces between pairs of dipoles and quadrupoles in thin planar cells, Škarabot et al.[45] demonstrated that the binding energy of quadrupolar structures is one order of magnitude weaker than that of the dipole–dipole interactions. As a consequence, kinked quadrupolar chains Fig. 1.18 are more fragile and may sometimes be affected by external perturbations, such as temperature changes and flows in the liquid crystal.

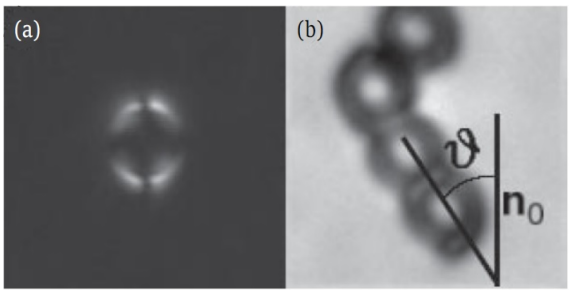

Figure 1.18: (a) Colloidal inclusion in a nematic liquid crystal observed under polarized light. Strong tangential anchoring at the particle surface induces the formation of two boojums indicating the quadrupular character of the particle. (b) Quadrupoles aggregate at an average angle of 30° with respect to the director, forming either linear or kinked chains. Extracted from[43]

The elastic interactions between hexadecapolar colloids were studied by Senyuk et al.[39]. Surprisingly, unlike dipolar and quadrupolar interactions, elastic forces between hexadecapoles are relatively short-ranged and become strong only at distances of four-to-five particle radii. Interestingly, they exhibit eight separated regions of favored interaction making the angular dependence of these forces extremely rich. In particular, the regions of attraction correspond to the bright zones in the POM micrographs (Fig. 1.19) and its angular orientation to the minima of the pair interaction potential U_{int}. Although this means that there are eight minimal potentials, only four sites can be occupied simultaneously per plane by particles of similar sizes due to excluded volume effects. In practice, hexadecapoles form linear chains oriented along one of these sites, i.e. with an angle $\theta_1 \approx 22° - 26°$ or $\theta_2 \approx 64° - 75°$ with respect to the director. Kinked chains with different combinations of angles θ_1 and θ_2 can be also produced, as shown in Fig. 1.19 (a-b). More complex structures such as planar colloidal lattices with rhombic elementary units were also predicted, but have not been experimentally observed so far.

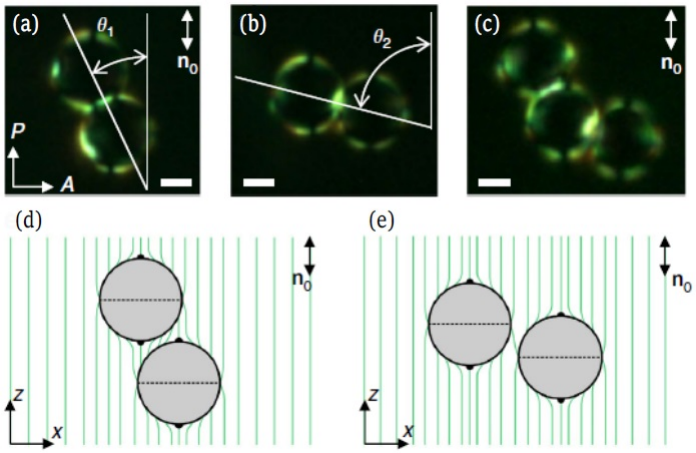

Figure 1.19: (a-c) Polarized light micrographs of hexadecapolar dimers and their respective field diagrams (d-e). Particles can form either linear chains oriented at angles $\theta_1 \approx 22° - 26°$ or $\theta_2 \approx 64° - 75°$ from the director, or kinked arrangements (c). Extracted from[39]

Although spontaneous self-assembly can lead to interesting colloidal assemblies, there are some issues that hinder the formation of well-organized large structures. For instance, large particles, where Brownian motion is negligible, are not able to explore the space and interact with distant particles. To address this issue, scientists usually rely on an alternative method which consists in manipulating the particles externally to force their approach. An appropriate tool for this is *optical tweezers*, which enable trapping micron-sized objects by focusing a strong laser light on them. Large structures have been produced by trapping the particles one by one, anywhere in the sample, and relocating them at customized positions and orientations close to each other[15,46]. The assembly can be either stabilized by simple elastic inter-particle interactions or by heating locally to induce the nucleation of different types of knots and entanglements that hold the structure together. For practical reasons, the details of optical trapping techniques will be presented in the Materials and Methods section. Examples of the resulting assemblies, on the other hand, will be shown in section 4.2. We would like to highlight that directed assembly enables a better control over the position, the type of topological interactions and the number of particles involved, than spontaneous self-assembly. The former approach offers interesting perspectives for scaling-up from the micro-scale to larger dimensions, paving the way for promising applications, such as electronic or optical devices.

1.1.9 General principles of particle motion

Brownian motion

In the simplest scenario, small particles dispersed in a isotropic fluid move randomly due to the thermal fluctuations of the medium. Typically, this leads to a Gaussian distribution of the particle displacement δ in the plane during a time lag τ (bottom panel of Fig. 1.20 (b)).

Another consequence of classical diffusion of Brownian particles is the linear growth of the mean square displacement (MSD) with time $\langle \Delta r^2 \rangle = 6D\tau$, where D is the diffusion coefficient expressed via the Stokes-Einstein relation, $D = \frac{k_B T}{6\pi\eta R}$ [29]. At the same time, the particle mean displacement is zero. In complex fluids, Brownian motion can diverge from this classical behavior and display anomalous modes of diffusion in different directions of space. In nematic liquid crystals, for example, where the director is invariant with respect to a rotational symmetry axis, Brownian motion is anisotropic and can be described by means of $D_{(\parallel)}$ and $D_{(\perp)}$, the diffusion coefficients along and perpendicular to $\mathbf{n}$ respectively. At relatively large time scales, the Stokes-Eintein relation thus becomes $D_{\parallel,\perp} = \frac{k_B T}{6\pi\eta_{\parallel,\perp} R}$, where the viscosities $\eta_\parallel \neq \eta_\perp$ depend on the nematic orientation around the particle[29]. This behavior was first evidenced in theory for a particle suspended in an anisotropic liquid where the drag coefficient was found to be also anisotropic[47–49] and in experiments by Loudet et al. who showed that $D_\parallel > D_\perp$ for tangentially anchored spherical quadrupoles in a nematic LC.

Beyond anisotropy in the diffusion coefficient, particles in complex fluids may exhibit anomalous MSDs, scaling as $\langle \Delta r^2 \rangle \sim \tau^\alpha$. The exponent α indicates whether the process is sub-diffusive ($\alpha < 1$), as in surfactant dispersions,[50] or super-diffusive ($\alpha > 1$), as in systems of swimming bacteria[51] and polymer-like micelles[52]. Eventually, anomalous diffusion may also be correlated with the director field configuration surrounding spherical inclusions, and hence, with the anchoring conditions imposed to the liquid crystal molecules. Particles with planar surface anchoring usually display a sub-diffusive behavior, while particles with homeotropic alignment behave as super-diffusive systems[53]. This particularly occurs at time scales of the order of seconds (above the typical time associated to the director relaxation around the sphere) at which diffusion is strongly affected by the director deformations and their relaxation. Both the director field $\mathbf{n}(r,t)$ and the velocity field $\mathbf{v}(r,t)$ of the continuous medium are subject to the fluctuations of the particle in space and time that make the particle either accelerate or decelerate. To better illustrate this concept, consider a tangentially anchored colloid. A displacement of the sphere, to the left for example (Fig. 1.20 (c)), results in an increase of the elastic energy on the left side and to an energy relaxation on the right side. This energy difference causes a restoring force that pushes the particle backwards in the opposite direction (from left to right) slowing the material flow down and decreasing $\mathbf{v}(r,t)$ (sub-diffusive behavior) in a process called the *backflow effect* [1]. Curiously, this phenomenon is reverted when the anchoring at the particle surface is normal. In such case, the dipolar elastic distortions display "fore-aft" symmetry around the particle giving rise to a topological defect near particle's surface. The fluctuations this time result in an elastic force towards the defect that is no longer counter-balanced, thus driving the particle into a super-diffusive translation.

[1] The backflow can be seen as an hydrodynamic flow, resulting from the director field deformations, that drives the particle into motion while restoring the equilibrium state of the LC material.

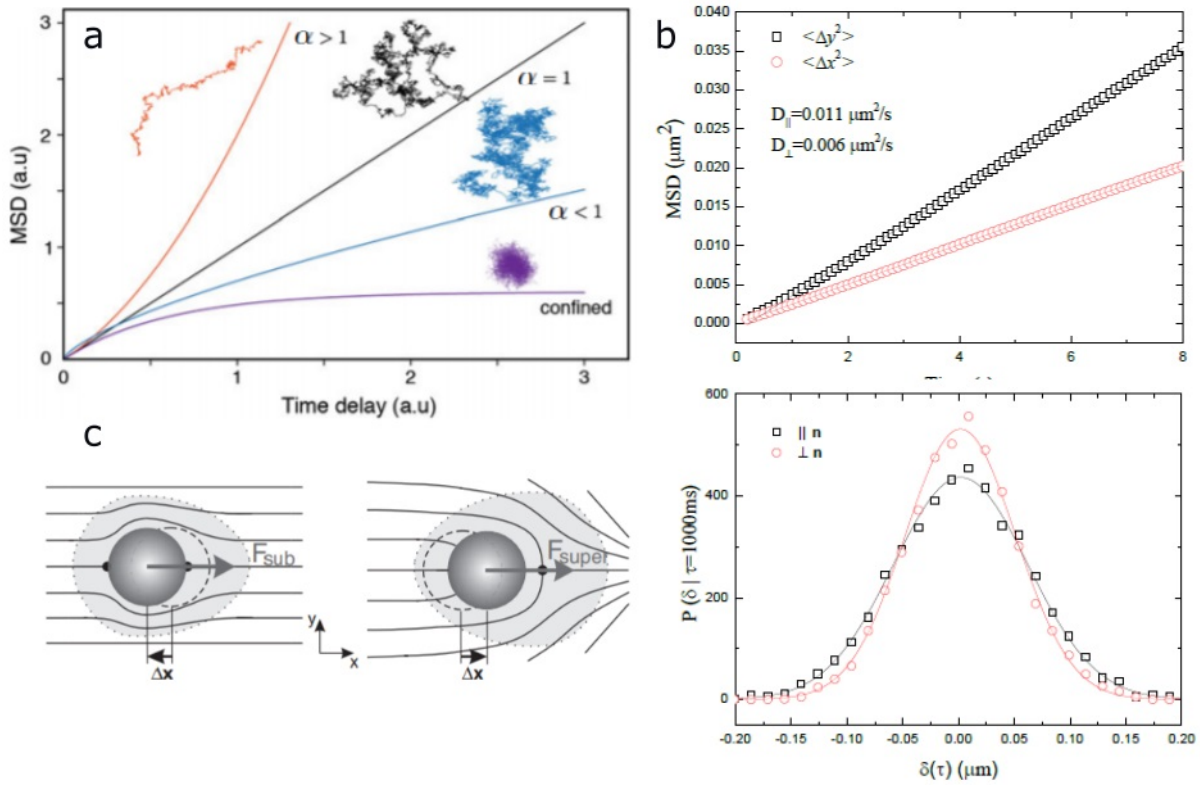

Figure 1.20: Motion of Brownian particles. (a) Classification of diffusive behaviors based on the mean square displacement (MSD) plots. The MSD grows linearly with time for a generic diffusive regime ($\alpha = 1$) and deviates from linearity for sub-diffusive ($\alpha < 1$) and super-diffusive ($\alpha > 1$) regimes. (b) Top: MSD vs time lag for the two components of displacement (along and perpendicular to n). Bottom: Gaussian probability distribution of displacements of normally anchored colloids dispersed in a nematic LC. (c) Director deformations around a tangentially anchored (left) and a normally anchored (right) colloid. In the first case a restoring force slows down the self-diffusion (sub-diffusion) and in the second, a fluctuative splay on the right side moves the sphere toward the defect. Adapted from[29,54,55]

Transport of active particles in liquid crystals

Anomalous diffusion in liquid crystals can be driven by different methods, and even controlled in terms of propulsion speed and particle orientation. These methods consist in either applying external forces to the particles, or internally driving the system by active forces. Typical examples of external actuation include linear and nonlinear electrophoresis, in which particles are driven by direct current (d.c) or alternating current (a.c) electric fields, respectively. In this case, anomalous super-diffusion is observed either along or perpendicular to the electric field, depending on the experimental details[56,57]. Additionally, with this method, the particle speed can be controlled by varying the amplitude and frequency of the applied field[53]. This method has been also employed to induce anomalous diffusion in anisotropic Janus particules, which are able to move along any direction in the oriented nematic when tuning the amplitude and frequency of an imposed electric field[58,59]. The second approach, involving internally generated motion, has been used to study the diffusion of both anisotropic and isotropic particles. The first case simply refers to rodlike particles, such as individual bacteria, that tend to swim unidirectionally in the nematic LC, aligning their long axis along $\mathbf{n}$[60–62]. Although the diffusive behavior of these systems has not being studied experimentally, theoretical studies have shown that equivalent self-propelled active rods in a nematic background display a ballistic transla-

tional motion parallel to $\boldsymbol{n}$ and a super-diffusive behavior in the transverse orientation[63]. Isotropic swimmers, on the other hand, can be active droplets composed of biological entities such as bacteria or cytoskeletal elements. Ramos et al. studied "bacterially" propelled droplets consisting of E.coli encapsulated inside water droplets dispersed in oil[64]. They showed that the droplets describe a persistent random walk, resulting from the internal turbulent flows generated by the bacterial suspension. Additionally, the persistence time, the diffusion coefficient and the average speed of the droplet were directly related to the bacterial concentration. Similar experiments were done by Rajabi et al. who replaced E.coli by B. subtilis bacteria, and the oily phase of the emulsions by a thermotropic nematic liquid crystal. Despite the chaotic internal flows, they observed that the trajectory of the droplets was rectified thanks to the anisotropic properties of the dispersing phase. Moreover, the diffusion speed was not only dependent on the concentration of the bacteria, but also on the type of defect configuration surrounding the droplets[65].

Despite the interesting phenomena observed experimentally, there is not a full theoretical framework to explain them yet, mainly because of the complexity of the problem. Yet, there have been some valuable contributions to the field. Hydrodynamic simulations coupled with a squirmer model have showed that the swimming direction of the active particles depends on the nature of the swimming mechanism: pushers follow the direction set by the nematic director, while pullers swim orthogonal to it (in a pusher the main source of propulsion is located in the back, while in a puller it is located in the front), consistently with experimental results. In particular, it has been shown that the reorientation of the particle is due to a torque originated from the coupling between the squirmer flow field and the anisotropy of the liquid crystalline viscosities[56,66]. These results were complemented by studies by Abdallah D. and Andreas M. demonstrating that the degree of anisotropy of the LC viscosities can be used to tune the direction of motion[67]. More recently, it has also been shown that the interplay between shape and surface anchoring contribute to the reorientation of the propulsion direction[68].

Other ways to induce anomalous diffusion in passive particles include the presence of inhomogeneities in the dispersing medium, such as temperature[69] or concentration gradients[69], or the incorporation of active entities in the continuous phase[70,71]. The last point, in particular, will be addressed in detail in section 4.1.3.

1.2 Active matter

Natural processes in living systems such as growth, motility and nutrition emerge from a continual flow of energy and information through complex networks, at multiple levels. The field of active matter seeks to explain how these phenomena take place; basically, how self-driven units interact with each other and with the medium they take energy from to exert mechanical forces or to systematically move. What makes them unique among more classical non-equilibrium systems is that energy extraction and dissipation occurs locally, at the level of each particle. For instance, motion in an animal or a bacterium results from an internal process, whereas in an inanimate object such as a grain of sand it usually comes from an external force imposed at the system scale. A consequence, symmetry is broken locally, allowing individuals to guide themselves autonomously rather than following a global direction dictated by an external force. Active units are usually anisotropic in shape or interact anisotropically, with their main symmetry axis setting

their direction of motion and the global orientation in a collection of particles.

Fascinating collective behaviors emerge when these active units interact with each other and with the medium they inhabit, specially at high density regimes. The active particles consume the stored or ambient energy to move systematically and autonomously exerting forces to their surroundings. The action of each particle is quickly dominated by the influence of its neighbors, which assume common directions of motion. This leads to intriguing steady states involving phenomena such as order-disorder transitions absent in systems in thermal equilibrium[72], the formation of large-scale patterns[70,73,74], uncommon mechanical and rheological properties[75,76] and sustained oscillations[77,78]. Given this generic definition, we proceed to discuss different examples of both living and non-living active systems.

1.2.1 Synthetic active matter

Motivated by the fascinating behaviors found in nature, researchers have made important efforts to synthesize model artificial active materials, which provide a controlled playground where to study the physics of these out-of-equilibrium systems. Different kinds of active particles have been conceived. Macroscopic self-propelled particles have been obtained, for instance, by vibrating colloidal[79] or granular particles[80], which can develop autonomous directional or rotational motion. Beautiful experimental systems have been also developed at a mesoscale. A recent example are janus micro-rods comprising a platinum and a gold segment immersed in an aqueous solution containing hydrogen peroxide. In this system, a catalytic reaction at the Pt end results in the individual propulsion of the rods at speeds comparable to those of multiflagellar bacteria[81]. Another interesting strategy to induce self-propulsion was proposed by Bricard et al., who exploited an electrohydrodynamic phenomenon, known as Quincke rotation, to induce the rotation of spherical micro-particles at a constant speed around a random direction in order to engineer self-propelled colloidal rollers[82] (Fig. 1.21 (i)). The examples mentioned above exhibit interesting collective behaviors when increasing the particle density. For instance, the micro-rollers developed by Bricard et al. exhibit a order-disorder transition at a critical particle concentration. At low particle densities, the system is in a disordered gas state. However, above a critical particle density, a flocking transition occurs, where the particles align their velocities along a well defined direction: the system becomes an active polar fluid with long-range order. On dry systems, Narayanan et al. have shown, for instance, that agitated back–front symmetrical particles in a quasi-two dimensional geometry develop dynamical regions that fluctuate coherently[80]. This behavior is a distinctive hallmark of the steady state of flocking systems, predicted also theoretically for dense suspensions of active colloidal particles[83,84]. Finally, we would like to mention that considerable efforts have been devoted to the development of programmable active matter made from small robots which replicate the collaborative action of animals and can be controlled to arrange into intriguing motifs by exchanging information among individuals[85,86] (Fig. 1.21 (ii)).

1.2.2 Living active matter

Active systems are predominantly of biological origin and their dynamics span over broad ranges of time and length-scales. Smallest ones involve bacteria or even nanometer-sized motor proteins, such as kinesin or dyneins, which move in a directional manner along

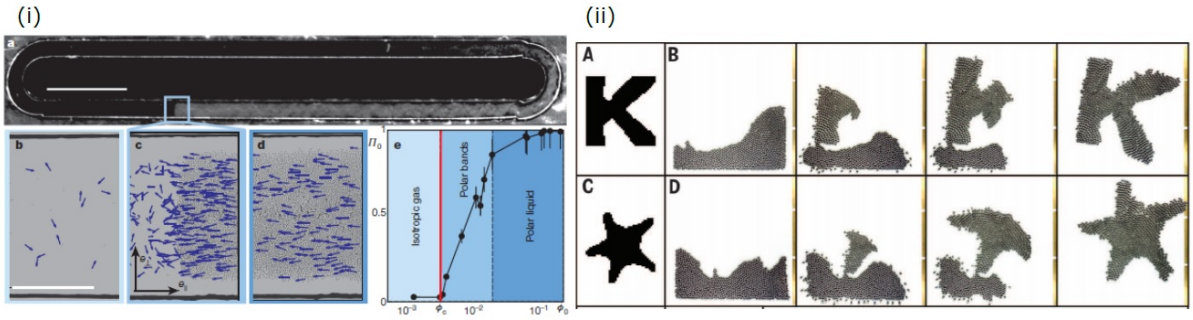

Figure 1.21: Non-living active matter. (i) Group of colloidal rollers organizing a directed collective motion. (a) The population spontaneously propagates along the racetrack. The rollers form (a) an isotropic gaseous phase, at low area fraction, (b) a single macroscopic band, at intermediate densities and (c) an homogeneous polar liquid, for high fractions. Extracted from[82]. (ii) Collective self-assembly of programmable robots (A, C) Desired shape programmed to the robots swarm. (B, D) Evolution of the self-aggregation process. Extracted from[85]

tubular materials. Larger structures include groups of social animals, which migrate over distances than can range from centimeters to kilometers while forming cohesive structures to escape from predation or to perform specific tasks. Despite operating at vastly different scales, active systems share similar properties based on well defined conservation laws and symmetry considerations, suggesting that their formation, morphology and dynamics belong to a universal class[78].

At large scales, animals such as fish or birds self-assemble and move together in flocks or schools, insects form swarms, and even human crowds or other mammalian herds organize themselves into complex patterns. A unifying characteristic between all these systems is that collective behavior emerges despite the absence of central coordination. This collective behavior results from the synergy between the autonomous motion of the active units and their chemical or biological communication. In practice, the time-space distribution of "real-world" crowd systems is detected at regular intervals via simple camera-based techniques or more complex remote sensing methods. In most cases, such tracking methods reveal that the transition from random to directed motion is mediated by the increase of the population density. A typical example is the desert locusts, which can exhibit a "solitary state" when there are few individuals and a "gregarious" collective state composed of huge oriented marching units which forage all vegetation in their path[87]. Generally these transitions are well-described by flocking models[84,88] such as the *Vicsek model* in which point-like particles evolve at constant speed and align their velocity with that of their neighbors in the presence of noise. In other cases, the interaction ruling animal collective motion depends on topological rather than metric distance. A clear evidence are birds which communicate on average with a constant number of neighbors, rather than with all of them within a fixed metric distance. The advantage of this is to maintain the flock's cohesion against the large density changes caused by external perturbations[89].

1.2.3 Active liquid crystals

Fluids composed of elongated individuals, such as bacterial suspensions[93], cytoskeletal gels[70] and cultured cells[94,95] are preeminent examples of active matter in which orientational order comes into play. Above a certain concentration, the constitutive units spontaneously self-organize giving rise to new aligned states referred to as *active* or

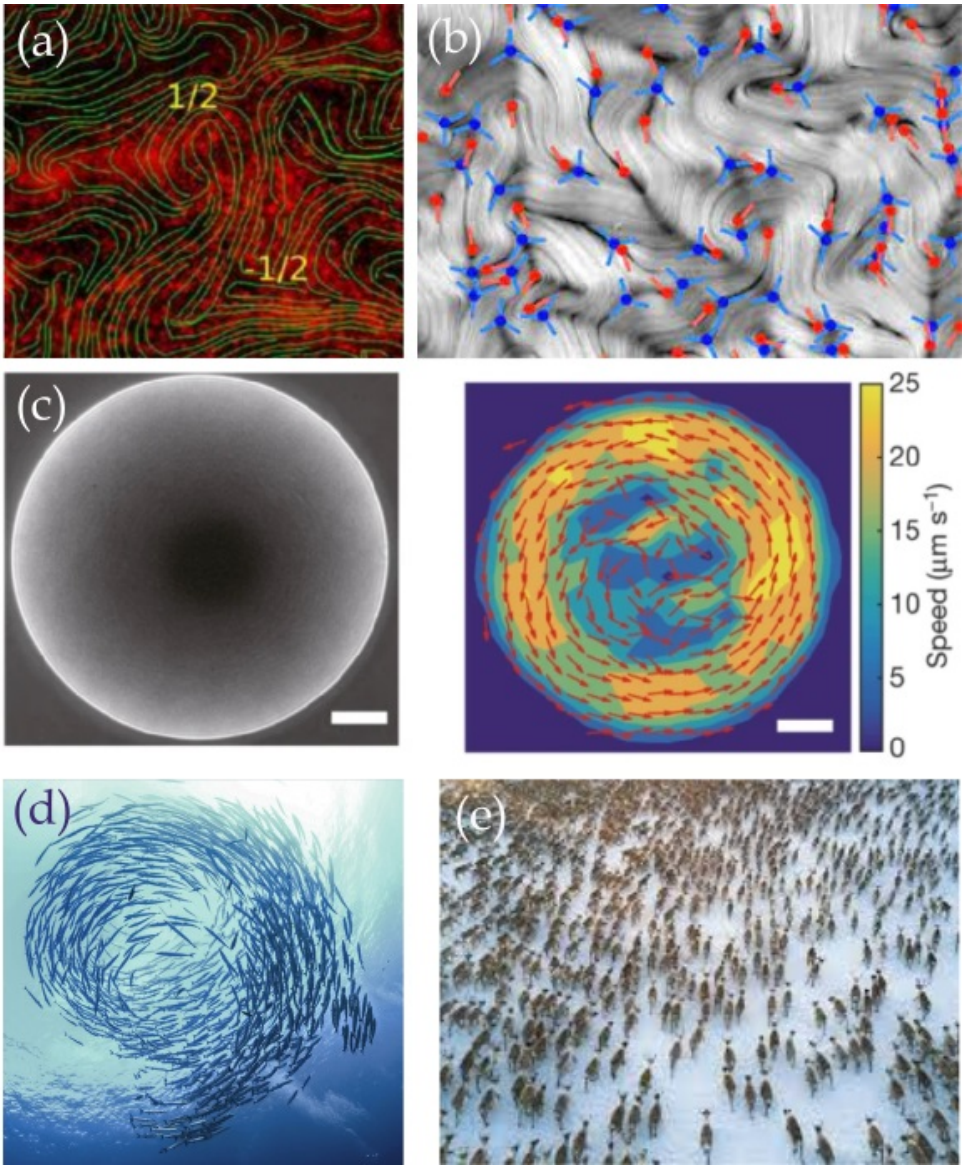

Figure 1.22: Living active matter systems. (a) Fluorescent micrograph of bacteria concentration and nematic director orientation in a living liquid crystal film[90]. (b) Microtubule-kinesin active nematics.[91] (c) Phase-contrast image and instantaneous velocity field of an active vortex of Escherichia coli cells[92]. Collective behavior of (d) fish shoals and (e) mammal herds.

living liquid crystals (ALCs) displaying a rich variety of non-equilibrium behaviors such as spontaneous flows and unusual rheology. ALCs can be defined as active systems composed of highly anisotropic units interacting with each other. They are globally classified according to two criteria: the symmetry of the active units and the nature of the forces these individuals exert between them and with the medium they inhabit.

In *polar* systems (with ferromagnetic order), such as bacteria, steric interactions between elongated particles are at the origin of the active stresses in the oriented phase[96]. In two-dimensional kinesin-tubulin active nematics, for instance, molecular motors crosslink antiparallel filaments and make them move: when two filaments meet at their minus ends, their corresponding motor heads tend to move toward the plus end, making the filaments slide with respect to each other, generating contractile stresses (Fig. 1.23 (a)). Once the filament midpoints are aligned, their minus ends separate and the filaments extend (see

Fig. 1.23 (b))[96]. This process is characteristic of *extensile* systems Fig. 1.23 (b). Note that, in this system, not all the ordered states result in microscopically moving states. Units with random head/tail orientation can organize themselves with *apolar* symmetry, meaning that the director remains unchanged under spatial reflection. In this configuration, the microtubules may move back and forward leading to a null mean velocity. In Fig. 1.23 (c) ,for example, we show an apolar conformation, where kinesin motors can walk towards the + end of the filaments without generating any stress.

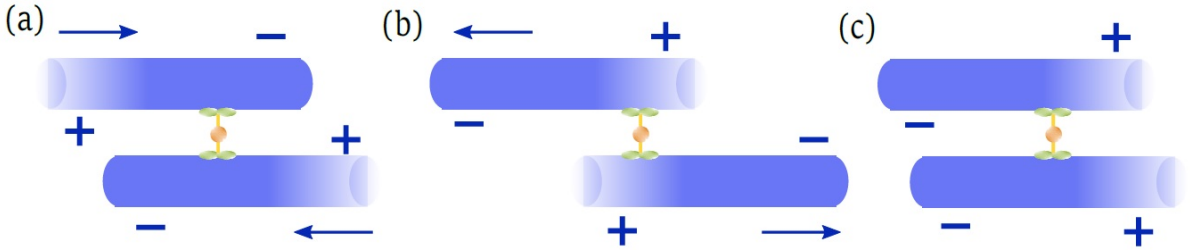

Figure 1.23: (a-b) Schematic representation of motor-driven inter-filament sliding. (a) In contractile systems, when the motor heads walk towards the plus ends, anti-parallel forces bring the filaments close to each other. When the system is extensile the filaments initially contract (a), and then extend (b) to finally separate from each other. (c) For polar-aligned filaments a motor step occur simultaneously on both rods inducing no net sliding.

A theoretical description of single ALC units is not currently achievable because of the large number of variables involved. However, global principles governing the spontaneous dynamical organization of these systems, such as topological constraints as well as length scales operating at various levels, provide a first insight for understanding the behaviors of ALCs.

Similar to passive systems, the simplest type of active nematic order is uniaxial and it is captured by the tensor parameter $\mathbf{Q} = S\langle \mathbf{n}\otimes\mathbf{n} - \frac{1}{3}\mathbf{I}\rangle$ (see section 1.1.2) where the scalar order parameter, S, measures the extent of orientational ordering. In general terms, the evolution of the local order obeys the following nematodynamic equation:

$$\frac{D\mathbf{Q}}{Dt} - \mathbf{S} = \Gamma\mathbf{H} \tag{1.30}$$

The nematic order parameter being traceless and symmetric can be decomposed by means of $\mathbf{A}$ and $\mathbf{\Omega}$, the symmetric and anti-symmetric parts of the velocity gradient tensor ($\boldsymbol{\nabla}\mathbf{v}$). The advection term is hence generalized by $\mathbf{S} = (\mathbf{A} + \mathbf{\Omega}).(\mathbf{Q} + \frac{1}{3}) + (\mathbf{A} - \mathbf{\Omega}).(\mathbf{Q} + \frac{1}{3}) - 2(\mathbf{Q} + \frac{1}{3})(\mathbf{Q} : \boldsymbol{\nabla}\mathbf{u})$ in response to the nematic order parameter. The relaxation dynamics of the nematic toward the minimum energy configuration are represented, on the other hand, by the molecular field $\mathbf{H} = -\frac{\delta F_{LdG}}{\delta Q}$, and are controlled though the collective rotational diffusion constant Γ.

Based on this description, one would expect to recover a perfect alignment along $\mathbf{n}$ as S approaches the unity. In motor-propelled cytoskeletal active nematics, such alignment exists at the level of single filaments: extensile active stresses drives bundles of parallel microtubules to extend along a preferential direction $\mathbf{n}$, so that in the absence of an external perturbation the system develops a long-range orientational order. However when expanding the study to the whole viscoelastic network, such description is not sufficiently accurate. Similar to many other active systems, in MT-based active nematics, emergent behaviors develop at larger scales and the alignment observed between microscopic filaments is replaced by large nematic domains undergoing buckling, folding, fracture and

simultaneous self-healing[70]. To understand these fundamental differences at both microscopic and mesoscopic levels, one should recall that the active units dissipate energy through a surrounding medium. When the medium is "wet" as in most living liquid crystals, hydrodynamic interactions may occur with the solvent and should be incorporated to the model[97]. Therefore the dynamics of the suspension of active units and fluid are accounted for by relating ρ, the fluid density, and $\mathbf{v}$, the fluid velocity in the generalized incompressible Navier- Stokes equation:

$$\rho \frac{D\mathbf{v}}{Dt} = \boldsymbol{\nabla} \cdot \Pi \tag{1.31}$$

where $\frac{D\mathbf{v}}{Dt} = \partial/\partial t + \mathbf{v} \cdot \boldsymbol{\nabla}$ is the material derivative. For incompressible active nematics, the total asymmetric stress tensor Π is expressed by the sum of elastic and active stresses as follows:

$$\boldsymbol{\nabla}\Pi = \eta \boldsymbol{\nabla}^2 \mathbf{v} + \boldsymbol{\nabla} p + \boldsymbol{\nabla} \cdot (\Pi^{active} + \Pi^{elastic}) \tag{1.32}$$

where η is the viscosity, p the bulk pressure and Π^{active} (resp. $\Pi^{elastic}$) the stress from the nematic activity (resp. elasticity). The active contribution $\Pi^{active} = -\alpha \mathbf{Q}$ depends on the isotropic energy input α, which we will refer later to as the activity of the system, yielding to the driving force:

$$f^{active} = -\alpha \boldsymbol{\nabla} \cdot \mathbf{Q} \tag{1.33}$$

This implies that any gradient in $\mathbf{Q}$ will produce a flow field, which is extensile for $\alpha < 0$ and contractile for $\alpha > 0$. Activity, also leads to a curvature-induced current, which displaces active units from fast flow regions towards slow moving zones[98]. The α parameter commonly depends on the concentration of cross-linkers and on the consumption rate of chemical energy.

In terms of the concentration c of active units, the governing equation can be formulated as:

$$\frac{Dc}{Dt} = \partial[\mathbf{D}\partial c + \alpha c^2 \partial \mathbf{Q}] \tag{1.34}$$

with $\mathbf{D}$ the anisotropic diffusion tensor. According to the concentration of nematogens of length l, the system will either behave as in an isotropic or a nematic phase, with the isotropic-nematic transition occurring at a critical concentration $c^* = 3\pi/2l^2$, in two dimensions. These emergent flows result in complex patterns, qualitatively similar to cytoplasmic streaming[70,99] with the continuous creation and destruction of defects pairs.

In this work, we focus on motor-propelled cytoskeletal extracts in which kinesin clusters are responsible for locally sorting the polarity of isolated bundles to develop rich dynamics driven by the interplay of activity, nematic order and directional flows.

1.2.3.0.1 Types of instabilities and active turbulence

In passive liquid crystals, instabilities and other out-of equilibrium behaviors such as shear banding[100], rheochaos[101] or transitions involving the reorganization of the director field are mediated by external forces[102], essentially shear flows or electric and magnetic fields. In active liquid crystals on the contrary, a similar wealth of phenomena occurs spontaneously by internally generated forces. A remarkable property of ALCs is the apparition of spontaneous flows under certain physical chemical conditions as predicted by seminal studies of Voituriez. et al. They identified an instability, reminiscent of the classical "Freedericksz" transition, in thin passive nematic LCs, but in which the driving force is the internal activity of the system rather than an external field[103,104]. Specifically,

they predicted that above a critical thickness or a critical activity the homogeneous state is unstable and transits to a flowing state[102]. The critical activity attributed to these instabilities can be written as follows:

$$\alpha^{\pm} = \frac{\pm 4\pi^2 K[2\eta + \gamma S_0^2(1 \pm \lambda)^2]}{\gamma c_0^2 L^2 S_0(1 \pm \lambda)} \tag{1.35}$$

In this equation, λ corresponds to the nematic flow-alignment parameter, γ to the rotational viscosity, K to the elastic constant of the system, η to the viscosity and S_0 to the order parameter in a homogeneous state of density c_0 . When $|\lambda|< 1$ the director continuously rotates and nematics are said to undergo flow-tumbling. When $|\lambda|> 1$, on the other hand, a flow aligning regime is attained and the director tends to orient along a unique angle with respect to the flow direction. Usually, molecular nematic LCs can align quickly and obey $|\lambda|> 1$; however, for larger objects, the alignment is less efficient than the reorganization of the material, and thus, they develop flow tumbling. Additionally, the sign of λ indicates the shape of the individual units: λ is positive for elongated particles, it is null for spheres, and negative for discoid objects.[103]. Regarding the behavior of active nematics beyond critical thresholds, it is admitted that for $\alpha > \alpha^+$, instabilities gives rise to splay deformations, while for $\alpha > \alpha^-$ the system undergoes bend deformations. In equation eq. 1.35, we notice that the sign of α is correlated to the sign of $1 \pm \lambda$, and to the sign of the overall fraction. As such, flow aligning nematics ($|\lambda|> 1$) undergo splay deformations under the action of extensile active stresses ($\alpha < \alpha^+ < 0$) and bending under contractile stresses ($\alpha > \alpha^- > 0$). Similar reasoning, in flow tumbling systems, where $|\lambda|< 1$, bend becomes dominant under extensile active stresses ($\alpha < \alpha^- < 0$), and splay under contractile stresses ($\alpha > \alpha^+ > 0$)[98].

In practice, most filamentous materials of biological origin, including actin and microtubules, are made of units exhibiting elongated shapes, with sizes much larger than those of typical molecular liquid crystals. As such, they organize into a flow-tumbling nematic phase, with $0 < \lambda < 1$. In extensile bundles of aligned filaments, instabilities thus manifest as spontaneous bend deformations propagating perpendicular to **n** and leading to the nucleation of defect pairs. This mechanism, which we will refer to as *bend instability*, is similar to that theoretically predicting the formation of *walls*[105]. Basically, in an ordered active nematic phase, small bend fluctuations are amplified by local shear resulting in hydrodynamic instabilities and in the creation of waves all along the material. These bent regions then sharpen and tilt the director to form almost equidistant lines of kinks that are called walls. The further tilt of the director causes pairs of oppositely charged defects to be created in the regions of strongest bend and to move along the walls. Such defects "unzip" the zones of high bend and restore a nematic configuration.

Both theoretical and experimental works have further demonstrated that, as defects proliferate, they are driven to interact with each other through convective swirling flows reminiscent of classical turbulent regimes in passive fluids. In this state, the continuous energy input favors the onset of a dynamic steady state in which pairs of $\pm 1/2$ defects continuously nucleate and annihilate at constant rate, perturbing the uniform structure in the director field. This chaotic flow regime, usually named as *active turbulence*, is present in multiple biological systems. Active turbulence is essentially different from hydrodynamic turbulence in conventional fluids. Despite both referring to the apparent disorder of the flows, their origin is completely different: Classical turbulence arises in systems with high Reynolds number ($Re > 1000$) due to the dominance of inertial effects, while active turbulence stems from dissipation in systems with negligible Re,

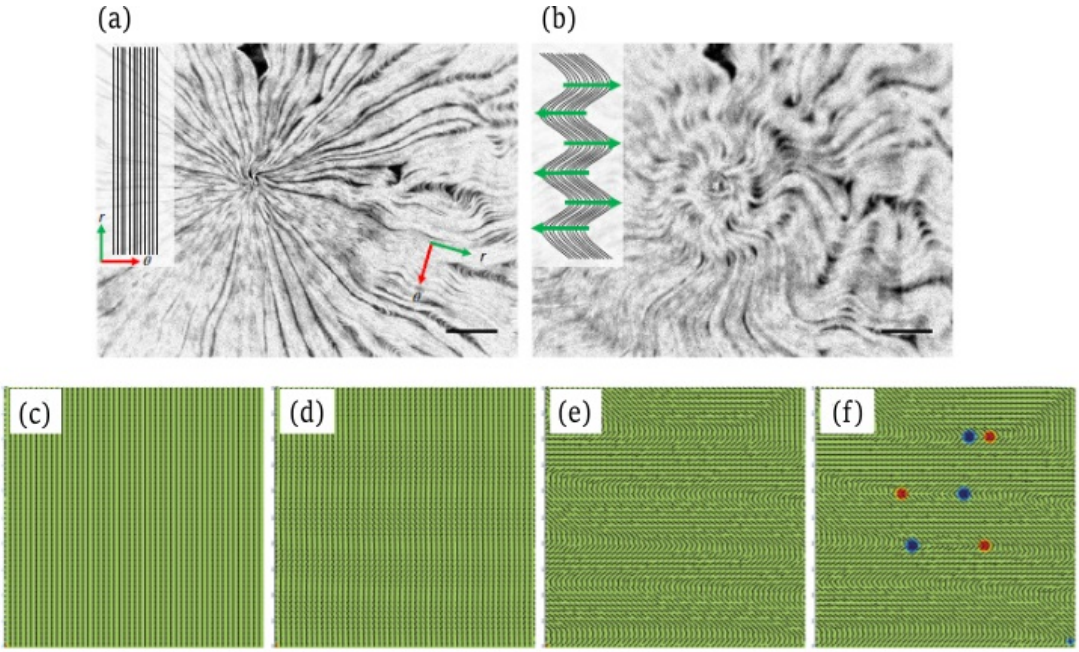

Figure 1.24: Bend instability in extensile active nematics. (a-b) Fluorescence micrographs show how radially aligned MTs-Kinesin bundles are unstable to bend deformations propagating perpendicular to the direction of alignment. (c-f) Numerical simulations of an ordered nematic , extensile system transiting towards the active turbulence. (c) Long-wavelength modes are unstable and form waves of bend deformations, which then sharpen and produce (d-e) equispaced lines of kinks called "walls". Extracted from[106] and[105].

where viscous forces dominate[107]. Furthermore, this active turbulent regime displays a distinctive spatial coherence, which involves a single length scale identified from the exponential distribution of vortex sizes. This *active length scale* l_α was first predicted from numerical simulations[108] and then confirmed experimentally[109] in MT based active nematics. In these studies, authors associated the prevalence of l_α to the role of the topological defects formed during the spontaneous folding of filamentous bundles. In more general terms, l_α corresponds to the mean defect spacing in the fully developed turbulent regime and is set by the following relation:

$$l_\alpha = (\frac{K}{|\alpha|})^{\frac{1}{2}} \tag{1.36}$$

Here $|\alpha|$ is the magnitude of the active stress and K is the free energy cost resulting from the spatial distortions of the director field[110,111]. In MT–kinesin systems it takes values of the order of tens of microns, i.e. a few tens of the length of the MTs.

This active length scale also controls the onset of spontaneous laminar flow in an active film, a phenomenon that has been referred to in the literature as the spontaneous flow instability.

1.2.3.0.2 Defects in active liquid crystals

Like in passive liquid crystals and other ordered condensed systems, ALCs host topological defects, namely singularities associated with discontinuities in the symmetry field. In equilibrium, pairs of defects with opposite charge attract each other and annihilate as the uniform ground state is approached. In active systems, defects exhibit a markedly

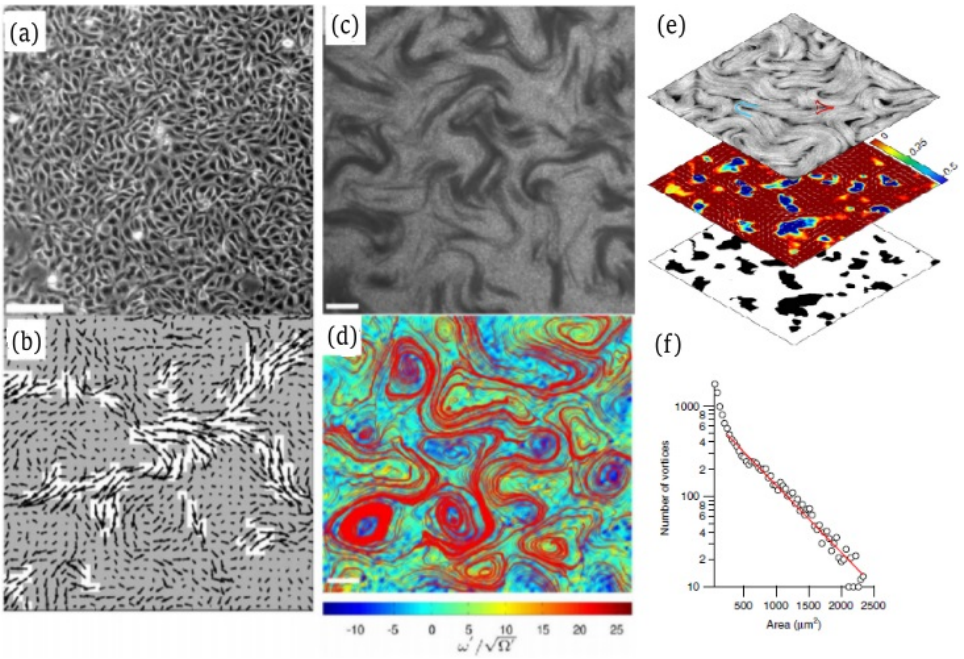

Figure 1.25: Active turbulence in living systems: Seemly chaotic patterns generated by (a-b) mammalian(MDCK) cells and (c-d) swarms of sperm. The colourmap in d) illustrates the vorticity field. e) Fluorescence micrographs of turbulent MTs-kinesin active nematics when in contact with an isotropic oil. Defects of charge $+1/2$ and $-1/2$ proliferate and move past each other in the form of vortices with various sizes. f) Statistical analysis of the size distribution of vortex areas during the active turbulent regime. The data is fitted by an exponential curve (red line). Adapted from[112] and[109]

different behavior: they are constantly created and destroyed, and they spontaneously move due to the asymmetry of their surrounding flow field, and more importantly, to the continuous influx of energy. In two dimensions, defects can exhibit different morphologies principally associated to the broken symmetry of the system itself. For instance, in polar active materials, the lowest energy configuration is subject to the formation of asters and vortices (Fig. 1.26), corresponding to $+1$ defects. In two-dimensional nematic liquid crystals, on the contrary, the equivalence between n and $-n$ allows the formation of positive comet-like defects ($s = +1/2$) and quasi static threefold symmetric defects ($s = -1/2$) (Fig. 1.27 (b)). These structures are a distinctive signature of broken symmetries and can be especially helpful to differentiate polar from apolar systems.

From a theoretical perspective, isolated defects in active nematic systems behave as active particles with complex dynamical behaviors evolving according to eq. 1.31 and eq. 1.34. A single active defect can be thus treated by means of an over-damped equation in the form:

$$\zeta(\frac{dr}{dt} - v) = F \tag{1.37}$$

where r is the defect location, F is the net force imposed on the defect, either by other defects or by external distortions. v and ζ, on the other hand, are the local flow velocity of the defect, and the effective drag coefficient associated with the rotational viscosity γ, respectively. In the absence of a flow, point defects do not move, unless experiencing external perturbations. In the presence of a flow, the hydrodynamic coupling between the flow and the local order gives rise to spontaneous flows advecting the defects, referred to as $backflow$. When the variations in defect velocities caused by elastic ordering are small compared to flow-coupling, the force F can be ignored and the flow velocity v can

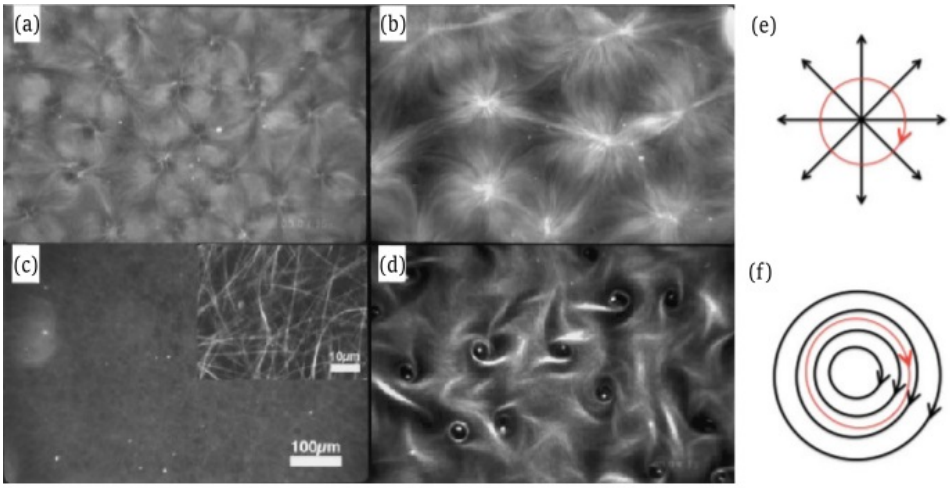

Figure 1.26: Large-scale patterns resulting from the self-organization of microtubules and molecular motor proteins. Micrographs correspond to uniform mixtures, each of them with different kinesin concentration, heated at 37°C and observed after 7 min. a) A lattice of asters(e) and vortices(f), with strength +1 occur at low kinesin concentration. b) An irregular lattice of asters is obtained at $37.5mg.ml^{-1}$ kinesin. c) At higher motor concentration, microtubules form bundles. d) At $15mg.ml^{-1}$ kinesin, the mixture organizes a lattice of vortices. Extracted from[113,114]

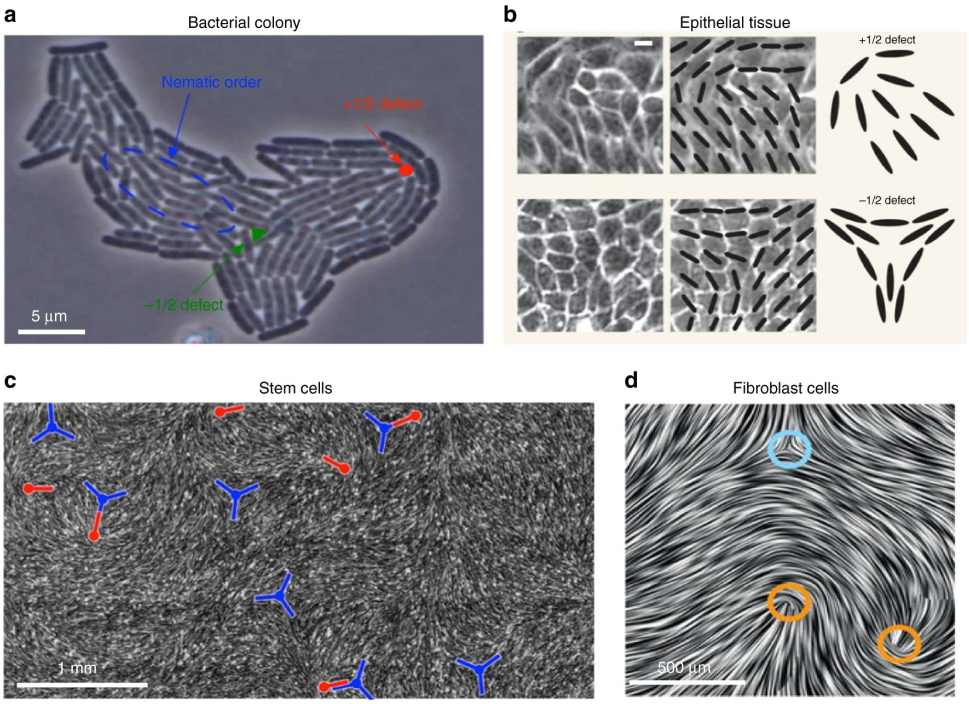

Figure 1.27: Two dimensional active nematics in biological systems. The motion and location of topological defects governs many cellular mechanisms such as shape changes of the colony and cell death and extrusion. a) Growing colony of E. coli bacteria[115]. b) Monolayer of MDCK (Madin Darby canine kidney) cells and the director configurations corresponding to $+1/2$ and $-1/2$ defects in nematic liquid crystals[116]. c) Neural progenitor stem cells culture[117]. d) Proliferating spindle-shaped mouse embryo fibroblasts[118]. Extracted from[119]

be obtained from the Stokes equation, analogous to eq. 1.32:

$$\eta \boldsymbol{\nabla}^2 v + \boldsymbol{\nabla} p + \boldsymbol{\nabla} \cdot (\Pi^{active} + \Pi^{elastic}) = 0, \boldsymbol{\nabla} \cdot v = 0 \tag{1.38}$$

This equation admits a solution v which can be described, after mathematical ma-

nipulation, by v_+ and v_-, the velocities of positive and negative half-integer defects. Assuming that the position r_+ of the $+\frac{1}{2}$ defect core is initially zero, one can resolve that positive defects self-propel along their symmetry axis, with constant speed $v_0 = \alpha R/(4\,\eta)$ according to the dynamic equation:

$$\zeta \frac{dr_+}{dt} = v_0 \hat{x} \tag{1.39}$$

For positive half-integers, the self-propulsion speed is proportional to the active stress α and thus in extensile systems ($\alpha < 0$) they will propel toward a negative direction ($\hat{x}$ in this setting), i.e. toward its "head" (Fig. 1.28 (a)). Negative $\frac{1}{2}$ defects, on the other hand, have a null velocity and thus their core is not propelled by the backflow, but rather dragged by the elastic distortions induced by neighboring defects.

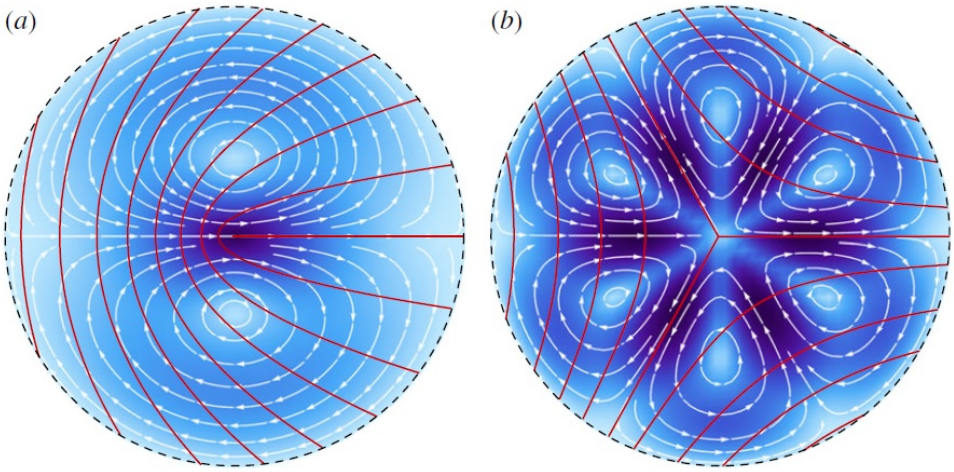

Figure 1.28: Flow fields of $\pm 1/2$ active nematic disclinations. In a 2D active nematic extensile system, the polar head of the positive defect directs the motion along the symmetry axis. Conversely, negative defects don't move by themselves due to their three-fold symmetry. The red lines represent the nematic director. Adapted from[98]

The final consequence of these behaviors is that depending on the relative position of positive and negative defects they will either recombine or separate. If the $s = +1/2$ defect is ahead its negative counterpart, the head of the defect will move away from the tail, driving a repulsive interaction (Fig. 1.29). If instead, this configuration is inverted, an attractive interaction results in the annihilation of $\pm 1/2$ defects.

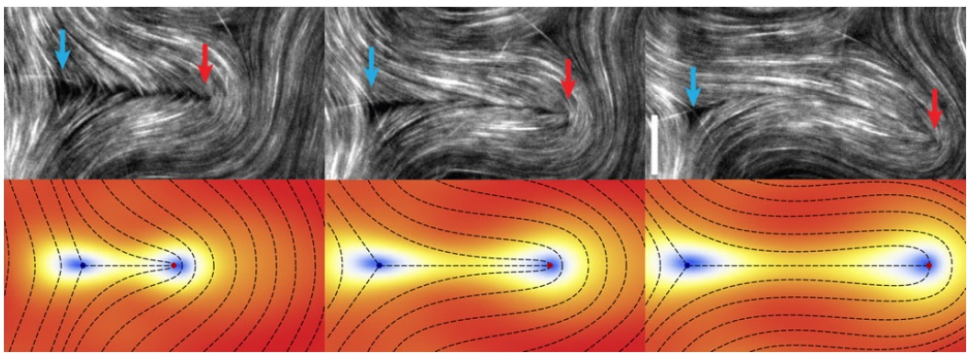

Figure 1.29: Creation of a defect pair in an active, extensile system, consisting of microtubules and kinesin motor proteins. Experimental observations and simulations were performed by[70] and[98] respectively.

1.2.4 Our active nematic system

Our system of study is an in vitro biological active gel fabricated for the first time in the Dogic Group at Brandeis University. In two dimensions, it forms a liquid crystalline phase composed of entropically self-assembled microtubules bundles, which are dynamically cross-linked by the action of kinesin molecular motors. Microtubules feature a cylindrical structure with helical wrapping of α and β tubulin chains, giving rise to distinct polarities at both ends of the structure. The positive pole designates the unpolymerized β-subunits and the negative poles the α-unpolymerized ones. On the other hand, activity arises from kinesin motor proteins bound into clusters with tetrameric streptavidin. They posses one or various heads that attach to specific sites on the microtubule surface. When fueled with chemical energy, in the form of adenosine triphosphate (ATP), the kinesins "walk" unidirectionally from the (-) end towards the (+) end of the tubular track. For this reason, when two microtubules of opposite polarity are close to each other, kinesin clusters cross-link them and make them slide in opposite directions, which is at the origin of the extensile nature of the system. Moreover, in the presence of a non-adsorbing polymer, such as polyethylene glycol (PEG), microtubules aggregate via depleting interactions, forming elongated bundles displaying complex dynamics. In three dimensions, and at finite concentrations, the latter self-rearrange into a viscoelastic network, undergoing repetitive cycles of filament extension, buckling, fracture and annihilation. Moreover, when in contact with an oily fluid, depleting forces drive the filaments in the bulk solution towards the interface where they continually pack, increasing their concentration. The densification of the actively sheared MT bundles at the interface leads to the spontaneous organization of a nematic phase as illustrated in Fig. 1.30.

Although this bio-inspired system is not the only one displaying this type of liquid crystalline behavior, we will denominate it as the "active nematic" (AN) system, for practical reasons. In the previous sections, we described some qualitative properties of active liquid crystals, which are general to all the experimental realizations; however, we would like to highlight and to deepen in some of them to ease the further understanding of this manuscript. As many other living systems, the motility of our active nematics is limited by the amount of energy (ATP) available in the medium. An intuitive way to keep it "alive" would be to continuously inject chemical fuel to it. However, the material being very sensitive to any external perturbation, it is preferable to include an energy regenerator during the synthesis, rather than manipulating it from outside once the active nematic is formed. By doing so, energy is continually created and dissipated as active stresses through the surrounding fluid. Moreover, our condensed material displays local orientational order and is therefore constantly subject to uniaxial tension making it unstable. Due to the extensile character of the active stresses, such instabilities manifest themselves as bend deformations in the director field when the filamentous material approaches a uniform aligned state. As the distortions grow in amplitude, a fracture line propagates, and defects nucleate at opposite ends of the crack. In fluorescence micrographs, the latter appear as dark regions devoid of microtubules, with either parabolic or hyperbolic shapes, characteristic of $+1/2$ and $-1/2$ topological defects respectively. The asymmetry of positive half-integers, in particular, imposes a strong bend deformation around the defect core, causing a net propulsion force which further extends the fracture line along the symmetry axis of the defect. Conversely, flow jets arising from the three fold symmetry of negative defects tend to cancel out, resulting in zero velocity. Consequently, the "head" of the positive defect moves forward, leaving its negative "tail" behind. Above a critical

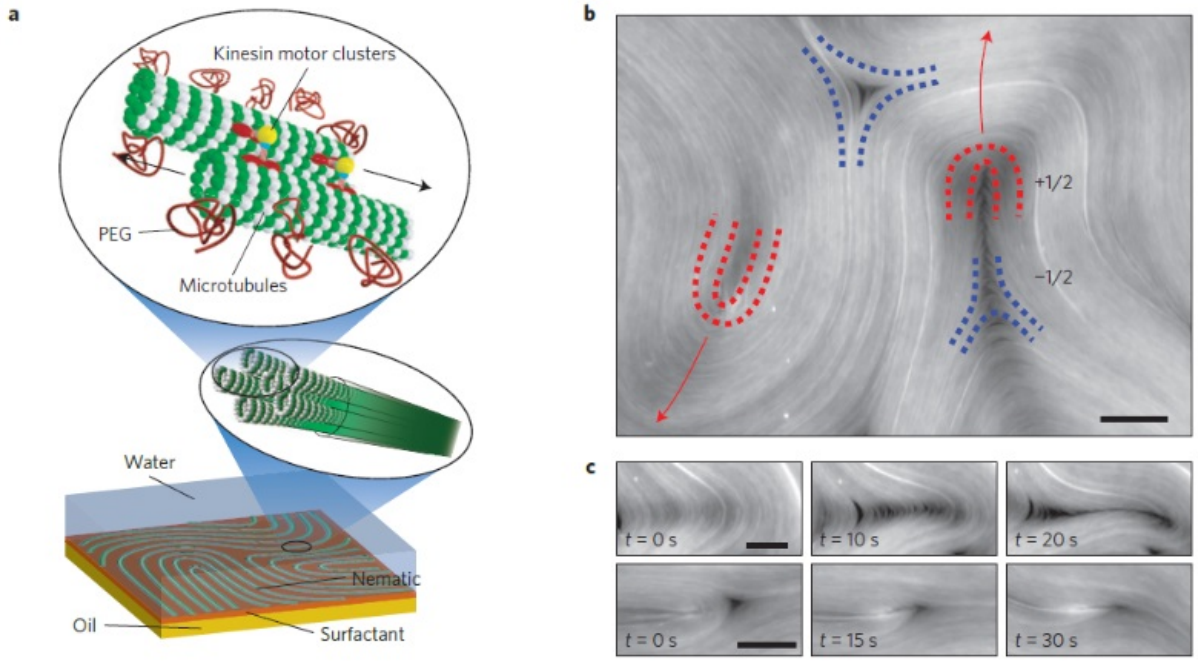

Figure 1.30: Microtubule-based active nematics in 2D. a) Kinesin-streptavidin motor clusters crosslink MTs and induce interfilament sliding. Under the depleting action of PEG coils the filaments are bundled together and migrate to a surfactant-stabilized aqueous/oil interface to organize a quasi-2D active nematic film. b) Fluorescence micrograph of MT-based active nematics punctured with positive and negative half-integer defects. c) Image sequence illustrating the creation (top) of a defect pair triggered by a bend deformation and the recombination (bottom) of oppositely charged defects. Extracted from[91].

separation distance, the fracture self-heals and the isolated defects undergo new cycles of destruction and creation. This continual dynamic dancing is at the origin of chaotic circulating flows or vortices, the distinctive hallmark of an active turbulent regime.

CHAPTER
TWO

MATERIALS AND METHODS

2.1 Active gel preparation

In this section, we provide a detailed bottom-up approach for synthesizing the active material. We first describe the provenance and the preliminary protocols for obtaining the main constitutive proteins and then we explain the mixture procedure to achieve a uniform active gel preparation.

2.1.1 Polymerization of microtubules

A high-concentration heterodimeric (α,β)-tubulin solution (provided by Z. Dogic's group at Brandeis University (Waltham, MA)) was obtained from bovine brain tissue through two cycles of polymerization–depolymerization in the presence of a high-molarity PIPES buffer, according to the protocol[120].

Tubulin (8mg/mL) was incubated at 37°C for 30 min in a M2B buffer (80 mM Pipes, 1 mM EGTA, and 2 mM $MgCl_2$) (Sigma; P1851, E3889, and M4880, respectively). A dithiothrethiol (43815, Sigma) reducing agent(DTT) and a non-hydrolysable guanosine triphosphate (GTP) analogue, GMPCPP (guanosine-5'- [(α, β)-methyleno] triphosphate) (NU-405, Jena Biosciences) were then added to suppress the dynamic instability of MTs. By adjusting the GMPCPP concentration, tubulin heterodimers associate in a controlled way to produce a high-density suspension of short MTs (1-2 μm). For observation under fluorescence microscopy, a portion of the initial tubulin (3 %) was labeled with AlexaFluor 647 (A20006, Thermo Fisher Scientific), a far-red–fluorescent dye with excitation ideally suited for the 594nm or 633nm laser lines. After incubation the final solution was kept at room temperature for 5 h, frozen in liquid nitrogen and stored at -80°C for future use.

2.1.2 Kinesin expression

Heavy-chain kinesin-1 K401-BCCP-6His from *Drosophila Melanogaster* (truncated at residue 401, fused to biotin carboxyl carrier protein (BCCP), and labeled with six histidine tags) was expressed in Escherichia coli using the plasmid WC2 from the Gelles Laboratory (Brandeis University) and purified with a nickel column as described in[121]. After dialysis against 500 mM imidazole buffer, the concentration of the suspension was adjusted to 60% (wt/v) with a sucrose solution and estimated by means of absorption spectroscopy. The final protein solution was stored at -80°C until use. The process was

performed in the BioNMR labs at the institute of bioengineering of Catalunya (IBEC) by B. Martínez-Prat (SOC&SAM group), M. Pons, A. LeRoux, and G. Iruela.

2.1.3 Active suspension

Kinesin/streptavidin motors clusters were prepared by incubating biotinylated kinesins with tetrameric streptavidin (43-4301, Invitrogen) at a 2:1 stochiometric ratio, for 30 min, under the reducing action of $2\mu M$ DTT. The resulting suspension was mixed with the microtubules in a standard solution containing the M2B buffer, and a PEG (20 kDa; 95172, Sigma) depleting agent that promotes the aggregation of filaments into bundles. The mixture is fueled with ATP (Sigma; A2383) and supplemented with phosphoenolpyruvate (PEP) (P7127, Sigma) and pyruvate kinase/lactate dehydrogenase (PK/LDH) (434301, Invitrogen) enzymatic ATP-regenerators. The latter transform ADP back into ATP maintaining a constant energy input in the system. To prevent protein denaturation and photobleaching during the fluorescence acquisition, several antioxidants and a 2.1 mM trolox (Sigma, 238813) solution were introduced in the mixture. The first set of antioxidants (AO1)includes 2.5 mM dithiothreitol (DTT) and 15 mg/mL glucose while the second solution (AO2) contains 1.75 mg/ml catalase (Sigma, C40), and 10 mg/mL glucose oxydase (Sigma G2133). It's also worth noting that, most of the ingredients (PEP, DTT, ATP, PEG, Streptavidin, Catalase, Glucose, Glucose Oxydase and Trolox) were buffered using the specially designed microtubule solution (M2B) to keep the enzymes and the motors in their preferred environments. A brief summary of the stock solutions and their proportions for the synthesis of the active gel is provided in table Fig. 2.1.

To procure a biocompatible acqueous/LC interface that enables the condensation of microtubles into a 2D layer, a PEGylated surfactant must be added to the previous preaparation. The selection of the surfactant is also crucial for determining the disposition of liquid crystalline molecules near a surface, therefore we will dedicate a more extended explanation of our choices in each introductory part of the results chapters.

2.2 Microscopy techniques

2.2.1 Liquid crystals and Polarized Light Microscopy

A standard beam of light propagates as individual waves, vibrating in all planes perpendicular to the propagation direction. Typically, the waves have different orientations and the vibrations have no favored direction. In some cases, however, the beam can be filtered with special materials in order to restrict the vibrations to parallel planes. The light is then referred to as linearly polarized with respect to the propagation path. Although this type of light cannot be seen by us normally, it can be used to improve image quality when examining anisotropic materials. To do so a polarizing microscope is equipped with two polarizing filters, placed below and above the sample (see Fig. 2.3). When a normal beam of light passes the first filter, called the *polarizer*, the rays will orient along an easy axis and become $plane - polarized$. In the presence of an optically active sample, such as a nematic liquid crystal, the incoming polarized light will be refracted into two rays propagating at different speeds, each associated to a refractive index ($n_{\parallel}$ and $n_{\perp}$). The property associated to these phenomena is called $birefringence$ and can be mathematically described as the difference between the two indexes $\Delta n = n_{\parallel} - n_{\perp}$. The first wave emerging from the material, the *ordinary ray*, vibrates perpendicularly

Compound	Stock solution	% v/v
M2B	80mM Pipes + 2mM MgCl2 + 1mM EGTA	-----
PEG	12% w/w	0.133
PEP	200 mM	0.133
trolox	20 mM in 20mM (K2HPO4)	0.099
MIX	933 uL M2B + 67 uL MgCl2(1M)	0.048
Glucose	300mg/ml in 20mM K2HPO4 + 70mM KCl	0.011
DTT	0.5 M	0.011
Catalase	3.5 mg/ml in 20mM K2HPO4 + 100mM KCl	0.011
Glucose Oxydase	20mg/ml in 20mM K2HPO4	0.011
ATP	50 mM	0.028
PKLDH	600-1000 units/mL	0.028
Streptavidin	0.352 mg/ml	0.023
Kinesin	0.07 mg/mL	0.226
Microtubules	8mg/mL	0.192

Figure 2.1: Composition and volume fraction of stock solutions for the synthesis of a MT-based active gel.

to the optical axis and is characterized by the isotropic refractive index n_0 (see Fig. 2.2). Note that since a nematic phase is hightly symmetric, it behaves as an uniaxial medium, with the optic axis being parallel to the director. The second component, termed the *extraordinary ray*, experiences the index n_e and exits the sample with a polarization perpendicular to the ordinary ray, in the plane defined by the optic axis and the wave vector, $\mathbf{k} = k_0 n(\theta)(sin\theta, 0, cos\theta)$[122]. Here, the index of refraction $n(\theta)$ depends on the angle θ of the wave vector with the optic axis (the director in a nematic LC). In general terms, the refractive indices corresponding to the ordinary and extraordinary components are associated to $n_\parallel$ and $n_\perp$ through the expressions[123]:

$$n_0 = n_\perp, \tag{2.1}$$

$$n_e(\theta) = \frac{n_\parallel n_\perp}{\sqrt{n_\parallel^2 cos^2\theta + n_\perp^2 sin^2\theta}}. \tag{2.2}$$

Lastly, when the two rays reach the second polarizer (the *analyser*), they recombine by interference to construct the final image. Generally the characterization of the defective texture of liquid crystals requires the polarizers to be crossed at right angles with each other. In such a configuration, if the orientation of the transmission axis of either polarizer is different from 0 and $\pi/2$ with respect to the director, the light will be able to pass leading to a bright signal. On the contrary if the easy axis of any of the polarizers matches the orientation of the director, the light will be filtered out and the field of view will turn completely dark.

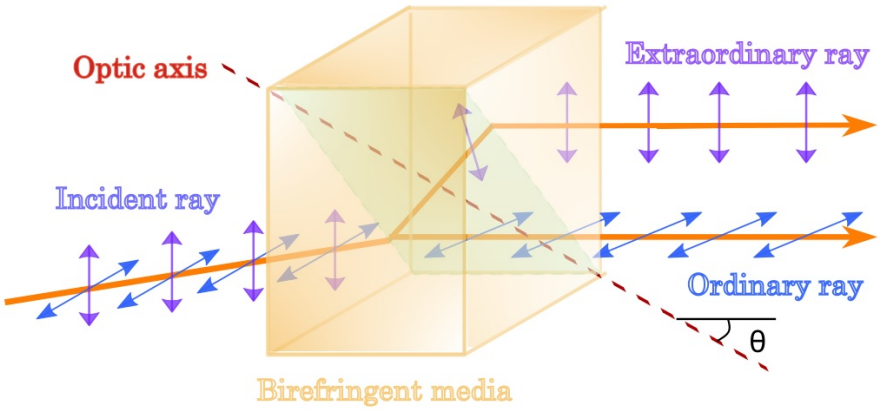

Figure 2.2: Schematic representation of light traversing a birefringent material. The polarized-wave is split into two rays perpendicular to one another.

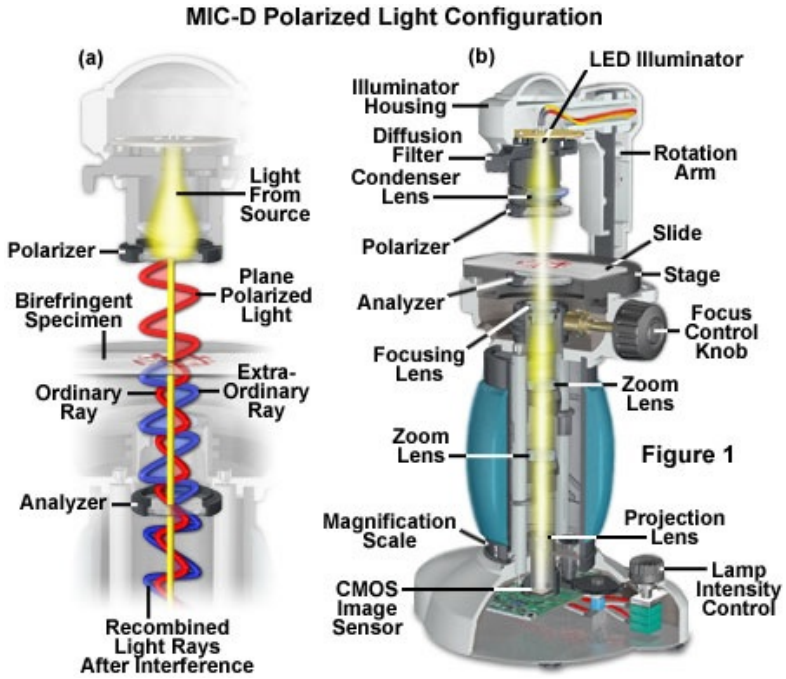

Figure 2.3: The polarized light microscope filters the light and exploits the interference of refracted rays, to extract information about anisotropic, birefringent materials.

2.2.2 Confocal Fluorescence Microscopy

The detailed description of a biological mechanism requires to selectively target its protagonists and to capture them with sensitive optical techniques. For example, the cell shape regulation involves the formation of networks of biological polymers (microtubules and actin filaments) which can be tagged with fluorescent markers making their structure visible on a dark background. Based on this principle, *Fluorescence Microscopy* is a potential approach to track the behavior of biological entities by mean of high contrast images, otherwise difficult to obtain with classical methods such as light reflection, scattering, and absorption. In a fluorescence microscope, the sample is excited by a source of light, typically a laser or a led. The light is then reflected toward the sample by a dichroic mirror which is oriented at 45° angle with respect to the incoming source (see Fig. 2.4). Note, that the mirror is selected in such a way that only the photons of the

chosen exciting wavelength are reflected whereas those of longer wavelength are allowed to pass through. In the sample, the light is absorbed by the fluorophores, which can be either intrinsically present or artificially added to label specific compounds. After absorption, light is emitted by the sample with a longer wavelength than that of the excitation. Although the fluorescence emission occurs in random directions, only a fraction of it is finally collected by the microscope objective.

Fluorescence Microscopy can be notably improved with the incorporation of confocal mode, which allows to optically slice the specimens and to create high-resolution images in three dimensions. This is accomplished by placing a pair of pinholes in the optical path. In front of the illumination source the first pinhole focuses a single point of the excitation light onto a confocal spot in the sample. With the illumination being reduced to a single point, the intensity above and below the focal plane decreases as the beam converges and diverges, leading to the decay of the excitation of fluorescence for interfering objects from off-focal layers. The focused light then follows the traditional path before reaching the exit pinhole. If the aperture of the pinhole is small enough, the light arising from regions far from the vicinity of the illuminated point is rejected, thus further attenuating the interference from out-of-focus planes. Interestingly, this classical method, allows to generate information about a single point at one time. To reconstruct an entire image, the focused spot of light has to be scanned across the sample, hence the technique's name *confocal laser scanning*. A final micrograph corresponds to the collection of the signals originated from the focused regions of space, registered by the detector.

Ideally the scanning system is sufficient for producing sharp, high-resolution images. In practice, this is only true for thin, static specimens and some difficulties appear when recording thick, living compounds. The time required to map point-by-point not only one layer, but the entire stack of layers, with a single laser beam can become really long as the size of the sample increases. A slow acquisition also increments the risk of phototoxicity of a living specimen and the photobleaching of the fluorophore associated to a longer light exposure on the sample. On the other hand, a fast movement during the scan can blur the edges of the objects leading to poor definition images and fuzzy textures. To manage these issues additional devices, such as the *Nipkow disk* (Fig. 2.5) can be supplemented to the microscope. The disk consists of a series of equally-spaced pinholes arranged into Archimedes spirals through which the excitation light passes. When the disk rotates, the spot pattern is scanned over the sample, exciting the fluorescent labels in the specimen in the shortest possible time. A fraction of the emitted light will return along the excitation path where it will be selectively filtered by the same confocal apertures. Generally, to increase the amount of transmitted light an additional disk (the collector), including an array of micro-lenses co-aligned to the pinholes of the other disk is inserted in the optical path. Since the sample is scanned by thousands of beams simoultaneously, multiple points will be detected at once and thus the imaging speed will be dramatically improved. In our experiments we used this second strategy named *Spinning disk confocal laser microscopy* since it allowed us to record a higher number of frames in a shorter time.

2.3 Micromanipulation techniques

2.3.1 Optical Tweezers

First introduced fifty years ago, optical trapping has demonstrated to be a tremendously powerful method for manipulating microscopic objects. Although it was initially envi-

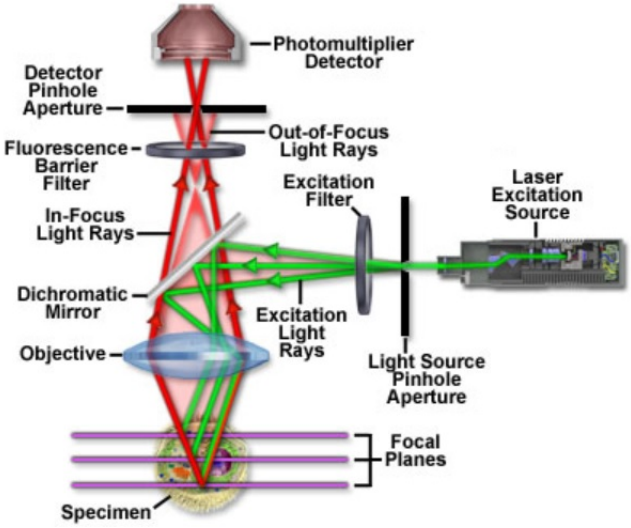

Figure 2.4: Fluorescence Confocal Microscopy. The confocal arrangement enhances the optical resolution of the conventional fluorescence microscope by filtering the signals coming form out-of-focus layers. This is achieved thanks to the incorporation of two pinholes: one in front of the light source and one in front of the detector. Adapted from [124]

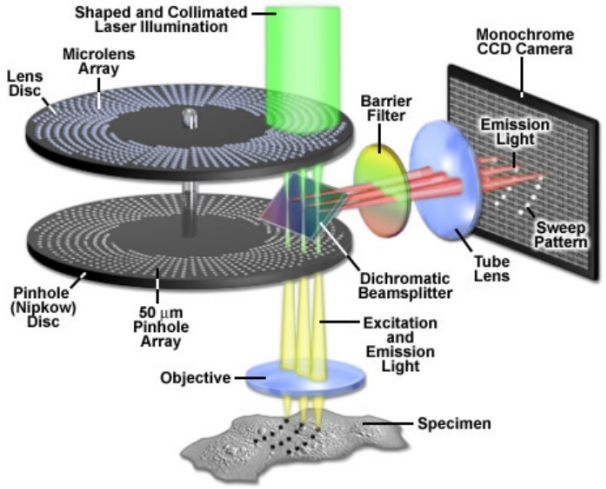

Figure 2.5: Dual Spinning Disk Unit. In addition to the standard Nipkow disk containing an array of pinholes there is a secondary micro-lens disk to improve light transmittance. The microlenses focus the excitation light with greater efficiency onto the imaging pinholes increasing the excitation throughput. Adapted from [125]

sioned for trapping neutral atoms and studying laser cooling, with time it also showed a good potential to address numerous bio-physical problems.

Optical tweezers rely on a laser beam which is tightly focused by a high-quality microscope objective to a spot in the sample. The focused light creates an attractive trap for small dielectric objects by exerting two forces on them. The first component is responsible for drawing a particle towards the region of greater light intensity and is known as the *gradient force*. In most experimental settings, the particle experiences the strongest electric field gradient close the narrowest part of the beam (the beam waist) and thus accommodates into it. The second mechanism that holds the object in place can be understood by analyzing how the light refracts through the object. Consider a bead which is not perfectly centered in the beam but slightly away in a transverse direction

from it, as represented in Fig. 2.6 (a). The region of the particle exposed to the beam waist will refract more light than the regions far from it. As a consequence more light will be redirected away from the centre of the trap than towards it. The change in the direction of the beam will also alter its momentum and according to Newton's third law to preserve it, the object undergoes an equal but opposite momentum, resulting in a restoring force, named the *scattering force*, which pushes the particle back towards the center of the beam. Once the bead is centered into the trap, the individual rays of light are refracted symmetrically, annihilating the net lateral force acting on the bead. The balance between the axial gradient force and the scattering force stabilizes the position of bead slightly downstream of the beam waist Fig. 2.6 (b). To perfectly center the object in all directions, the force of the light scattering from the bead along the positive z–direction is usually compensated by the gradient force along the negative z-direction. This is achieved by choosing a lens with high numerical aperture, capable of focusing the laser very tightly with a Gaussian intensity profile.

Other recent applications of optical traps include force measurement in the pico-Newton range. The principle behind it typically consists of determining the proportionality constant k relating the restoring scattering force to the distance between the center of the sphere and the focus of the laser. The constant k is referred as the *trap stiffness* and thanks to modern image analysis techniques it can be determined with a precision up to 0.5 pN in force measurement.

Optical tweezers are typically mounted on top of a commercial microscope. In our case we used a conventional nikon ECLIPSE Ti2 with brightfield, Differential Interference Contrast illumination through a condenser and detection lenses, an intermediate magnification and high numerical aperture objective lenses. The trapping apparatus included an infrared laser to avoid biological photo-damage and to ease its incorporation into the imaging system that uses visible light. The setup was completed by a sensitive camera IDS-uEye for image acquisition. Despite the fact that optical tweezers are usually employed for displacing sub-micrometer objects such as colloids or cell components, in our experiments we went a step further by successfully manipulating objects in the range of $100\mu m$. We employed the apparatus exclusively for displacing colloids and for this time we did not perform any force quantification.

2.4 Emulsions: types, stability and production techniques

2.4.1 Emulsions basic principles

Emulsions are metastable colloids made out of tiny liquid droplets dispersed into another continuous liquid medium, the later being immiscible with the former. They are usually produced by shearing the two immiscible phases resulting in the fragmentation of one phase into the other. Depending on the nature of its components, several classes may be distinguished: the classical ones being the oil-in-water (O/W), water-in-oil (W/O) and oil-in-oil (O/O) emulsions. The surface tension of both phases being non-null, the system is not in perfect equilibrium and the thin liquid film that separates two adjacent droplets may collapse. This mechanism known as *coalescence* results in the fusion of neighboring

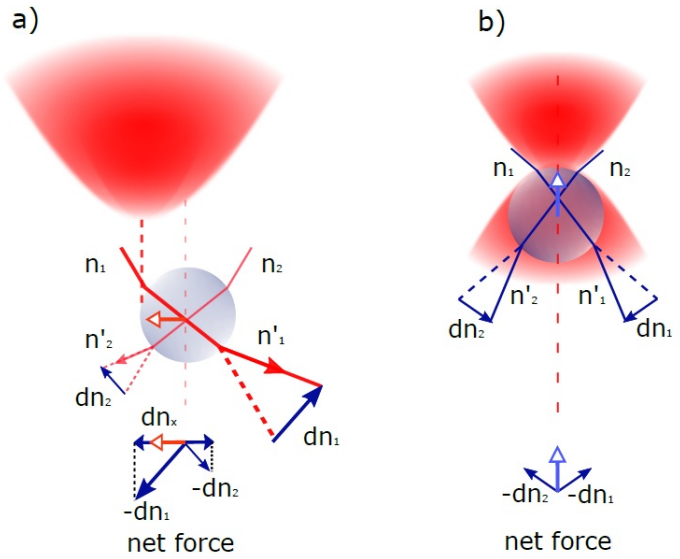

Figure 2.6: Schematic representation of the optical trapping principle. (a) When the bead is slightly deviated in a transverse direction from the center of the laser beam, the more intense rays are refracted away from the center of the laser. The larger momentum change (dn_1) causes a net force along the x-axis, to be applied back toward the center of the trap. When the object is laterally centered on the light-path (b), the rays refract symmetrically and the lateral force is null. (b) In the absence of a tight focus of the light the bead usually accommodates slightly downstream of the center of the trap. By adjusting the focus, the symmetric momentum changes (dn_1 and dn_2) of the rays induce a force which pulls the bead towards the focal point. Adapted from [126]

droplets and in the destruction of the emulsion. To increase their lifetime, emulsions may in principle contain suitable surface active species, capable to protect the interfaces by decreasing the interfacial tension. Such species are usually made of amphiphile molecules that act by surrounding the dispersed droplets, stabilizing the emulsions for longer periods. In the best cases the systems can stand for months or even years, while in other cases they may collapse within a few seconds or are just impossible to form regardless of the preparation procedure. Interestingly, such variability depends on the surfactant solubility within the continuous phase. For example, a direct emulsion (O/W) will be preferentially produced with a water soluble surfactant whereas the inverse configuration (W/O) requires an oil soluble one. To determine the adequacy of a surfactant based on its solubility in the continuous medium one can generally look at the *hydrophilic–lipophilic balance* (HBL) of each surfactant molecule, ranging from zero for fully oil soluble compounds to 40 for fully water soluble ones [127]. Besides the choice of the type of surfactant, the stability of the emulsions can be drastically improved by adjusting adequately its concentration. In fact, the surface energy of the system decreases more and more with the increasing concentration of surfactant up to a certain threshold called the *critical micellar concentration* (CMC). Beyond this limit the free molecules in the bulk start self-aggregating into micelles instead of covering the droplet's surface, thus leaving the final surface tension relatively unchanged.

Occasionally, conventional emulsions contain smaller droplets of the continuous phase within the droplets of the dispersed fluid. Such structures are named *double* (resp. *multiple*) *emulsions* when there is one (resp. multiple) inner compartment inside each droplet. Similar to single ones, double emulsions can be either direct (W/O/W) when each oil globule includes an aqueous droplet or indirect (O/W/O) when the dispersed aqueous

droplets contain an oil globule inside. Moreover they can display certain instabilities at various levels, the most notorious being those occurring among the large dispersed globules, and those occurring between the globule and the small droplets dispersed within it. In addition to coalescence, diffusion is considered to be the most likely cause behind this phenomena. As a matter of fact, the concentration gradient of the molecules present in the continuous phase and those contained in the most interior droplets, induces a osmotic transport resulting either on the swelling or on the shrinkage of the entrapped inner droplet and on its posterior breakdown. In general, the stabilization of double emulsions is far more complicated than that of single ones and in certain cases it is even unknown. General guidelines recommend however to use two surfactants of opposite solubility, in a two-step process[127]. More recently, many reports also suggested the use of block copolymers instead of small molecule surfactant combinations, to fabricate multi-compartement emulsions and to stabilize them in one step[128,129].
There are many ways to fabricate emulsions. The most simple method consists of shaking the sample, containing both immiscible fluids, by hand or using a vortex apparatus to induce high-speed shearing. The stresses generated by mechanical agitation, however, are not uniform across the system, nor can they be finely controlled. As a consequence, emulsions contain droplets that are highly polydisperse in size. In order to gain a better control over the size distribution new emulsification methods have been developed. Among them, microfluidics have demonstrated to be a promising and versatile route to achieve these goals. Unlike bulk emulsification techniques, microfluidic devices allow to produce one droplet at a time with great accuracy. In these conditions one can obtain a uniform population of droplets with a controllable size and at a high speed rate. Another attractive feature of this technique is that it enables the fabrication of single, double or multiple emulsions, while controlling simultaneously the size and the number of the encapsulated droplets with an unprecedented precision. In the following section we will provide a clear overview about the different microfluidic techniques and their associated mechanisms for emulsion fabrication.

2.4.2 Emulsions fabrication through microfluidics

When hearing about microfluidics probably the first thing that comes to mind may be a soft, flexible and transparent block with minuscule channels connecting to one another. In fact, this vision is not so far from reality. The most popular kind of microfluidic devices consists of a network of micro-channels molded into an elastomeric material such as polydimethylsiloxane (PDMS). Typically, the set of conduits is connected to the outside by inputs and outputs through which the fluids to be studied can be injected or removed. The popularity of PDMS chips basically resides on the ease with which they can be reproduced. Once a mold is designed, a large number of devices can be fabricated by a stamping method, thus making them relatively inexpensive. Moreover, soft lithography enables the design of very complex circuits to perform multiple task within a single device, a common example being the sorting of droplets based on their size[130]. There are however many drawbacks associated with PDMS. The material is mechanically soft and may be sensitive to ambient conditions. The channels are prone to shrinking and to becoming thinner and deeper when exposed to sudden temperature changes and to low humidity levels. Furthermore the chemical compatibility of PDMS is restricted to certain products and hence to certain applications. For instance, when in contact with nonpolar solvents such as hydrocarbons, toluene, or dichloromethane, PDMS swells reducing its

performance[131]. Besides, small hydrophobic molecules are prone to be absorbed and released into and out of bulk PDMS, potentially modifying the properties of the channels' surface and the fluids running through them[132].
A second widespread strategy is based on devices made out of glass capillaries. Optically transparent, chemically inert, temperature resistant and with low autofluorescence, glass is considered by many users as the gold standard material for microfluidic systems. Probably this is not only because of its physical-chemical properties but it is also due to the complexity and thoroughness required for its manipulation and assembly. In typical systems for emulsions production, glass capillaries have to be heated, tapered and cut in order to fix the diameter of their orifices. Additionally, they have to undergo different chemical treatments to control their wetting properties and hence to adjust the surface affinity for either the aqueous or the oily phase. Only once they have been physically and chemically treated, capillaries can be, in the simplest case, directly used for producing one droplet at the time or in more complex situations such as the continual production of emulsions, assembled co-axially into one another, sealed and finally connected to the fluid entries controlled by syringe pumps. As it can be noted, the main disadvantages of this technique may be the long treatment and manufacturing process of the devices and the economic cost associated with each step. The fabrication of a glass circuit demands a high level of skill and access to a chemistry lab equipped with the complex hardware for fusing and handling the glass at a microscopic scale.
In essence both strategies exhibit pros and cons and the best criteria for choosing either one should be the adequacy of the material platform for a targeted application. An exhaustive list of requirements principally related to the chemical inertia to the circulating fluids and the overall thermomechanical properties should be conducted preliminary to the device fabrication. In the next sections we will present the microfluidic setups to produce different kinds of emulsions.

2.4.2.1 Capillary microfluidics for continual emulsions generation

The mechanism responsible for droplet formation in a microfluidic device can be illustrated by a liquid being drained out through a valve in a funnel. By turning very carefully the valve the fluid will start dripping out one drop at the time. In this case, the size of the droplet will be controlled essentially by the forces acting on it, namely the surface tension and the gravity. Because the valve aperture and the surface tension are constant the droplets coming out of the funnel will be relatively uniform in size. Nevertheless, if we fully open the valve and we increase the flow rate a fluid stream will be sprayed out instead of single droplets. Glass microfluidic devices for single emulsions fabrication operate on this principle but display two main differences. The first one is that the capillaries in which fluids are introduced have sizes on the order of tens of micrometers and the second is that droplets are produced in another immiscible liquid, instead of being formed in the air. From a technical point of view, the simplest device configuration comprises one cylindrical capillary inserted into a bigger square capillary of similar dimensions. While the first liquid flows inside the circular capillary, the other circulates through the voids left between the square and circular cross-sections of the two capillaries. The first fluid then leaves the inner capillary by the orifice at the tip and meets the other phase to form unstable parallel streams Fig. 2.7(a). Such geometry is named as the $co-flow$ geometry and permits the continuous production of individual monodisperse droplets at low flow rates. Another configuration for creating single emulsions is the $flow-focusing$

technique Fig. 2.7(b). It replicates the capillary arrangement of the previous geometry, but differs from it in that the two immiscible fluids are injected from the two opposite ends of the square capillary. In this case, the two liquids meet in front of each other close to the tip and the first one is hydrodynamically focused through the small orifice of the tapered capillary by the second one. Both the produced droplets and the injected fluids are collected at the exit of the cylindrical capillary. The main advantage of this technique over the previous one is that it enables the fabrication of droplets with diameters smaller than that of the orifice without risking to clog the capillary tip.

In general, the design of microfluidic systems is subject to the degree of complexity of the emulsions to be produced. For encapsulating a droplet inside another droplet, namely for building a double emulsion, both co-flowing and flow-focusing techniques have to be combined within a single device (see Fig. 2.8). To do so, two cylindrical capillaries with different orifices diameters are inserted in the opposite ends of a square capillary. The inner fluid is introduced through the circular capillary with the narrowest orifice while the middle fluid, which is immiscible with the other two phases, runs through the square capillary in the same direction. When the two flows reach the tip, the middle fluid surrounds the inner one and forms a thin layer around it. Meanwhile, the outermost liquid known simply as the outer phase runs through the other circular capillary (with the higher aperture) in the opposite direction. When meeting the other fluids between the two tips, the latter hydrodynamically focuses the co-flowing streams through the tip of the collection tube, forming perfectly defined double emulsions. The rupture of the coaxial jet into double emulsions is due to Rayleigh-Plateau instabilities[133,134] which occur if the effective capillary number $Ca = \eta_{out} V/\gamma_{mid-out}$ is of order unity, with V being the downstream velocity of the inner fluid and $\gamma_{mid-out}$ the surface tension between the middle and outer fluids[135]. Below this value, capillarity dominates and the size of the droplets is governed by the interactions with the solid walls. The perturbations at the origin of drop pinch-off grow very close to the entrance of the collection tube and at a constant frequency, leading to highly monodisperse emulsions. This regime is known as the *dripping* regime. On the contrary, *jetting* occurs at high capillary numbers, when the viscous effects dominate. The perturbations extend over several orifice diameters along a cylindrical jet before rupturing into droplets, causing a random variation in the pinch-off location. As a consequence, emulsions produced in jetting mode are highly polydisperse.

In the coming sections, we will exhaustively share the know-how behind smectic shells fabrication.

2.4.2.2 Step by step: Microfluidic fabrication of liquid crystalline shells

Classical liquid crystal shells are direct double emulsions (W/LC/W): The inner droplet and the continuous phase are composed of an aqueous solution containing one or various surfactants and the outermost droplet is made of liquid crystalline molecules either in the nematic or the smectic phase. As previously mentioned the most efficient way of producing such structures through glass microfluidics is to build a device combining both co-flow and flow-focusing configurations. In practice, this can be achieved by following a four steps process involving: (i) The capillary selection, (ii) the capillary tapering, (iii) the capillary cutting, (iv) the capillary surface modification and (v) the mounting of the device.

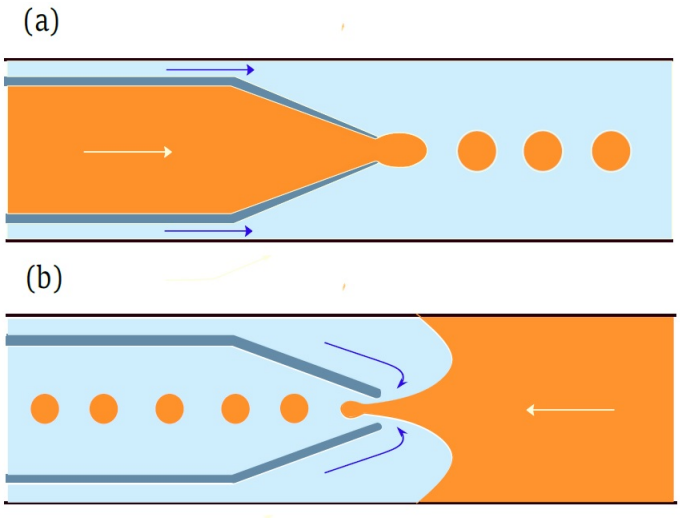

Figure 2.7: Schematics of glass capillary microfluidic devices for emulsion preparation. Arrows indicate the direction of the flows. (a) In the Co-flow configuration the two immiscible phases flow in the same direction. (b) Flow-focusing occurs when the dispersed phase is focused by the continuous phase through the narrow orifice of the collection capillary.

The first step consist of selecting two cylindrical capillaries of the same dimensions with outer diameter of 1.00 mm. Although this may perhaps appear obvious and even unnecessary for capillaries coming from the same batch, the margin of error in the commercial product can be large enough to find around ten percent of them displaying smaller diameters (0.98mm). Additionally the cylinders have to fit precisely inside a bigger square capillary of inner dimension 1.02 $\pm$ 0.01mm and the gap between them should not be too small nor too large. In the first case the two capillaries may become stuck and in the second the inner capillary may be lost inside the larger one, making it more difficult to center it coaxially with the other cylinder during step (v). This process is performed manually, by inserting each tube inside the square capillary and by noting how tightly they match each other without sticking.

The second step consists of tapering off the central part of a cylindrical capillary by using a pipette puller. For this, a glass tube is slid through a heater chamber and into V-grooves of opposite puller bars. Once a program is launched the filament in the chamber heats up and melts at the same time that the two bars containing the capillary are pulled apart in opposite directions. In less than 10 seconds the glass is stretched and separates in two halves. At one end the capillaries display a conical shape resulting from the stretching process while at the opposite end the cylindrical geometry remains unchanged. The apparatus permits to regulate the length and tip size by adjusting simultaneously the temperature of the heating filament, the strength of gravitational pull on the puller bars, the velocity of the heating and the pressure of the cooling air delivered to the filament. In our experiments, we carefully select the parameters for generating blunt tips, with length equal to one or two outer diameters, to ensure the symmetry and the stability of the flow.

In the third step the tapered capillary is cut by fusing the tip thanks to a microforge system. In the lab we used a Narishige MF-830 apparatus which comprises a heating filament, a microscope, illumination and manual micromanipulators. The capillary is

placed vertically in a metallic support with the conical side facing downwards. Right below it, there is a low-melting-point borosilicate bead lying on the platinum filament whose location can be adjusted in three dimensions by manually moving the micro-screws. By looking through the microscope the bead is roughly centered in front of the tip with its center of mass being on the same focal plane as that of the capillary. The glass bead is then progressively heated and moved vertically towards the capillary until coming in contact with its tip. As the bead gradually wets the capillary, it forms a meniscus delimiting the solid and the locally molten zone. The meniscus is gradually displaced along the cone until matching the targeted orifice diameter. This position generally corresponds to the trim perimeter, which in our case was regulated to attain inner diameters of 60 and $120\mu m$ for the injection and the collection capillaries respectively. Once this happens, the bead is cooled down and both the capillary and the bead solidify. The capillary is rapidly pulled apart from the bead splitting both of them along the trim perimeter. This results in a straight cut and in a uniform aperture on the tip. From time to time, when approaching the bead to the tip the molten glass is seen to rise inside the capillary faster than the surface of the bead. This generally occurs if the temperature of the glass is high enough to decrease its viscosity to the point of favoring the liquid penetration. In such cases it is recommended to continue rising the column of glass inside the capillary up to the desired height. After that, when heat is stopped, a fracture will propagate by itself, and the inner column of glass could be extracted with the surrounding walls of the capillary giving rise to beveled edges on the capillary tip. Either of these orifice textures can be used in a microfluidic device as long as they display a perfectly symmetrical shape to ensure a good alignment of the flows.

Step four: In any device including a co-flowing geometry, the aqueous droplet detaching from the injection capillary tip has to follow the direction of the parallel flows, whether for producing single or multiple emulsions. Any displacement in the opposite way should be prevented. The surface of the injection tip has thus to be modified hydrophobically to avoid wetting with the aqueous phase. Experimentally, we used octadecyltrichlorosilane (OTS), an amphiphilic molecule made of a polar head with three hydrolyzable substituents and a very long alkyl tail. In principle, when in contact with glass, the three labile groups condense and bond the -OH groups of the substrate. From their side, the non-polar alkyl groups remain available for physically repelling and shielding the surface from any aqueous compound. Before treatment, the capillary is first rinsed with acetone, ethanol and DI water to eliminate any deposition or accumulated dust. The glass tip is then is immersed for 5 min into a $2mmol.L^{-1}$ OTS solution $4:1$ in volume hexane-chloroform mixture. For a single dose, this corresponds to 8mL of hexane, 2mL of chloroform and 20 μL of OTS. The tip is then rinsed 2min with chloroform and finally heated at 200°C overnight.

In the last step all the pieces are assembled together to make a device. First, the clean square capillary is centered and glued onto a large microscope glass slide with a fast curing resin. Then, the two cylindrical capillaries are carefully slid in the opposite ends of the square one and pushed close to each other until reaching a separation distance of approximately 80 μm at the center of the system. Since both tubes have to be perfectly aligned with one another along the three dimensions, they are rotated and translated until a good focus and overall alignment is found. They are then glued onto the slide while attentively controlling that the alignment is not disrupted by the hardening nor the shrinkage of the resin. Once the glass circuit is fixed, it should be connected to the outside by a series of inputs and outputs. The inlets are made from syringe needles

displaying short and blunt tips, either obtained commercially or fabricated in the lab by simply cutting and polishing the tip. The needles are glued in three locations of the circuit: the first one at the beginning of exposed part of the injection capillary and the second and third at both ends of the square capillary. Lastly, the fluid exit corresponds to the exposed end of the collection capillary and is simply connected without sticking to a tubing of approximately 10cm long.

2.4.2.3 Device operation and smectic shells preparation

Once the device is ready for use, it should be connected and filled with the different solutions. The first one is pure water that serves for removing the remaining microscopic debris and all the air bubbles stuck inside the circuit. Then the syringes are filled with the solutions to be injected. For smectic shells we used $2wt\%$ of Pluronic F-127 in water as the inner phase, 8CB thermotropic liquid crystal as the middle fluid and a mix of Pluronic F-127 $2wt\%$ and glycerol $60wt\%$ for the outer phase. Pluronic F-127 is a tri-block copolymer surfactant which accommodates parallel to a water-oil (liquid crystal) interface, to stabilize the emulsion. Glycerol on the other hand is used to increase the viscosity of the outer solution and thus to adjust the capillary number to unity at which the dripping to jetting transition may occur. Both the inner and the outer aqueous phases pass through a filter with a pore size of 0.45 μm before injection. The middle phase on its side is injected directly. The three syringes are placed on syringe pumps (Harvard Apparatus Elite 11) and connected to the tubing from each of the device inlets. A complete sketch of the setup is presented in Fig. 2.8

Finally each pump is programmed to dispense the fluids at a specified constant rate. Typical values for thin smectic shells are 1000 $\mu L.h^{-1}$, 400 $\mu L.h^{-1}$ and 7500 $\mu L.h^{-1}$ for the inner, middle and outer phases respectively. Although there's no strict order for launching the pumps, we suggest to start by the outer phase (the cheaper and with the higher flow rate), then the inner phase (the cheaper and with low flow rate), and finally the middle phase (the most precious). The formation of the double emulsions can be observed and recorded at the exit of the collection capillary by means of a high speed camera. In the lab we used a Phantom camera which is able to capture up to 10000 frames per second. From real time images on the display, we can guess important information about the shells: their type, their size, their thickness, etc. It can be also helpful to detect eventual instabilities on the flows that disrupt the emulsion production. In such cases the rates on the pumps can be corrected at any time until fitting the required specifications.

2.4.2.4 Microinjection for single droplet generation

In the previous section, we described the potential of glass microfluidic devices to produce highly monodisperse emulsions at constant flow rates. One of the drawbacks of such systems is the difficulty for making only one droplet at a time, with a specific size and at a specific location. Even if achievable, this process would be time consuming and costly in terms of emulsion constituents, in particular when it comes to liquid crystals or bio-based solutions. To overcome these issues, we propose a new experimental setup consisting of a single capillary linked to a pressure controller apparatus, namely a micro-injector. Such configuration allows to "switch on and off" the flow in a controllable manner to generate locally a single droplet at once.
Similar to conventional glass microfluidics a capillary is tapered with a pipette puller and

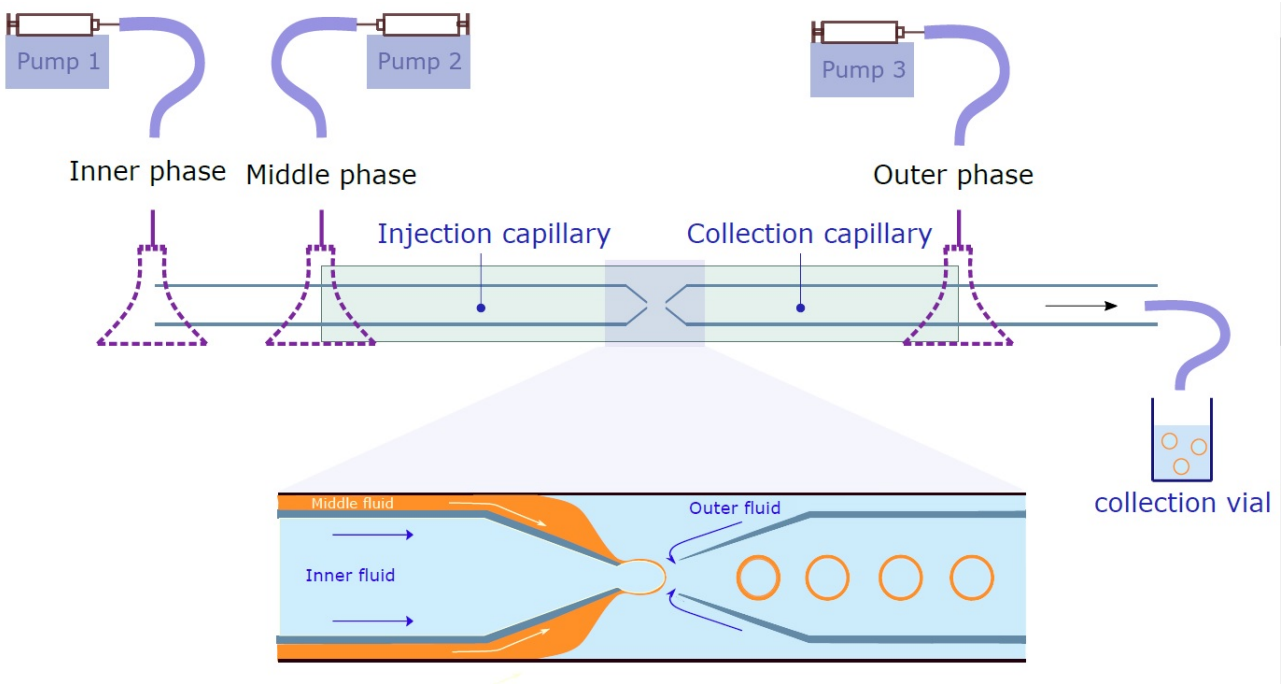

Figure 2.8: Schematic diagram of the experimental setup for double emulsions preparation. The microfluidic device comprises two tapered cylindrical capillaries inserted end-to-end into a square capillary. Dispensing needles are fixed at the three inlets of the device by epoxy glue: one at the entry of the collection tube, and two other at both ends of the square capillary. The inner, the middle and the outer solutions are injected to each inlet by means of three independent syringe pumps. A magnified view of the microfluidic junction shows the formation of double emulsions in the dripping regime: The outer phase flow-focuses the parallel streams coming from the inside and the outside of the injection tube, into the collection capillary. This causes the co-flowing jet to destabilize between the two tips and to simultaneously form the desired shells.

cut with a microforge. For our desired application (the fabrication of inverse emulsions), we adjusted the orifice diameter to $14 \pm 2\mu m$. The capillary is then treated with the octadecyltrichlorosilane (OTS) solution described in section 2.4.2.2. to render its surface hydrophobic. Next, the needle is filled with an aqueous fluid with the help of a microloader, mounted on a pipette holder and is finally connected to a pressure pump through an air tube. In the lab we used an Eppendorf electronic micro-injector Femtojet 4i with a built-in compressor. The apparatus operates by applying small pressures (down to 5 hPa above the ambient pressure) at one end of the injection needle in order to deliver a constant flow of the sample to be injected. When coupled to an automated control system, in our case the InjectMan 4 (Eppendorf) micro-manipulator, the pump is able to impose punctual pulses programmed according to individual needs, hence making the flow delivery more controllable. InjectMan also includes a joystick which can be moved along the horizontal plane and rotated clockwise and anticlockwise to precisely displace the capillary along the X and Y directions and along the vertical axis respectively. Once the capillary is connected to the Femtojet, the needle is immersed in the continuous fluid. When no injection pressure is imposed, the latter phase generally tends to enter the injection needle by capillarity, so a compensation pressure at the other end of the injection needle is applied by the Femtojet to balance the capillarity until the interface between the two fluids reaches the tip of the injection needle. In our experiments this pressure was not higher than 6 hPa. When reaching the desired position of injection along the three axis the first set of coordinates is stored momentarily in the machine. Next the needle

is extracted from the continuous fluid not so far from the interface and the new coordinates are saved as the second position. When both positions are stored, and the capillary tip is outside of the continuous medium, the injection pressure and time are set in the FemtoJet. In our case, we selected values comprised between 18 and 40 hPa and 0.10 to 0.30 s. To trigger the pulse that releases the sample out of the capillary tip, the button on the top of the joystick is pressed once. The needle rapidly moves forward and back from position 2 to 1 and vice versa embedding an aqueous droplet inside the dispersing phase. One of the advantages of inducing such sudden motion is that the droplet is easily detached from the tip through the viscous shear stress exerted by the continuous phase. Ideally, for emulsions composed of 5CB liquid crystal as the continuous phase and the aqueous cytoskeletal extract described in section 2.1. as the dispersed fluid, this strategy leads to typical droplet diameters comprised between 30μm and 100μm. In practice the dimensions of the droplets can display variabilities from one experiment to the other and have to be regulated by finely adjusting some parameters such as the tip diameter, the injection pressure, the time of injection and the viscosities of both inmiscible fluids.

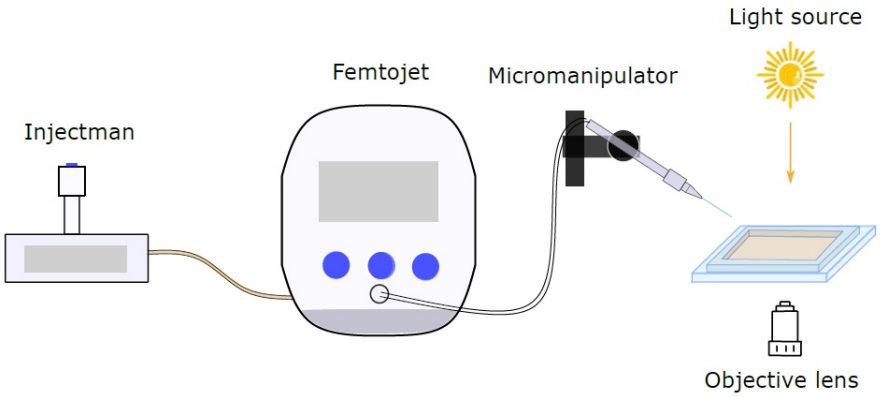

Figure 2.9: Schematic representation of the automated fabrication of an isolated droplet. The Femtojet pressure pump is connected to the Injectman micro-manipulator and to the injection needle. A single droplet can be embedded into the continuous medium by pressing the button on the joystick: The pump delivers a pulse of pressure in the air tube so that a small amount of fluid is liberated inside the cell. The position and the size of the droplet can be controlled thanks to the joystick and to the buttons of the Femtojet which determine the pressure to be applied and the duration of injection.

2.4.2.5 Hybrid microfluidics: Microinjection in PDMS channels

In chapter 1 we described the sensitivity of liquid crystals to the confining boundaries. Close to a surface, mesogen molecules align themselves along a preferential orientation which can be transmitted or not to the bulk depending on whether the anchoring is strong or weak. Sometimes however, the field alignment is gradually lost far from the interface in large or thick samples, even under strong anchoring conditions. In such cases topological imperfections such as point defects or disclination lines are unstable and vanish away or are just impossible to form. One efficient way to reverse this problem and to produce topological defects in a controllable manner is to decrease the separation distance between the confining boundaries and to impose suitable anchoring conditions. Experimentally this can be achieved by fabricating very small circuits, where the liquid crystal will be introduced, by means of soft litography techniques. We used, in particular, photolithography, which is a standard method to pattern a thin film of a silicon-based

substrate with the help of light. Fig. 2.10 shows the steps involved in the micro-fabrication process. The first step consists of designing the pattern to be produced: in our case a set of channels of inner dimensions $4mm$ long and $300\mu m$ wide. Next, the motif is etched with an opaque material on one of the surfaces of a transparent substrate to produce a photomask Fig. 2.11 (a). In parallel, a photo-sensitive material called photoresist is spin-coated on another substrate called the $wafer$ and baked at moderate temperatures to evaporate the traces of solvent, making the material more solid. The thickness of the deposited photoresist layer is dictated by several parameters including: the speed and the duration of the speed-coating, the heating temperature and the duration of the soft bake, and the nature of the photoresist. To obtain a thickness of $110\mu m$ (corresponding to the heigh of the channels) with a $SU-82075$ resin , we use the parameters detailed in the diagram Fig. 2.12. The patterned photomask is then placed adjacent to the negative photoresist for UV exposure. For this, we used the UV-KUB 2 exposure-masking system. The light travels through the photomask, exposing the regions of the photoresist on the adjoining substrate, while the dark zones protect the photoresist from being exposed. As a result the inverse pattern is cured while the original one remains soluble. To dissolve the uncrosslinked monomers of the photoresist the coated wafer is immersed and stirred in a suitable solvent known as the *developer*, leaving behind the patterned structure. Since SU-8 is a thermal resin and its properties can continue to change when exposed to a higher temperature than the maximum operating temperature, the photo-resist then undergoes a "hard bake". This step simply consists of heating the SU-8 at high temperatures (usually more than 120°C) for 5 to 30 minutes. As such the risk of eventual cracks disappears, improving the mechanical properties of the SU-8 resin. The final photoresist mold and the description of the parameters for the photolitographic fabrication of the channels is detailed in Fig. 2.11(b) and diagram Fig. 2.12 respectively.

Subsequently, polydimethylsiloxane (PDMS) channels are prepared following standard soft lithography. The PDMS-base backbone precursor and the cross-linking agent are mixed in a ratio 10:1 (by weight) and are then poured on the photoresist. Next, the mixture is placed within a vacuum desiccator until removing all air bubbles for then being spin-coated at 2000 rpm for 25 s. These values allow to spread the mixture all over the mold while preventing it from overgrowing over the channel boundaries. Lastly the photoresist is placed in the oven set at 70°C for at least two hours. The hardened PDMS channels are gently pulled off from the photoresist by introducing a sharp cutter between the side of the mold.

Thereafter the channels can be bonded to a glass substrate by exposing them to oxygen plasma for $50s$. For this we used a Harrick plasma cleaner which is able to deliver plasma within a closed chamber both to remove the organic contamination and to modify the physical chemical properties of the surface to improve its adherence. Once the channel is set it should be pressed mechanically on the glass substrate, to secure its adhesion to the surface. The system is left to stand for at least 48 hours before conducting the experiments to allow the channel walls constituted by PDMS to fully recover their original surface properties, namely its hydrophobicity.

When the system is ready to use, the channels are filled with the continuous phase by capillarity. Finally, with the help of the microinjector, small amounts of the other fluid are introduced inside the channels by following the protocol (section 2.4.2.4) to form tiny droplets. In chapter 4 we will show that this method can be used for assembling spherical emulsion droplets together in a disclination line running along the narrow channels.

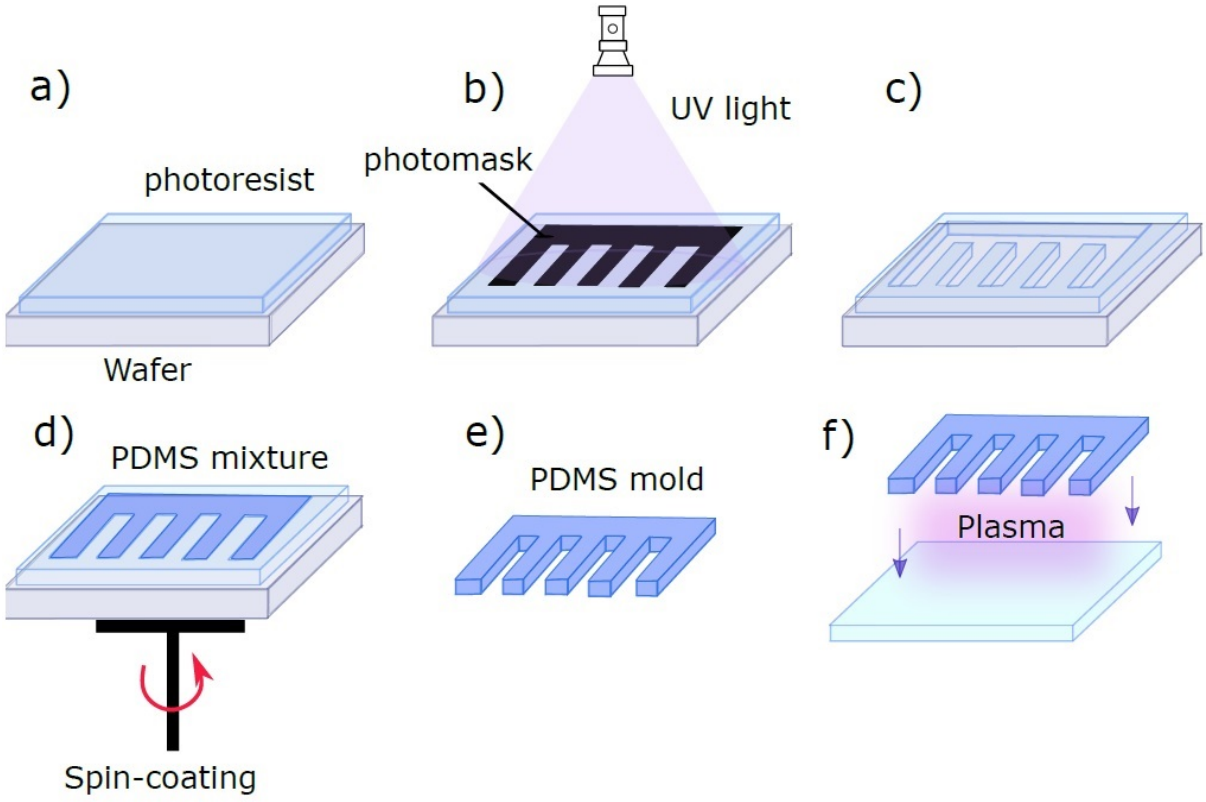

Figure 2.10: Fabrication process of PDMS micro-channels. a)The photoresist is deposited on the wafer. b) A negative photomask is placed on the photoresist and the system is exposed to UV light for curing the uncovered regions of the resin. c) After washing the system with the developer, only the cured photoresist remains, whereas the rest is dissolved and eliminated. d) The mixture of PDMS precursor and cross-linking agent is poured over the wafer with the photoresist cast. The whole system is then spin-coated to attain the desired channel depth. e) The PDMS mold is thermally cured and pulled out from the photoresist f) The PDMS channels are exposed to plasma to be bonded to a coated glass slide.

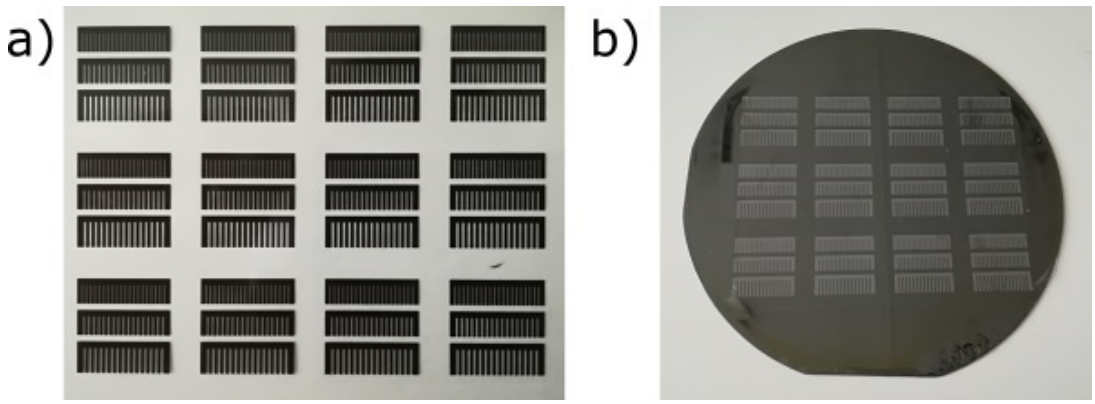

Figure 2.11: Photography of channels mold. a)Photomask with several channels patterns. b) Silicon wafer coated with the patterns etched on a SU-8 photoresist.

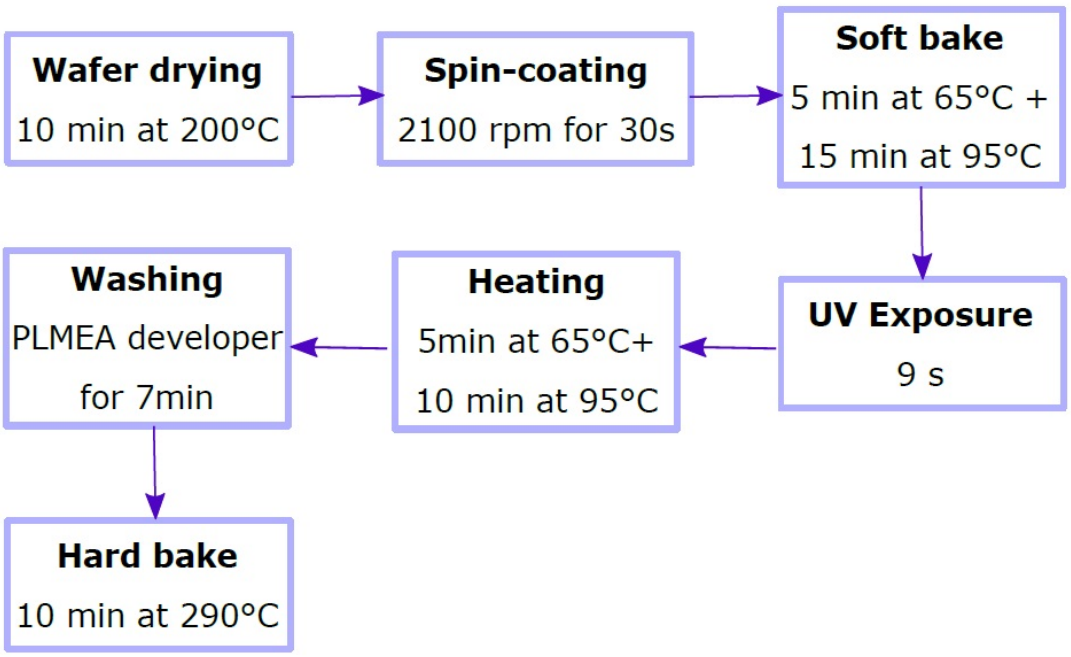

Figure 2.12: Preparation steps and production parameters of the channels photoresist

CHAPTER

THREE

COUPLING OF ACTIVE AND PASSIVE SYSTEMS IN COMPLEX GEOMETRIES

In-vitro biological active matter is a potential platform not only for studying fundamental questions regarding non-equilibrium systems, but also for inspiring the design of new responsive soft materials. One could envision, for example, to program the preferred flow lines, the deformation directions, or even the apparition of entire flow patterns at specific frequencies. Such commands involve an exhaustive control over the behavior of active flows which, in many cases, can be spontaneously chaotic. For many out-of-equilibrium materials, external actuation by means of electric or magnetic fields is an efficient strategy to tame the dynamic flows, yet, in active gels featuring a high ionic strength, electric responses are easily screened and low magnetic susceptibilities make them relatively insensitive to modest magnetic forces. In this context, other techniques that do not require an energy input nor an external actuation need to be implemented.

Such strategies, which we will refer to as passive techniques, in most cases involve the use of a contacting material or confining boundaries that restrict the flows to specific trajectories. A good example are anisotropic viscous fluids, such as liquid crystals, which exert hydrodynamic friction on the active material and can, under certain conditions, organize the chaotic flows. Indeed, regulatory forces of the passive fluid can force the AN to adopt well-established laminar flows or patterns at different scales dictated by the activity of system. In this thesis, this strategy will be often mentioned as the active/passive coupling. Another efficient approach to tune the inherent chaos of ANs is the imposition of strong lateral confinement, for example, by trapping the active material inside a disk or a narrow channel. In this situation, the defects acquire strong orientational order and guide the active flows along specific paths determined by the geometry of the confining boundaries. This technique can be extrapolated to 3D space, by confining the active material on curved and closed surfaces, bringing new tools for controlling spatio-temporal organization of the AN, thanks to the incorporation of new geometrical and topological constraints. Because studying this type of curved systems is extremely challenging, most studies have adopted a numerical approach and only a few experimental examples exist on active nematic spheres and toroids[136,137]. To fill that gap, in the following section, we will present a platform that allowed us to explore these questions experimentally: an active nematic ellipsoid. The distinctive characteristic of the ellipsoidal geometry is that its Gaussian curvature is not uniform, as in the case of the sphere. This feature dramatically impacts the organisation of the AN flows, leading to richer regimes than that attained on the sphere. We explain these behaviors by combining experiments and simulations. This

study is accompanied by a brief preamble on the coupling between active and passive fluids on flat surfaces, followed by a comparative study on ANs confined to the surfaces of other non-spherical objects.

3.1 Passive constraints: viscous oils and structured LC materials

In section 1.2.3, we have described some of the remarkable effects of interfacing an aqueous MT-based active nematic with a passive isotropic oil. In most experimental realizations, active nematics are put in contact with fluids that practically do not impose any frictional damping drag, while in theoretical studies, they are considered as "free floating" systems where the hydrodynamic coupling with their environment is often neglected. In recent studies, Guillamat and coworkers investigated the effect of hydrodynamic interactions on the organization of MT-based active nematics[109,138,139], by interfacing the active system with passive oils of different viscosities. They suggested that the effect of viscous damping at the interface could be measured by counting the number of defects N at the steady state. They first observed that increasing the viscosity of the oil results in slower defect motion, accompanied by an increase of their density and area fraction. These results were explained as a consequence of an imbalance between the defect annihilation and creation rates, in favor of the second type of event. Additionally, they indicated that large viscosities promote bundle concentration, and thus, the amplification in size of the regions void of MTs, identified as the defect cores. The measurement of defect speed and number, finally confirmed the predictions about a characteristic power law relating defect density and speed for MT-based active nematics[138]: $n \sim \frac{|\alpha|}{\sqrt{Kv}}$, with α being the activity strength, K the elastic constant of the nematic, and v the defect speed.
These seminal results highlighted the importance of the viscosity of the contacting fluid in the organization and dynamics of the flows in the active nematic. Additionally, the authors proposed to replace the isotropic oil by a structured anisotropic fluid: a passive liquid crystal. They specially selected a thermotropic 4-octyl-4'-cyanobiphenyl (8CB) LC which features a layered smectic-A phase at temperatures compatible with those permitting the development of the active material. They considered an open cell, where the 8CB is placed on top of the active gel containing a polymeric surfactant. In this configuration, the 8CB molecules are tangentially anchored to the aqueous interface, and thus, the smectic layers form striped patterns at the surface in contact with the active nematic. Since air imposes homeotropic anchoring to the 8CB molecules, *i.e.* they are perpendicular to the 8CB/air interface, the smectic layers form curved structures named *toroidal focal conic domains* (TFCDs)[140], leading to the formation of concentric rings at the interface with the active nematic[109,141]. In such structures, diffusion is favored along the smectic layers and is severely penalized in the perpendicular direction. As a result, the interfacial shear stress sensed by the active material is notably anisotropic, driving MT bundles to extend along circular trajectories centered at the TFCDs[109]. The authors showed that, depending on their sizes, the smectic structures can command the geometry of the active flows. Above a certain length scale, intrinsic to all constrained AN systems, the TFCDs can locally imprint swirls on the active material. On the contrary, small domains are only capable to scatter the moving defects[109].

3.2 Constraining active nematics on curved, closed surfaces

In the previous section, we discussed the potential of employing soft patterned structures to organize the chaotic flows of active nematics confined to two dimensional flat interfaces. The number of possibilities drastically increases when allowing the interface to bend in the third dimension, where topology and geometry can be exploited to impose additional constraints to the system. On a sphere, for example, topological defects are subject to two new constraints that have a tremendous impact on their dynamics: strong confinement and topological requirements . The first constraint acts on the total number of defects, so that only topologically required defects are present. The mutual repulsion of like-sign defects plays a key role in the dynamics of the system: similar to charged particles, like-sign defects repel each other, and thus, maximize their separation distance. The second constraint refers to the global topological charge on the sphere and sets the minimum number of defects in the system (see section 1.1.6.1). These ideas were confronted experimentally by Keber et al, who studied the dynamics of MT-based active nematics on the surfaces of spherical vesicles. They observed that the $s = +2$ net topological charge required by the Poincaré theorem for a nematic sphere was ensured by the presence of four $+1/2$ defects traveling along regular trajectories over the vesicle surface. Moreover, defects accommodated at the vertices of a tetrahedron to maximize their separation distance as a result of their mutual repulsion[136]. Another minimal energy configuration occurred when the defects arranged at the corners of a square, allowing them to transit periodically between the two states as shown in Fig. 3.1 (b). These results motivated a number of numerical studies, which provided interpretations of this oscillatory behavior[142,143] or exploited the topology of spheres to develop a broad diversity of patterns such as vortices[144–147], stable rotating bands, and ring-like structures in the active nematic[148].

Later on, active flow regulation was addressed experimentally and theoretically on more exotic geometries, introducing a new variable to the problem, namely Gaussian curvature, which is constant on a sphere. As mentioned in section 1.1.6.1.1, the latter defines whether a surface is concave ($\kappa > 0$) or convex ($\kappa < 0$) and can be used to direct defect motion. Briefly, Gaussian curvature acts as an external field, making defects migrate towards regions of like-sign Gaussian curvature. This behavior was shown experimentally by Ellis et al.[137], who confined an active nematic to the surface of a large toroidal droplet. This geometry is characterized by regions of positive Gaussian curvature (outer part of the torus) and regions of negative Gaussian curvature (inner part of the torus), as shown in Fig. 3.2 (a). Additionally, its Euler characteristic is equal to zero (see section 1.1.6.1.2), which implies that the toroidal surface is either populated by an equal amount of positive and negative defects or totally devoid of them. Since the synthesized structures were much larger than the typical active length scale, the active nematic displayed a turbulent regime, with a great number of $\pm 1/2$ defects being continually created and annihilated. By computing the local average topological charge S_A in various areas of the torus the authors found a linear correlation with $1/(2\pi) \int \kappa dA$, the integrated Gaussian curvature of the region. This confirmed that, on average, topological defects were sorted in regions of opposite Gaussian curvature despite the chaotic and highly non-equilibrium dynamics of the system[137]. A qualitative agreement was also achieved by comparing these results with those obtained from numerical simulations in

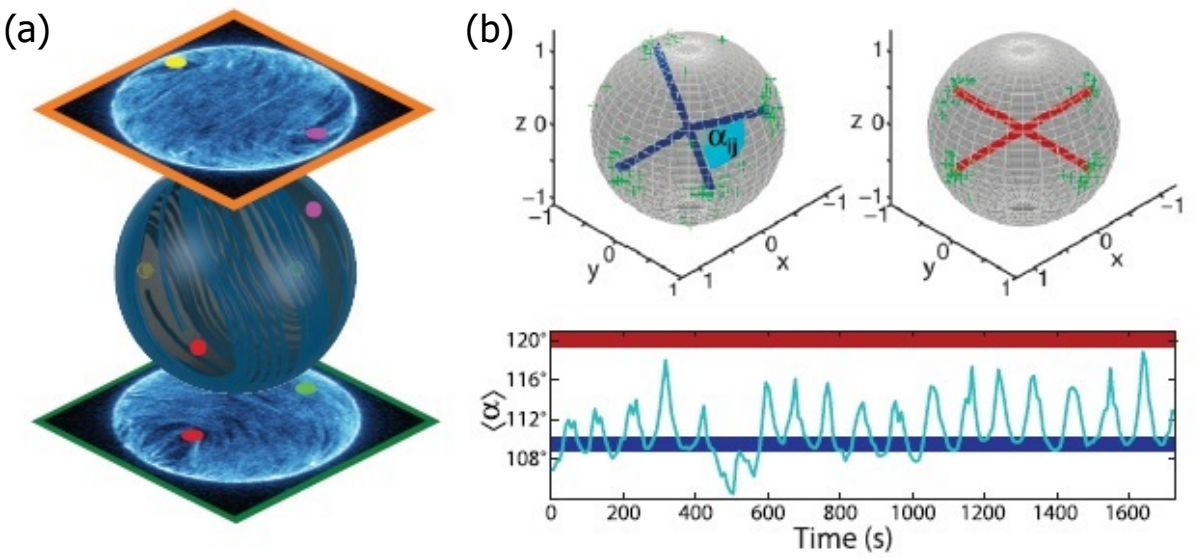

Figure 3.1: Active nematics on spherical vesicles. a) Four topological +1/2 defects (colored spots) develop at the surface of the sphere to satisfy the topological requirements. A reconstitution of the defects' trajectory is possible by tracking them on the bottom and top of a droplet hemisphere of 3D confocal stacks. b) Defects oscillate periodically between tetrahedral (blue) and planar (red) conformations. These oscillations are captured by computing the average angle distance $\langle\alpha\rangle$, as a function of time. Typically $\langle\alpha\rangle = 109.5°$ for the tetrahedral and $\langle\alpha\rangle = 120°$ for the co-planar arrangement. Adapted from[136]

both passive[149] and active systems on toroidal geometries[150].

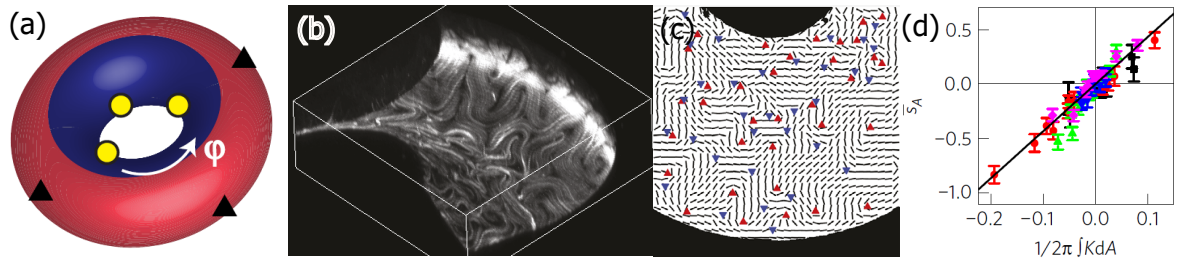

Figure 3.2: Active nematic toroidal shell. a) Color plot representing the topological charge as a function of the integrated Gaussian curvature. The blue (resp. red) region corresponds to $\kappa < 0$ (resp. $\kappa > 0$). b) 3D confocal fluorescence micrograph of a portion of the torus. c) Director field obtained from the intensity projection of (b) along z. Red triangles represent +1/2 defects and blue ones -1/2 defects. d) Time-averaged topological charge in a region as a function of the integrated Gaussian curvature of that region for five different experiments varying, the slenderness of the torus.

The experimental and theoretical realizations exposed so far have proven how active nematics couple to their background either by sensing their rheology or by adapting to their local geometrical properties. On the one hand, the layered structure of passive liquid crystals in the SmA phase offer interesting possibilities to direct the motion of defects along specific trajectories, characterized by a scale-free size distribution. On the other hand, when confined to a curved surface, nematics develop a certain number of defects which self-organize based on the global topological properties (Euler characteristic) and local geometrical features (Gaussian curvature) of the surface. The former determines the minimal number of defects in the director field, while the latter sorts them according to the sign of their topological charge and the concavity or convexity of the underlying

surface. Highly controlled flow regulation could thus be achieved by combining all these factors together. In this chapter, we show the first experimental evidence of organized flows induced by the combined effects of curvature gradients and viscous anisotropy.

We show that imposing gradients of Gaussian curvature to a surface with the same topology as the sphere ($\chi = 1$) can lead to spatio-temporal behaviors drastically different from those reported for active nematic vesicles. Producing these non-spherical interfaces is challenging, since surface tension is highly unfavourable to curvature gradients and most free interfaces relax into a spherical shape. Here, we take advantage of the remarkable elastic properties of smectic liquid crystals to produce ellipsoidal, textured micro-droplets, whose fundamental interest is twofold. These systems provide a playground to study the effect of Gaussian curvature simultaneously with the effect of the smectic texture in the dynamics of active nematics. We show that the interplay between these parameters results in unprecedented, regular trajectories.

First, we will detail the fabrication process of the ellipsoidal smectic droplets, which was briefly introduced in section 2.4.2.3. Subsequently, we will describe the technique to create an active nematic shell on the surface of the passive ellipsoid, as well as the microscopic techniques employed for image acquisition. We further describe the dynamical behavior of the active nematic when confined to an ellipsoidal surface. In particular, we show the existence of two dynamical states with dipolar and quadrupolar symmetries, respectively. In both states, the system undergoes periodical oscillations between a rotational and a translational regime, directed by the motion of pairs of topological defects. To decouple the effects of the curvature gradients on the ellipsoid surface and the viscous anisotropy induced by the smectic layers, we use numerical simulations, performed by A. Mozaffari from de Pablo group (University of Chicago). Finally, we extend our analysis to smectic droplets with the same topology as the sphere or the ellipsoid, but with more exotic geometries. These results are pertinent, not only for understanding how geometry, and in particular Gaussian curvature, can lead to the emergence of order in active systems, but also for developing in vitro platforms to study biological processes connecting shape and function.

3.3 From smectic shells to ellipsoidal smectic droplets

The production of smectic droplets is the result of a two-step process. First, thin double emulsions (W/LC/W) are fabricated by means of glass capillary microfluidics and second, a temperature-driven collapse of shells is induced to form elongated SmA droplets. In the first step, three fluids are injected in a microfluidic device at different flow rates, as detailed in section 2.4.2.2. A droplet of a $2wt\%$ Pluronic 127 solution is encapsulated inside a bigger droplet a pure thermotropic 8CB liquid crystal, which is finally dispersed in a mixture of Pluronic 127 $2wt\%$ and glycerol $60wt\%$ solutions. While producing the shells, the microfluidic device is heated locally at a temperature between 33.5°C and 40.5°C, to maintain the 8CB LC in the nematic phase. The shells are then collected in a solution with the same composition as the inner phase, preheated at 60°C. Although at this temperature 8CB is supposed to be in the isotropic phase, the shells are rather found to be nematic in the vial, because of the heat exchange with the room when collecting the shells. Subsequently, the vial is kept at room temperature for at least 15 minutes, during which the nematic shells cool down to become smectic shells. The resulting shells are very similar to those reported in early works by T. Lopez-Leon and collaborators, in which

polyvinyl alcohol (PVA) was used to stabilize the system and to enforce planar anchoring at the boundaries of the shell[151,152]. In our case, we employed a pegylated surfactant, Pluronic F-127, which is suitable for adsorbing the active material at the surface of 8CB while also ensuring planar anchoring. The molecular structure of the smectic shells is described in the following section.

3.3.1 Smectic shells

The nematic-smectic phase transition in liquid crystalline shells was studied for the first time by Lopez-Leon at al[152]. Their experimental nematic shells were not homogeneous in thickness. This was due to the density mismatch between the inner aqueous phase and the outer liquid crystalline phase, which made the inner drop drawn to the bottom of the outermost drop. As a consequence, the shell was thicker at its top part and thinner at its bottom part. For this study, the authors focused on nematic shells displaying four +1/2 defects. The birefringent texture of the shells revealed that, far from the nematic-smectic phase transition temperature T_{NS}, the four +1/2 defects were placed at the thinnest part of the shell to minimize the energy associated with their cores. When approaching T_{NS}, however, they observed that the defects progressively moved away from each other, because of the drastic increase of bend-splay elastic anisotropy of the LC, until reaching configuration where bend distortion is minimized, presented in the last panels of Fig. 3.3(e) and (f). From this image and its corresponding sketch, we observe that at $T = T_{NS}$ the defects end up sitting along a great circle of the shell. In our experiments, we do not observe the planar defect configuration because the temperature transition is abrupt and the smectic texture appears before the nematic relaxation. As it can be seen in Fig. 3.4, the defects in our shells remain in the thin part when the smectic texture appears.

In the absence of any constraint, SmA liquid crystals adopt a structure where the layers are equidistant flat planes perpendicular to the director. In smectic shells, however, their structure is more complex because of geometrical constraints. Under planar anchoring, the smectic layers orient themselves orthogonal to the curved surface of the shell. On a two-dimensional shell, the interlayer distance can be respected, as shown in Fig. 3.3 (c) and (d). However, as soon as the shell develops certain thickness, geometrical frustration comes into play: the difference in area between the inner and outer surfaces of the shell forces the smectic layers to dilate as they grow from the inner to the outer surface. To partially release the energy associated to this dilation, the smectic layers progressively bend, as in a Helfrich-Hurault process, leading to the formation of a periodic chevron structure at the outer surface of the shell. In this chevron structure, layer dilation is concentrated along curvature walls that divide the shell into crescent domains, as shown in Fig. 3.3 (a), (b). The tilt angle of the smectic layers with respect to the curvature wall depends on the thickness of the shell[153]. In our experiments, the fast cooling of the shells makes them unstable and triggers their collapse. In works of Lopez-Leon et al., where the temperature decreased smoothly, bursting only occurred for a small number of droplets.

We found that shells burst by following two main pathways, illustrated in Fig. 3.5. At the instant when the water droplet is expelled from the double emulsion, the resulting liquid crystal droplet has a concave shape, with a *croissant*-like cross-section, see the schematics in Fig. 3.5(a). This geometry is unstable and relaxes towards an ellipsoidal one following two different pathways. In the first one, the *croissant* arms open up (Fig. 3.5(a)

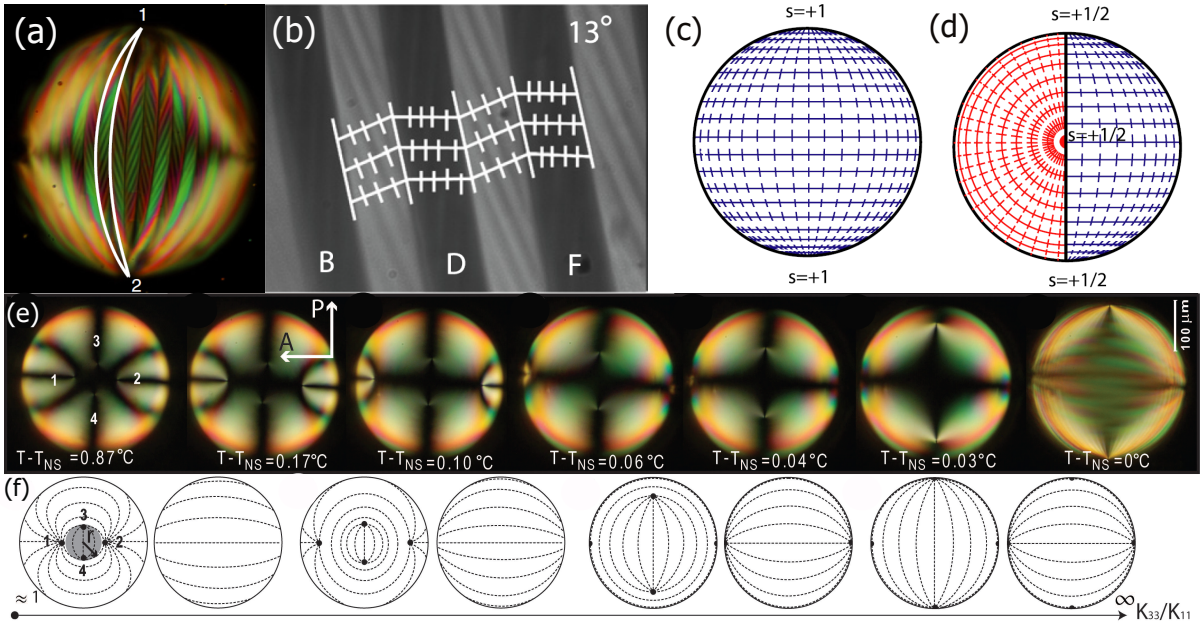

Figure 3.3: 8CB Smectic shells. a) A magnified view into a shell reveals a complex chevron texture characterized by a set of curvature walls that divide the sphere into crescent domains. b) In the birefringent texture of the shells the director (dashed lines) is tilted in opposite directions in adjacent crescent domains. The zig-zag lines are the smectic layers. c) In the bipolar structure the director field lines (discontinuous lines) runs along the meridians connecting the two $s = +1$ defects at the poles. The smectic layers (continuous lines) are perpendicular to the director. d)In another configuration two hemispheres and their corresponding crescent domains are tilted 90° with respect to each other. The $s = +1$ defects split into four $s = +1/2$ defects which align along the great equatorial circle. (e-f) Cross-polarization images and schematic representation of a 8CB nematic shell transiting towards the smectic phase. As temperature approaches T_{NS} defects in the thinner part from the shell separate from each other. Adapted from [151,152]

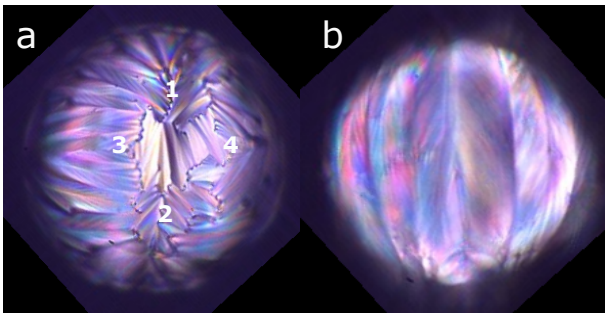

Figure 3.4: Optical micrograph of smectic shells before collapse. a) Thinner part of the shell with 4 $s = +1/2$ defects close to each other and b) thicker part of the shell.

(iv)), while in the second path they close out (Fig. 3.5(b) (iv)) leading in both cases to an elongated structure. Afterwards, the liquid crystal relaxes forming an ellipsoidal or derived geometry (Fig. 3.5(a)(v) and (b)(v)) with bipolar defect structure.

3.3.2 Smectic droplets

The resulting ellipsoids are metastable in solution and tend to become spherical after 48 hours approximately. Nevertheless, the elongated shape of the droplets remains long enough to be manipulated and observed. The temporary stability of the ellipsoids stems from the presence of Pluronic surfactant in the continuous phase, which decreases surface

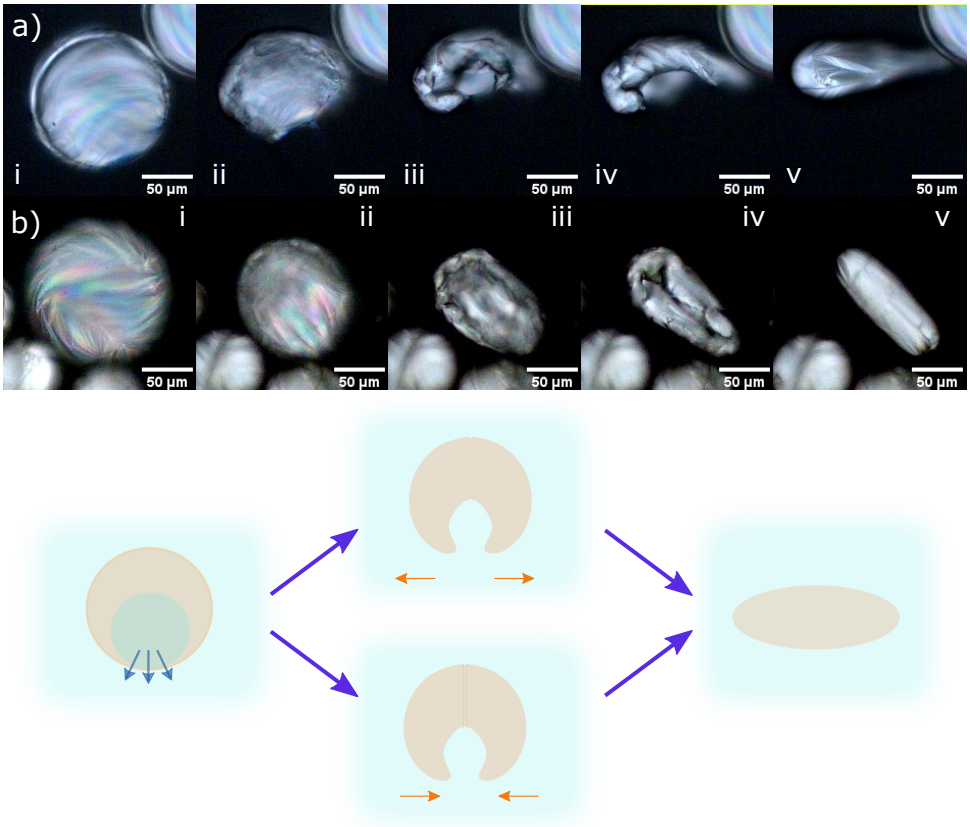

Figure 3.5: Image sequences of smectic shells collapsing. When the shells burst the LC material can either a) Extend along one axis or b)wrap around it to form elongated smectic droplets. The bottom sketches represent the structure of the shells during and after the collapse.

tension and ensures planar alignment of the 8CB molecules at the surface of the droplet, favoring a barely distorted layer organization in the ellipsoidal geometry. Although surface tension dominates over elasticity, and then, the droplet eventually becomes spherical, elasticity imposes an energy barrier that slows down the relaxation process.
Similar to spherical shells, smectic droplets exhibit chevron-like periodic patterns on their surfaces, resulting from the frustration arising when confining a layered system to a curved three-dimensional space with planar boundary conditions. There are however interesting differences between the two systems, which can be seen from the birefringent texture of the outermost layers. In the shells in Fig. 3.3 (a-b), the director $\mathbf{n}$ is aligned along the geodesics with the absolute value of the tilt angle $\phi = 13°$ and a period $p = 2\pi R/q = 15\mu m$; with R the sphere radius and q the wavenumber associated to the layer undulations. Additionally, from Fig. 3.3 (a), we can also distinguish that in a single hemisphere there are approximately 15 crescent domains delimited by curvature walls. Within each domain the tilt of the director with respect to the curvature walls can be expressed as $\phi = arctan\frac{tan(\psi_{max})\times 2h}{p}$, suggesting that an increase in the shell thickness h is also accompanied by an increase in the tilt angle[151,154]. In typical ellipsoidal droplets, whose thickness is of the order of tens of microns rather than just a few, one would thus expect the texture to be more pronounced than in shells. Consistently with these assumptions, the cross-polarized image in Fig. 3.6 reveals that the director tilts almost 20° with respect to the domain walls. The increase of ϕ is also accompanied with an increase of the period (domains' width), from $15\mu m$ in shells (of comparable dimensions)

to $21\mu m$ in the hemiellipsoids. A closer inspection of the field lines reveals that the tilt angle diminishes to $\phi = 13°$ near the poles. This is consistent with the lower thickness of the ellipsoid near the poles, which induces less frustration to the smectic layers between the inner and outer layers.

As a whole, the texture of smectic ellipsoids can be understood by the representation in Fig. 3.6(b). The spaced crescent domains are composed of smectic layers (red lines), oriented perpendicular to the director field (discontinuous black lines). On average, one can visualize these layers as being perpendicular to the main axis of the ellipsoid. This information is valuable to understand the rheological (viscous) anisotropy of the droplets. Along the smectic layers, corresponding to the parallels perpendicular to the long axis, molecules are free to diffuse. Conversely perpendicular to the layers, i.e along the meridians of the droplet, motion is penalized because of the energy cost associated to the elastic distortions. Additionally, these effects compete with the surface tension, that promotes relaxation into spherical shape, by increasing the effective viscosity along the long axis by several orders of magnitude. Because the viscosity is not infinite, surface tension eventually takes over and the ellipsoids recover a spherical shape. This restoration process is, however, long (approximately 2 days) facilitating the manipulation of the droplets.

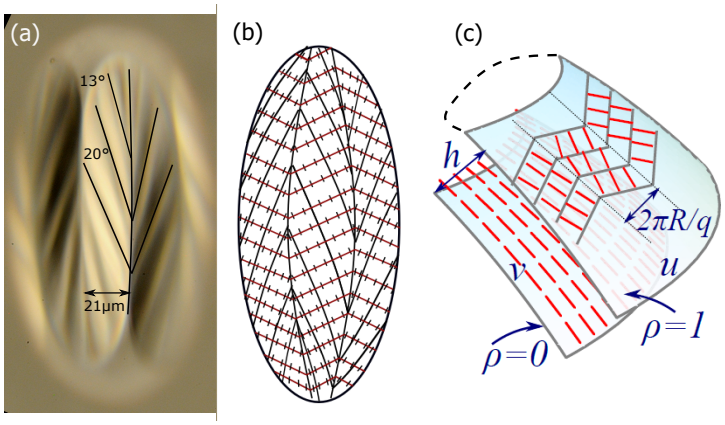

Figure 3.6: Ellipsoidal smectic droplets. a) Birefringence texture of the droplets observed under polarized light microscopy. **n** is tilted by an angle of 20° with respect to the domain boundaries. (b)Schematic representation of the zig-zagging smectic layers (red lines), which are perpendicular to the director field (black lines). c)The amplitude of the undulations of the smectic layers increases as the layers grow out from the inner ($p = 0$) to the outer ($p = 1$) ellipsoid. Adapted from[155]

3.4 Active nematic ellipsoids

A rigorous implementation of the previous protocols results in almost 60% of smectic droplets with elongated shapes. Among them one to two thirds fit the standards of what we consider in our experiments as "model" ellipsoids. These are prolate spheroids with principal semi-axes lengths $a = b = 30 \pm 10\mu m$ and $c = 70 \pm 20\mu m$, yielding an aspect ratio $c/a \approx 2$. The purpose of selecting these dimensions is to be close to the typical active length scale of the active material for reasons that we will explain later. Smectic ellipsoids are pipetted from the top part of the solution in the collection vial where droplets accumulate because of buoyancy effects related to a mismatch of densities between the aqueous and liquid crystalline phases. Although the collected volume contains droplets of different shapes and sizes, the number of droplets is usually large enough to have a

good incidence of the desired ellipsoids. The extracted volume is then dispersed in the aqueous bath of MTs and kinesin molecular motors described in Materials and methods, section 1.2.4, allowing the active nematic to form on the surfaces of the ellipsoids.

This strategy to produce active nematic shells is new, since in previous works[136,137] the active fluid was encapsulated inside the droplet. Using the active fluid as dispersing phase surrounding the droplets offers interesting advantages. First, the dispersed droplets can adopt exotic shapes. In emulsions prepared with the classical method, the dispersed droplets are aqueous, and thus, adopt essentially a spherical shape. With our approach however, any compound non miscible with water, such as anisotropic liquid crystals, can be used to form the droplets, opening the doors to the formation of interphases with non-spherical geometries. Second, the continuous phase acts as a buffer solution for all the constituents of the active solution (activity, motor, filaments) and hence all droplets are equivalent in a given sample. Essentially, individual active shells are exposed to the same concentration of chemical energy and during the same amount of time. Furthermore, the active fluid is accessible and can be easily manipulated from outside. For example, for renewing the energy after the extinction of the activity to increase the lifetime of the sample. Despite these differences, the aggregation mechanism occurring at the aqueous/LC interface is the same, yielding a thin active nematic film on the surface of the droplet.

In the following section, we will analyze the dynamics of the active nematics formed at the surface of the smectic ellipsoidal droplets dispersed in the active bath. We highlight two novel dynamical states, in which the system periodically oscillates between a rotational and a translational state, whose dynamics are controlled by the motion of pairs of associated defects. Such states, alternating vorticity and transport, arise from a rich interplay between curvature gradients and layered patterning of the droplet surface, as well as hydrodynamics of the outer phase. In parallel, we will discuss the transition from chaotic to well-ordered modes in terms of a characteristic length scale defined by the balance of active and elastic stresses in the system. These results are supported by numerical simulations performed by our collaborators Ali Mozaffari and Rui Zhang from de Pablo's group at the University of Chicago.

3.4.1 Oscillatory dynamic states

To ease the handling and observation, the active suspension containing the passive droplets is gently introduced into a polyacrylamide-coated square capillary of 0.6 mm inner width. This coating prevents the adhesion of the active material to the glass walls, ensuring an homogeneous composition of the aqueous bath throughout the system. The ends of the capillary are kept open to renew as often as needed the ATP chemical energy, before the exhaustion of the activity. Note that an enzymatic PEP regenerator is also contained in the initial formulation of the continuous phase, but, despite its high concentration, it remains insufficient for maintaining the desired ATP levels during all the experiment. The acquisition of fluorescence images was performed with a spinning disk confocal Nikon TI-E inverted microscope equipped with a Perfect Focus System (PFS). Images were captured every 500ms with a 10x objective and a camera Andor Zyla 4.2MP operated with NiS-Elements software.

The dynamic self-assembly of microtubules and motor clusters, can be observed a few minutes after filling the capillary with the active mixture. The dispersing phase is

decorated with fluorescent filaments, tens of microns long, that continually extend, and disintegrate to organize large active turbulent flows around the passive droplets. Initially, only a small portion of the active filaments that continually contact the ellipsoidal surface gets adsorbed on it, while the remaining filaments move into the surrounding bulk fluid. Since the available space on the interface is much larger than the amount of initially adsorbed material, microtubules distribute randomly and slowly orient themselves in alternating directions, giving rise to short wave-length instabilities, analogous to zig-zag flows[156,157], as shown in the image sequence of Fig. 3.7. As the active filaments accumulate with time, the active network on the droplet surface becomes denser and stiffer, driving the active length scale (the relation between active and elastic stresses) $l_\alpha = \sqrt{\frac{K}{\alpha}}$, to higher values. As a consequence, the incoherent flows, reminiscent of a turbulent regime, are appeased and replaced by laminar flows displaying a well-defined nematic order and a remarkable periodicity.

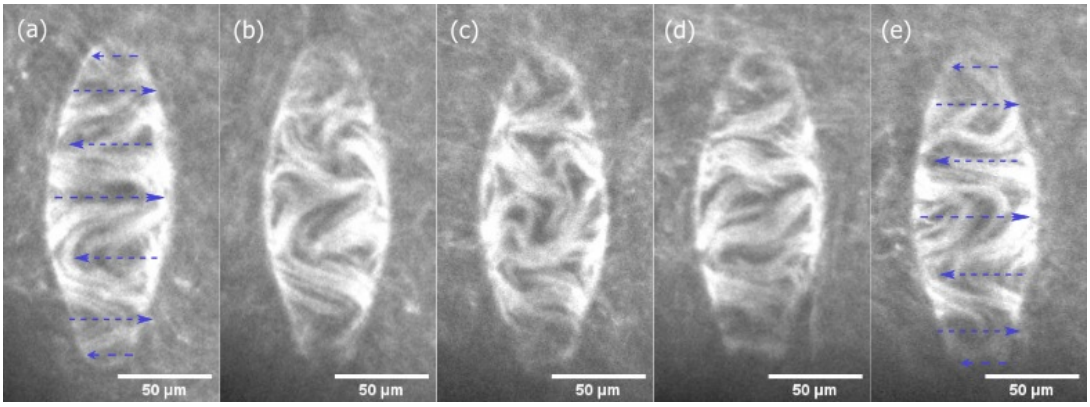

Figure 3.7: Formation of 2D active nematics on ellipsoidal droplets. Fluorescence micrographs of active nematics from $t = 0$ (a) to $t = 3min$ (e). (a-b) At $t = 0s$, active filaments organize alternating flow patterns parallel to the equatorial plane, matching the orientation of the smectic layers. $+1/2$ and $-1/2$ defects move in opposite directions in adjacent lanes. (c-d) The active material destabilizes and flows become chaotic. (e)Every 3min the bundles reorganize to form the initial zig-zag flow pattern.

Transitory dynamics: the quadrupolar state

About two hours after mixing the passive and the active fluids together, the packing density of MT bundles becomes large enough to organize a dynamic state characterized by an ordered pattern of textures and flows that oscillates in time. The dynamics of this first state can be decomposed into two distinct regimes: A rotational regime, where defects describe spiral trajectories along latitudinal lines, and a translational state, where defects move quasi-longitudinally from pole to pole. The temporal evolution of the ellipsoidal AN over half a period is represented in the image sequence Fig. 3.8 (a-d).

Rotational regime: Initially, two pairs of $+1/2$ defects (highlighted in red) occupy the poles of the ellipsoid, one pair sitting on each pole. The two pairs behave similarly, displaying mirror symmetry with respect to the equatorial plane. Those defects move around the ellipsoid main axis, describing co-rotating spiral trajectories at the poles, while locally aligning the flows along lines of constant latitude. Although defects lying on the back plane are not visible in this representation, their pairing behavior can be deduced from the traces left in the director (Fig. 3.8(a)). To commensurate the dynamics at the poles, a counter-rotating belt appears at the waist of the ellipsoid, with alternate

positive and negative 1/2 defects (highlighted in cyan) moving along the same circular line. The topological charge at the equator cancels out, leading to a global charge of +2, consistently with the topological constrains dictated by Poincaré-Hopf theorem[158,159]. Interestingly, the motion of the defects induces the formation of white parallel bands (blue arrows in Fig. 3.7 (a), (e)), corresponding to the easy flow direction set by the underlying smectic layers. At the end of the rotational regime, the whole AN configuration displays quadrupolar symmetry.

Translational regime: Since aligned active nematics are unstable against bending due to their extensile nature, the latitudinal bands of MTs are periodically disrupted by four crimps, which gradually evolve into cracks and propagate longitudinally over the ellipsoidal surface. Defects use these cracks to migrate and repopulate the poles, while locally reorienting the director field along the main axis of the ellipsoid. This regime that begins with the bending instability (Fig. 3.8(b)) is denoted as the translational regime. The longitudinal alignment at this stage causes a rapid destabilization of the new texture, which gradually bends at the equator (Fig. 3.8(c)) and develops parabolic domains extending around the waist of the ellipsoid (see Movie 1). As the two pairs of defects reach the new poles, parabolas gradually reconstitute the equatorial ring with a well-balanced population of positive and negative defects at the same time that transversal bands reappear, recovering the initial rotational state, but with an exchanged location of defects at the poles (Fig. 3.8(d)).

At the poles, the two defects wind around each other without touching. As the active material realigns, it destabilizes again near the waist, and bends to form the rotating belt, that separates the two symmetric regions of co-rotating polar flows. This triggers the reorientation of the director field perpendicular to the main axis, to regain the initial configuration (Fig. 3.8(a)). This incessant switch between rotational and translational regimes persists for up to nearly two more hours, during which the active material continues to accumulate at the surface of the ellipsoid.

To analyze the trajectories of topological defects in active nematic ellipsoids, we first isolated and stabilized the position and orientation of the droplets of interest in the micrographs by means of a homemade Matlab processing program. We accessed the defects location on the AN by tracking them manually via the conventional *Manual tracking* ImageJ plugin. The analyzed movies were typically 15 minutes long to have a representative sample of the system dynamics and a clear overview of the distinct regimes.

From the accumulated data, we computed the probability distribution associated to defect position along the main axis of the ellipsoid (x-axis in the bottom panel Fig. 3.8 (a) and (e)), in order to evaluate an eventual correlations between defect location and surface curvature. In the histogram in Fig. 3.8(e), blue bars, representing the frequency density of either sign defects (the probability that $\pm 1/2$ defects occupy a position x along the main axis), organize almost symmetrically with respect to zero, corresponding to the equatorial plane of the droplet. The height of the bars is also much more pronounced in the middle and the sides of the figure, meaning that defects occupy preferentially the equator and the poles. These observations are compatible with both, a preferential attraction of positive defects towards regions of maximal like-sign Gaussian curvature at the poles, and a persistent circulation of positive and negative defects trapped at the equator during the rotational regime.

It is worth insisting at this point that this quadrupolar configuration is a transient state towards a more stable flow organization of different symmetry and displaying large

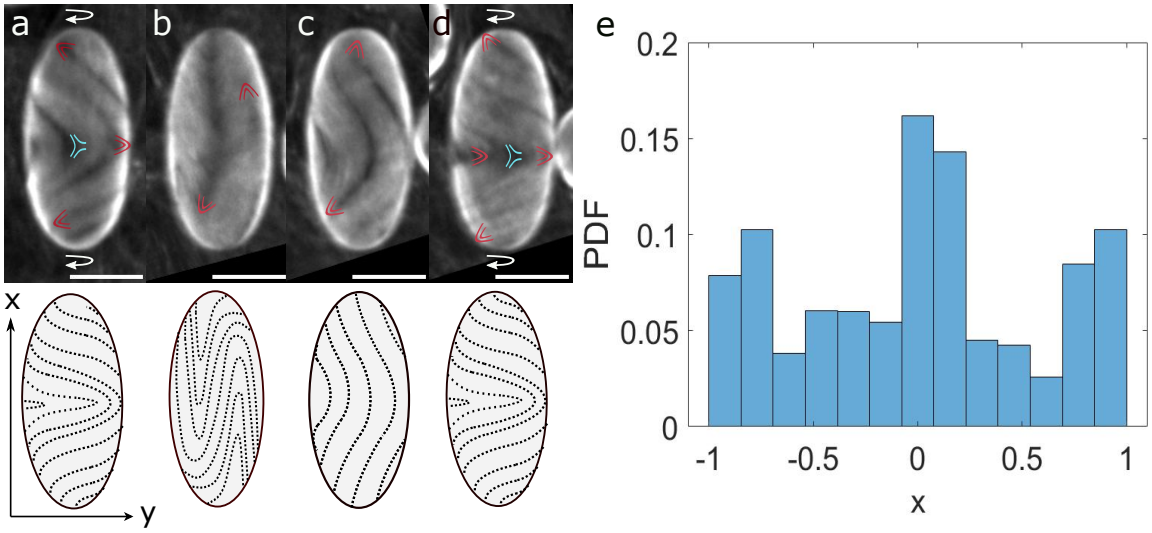

Figure 3.8: Defect dynamics in the transitory, quadrupolar, dynamical state.(a-d) Fluorescence confocal micrographs of active nematics constrained to ellipsoidal surfaces from t = 0 (a) to t = 23 s (d). Parabolic and hyperbolic marks illustrate +1/2 and −1/2 defects, respectively. Sketches in the bottom panel display the director field configuration of the snapshots in the top of the figure. (a), (d) Rotational regime: +1/2 defects spiral by pairs towards the poles while a series of oppositely charged defects circulate around the waist of the ellipsoid. Note that co-rotation at the poles is coupled with counter-rotation at the equator. b) Translational regime: The aligned material destabilizes under extensile stresses, leading to bend distortions which evolve into cracks. Defects propagate longitudinally along the cracks exchanging from one pole to the other. The two regimes repeat periodically for over two hours. (e) Normalized probability distribution of defects along the main axis of the ellipsoid in the transient dynamical state.

wave-length undulations, which will be described later.

Dense active nematics

Although the mechanism triggering the transition between the initial (quadrupolar) and final (bipolar) periodic states is not fully understood, in this section, we show strong evidence that it is related to the densification and subsequent stiffening of the MT-network at the droplet surface. According to this scenario, the transition should occur when the active film reaches a saturation threshold arising from the balance between the number of adsorbed and desorbed microtubule bundles. To investigate this initial assumption, we considered a flat interface, where the dynamics of condensation of the active material can be studied more easily. Inside a PDMS cylindrical chamber, we built a typical planar cell, where the active fluid is underneath a volume of a 8CB liquid crystal. The condensation of the microtubules at the aqueous/LC interface was monitored with a camera for about 4 hours and the MT density was subsequently measured in terms of fluorescence intensity. From Movie 2, we observe a gradual migration of the filaments from the bulk towards the smectic surface until forming a dense two-dimensional layer. Additionally, the plot in Fig. 3.9 reveals that fluorescence intensity grows continuously with time, indicating a progressive accumulation of MT-bundles, specially during the first two hours. The condensation then becomes slower until the layer density reaches a saturation *plateau* after three hours. After that, the intensity remains almost constant until the end of the experiment.

To complement these measurements, we evaluated the thickness evolution of the active nematic film with time. This experiment was performed by Claire Doré, a PhD student

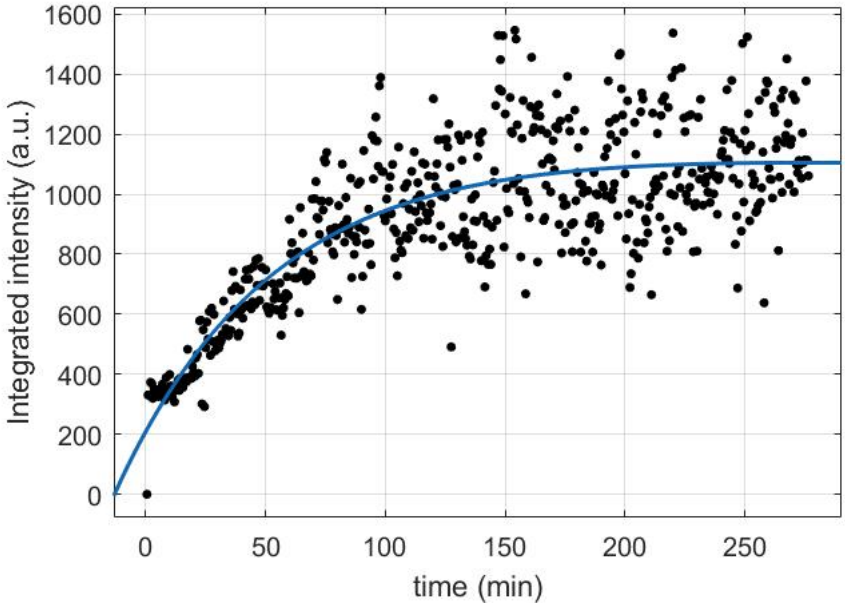

Figure 3.9: Evolution of fluorescence intensity of active nematics on a planar 8CB/aqueous interface. The intensity grows with time according $I(t) = a.e^{bt} + c.e^{dt}$ with $a = 2.4 \times 10^3$, $b = 2.1 \times 10^{-4}$, $c = -2 \times 10^3$ and $d = -1.5 \times 10^{-2}$. A saturation plateau is reached about three hours after the beginning of the experiment

in Gulliver lab at ESPCI. She employed the same type of open cell mentioned above to analyze the formation and densification of an active nematic layer on a flat 8CB surface with time. For imaging, she used confocal fluorescence microscopy, which allows scanning the sample along the axis orthogonal to the plane of the active nematic (z axis). By extracting the average intensity of each cross section, she plotted the intensity profiles along z at different times, ranging from 5 to 20 minutes after the preparation of the sample. The different curves in Fig. 3.10 revealed that the intensity of the signal increases with time, consistently with the results in Fig. 3.9. Furthermore, she demonstrated that regardless of the monitoring time, the intensity peaks have the same width, meaning that the layer does not necessarily become thicker, but rather denser with time. The final layer thickness was estimated to be around $2\mu m$.

From the latter results, we find that the characteristic time associated to the saturation of the active nematic layer on a flat interface (3h00) is shorter than that needed to reach the final dynamical state on an ellipsoidal droplet (4h30-5h00). This discrepancy is likely due to the fact that the condensation rate at a macroscopic flat surface might be larger than at the highly curved surface of a micrometric ellipsoid. Since an experimental comparison between the two systems is extremely complicated and may lead to significant errors, we supported our argument with the numerical works by Kampmann et al.[160] and Stepanow[160]. The authors simulated the adsorption of semi-flexible polymers on planar and curved substrates, such as spheres and washboards. They found that, on flat surfaces, the adsorption was mainly controlled by the stiffness of the polymer, while in curved geometries, it was additionally controlled by the curvature of the structure. Notably, they demonstrated that, on curved substrates, desorption, promoted by the bending energy cost, dominates over attractive interactions. In other words, the aggregation of semiflexible polymers on curved surfaces is harder than on flat surfaces, and thus, takes longer. Consequently, we presume that, on ellipsoidal droplets, there is

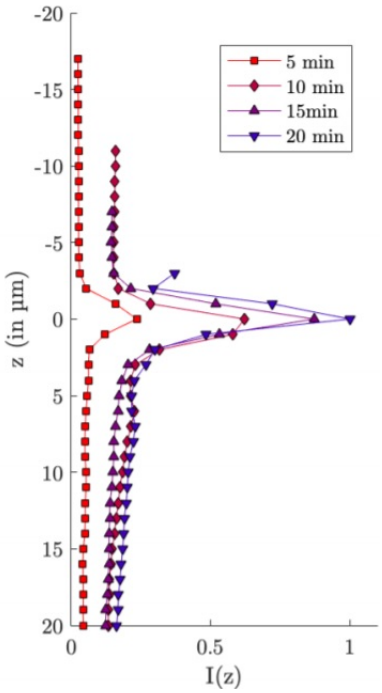

Figure 3.10: Evolution of the AN layer during the first 20 minutes. The fluorescence intensity grows with time but the maximal intensity position remains unchanged. The layer becomes denser rather than thicker with time. Experiment conducted by Claire Doré

still a net adhesion of MT-bundles after three hours, which is the time associated to the saturation threshold on planar interfaces. As times goes by, the active layer becomes denser and more rigid, bringing the active length scale, $l_\alpha = \sqrt{\frac{K}{\alpha}}$ to higher values, with α being the activity and K the elastic constant of the system.

Additionally, the stiffening process is boosted by the gradual consumption of ATP. Since the energy availability in the active bath decreases with time, molecular motors move slower decreasing the effective elasticity of the active network. Briefly, if we assume that the activity scales as $log[ATP]$, the free energy cost that results from spatial distortions in the director field is parametrized by $K \sim l_\alpha^2 log[ATP]$. Therefore, at lower ATP concentrations the gel behaves more as a conventional cross-linked solid than as an equilibrium nematic fluid. Qualitatively, one can observe that, as the early oscillatory state transits towards the final state, the alignment of the MT bundles becomes stronger, making the flows straighter and the equatorial belt, where the active nematic buckles, disappear. The total number of $\pm 1/2$ defects also decreases and their mutual separation increases, which is a natural evidence for the increment of l_α. This transition occurs from two to three hours after the development of the initial quadrupolar periodic state. In the following part, we will describe the behavior of the new oscillatory mode characterized by higher l_α values, and thus, by larger wavelength undulations.

Final dynamics: the dipolar state

After few hours, the amount of active material adsorbed at the ellipsoid surface seems to saturate, making the whole AN network stiffer. As a consequence, the textures and flows get organized at larger length scales giving rise to a new dynamical steady-state (Movie 3), displaying striking similarities but also substantial differences with respect to the just described transitory state. As in the quadrupolar state (Fig. 3.8), here the active

flows continually switch between a rotational and a translational regime (Fig. 3.11 (a-e)). The transition between the two regimes is driven by the motion of two pairs of defects, which continuously migrate from one pole to opposite one, so exchanging their positions (Fig. 3.11(b-d)). A closer inspection of each regime, however, reveals main differences with respect to the early state. For instance, in the rotational regime, the system does not display quadrupolar symmetry but rather adopts a dipolar one.

As sketched in Fig. 3.11 (a), the AN is initially aligned essentially perpendicular to the long axis of the ellipsoid, with a slight diagonal inclination. In this situation, the equatorial belt and its accompanying defects, which otherwise separated the northern and southern parts of the ellipsoid, are no longer present. In parallel, the four previously observed +1/2 defects are now grouped by pairs at the poles to conform a dipolar configuration. In contrast to the quadrupolar state, the two defect pairs counter-rotate at the poles, forming spirals of opposite handedness. To relax the accumulated stress on this aligned conformation, the active material undergoes bend-like deformations which propagate longitudinally, following the +1/2 defects' head (Fig. 3.11(b-d)). Again, these episodes depict a notable difference with the previous state: defect trajectories are no longer interrupted by an intermediate equatorial belt but rather follow direct diagonals from pole to pole (Fig. 3.11(b)). The longitudinal bands progressively tilt away from the ellipsoid main axis (Fig. 3.11(c)) while the defects reorganize the two swirls at the poles to complete the first half period of the oscillatory dynamics (Fig. 3.11(d)). At the end, defect pairs regain their initial neighborhood (Fig. 3.11(a)) to repeat the whole process over and over by continual successions of destabilization/reorganization steps.

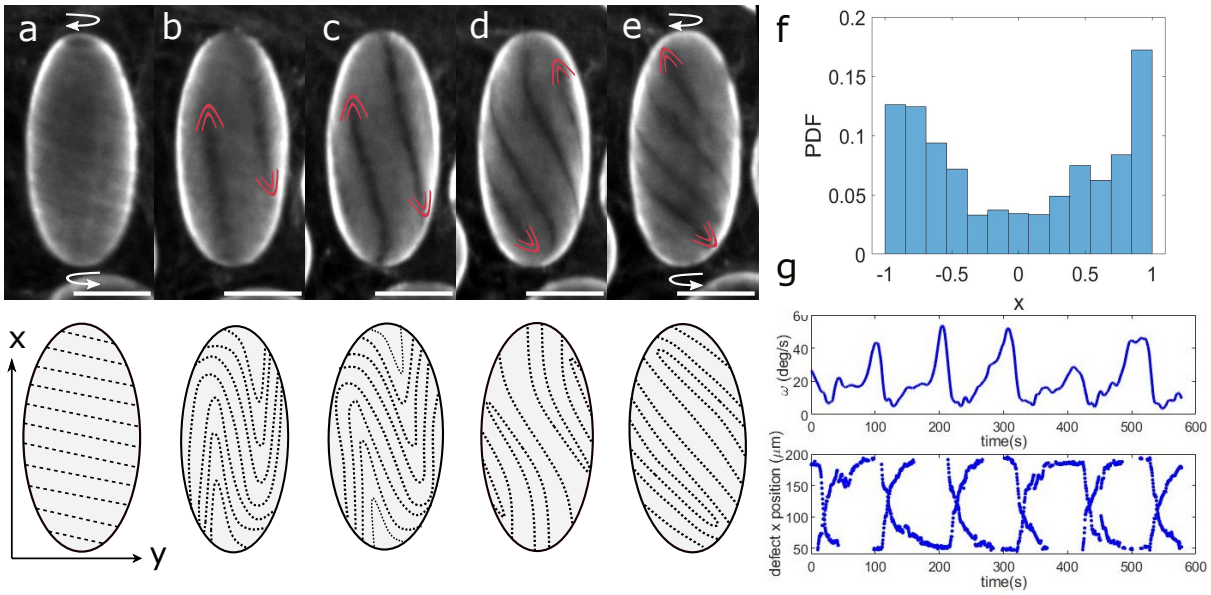

Figure 3.11: Defect dynamics in the final, dipolar, dynamical state. (a-e) Fluorescence confocal micrographs of active nematics constrained to ellipsoidal surfaces from t = 0 (a) to t = 15 s (e). (a, e) Rotational regime: Four +1/2 defects (parabolic marks), coupled by pairs, counter-rotate towards the poles. (b-d)Transient regime: Bend deformations propagate diagonally paving the way for defect migration. (f) Normalized probability distribution of defect position along the main axis of the ellipsoid. Defects distribute symmetrically, with a higher frequency at the poles.(g) Temporal evolution of the average angular speed (top) and trajectory of the defects along the main axis of the ellipsoid (bottom).

The analysis of the defect distribution (Fig. 3.11) (f), in line with the described scenario, reveals a higher likelihood of finding the topological defects near the poles.

As in the previous state, this is consistent with the curvature inhomogeneity of the droplets which promotes a symmetric segregation of the positive defects towards the zones of maximal Gaussian curvature. On the other hand, from the dynamic sequence in Fig. 3.11(a)-(e), we can obtain the time-periodic modulation of the angular speed of the defects all over the ellipsoid surface. The latter exhibits a remarkable correspondence with the trajectory of the defects along the main axis as shown in the bottom panel Fig. 3.11(g). Maximum values of the angular speed coincide with *plateaux* in the defect trajectory curve, and correspond to the episodes of defect swirling at the poles. Minimum values of angular speed, i.e. no rotation velocity components, correspond to the moment where defects cross the equatorial plane while commuting between poles. In a few words, defects move faster latitudinally during the rotational regime, and slower in the transverse direction, during the translational regime. Note also that, in our experiments, a typical half oscillatory period is on average equal to $100s$. This value can nevertheless vary from one experiment to another one depending on the amount of energy available in the system.

Our results prove the existence of two oscillatory states that are essentially different from that reported for spherical active nematics[136]. These two states have quadrupolar and bipolar symmetry, respectively, and combine a chiral rotational regime with translational regime. Although we largely attribute the new dynamic features to the Gaussian curvature gradients on the surface of the ellipsoid, we cannot completely rule out other contributing factors that may be equally crucial[109]. The most important is the eventual role played by the viscous anisotropy of the smectic phase in contact with the active shell. In fact, the migration of topological defects towards the poles (zones of maximal Gaussian curvature) is not random, but follows specific paths such as in a well-structured material. During the rotational regime, in particular, active nematics flow on average latitudinally i.e. along the easy direction set by the smectic layers. To understand these phenomena, in the following section, we resort to numerical simulations to decouple the effects of Gaussian curvature and viscous anisotropy, otherwise impossible to disentangle in experiments.

Numerical methods

The numerical methods used by Ali Mozaffari and Rui Zhang, from university of Chicago, to simulate active nematic ellipsoids are based in the model detailed in section 1.2.3. The latter consists of a continuum description of a two dimensional active gel on an ellipsoidal geometry, considering the evolution of the nematic alignement and the hydrodynamic coupling with the solvent. For uniaxial systems, the alignment is accounted for by the nematic order parameter $\mathbf{Q} = S\langle \mathbf{n}\otimes\mathbf{n} - \frac{1}{3}\mathbf{I}_{ij}\rangle$ where unit vector $\mathbf{n}$ is the nematic director and S is the scalar order parameter. $\mathbf{Q}$ evolves with time according to the following non-linear equation:

$$(\frac{\partial}{\partial t} + \mathbf{u}\cdot\boldsymbol{\nabla})\mathbf{Q} - \mathbf{S} = \Gamma\mathbf{H} \tag{3.1}$$

Here, the advection term $\mathbf{S} = (\xi\mathbf{A} + \boldsymbol{\Omega})\cdot(\mathbf{Q} + \frac{\mathbf{I}}{3}) + (\mathbf{Q} + \frac{\mathbf{I}}{3})\cdot(\xi\mathbf{A} - \boldsymbol{\Omega}) - 2\xi(\mathbf{Q} + \frac{\mathbf{I}}{3})(\mathbf{Q} : \boldsymbol{\nabla}\mathbf{u})$ describes the response of the nematic order parameter to the symmetric $\mathbf{A}$ and antisymmetric $\boldsymbol{\Omega}$ parts of the velocity gradient tensor ($\boldsymbol{\nabla}\mathbf{u}$). The relaxation rate is controlled by the collective rotational diffusion constant Γ.The term ξ on the other hand, is the flow alignment parameter and has been fixed to $\xi = 0.7$ for flow-tumbling

nematics. The relaxation dynamics are incorporated by means of the molecular field $\mathbf{H} = -(\frac{\delta \mathcal{F}_{\mathrm{LdG}}}{\delta \mathbf{Q}} - \frac{\mathbf{I}}{3}\,\mathrm{Tr}\,\frac{\delta \mathcal{F}_{\mathrm{LdG}}}{\delta \mathbf{Q}})$, which drives the system to the lowest value of the energy configuration, with Landau-de Gennes free energy

$$\mathcal{F}_{\mathrm{LdG}} = \int_V f_{\mathrm{LdG}}\,\mathrm{d}V \tag{3.2}$$

The free energy density, f_{LdG}, is sum of bulk and elastic energies given by:

$$\begin{aligned} f_{\mathrm{LdG}} \;=\; & \frac{A_0}{2}(1-\frac{U}{3})\;\mathrm{Tr}(\mathbf{Q}^2) \;-\; \frac{A_0 U}{3}\;\mathrm{Tr}(\mathbf{Q}^3) \\ & +\frac{A_0 U}{4}\;(\mathrm{Tr}(\mathbf{Q}^2))^2 + \frac{L}{2}(\boldsymbol{\nabla}\mathbf{Q})^2. \end{aligned} \tag{3.3}$$

The coefficient A_0 sets the energy scale while U controls the magnitude of the order parameter. Furthermore, L is the elastic constant arising from the one elastic constant approximation. The anchoring conditions at the boundary surface, with unit normal $\boldsymbol{\nu}$, are set by incorporating a surface term to the free energy $\mathcal{F}_{\mathrm{surf}} = \int_{\partial V} f_{\mathrm{surf}}\,\mathrm{d}S$. To impose non degenerate planar anchoring we use the fourth order Fournier-Galatola free energy density:

$$f_{\mathrm{surf}} = \frac{1}{2}\mathcal{W}(\bar{\mathbf{Q}} - \bar{\mathbf{Q}}_\perp)^2 + \frac{1}{4}\mathcal{W}(\bar{\mathbf{Q}} : \bar{\mathbf{Q}} - S^2)^2, \tag{3.4}$$

where $\mathcal{W}$ represents the anchoring strength, $\bar{\mathbf{Q}} = \mathbf{Q} + \frac{1}{3}S\boldsymbol{\delta}$, and its projection to the surface $\bar{\mathbf{Q}}_\perp = \mathbf{p}\cdot\bar{\mathbf{Q}}\cdot\mathbf{p}$, with $\mathbf{p} = \boldsymbol{\delta} - \boldsymbol{\nu}\boldsymbol{\nu}$.

As mentioned in section 1.2.3. the hydrodynamic coupling with the solvent is expressed via the generalized incompressible Navier-Stokes equation:

$$\rho(\frac{\partial}{\partial t} + \mathbf{u}\cdot\boldsymbol{\nabla})\mathbf{u} = \boldsymbol{\nabla}\cdot\boldsymbol{\Pi} - \mathbf{f}\mathbf{u}, \tag{3.5}$$

with ρ and $\mathbf{u}$ the fluid density and velocity, respectively. The equation also includes a dissipative term $\mathbf{fu}$, in which the diagonal tensor $\mathbf{f}$ ensures the frictional damping between the nematic fluid and the underlying substrate. The symmetric tensor $\Pi = \Pi^p + \Pi^a$ embodies the viscoelastic properties of the material and results from the addition of passive

$$\begin{aligned} \boldsymbol{\Pi}^p \quad & = 2\eta\mathbf{A} - P_0\mathbf{I} + 2\xi(\mathbf{Q}+\frac{\mathbf{I}}{3})(\mathbf{Q}:\mathbf{H}) - \xi\mathbf{H}\cdot(\mathbf{Q}+\frac{\mathbf{I}}{3}) \\ & -\xi(\mathbf{Q}+\frac{\mathbf{I}}{3})\cdot\mathbf{H} - \boldsymbol{\nabla}\mathbf{Q} : \frac{\delta\mathcal{F}_{\mathrm{LdG}}}{\delta\boldsymbol{\nabla}\mathbf{Q}} + \mathbf{Q}\cdot\mathbf{H} - \mathbf{H}\cdot\mathbf{Q}, \end{aligned} \tag{3.6}$$

and active stresses:

$$\boldsymbol{\Pi}^a = -\alpha\mathbf{Q}. \tag{3.7}$$

Here, η and P_0 the isotropic viscosity and bulk pressure, respectively. α on the other hand measures the activity strength and varies whether the system is extensile ($\alpha>0$) or contractile ($\alpha<0$).

The governing differential equations eq. 3.1 and eq. 3.5 were solved by employing a hybrid lattice Boltzmann method. The time integration is performed using an Euler forward scheme and the spatial derivatives are calculated using a second order central

difference. Additionally, the coupling is enforced by exchanging local fields between these algorithms at each time step. To mimic the experimental shell, simulations were performed on a three-dimensional lattice where the active layer was confined between two ellipsoids with uniform thickness of 4 lattice spacing. The inner semi-minor and semi-major axes of the ellipsoid were chosen to be 20, 20 and 40 to fix the aspect ratio of the inner shell to 2. Note that all these dimensions are expressed in lattice Boltzmann units. The medium viscosity was set to $\eta = 1/6$ and the collective rotational viscosity to $\Gamma = 0.3$. The values of the other parameters were assigned as follows: $A_0 = 0.1$, $L = 0.1$, $U = 3.0$. Planar anchoring was ensured by choosing $\mathcal{W} = 0.1$, while a no-slip velocity field was enforced at the surface of the inner and outer ellipsoids. The system was initialized with the director field tangentially oriented along the main axis and the layer in between the inner and outer ellipsoids was activated by applying uniform extensile active stresses to the nematic.

Role of the curvature

To explore how the varying Gaussian curvature gradients influence the spatio-temporal trajectories of the topological defects, we simulate a thin shell of active nematic in the tangent plane between two concentric prolate spheroids that reproduce the experimental active cortex coating the elongated droplets. At this stage, no considerations are made regarding the smectic structure of the droplets to restrict our analysis to pure geometric effects. Since this first simulation neglects the effect of the underlying smectic layers, we will refer to it as the *frictionless system*.

Initially, the director field is tangentially aligned along the main axis of the ellipsoid with two pairs of topological defects sitting at the poles. This configuration allows to minimize the elastic free energy while also ensuring nearly uniform alignment of the director in low curvature regions. In the presence of active stress, the system is driven out of equilibrium. On each pole, the defects start rotating pairwise on antipodal points of a circumference to maximize their separation distance - note that defect spacing at each pole is usually constant due to the mutual repulsive interactions existing between the defects (Movie 4). In the body of the ellipsoid, the director field rearranges into a steady configuration, slightly tilted from the major axis. By increasing the activity strength, defects accelerate, amplifying the inclination of the director with respect to the main axis. Above a certain value of activity, the defects change their trajectories, from circular to spiral, and leave the poles with a smooth twist. Defect pairs then migrate from one side of the ellipsoid to the other one in a similar fashion to that observed in the experimental translational regime. This well-organized dynamics is periodically repeated over time, and thus, the system switches between a circulation-dominant motion at the regions of maximal curvature to linear translation near the equatorial plane (Movie 5), as observed in the experiments. Surprisingly, and in contrast with experiments, the handedness of the spirals described by the defects and associated flows at the poles get inverted every time that the defects exchange poles, as shown in Fig. 3.12(a), (f). We further computed the defect residence time along the ellipsoid major axis through the probability distribution function (PDF) histogram shown in Fig. 3.12(g). We find that defects mostly accumulate at the regions of maximum Gaussian curvature. By increasing the activity, this histogram becomes more uniform since the residence time at the poles decreases.

These results show that the frictionless system is able to capture many of the experi-

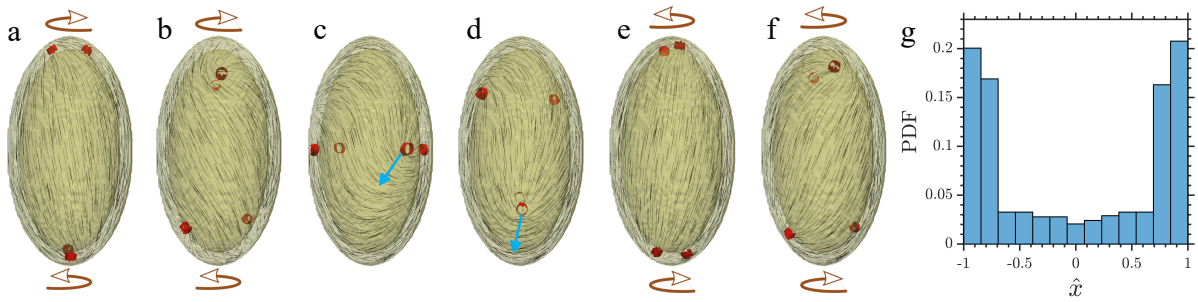

Figure 3.12: Numerical simulation of a frictionless active nematic ellipsoid on the final state. (a-b) In the rotational regime pairs of defects counter-rotate at each pole. Brown arrows indicate the sense of motion of the +1/2 defects (red isosurfaces). Black lines represent the local director field. (c-d) In the translational regime defects leave the poles and migrate towards the opposite end. (e-f) While defects switch the poles they invert their sense of rotation. (g) Normalized probability distributions of defects position along the main axis of the ellipsoid.

mental features observed experimentally in the final dipolar state, but fails at predicting others. On the one hand, it predicts the existence of four +1/2 defects, periodically commuting in pairs between a rotational and a translational regime. On the other hand, it demonstrates that these two events are associated to different forms of spatial occupancy: in the rotational regime, the poles are densely populated by the topological defects, while in the translational regime, defects are rather spread in the body of the ellipsoid. In contrast with experiments, the poles switch handedness every half-period. Therefore, the dynamics of the experimental dipolar state can be explained only partially by geometric considerations. Indeed, the motion of the self-propelled topological defects might also be influenced by the anisotropic friction induced induce in the active system by the layered smectic structure of the droplet. To address this question, in the next section, we include the effect of the smectic layers in our simulations.

Coupling with the underlying passive structure

The layered texture of the smectic phase confers the ellipsoidal surface remarkable properties. The most apparent is the uniaxial rheological anisotropy which is supposed to guide the active flows along preferential paths where the viscosity is minimal. To implement this property numerically, we incorporate a frictional damping force to the equation of motion that penalizes the fluid flows in certain directions. The strength of the force is regulated via a diagonal tensor $\mathbf{f}$. To be as close as possible to the experimental system, where the smectic layer roughly follow latitudinal lines, we consider a uniform frictional pattern that penalizes the flows along the main axis of the ellipsoid. The easy flow direction is imposed to be parallel to the equatorial plane (red lines Fig. 3.6(b)) in such a way that it follows the average orientation of virtual smectic layers. With this configuration, we observe that the topologically required defects organize by pairs at the poles and counter-rotate around the main axis of the ellipsoid. As defects spin around each other, the director field gets slightly tilted away from its original orientation. Although the main tendencies match those observed experimentally, the uniform frictional system also fails to accurately predict the defects trajectories, and even more importantly, the conservation of the flow handedness at the poles (Movie 6). Here again, the defects counter-rotate at the poles of the ellipsoid, but exchange their sense or rotation every half-period. The improvement with respect to the frictionless system is that there is a better agreement with experiments regarding the residence time distribution of the defects along the ellip-

soid (Fig. 3.11 (f)).

Considering uniform frictional anisotropy is not enough to reproduce the details of the dipolar dynamic state observed experimentally. In particular, the model fails at explaining the conservation of the flow handedness at the poles. To understand what guides defects to travel along certain specific directions in the experimental system, we explored numerically other frictional textures, including non-uniform frictional patterns, which might result from the complex interactions between the ellipsoid and its surrounding environment.

Coupling with the external flow fields

To overcome the discrepancies between the experimental and simulation results, we adopted a non-uniformly oriented frictional pattern. The proposed frictional pattern imposes two favorable paths which are almost perpendicular to each other. Near the poles, the easy flow direction is oriented along latitudinal lines, while on the body of the ellipsoid, the easy direction is tilted 25° with respect to the ellipsoid main axis, see Fig. 3.13(a). This texture is different to the one in Fig. 3.6, emulating the smectic layers, but seems to portray complex hydrodynamic phenomena occurring close to the ellipsoidal surface. Indeed, interesting dynamics can be observed when investigating the solid-body behavior of the ellipsoids. In the final bipolar state, they undergo a continuous solid-body rotation around an axis that is perpendicular to the glass plate on which the ellipsoid lie. Fig. 3.14 shows the time evolution of the orientation of the ellipsoid major axis θ with respect to the horizontal axis, proving that the droplet rotates at a constant rate, with θ increasing linearly with time. Note that our analysis is restricted to two dimensions, since buoyancy prevent the droplet from leaving the glass plate. It is plausible to expect that the final dynamics of the active shell is connected to the persistent rotation of the droplet, which stems from hydrodynamic interactions of the droplet with the confining boundaries.

To investigate the origin of this solid-body rotation, we simulate two pairs of defects counter-rotating at the poles while placing a rigid wall close to the surface of the ellipsoid, as in the experimental case (Movie 7). We observe that the spinning behavior of the defects induces strong shear flows in the thin gap between the droplet and the nearby substrate with opposite signs at the poles. This results in a net hydrodynamic torque that promotes the rigid body rotation of the ellipsoid perpendicularly to its main axis, see Fig. 3.15. Note that the sense of rotation of the droplet is dictated by the handedness at each pole. Looking from the left side of the red axis of the ellipsoid in Fig. 3.15, defects on the blue pole circulate counter-clockwise while those on the yellow pole rotate clock-wise. This configuration leads to a global clock-wise rotation of the droplet in a top view along the blue axis. This type of behavior is also observed in experiments: in frames (a-b) of Fig. 3.14 the upper pole (resp. the lower pole) is left-handed (resp. right handed) resulting in a clockwise rotation of the droplet (a-d). Droplets displaying a reverted chirality at the poles also exhibit an inverted sense of rotation in the active solution.

Our hypothesis is that, as the ellipsoid continuously rotates, the surrounding hydrodynamic force couples to the anisotropic friction of the droplet, relative to the smectic texture, leading to new easy flow patterns (Fig. 3.13(a)) that determine the navigation of defects. Near the poles, the easy flow directions orient along the latitudinal lines of

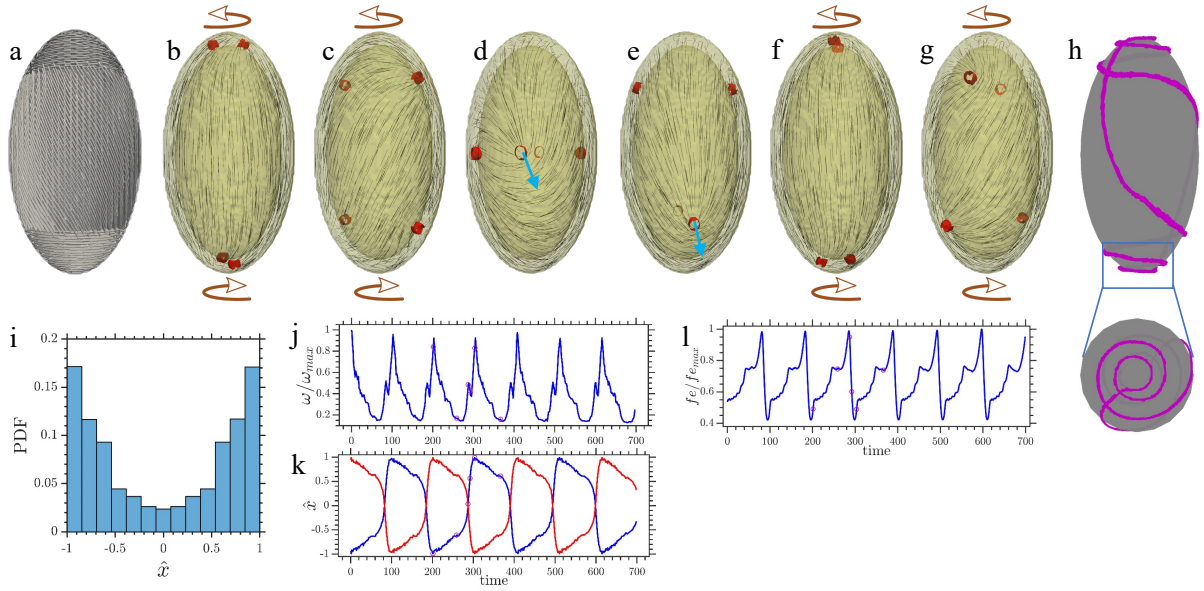

Figure 3.13: (a) Easy flow pattern resulting from the anisotropic frictional damping used in this simulation. (b)-(g) Evolution of nematic director (black lines) and the position of defects (red isosurfaces) with arrows indicating the direction of circulation at the poles. The direction of motion of +1/2 defect is identified by a blue arrow. (h)Side and top view of a single defect trajectory, which shows the spiraling motion at the poles and a linear translation away from the poles. (i) Probability distribution function for the position of defects along the long axis of the ellipsoid. (j) Time evolution of the magnitude of average angular velocities of defects. (k) Normalized position of two defects propelling from the opposite poles as a function of simulation time. (l) Variation of elastic free energy of the system. Six purple open circles marked on the plots of Fig. 4(j)-(l) correspond to the snapshots of Fig. 4(b)-(g), respectively. Positions are normalized with the average of the major axes of the inner and outer shells.

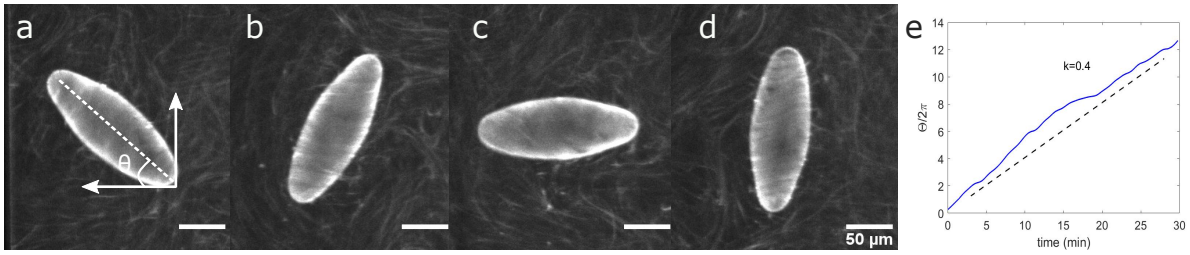

Figure 3.14: Rigid body behavior of an active nematic ellipsoid dispersed in the active bath during the final state. (a-d) Fluorescence confocal micrographs of the droplets rotating at constant speed (images were taken every 60s). (e) The rotation angle θ of the ellipsoid increases linearly with time. θ corresponds to the normalized orientation of the main axis of the ellipsoid with respect to the horizontal direction.

the ellipsoid (matching the smectic layers). We suggest that this is due to the swirling behavior of defects which is transferred to the surrounding media promoting external toroidal flows around the poles, in the same direction than the circulation of the defects. In the body of the droplet, on the other hand, the easy diffusion axis tilts away form the equatorial plane because of the external anti-parallel flows propagating from the poles towards the body or by the sustained rotations of the droplet perpendicular to its main axis.

By simulating the dynamical changes this hybrid friction template induces on the defect trajectories, we successfully reproduced the dynamics observed in the final exper-

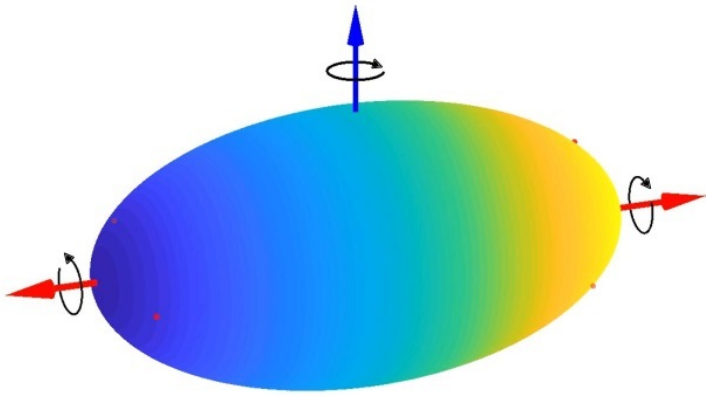

Figure 3.15: Representation of an active nematic shell in contact with a substrate during the final dynamical state. Counter-rotating defects at the poles induce a torque dipole which promotes the rotation of the ellipsoid around the blue axis. The system can rotate either clock-wise or anti-clockwise depending on the handedness at the poles.

imental state. Pairs of defects periodically oscillate between the rotational and translational regimes, giving rise to counter-rotating vortices at the two opposite ends of the ellipsoid and to a linear translation away from the poles, as shown in Fig. 3.13(b)-(g). The longitudinal migration of defects being shorter than the swirling regime, leads to a higher likelihood to find the defects at the poles, as shown in Fig. 3.13(i), thereby explaining the propensity of defects to be in regions with higher Gaussian curvature. Moreover, rotation/translation cycles are regulated by the anisotropic friction of the hybrid pattern, which promotes a fast circulation of defects at the poles, but delays it near the waist of the droplet (Fig. 3.13(j), (k)). In panels (j), (k), open circles corresponds to time series of snapshots displayed in (b)-(g). Furthermore, by analyzing the temporal evolution of the elastic free energy we notice that at the poles, where defects reach the highest angular velocity, elastic free energy is minimized. When energy is injected in the system, however, the uniformly aligned active system destabilizes, enabling defects to escape from the poles and to travel diagonally until the mid-plane, where the elastic free energy is maximized (Fig. 3.13(l)). Most importantly, after this translation, the sense of defect rotation is preserved, in accordance with the experimental results. Therefore, we can affirm that this ansatz for a non-uniform frictional pattern reproduces adequately the dynamical patterns of the experimental final state. The final trajectory of defects on the active nematic ellipsoid is captured in Movie 8 and translated into the spatiotemporal variation of the nematic field in Movie 9.

3.4.2 Summary

In this chapter, we have studied the intricate dynamics of topological defects in active nematic ellipsoids. The first challenge is the fabrication of an ellipsoidal interface, compatible with cytoskeletal extracts, where the active nematic can form. This step is achieved by exploiting the elastic anisotropy of a thermotropic liquid crystal, 8CB, which forms metastable elongated droplets after the collapse of classical smectic shells. By dispersing the resulting ellipsoids into a MTs-kinesin active bath, an active nematic forms at the surface of the droplet, displaying remarkably periodic flow patterns. An early periodic state, referred to as the quadrupolar transient state, is characterized by short wave-length undulations and two oscillatory regimes. In the first regime, the geometry of the droplet

drives the defects towards the zones of maximal Gaussian curvature, namely the poles, where they rotate describing spiral trajectories. The co-rotation at the poles is compensated at the equator by a counter-rotating band populated by pairs of defects of opposite topological charge. Periodically, bend instabilities disrupt the steady vortices, leading to a second regime in which the defects migrate along the main axis of the droplet from one pole the opposite one. With time, the physical properties, as well as the activity of the system, evolves so that the active length scale characterizing the separation distance between defects is increased. As a consequence, a more robust and persistent state is attained. In this final state, the waist of the ellipsoid is no longer populated by topological defects and the active flows at the poles organize counter-rotating spirals. To inquiry about the origin of these dynamics, several sets of continuum simulations were performed, demonstrating that the dynamics are not only controlled by the non-uniform Gaussian curvature of the ellipsoid, but also by internal and external forces exerted on the active shell. In fact, the interfacial material is capable to sense the friction anisotropy imposed by the smectic droplet as well as the external hydrodynamic forces of the surrounding medium.
To conclude, these results offer a promising perspective for engineering rich dynamical states differing from those of observed in the well-studied spherical droplets. In particular, the incoherent behavior of turbulent active flows can be drastically organized by sculpting the shape of the confining substrate and by tailoring soft rails of viscous friction to guide defects periodically along specific paths.

In this first part, we have focused on studying active nematics on "model" prolate spheroids which can be considered as ideal systems. First, because they have dimensions comparable to the typical active length scale of the active fluid, restricting the number of defects, and second, because they have a high degree of symmetry, which is evidenced for example in the geometrical equivalence between the north and south poles of the ellipsoid. There are still however many open questions that we would like to address in the next part. Essentially, how does the shape of the droplets affect the dynamical behavior of topological defects? How does the size of the droplets influence the active length scale and the behavior of the active flows?

3.5 Large active nematic ellipsoids

Large ellipsoidal droplets are produced with the two-step method described in section 3.3. Basically, W/LC/W double emulsions are fabricated with the microfluidic device schematically described in section 2.4.2.3, but this time the incoming flows are readjusted to increase the diameter of the shells. Typically, the outer and inner fluid rates are set up to $6500\mu L/hr$ and to $1100\mu L/hr$, respectively. The middle LC fluid rate can be varied accordingly to make the shells as thin as possible, while keeping the dripping regime stable. When the larger shells collapse because of the temperature change, the resulting ellipsoids are larger than those studied above in this chapter. In this section, we focus on ellipsoids of length $a = b = 45 \pm 5\mu m$ and width $c = 90 \pm 10\mu m$, maintaining the aspect ratio constant to $c/a \approx 2$. The large smectic ellipsoids are dispersed in the active bath, following the previously described protocol. The condensation of the active bundles at the surface of the droplets eventually leads to the formation of a well-defined nematic phase. Since the surface area of the ellipsoids is, this time, larger than the active length scale l_α, we expect activity to dominate and elasticity to regulate the organisation of the

nematic director.

After a while, a turbulent regime, typically observed in unconfined MT-based active nematics, develops on the surface of the ellipsoid, where a large number of $s = \pm 1/2$ defects are dynamically created and annihilated in a chaotic fashion. It is not until 1.5h later that we witness the emergency of a highly periodic dynamical state (Fig. 3.16) with quadrupolar symmetry. This early state is richer than that previously described, due to the larger number of positive and negative half-integer defects as well as the more important flow instabilities all over the body of the droplet. Here again, the system oscillates between a rotational and a translational regime. In the rotational regime, the fluorescent active material forms bands of alternating flow directions, which are separated by strings of rotating topological defects (see Fig. 3.16 (a,e)). While in small droplets a single belt dissociates the dynamics of the two poles of the sphere, see Fig. 3.8(a), here, because of the larger area of the droplet, two rotating belts structure the flows in three distinct regions, as shown in see Fig. 3.16 (e). Since the flow direction is opposite in adjacent bands, a counter-rotating configuration is observed at the poles (see Fig. 3.16 (a-e)). As in small ellipsoids, the rotating belts do not contribute to the total topological charge of the systems since the charges of the positive and negative defects cancel out.

The aligned configuration becomes unstable near the central part of the droplet first, where bend-type distortions grow to eventually form cracks that propagate along the principal axis of the ellipsoid (Fig. 3.16 (b,c)), triggering the onset of the translational regime. Near the poles, the instability starts a few seconds later, causing the previously formed cracks to extend from pole to pole. The cracks are not straight but rather wavy, as a result of a fast buckling of the bundles in a direction perpendicular to the nematic alignment. Interestingly, 4 cracks propagate on each of the hemi-ellipsoids of the big droplets (Fig. 3.16 (c)), instead of 2 (Fig. 3.8 (b)). This corresponds to a total of eight $s = +1/2$ defects travelling from pole to pole in alternating directions. However, as stated by the Poincaré–Hopf theorem, the total topological charge at the surface of the ellipsoid is necessarily $s = +2$. This means that the charge of the defects on the cracks ($s = 8 \times 1/2 = 4$) is partially compensated elsewhere on the system. In fact, we suggest that the spontaneous bending of the extensile material at the poles by the end of the rotational regime results not only in the creation of 4 $s = +1/2$ defects on each pole but also in the formation of a singularity of charge $s = -1$. Therefore, the charge at each pole adds up to $s = 4 \times 1/2 - 1 = +1$ leading to a global charge of $+2$ on the droplet surface, consistent with the topological requirements. Although the observation of the negative integer defects is slightly unclear due to presence of opaque filamentous material in the active bath, we can distinguish dark rotating crosses at each pole of the droplet, indicated by blue marks in Fig. 3.16 (c). The evolution of the director field as well as the configuration of defects at the poles is schematically represented on the lower panels of Fig. 3.16 .

The rest of the dynamics up to recovering the initial state is very similar to the that observed in smaller ellipsoids: The periodically spaced undulations grow in amplitude (Fig. 3.16 (c-d)) until releasing the accumulated elastic stress of the material via the creation of defect belts. Beyond being more than one belt on the surface, the defects contained inside are more numerous as well. While for the typical transitory state of classical droplets there are 2 to 3 visible topological defects per face on a belt (Fig. 3.8 (a, d)), in this new early state, we count 3 to 4 of them (Fig. 3.16 (e)). Additionally we estimate that the number of defects on the belts does not alter the global topological charge of the system since $\pm 1/2$ defects are originated in pairs in the body of the ellipsoid

and thus balance the local charge of each belt. Therefore, the net charge is distributed between the two poles in a similar fashion than in the translational regime, i.e with four $s = +1/2$ defects surrounding a $s = -1$ singularity. As defects rotate both at the poles and at the body, shear flows force the tangential re-alignment of the bundles between neighboring lanes to restore the configuration (Fig. 3.16 (a)). Note that, even if the trace of the negative integer defect seems to vanish in the micro-graphs as the polar rotation occurs, the defect is still present to satisfy the charge conservation. We believe that the progressive alignment near the poles tends to contract the traces of both $s = -1$ and $s = +1/2$ defects as shown in the sketch (a), making them less visible in the images.

These qualitative observations are also supported by the probability distribution of finding positive and negative half-integer defects along the ellipsoid main axis Fig. 3.16 (f). The plot contains two central regions of higher likelihood of finding the defects, that match the regions where the circular belts develop on the ellipsoid. Contrary to the results in Fig. 3.8 (e), showing the PDF for smaller ellipsoids, the defects on this state do not seem to accommodate preferably at both ends of the ellipsoid, but rather in the area between the poles.

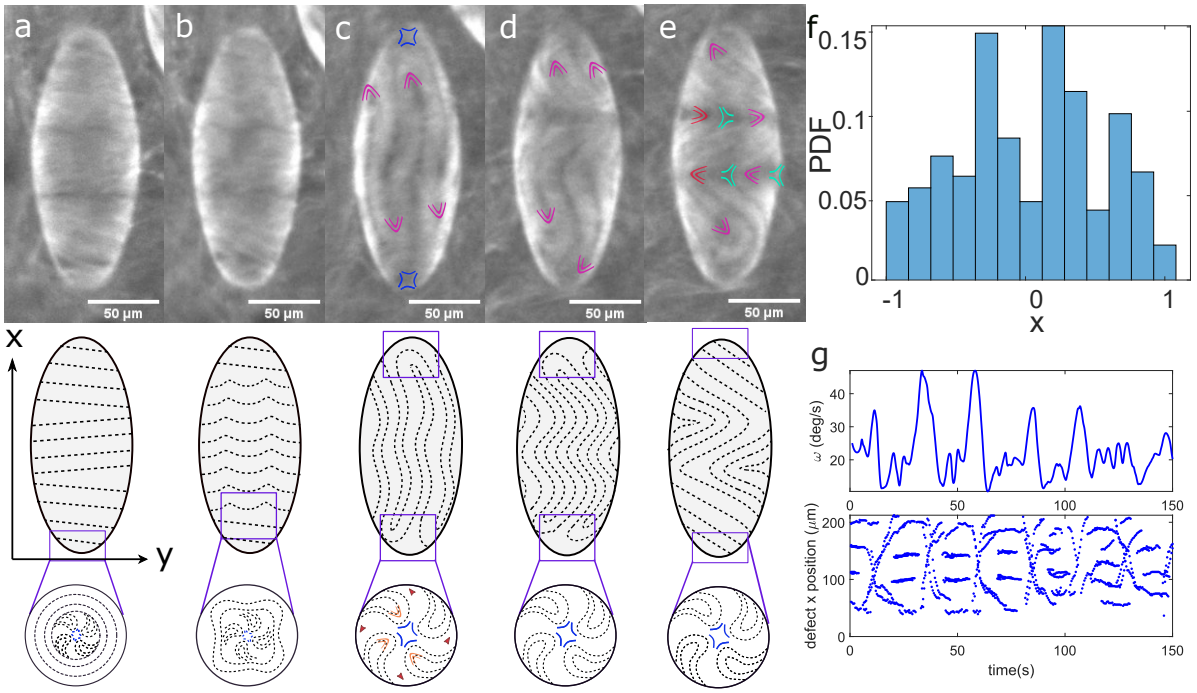

Figure 3.16: Defect dynamics and distribution in the early transient dynamical state of large ellipsoids. (a-e) Fluorescence confocal micrographs of ANs from t = 0 (a) to t = 16 s (e). (a,b,e) Rotational regime: Counter-rotation of $s = +1/2$ defects at the poles is coupled with the circulation of two anti-parallel defect rings in the body . (c, d) Translational regime: Bend deformations propagate longitudinally paving the way for defect migration. Parabolic and hyperbolic marks illustrate $s = +1/2$ and $s = -1/2$ defects, respectively. The sketches of the director field and the defect distribution at the poles are represented in the bottom panel. The topological charge at each pole results in (a, b, d, e) $S = 4 \times (+1/2) - 1$, (c) $S = 4 \times (+1/2) + 2 \times (-1/2)$.(f) Normalized probability distribution of defect position along the main axis of the ellipsoid. Defects distribute with a higher frequency at the two central rings. (g) Temporal evolution of the average angular speed and trajectory of the defects along the main axis of the ellipsoid.

One to two hours later, the system evolves to an intermediate stage that we will call the late transitory state, reminiscent of the classical quadrupolar transitory dynamics of model ellipsoids. One of the principal differences between the ”late” and the ”early”

modes is the absence of one of the defect strings during the rotational regime. As shown in Fig. 3.17(a), (d), (e) a single belt divides the active material at the equator into two symmetric bands as in the classical case described in the previous section. We speculate that the suppression of one of the two strings and one adjacent band is related to the increase of the active length scale l_α with time. In short, as the stiffness of the network grows and the active stress decreases, the distortions of the local nematic order occur over a larger length. The regions of higher distortion corresponding to the defect belts in the rotational regime are thus prone to separate from one another with time. Because the size of the ellipsoids remains constant, and do not grow accordingly with l_α, they can accommodate only a portion of the initial number of nematic distortions on their surface. Therefore, the number of intermediate defect strings on the droplet changes from two to one in the late transitory state. The subsequent dynamical stages occur in a similar way to those of the early transitory state in which a rotational regime is succeeded by a translational regime and vice-versa. Essentially, when the circular shear exerted at the poles and at the equator realigns the material at both hemi-ellipsoids (Fig. 3.17 (a)), eight bend-type instabilities nucleate and further organize alternate lanes for defect longitudinal migration (Fig. 3.17 (b, c)). It is worth noting that once again the eight cracks start to form before the spiraling defects attain the poles. This is evidenced in the micrograph and in scheme (b), showing two horizontal bands at the poles and vertical dark lines in the body. Once the cracks extend all along the principal axis, the vertical alignment is dismantled at the equator, where the active bundles buckle to form the characteristic defect belt of the rotational transitory state and the combination of four $s = +1/2$ and one $s = -1$ defects at the poles.

Regarding the probability distribution of the defects along the principal axis, we observe in Fig. 3.17 (f) that the topological $s = \pm 1/2$ defects organize symmetrically, in a similar fashion to the classical quadrupolar state of small ellipsoids. However, once again the highest occurrence doesn't correspond exactly to the polar region of maximal Gaussian curvature but to the zones close to it.

A few hours later, the active systems progresses towards another state, which is equivalent to the classical final dipolar state observed for model ellipsoids. The superficial material oscillates persistently between the two characteristic regimes with topological defects swirling regularly toward the poles (Fig. 3.18 (a, d)) and exchanging every time an instability disrupts the nematic alignement (Fig. 3.18 (b, c)). The distinctive characteristic of this system compared to small active nematic ellipsoids is the significant number of defects which tend to organize over the surface. This includes the cross arrangement at the poles with 4 $s = +1/2$ defects on the corners and a $s = -1$ singularity at the center during the rotational regime and the 8 anti-parallel lines and the 2 polar spots in the translational regime.

To summarize, large active nematic ellipsoids display a similar behavior to their smaller counterparts but with more complexities related to the larger number of defects. When laminar flows develop at the surface of the droplet, defects periodically oscillate between two characteristic dynamical patterns regardless of the intricate properties of the active material. Increasing the size of the droplet, however, is not without consequences. First, the confinement area is much larger making the adhesion of the MTs bundles take longer. As a result, at short times the network is very flexible and a new transitory state develops under high activity conditions. This early state features typical rotation of defects at the poles but also two defects strings at the body of the ellipsoid. With time, the characteristic length along which distortions propagate increases and one of the rotational

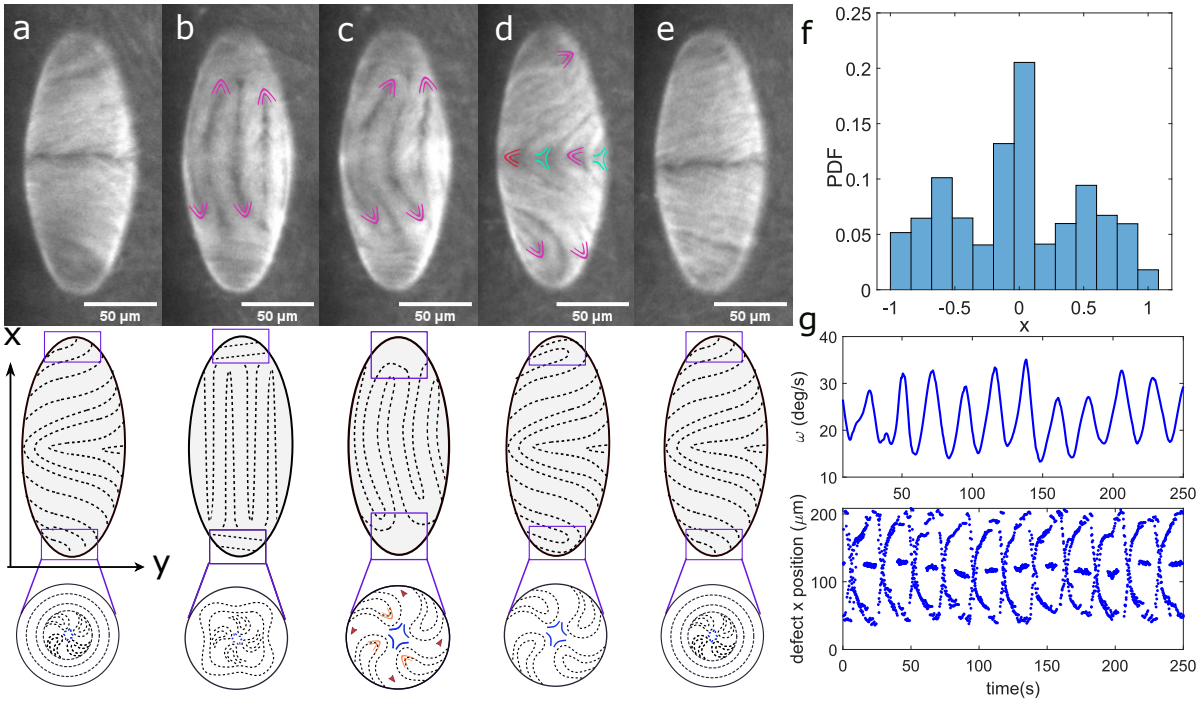

Figure 3.17: Defect dynamics and distribution in the late transient dynamical state of large ellipsoids. (a-e) Fluorescence confocal micrographs of ANs from t = 0 (a) to t = 22 s (e). (a,d,e) Rotational regime: Co-rotation of $s = +1/2$ defects at the poles is accompanied by the circulation a single defect band at the waist of the ellipsoid. (b, c) Translational regime: Bend deformations propagate longitudinally, paving the way for defect migration. Parabolic and hyperbolic marks illustrate $s = +1/2$ and $s = -1/2$ defects, respectively. The sketches of the director field and the defect distribution at the poles are represented in the bottom panel. The topological charge at each pole results in (a, b, d, e) $S = 4 \times (+1/2) - 1$, (c) $S = 4 \times (+1/2) + 2 \times (-1/2)$. (f) Normalized probability distributions of defects position along the main axis of the ellipsoid. Defects accumulate mostly at the equator and near the poles. (g) Temporal evolution of the average angular speed and trajectory of the defects along the main axis of the ellipsoid.

belts of defects vanishes leading to a single belt in circulation in the late transitory state. After more than 6 hours, the nematic layer attains a classical final state where defects mostly swirl towards the poles and migrate longitudinally to attain the opposite end. The evolution of the defects' trajectory along the main axis during the 3 states can be seen on the bottom panel of (g) in Fig. 3.16, Fig. 3.17 and Fig. 3.18 (f). The top curves of the panels (g) and (f) in Fig. 3.18 correspond to the angular speed of the defects over time and they apparently follows a similar tendency to that of model ellipsoids. Therefore, for large droplets, a favorable diffusion occurs along the latitude lines of the droplet coinciding with the smectic layers of the shell core and the penalization occurs in the longitudinal direction. These changes of state are also accompanied by a decrease of the number of adjacent bands of active material and thus by an inversion of the handedness of the spirals at the poles. An odd number of bands, encountered for example in the early transitory state (3) and in the final states (1) leads to counter-rotating flows at the poles while an even number of bands such as those in the late transitory state lead to co-rotating defects at the poles.

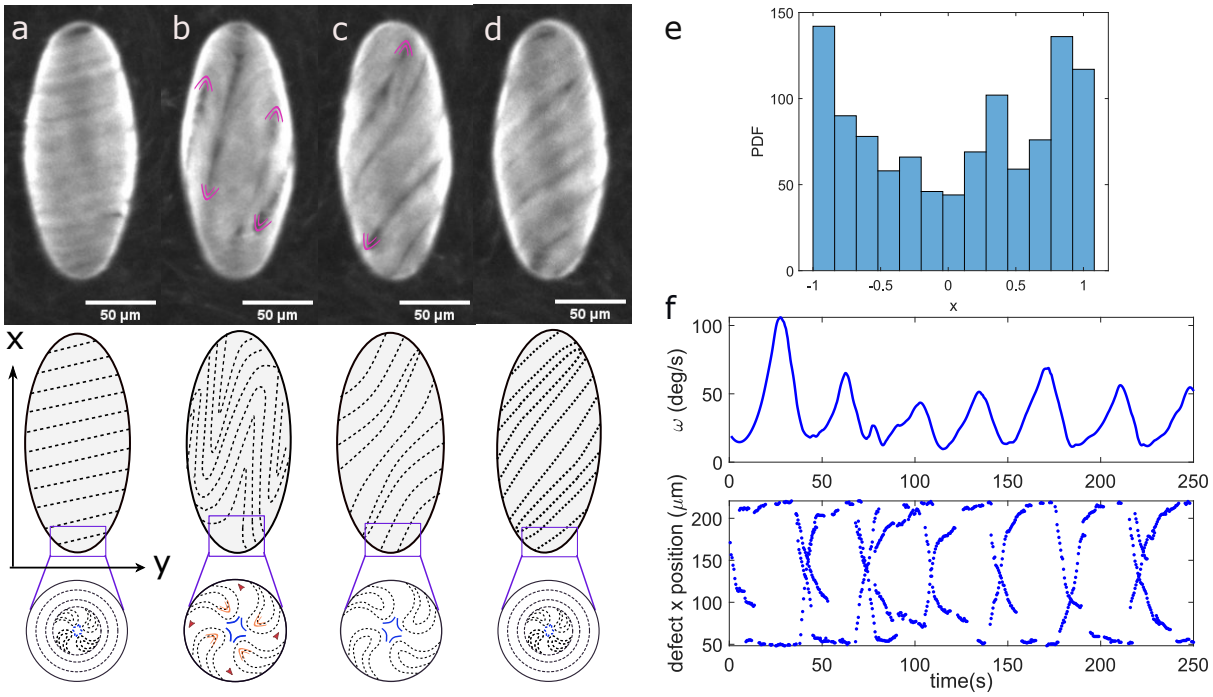

Figure 3.18: Defect dynamics and distribution in the final dynamical state of large ellipsoids. (a-d) Fluorescence confocal micrographs of the AN from t = 0 (a) to t = 23 s (e). In the rotational regime (a,d), $s = +1/2$ defects counter-rotate at the poles. In the translational regime (b,c) the active material destabilizes and defects migrate along vertical cracks from one pole to the other one. Parabolic and hyperbolic marks represent $s = +1/2$ and $s = -1/2$ defects, respectively. The sketches of the director field and the defect distribution at the poles are illustrated in the bottom panel. The topological charge at each pole results in (a, c, d) $S = 4 \times (+1/2) - 1$, (b) $S = 4 \times (+1/2) + 2 \times (-1/2)$.(f) Normalized probability distribution of defect position along the main axis of the ellipsoid. Defects occupy more frequently the regions close to the poles. (g) Temporal evolution of the average angular speed and trajectory of the defects along the main axis of the ellipsoid.

3.6 Geometrical effects: Spherocylinders and pear-like active nematic shells

Smectic droplets resulting from the collapse of W/LC/W double emulsions usually do not relax into a unique geometry with $\chi = 1$ but into a wide variety of them, with different proportions and degrees of symmetry. Two shapes are of particular interest because of their local geometrical properties: spherocylindrical and pear-like droplets.

Spherocylindrical active nematics

Spherocylinders consist of a cylinder with hemispherical ends. At first glance, this geometry does not look very different from that of the ellipsoid, due to its elongated shape and to the positive Gaussian curvature near the poles. Nevertheless, in the central cylindrical region of the spherocylinder, Gaussian curvature is constant and close to zero. The spherical cups at both ends, on the other hand, are ideally characterized by positive and constant mean and Gaussian curvatures. In practice, the Gaussian curvature at the body and at the poles of spherocylindrical smectic droplets is not perfectly constant and displays minor variations that can be seen in Fig. 3.19 (b). This 3D representation shows the

surface of droplets reconstructed from 2D micrographs by means of a homemade Matlab program, and their Gaussian curvature calculated via the *Surfature* function[161]. In the spherocylinder on the right (Fig. 3.19 (b)), values of Gaussian curvature grow smoothly from approximately 0.4×10^{-3} (arbitrary units, a.u) in the upper (resp. lower) third of the droplet to 1.1×10^{-3} (a.u) at the highest (resp.lowest) point of the cup, contrary to ellipsoids where the increment at the poles is much more pronounced (left figure). Note that these values correspond to spherocylinders with similar proportions to the typical ellipsoids considered in this work, namely, with an aspect ratio of 2 and a long axis of $140\mu m$ approximately.

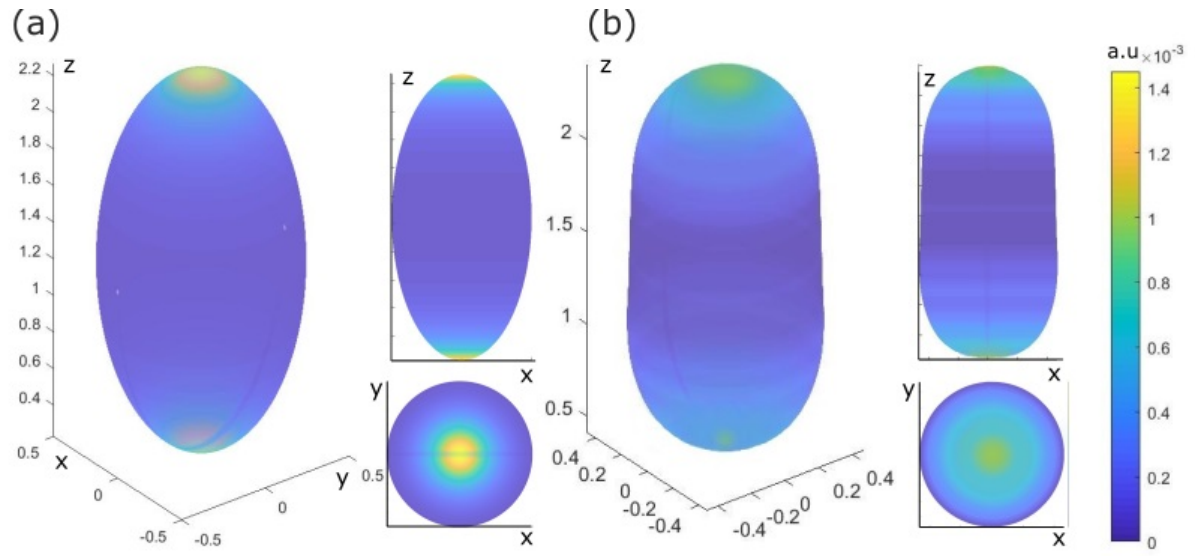

Figure 3.19: 3D reconstruction and Gaussian curvature of ellipsoidal and spherocylindrical droplet surfaces. Left figures in (a) and (b) represent the 3D view of typical ellipsoids and spherocylinders. The figures on the right show the lateral and top views of the surfaces.

To study the behavior of the active nematic flows at the spherocylinder surface, we perform the usual protocol and we track the evolution of the active network with time. In Fig. 3.20, we show the dynamics of the topological defects during the final state, which occur approximately in the same time intervals reported before for small ellipsoids in the dipolar state. From both qualitative and quantitative analysis, we notice that there is no major differences between the behavior of spherocylindrical nematics and ellipsoidal ones. The image sequence in Fig. 3.20(a-d) reveals regular oscillations between the rotational and translational regimes, while the histogram panel in Fig. 3.20(e) proves the propensity of the four defects to occupy preferentially the poles and to distribute symmetrically along the droplet. On the other hand, Fig. 3.20 (f) highlights the fact that defects speed up at the poles and slow down while crossing the body of the droplet.

More interesting behaviors occur when changing the proportions of the confining droplet. In Fig. 3.21, we show a very elongated droplet with an approximate aspect ratio of 3. Visually, the structure seems to be closer to a spherocylinder than to an ellipsoid, because of the negligible Gaussian curvature of the lateral boundaries delimiting the body and the slow curvature gradient at the poles. In this geometry, the active nematic shell evolves in the usual way, with four defects guiding the active flows periodically in different regions of space. In the final state, there are no particular differences in the trajectory of defects, nor in their speed in the different regimes (Fig. 3.21(g)). Nevertheless, what makes this structure intriguing is the significant time that defects spend at the poles. As

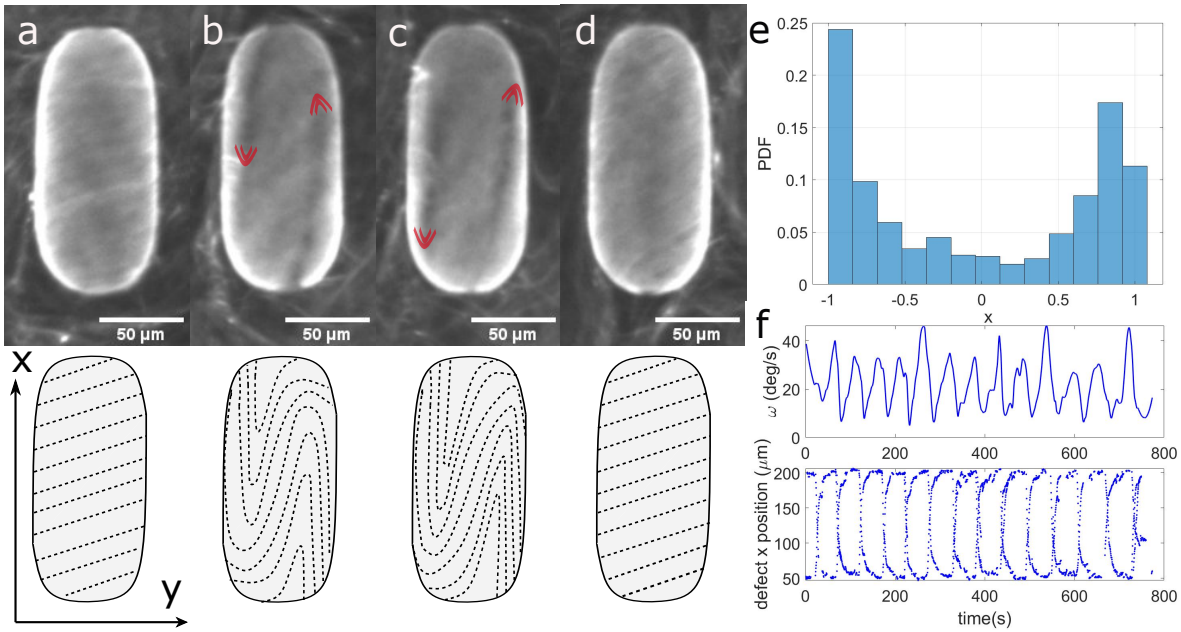

Figure 3.20: Defect dynamics in the final state of an active nematic spherocylinder. (a-d) Fluorescence confocal micrographs from t = 0 (a) to t = 44 s (d). Parabolic marks represent $s = +1/2$ defects. The sketches of the director field are shown in the bottom panel. (a, d) Rotational regime: $s = +1/2$ defect pairs counter-rotate at the poles. (b,c) Translational regime: Bend deformations propagate diagonally, paving the way for defect migration. (e) Normalized probability distributions of defect position along the main axis of the ellipsoid. (f)Temporal evolution of the average angular speed and trajectory of the defects along the main axis of the ellipsoid.

can be seen in Fig. 3.21(f), there is a large gap between the probability of finding the defects at the curved cups and the probability of finding them near the equator or in any other part of the droplet. In fact, this gap is not so pronounced in conventional ellipsoids for which the PDF plot (Fig. 3.11 (f)) is rather v-shaped with probability decreasing slowly from the poles towards the equator. For this reason, we suggest that increasing the aspect ratio of the droplet may contribute to increase the residence time of defects at the poles. One possible explanation of this is that, in high aspect-ratio ellipsoids, during the rotational regime, the time needed to reorient the director field parallel to the equator is longer, and thus, the defect spend more time rotating at the poles. While for short droplets the torsion propagates fast from the poles towards the body, for long droplets, more cycles of torsion are required to propagate the transversal alignment all along the body. As a consequence, defects may stay longer at the poles before the latitudinal alignment is reached and disrupted by bending instabilities.

Pear-shaped nematics

Pear-shaped droplets are sometimes described as a ”teardrops”, since they are slightly elongated, flattened on one side and bulged on the other one. Mathematically, they can be constructed by overlapping a prolate spheroid with half of a sphere. Contrary to typical ellipsoids, pear-shaped droplets lack reflection symmetry across the equatorial plane and display significant differences of curvature between the two poles. In Fig. 3.22, we represent a 3D reconstructed smectic teardrop with dimensions comparable to those of model ellipsoids. We observe, for example, that the Gaussian curvature values on the north pole vary from 0.4×10^{-3} a.u to 1.2×10^{-3} a.u, which is a much larger curvature

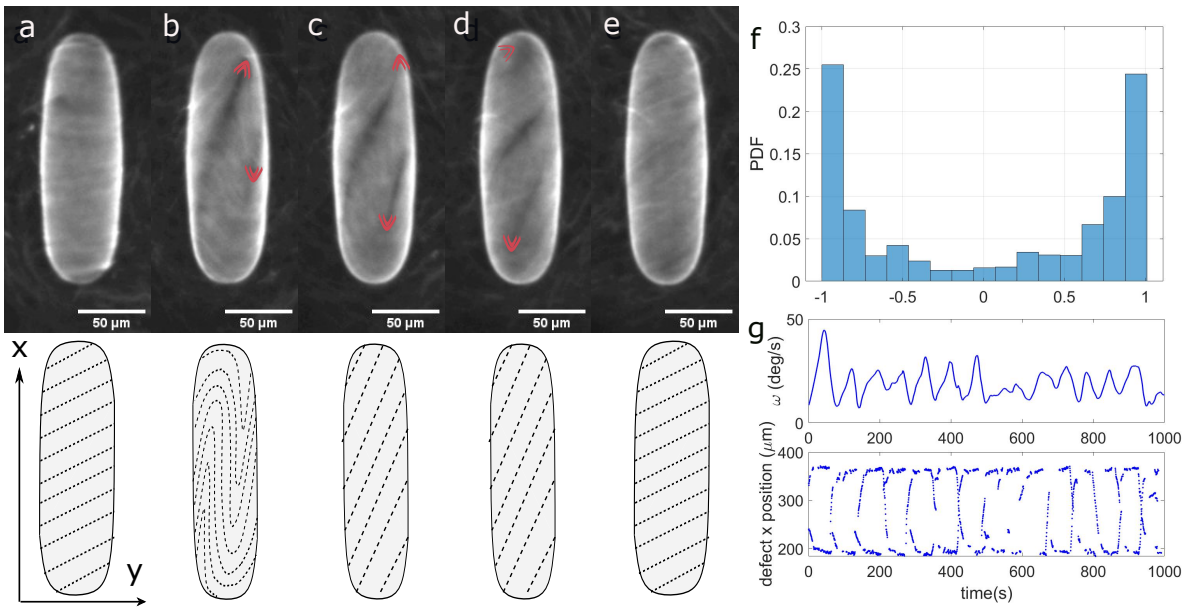

Figure 3.21: Defect dynamics in the final state of an elongated active nematic spherocylinder. (a-e) Fluorescence confocal micrographs from t = 0 (a) to t = 33 s (e). Parabolic marks represent $s = +1/2$ defects. The sketches of the director field are illustrated in the bottom panel. (a, d, e) Rotational regime: $s = +1/2$ defect pairs counter-rotate at the poles. (b,c) Translational regime: Bend deformations propagate diagonally, paving the way for defect migration. (f) Normalized probability distributions of defect position along the main axis of the ellipsoid. (g) Temporal evolution of the average angular speed and trajectory of the defects along the main axis of the droplet.

gradient than in the south pole, where curvature hardly reaches 1×10^{-3} a.u.

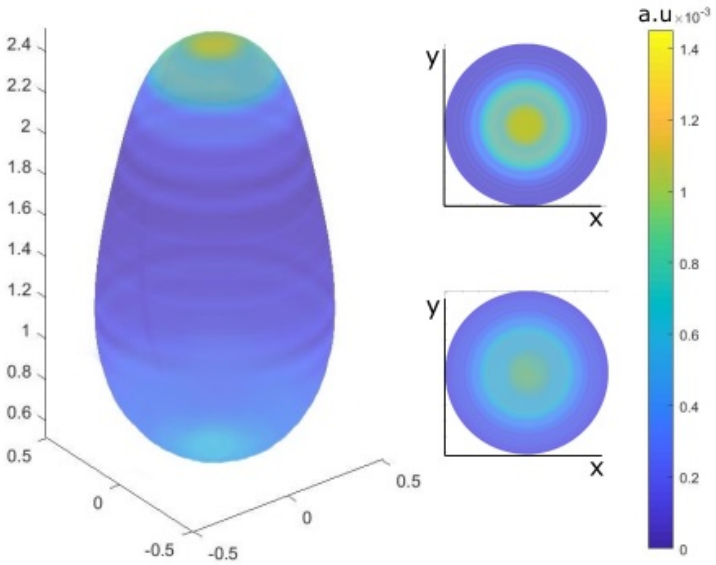

Figure 3.22: 3D reconstruction and Gaussian curvature of a pear-shaped surface. The figure on the left represents the 3D view of the droplet and those on the right the top and bottom views.

The geometrical asymmetry allows us to probe the effect of Gaussian curvature variations on active nematics on a single surface. The behavior of the condensed material on teardrops is first analyzed during the transitory state Fig. 3.23. From the image sequence in Fig. 3.23 (a-e), we observe that topological defects describe similar trajectories than

those found in typical ellipsoids. The rotational regime, see Fig. 3.23(a,d,e), is characterized by co-rotating swirls at the poles coupled to a classical counter-rotating, zero-charge ring of defects at the equator. In the translational regime, see Fig. 3.23(b,c), the migration of four $s = +1/2$ defects from pole to pole is accompanied by longitudinal alignment, which is slowly disrupted by bend distortions at the mid-plane. These similarities are also supported by Fig. 3.23 (f), showing the prevalence of a symmetric distribution of defects at the poles with also an important density peak close to the waist.

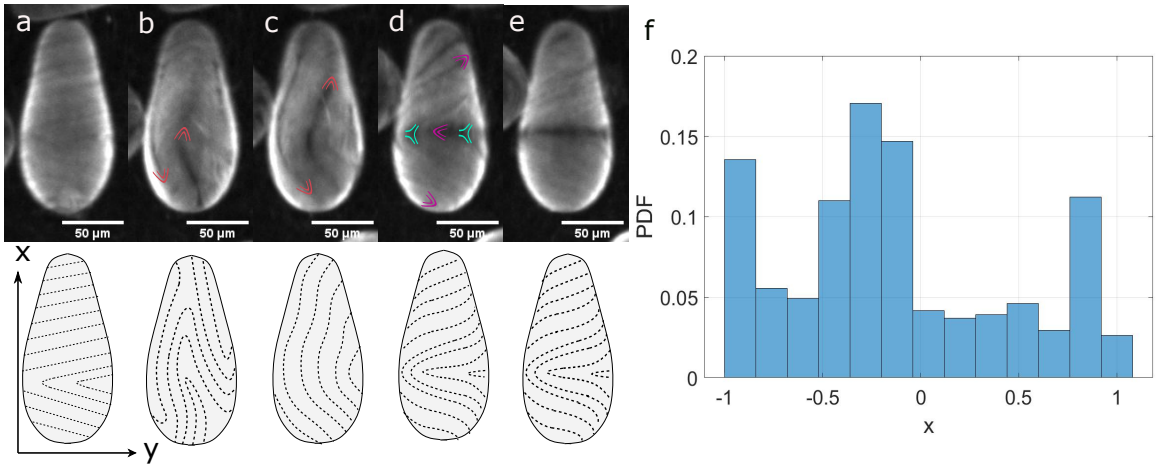

Figure 3.23: Defect dynamics in the transient state of an active nematic with pear-like geometry. (a-e) Fluorescence confocal micrographs from t = 0 (a) to t = 17 s (e). (a, d, e) Rotational regime: The co-rotation of $s = +1/2$ defects at the poles is coupled with a counter flow of defects at the equatorial plane. (b, c) Translational regime: Bend deformations propagate longitudinally, paving the way for defect migration. Parabolic and hyperbolic marks represent $s = +1/2$ and $s = -1/2$ defects respectively. The sketches of the director field are represented in the bottom panel.(f) Normalized probability distributions of defect position along the main axis of the ellipsoid. Defects mostly accumulate near the equator and at the poles. (f) Temporal evolution of the average angular speed and trajectory of the defects along the main axis of the droplet.

With time, the active flow patterns organize themselves according to the characteristic length scale of typical ellipsoidal shells in the final state. Despite the local geometric differences at the poles, the final dynamics of pear-shaped nematics does not exhibit important differences with respect to the ellipsoidal case, as can be seen Fig. 3.24 (a-e). However, when analyzing the PDF histogram, see Fig. 3.24 (a-e), defects seem to occupy preferably the low Gaussian curvature pole, contrary to what might be expected. Our intuition in this regard is that $s = +1/2$ defects are not particularly attracted towards the less curved pole *per se*, but they rather spend more time close to it because of its large surface area. If we consider again Fig. 3.22, we clearly notice that the available surface in the low Gaussian curvature pole (south pole) is much larger than that in the more curved region (north pole). If the four $s = +1/2$ defects move at constant speed during the rotational regime, defects in the south pole will take longer than those of the north pole to scan all the surface. In this case, we presume that the difference of Gaussian curvature between the poles of a teardrop is insufficient to induce substantial relocation effects, other than those already described for ellipsoids. On the other hand, these results prove that geometrical distances can also contribute to organize the spatio-temporal trajectories of defects in a very subtle way.

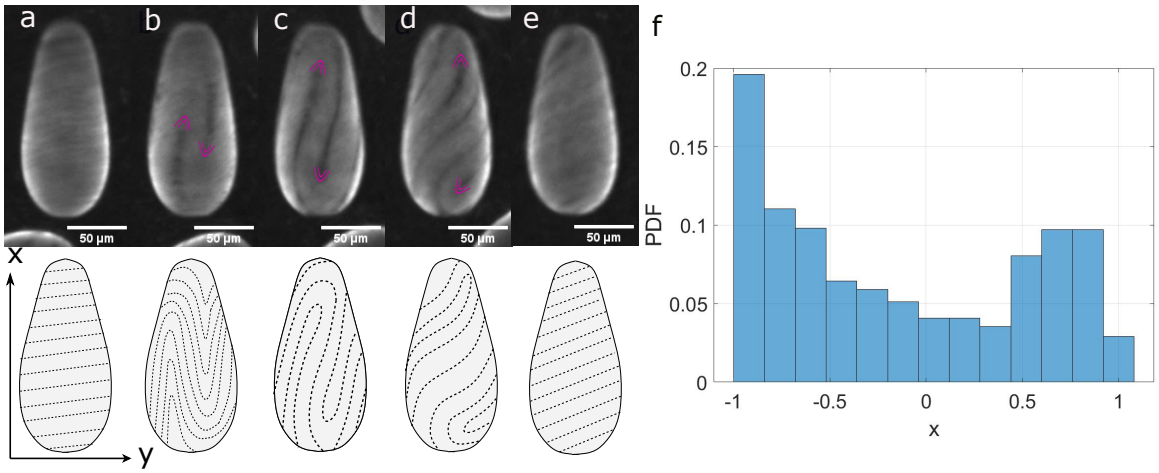

Figure 3.24: Defect dynamics in the final state of an active nematic with pear-like geometry. (a-e) Fluorescence confocal micrographs from t = 0 (a) to t = 18 s (e). (a, d, e) Rotational regime: pairs of $s = +1/2$ defects counter-rotate at the poles. (b, c) Translational regime: Bend deformations propagate longitudinally, paving the way for defect migration. (f) Normalized probability distribution of finding the defects at a given position along the main axis of the ellipsoid. Defects mostly accumulate near the poles. Parabolic marks represent $s = +1/2$ defects, respectively. The sketches of the director field are represented in the bottom panel.

CHAPTER

FOUR

ACTIVE DROPLETS INSIDE A PASSIVE LIQUID CRYSTAL

In the previous chapter, we probed the effect of curvature gradients on the dynamics of active nematics confined to closed surfaces with interesting morphologies. To achieve this type of geometry experimentally, we adopted a particular strategy in which metastable LC droplets were immersed inside an active bath of filaments and molecular motors. Interestingly, it is also possible to create direct emulsions by embedding spherical active droplets inside a passive liquid crystalline matrix. In this configuration, the active nematic is forced to lie on a spherical surface, but it can influence the organization and dynamics of the passive liquid crystal in which it is embedded. Indeed, the active inclusions organize a rich variety of dynamical patterns and flows that are continuously transmitted to the passive environment in the form of interfacial stresses. The latter propagate into the host matrix, distorting the local orientational field at the vicinity of the droplet. In response, the passive material counterbalances these effects by regulating the rhythm of the active flows. So far, this active/passive coupling has mainly been studied for single droplets embedded in liquid crystals, however much less is known on how the coupling occurs for more complex structures, such as dumbbells or larger droplet assemblies. Moreover, there is little to no evidence of the physical behaviors this coupling induces at the mesoscale.

In the following chapter, we will address these questions by studying the behavior of MT-based aqueous spherical droplets embedded inside a passive nematic liquid crystal. On the one hand, we will analyze the oscillatory dynamics and transport of the active inclusions on the passive media and the mechanisms at the origin of this phenomena. On the other hand, we will exploit topological defects to bind active droplets together and to form complex assemblies with remarkable oscillatory behaviors that attest for the passive/active interfacial interactions.

4.1 Self-driven active nematic emulsions

4.1.1 Motivation

For relatively large particles, motion is not as trivial as for small ones. They are less sensitive to the noise of the surrounding medium[162] and their displacement is very limited or even nonexistent in the absence of a source of power. Cells, whose diameters are of the order of tens of microns, are usually little affected by the thermal fluctuations of their environment but are rather propelled by the internal work of small active agents. Recently, the way in which the internal motility of these active constituents relates to the propulsion

of the whole object has attracted particular attention, since it provides significant clues for understanding cellular transport occurring during wound healing, immune response or embryonic development[163–165]. One of the principal mechanisms connecting the microscopic and mesoscopic dynamical behaviors is the coupling of internal active stresses with counter-acting forces of the surrounding media. This can be observed, for instance, in shape-varying cells such keratocytes (corneal fibroblasts), which persistently 'glide' due to cell-substrate friction originated by internal cycles of actin polymerization, contraction, and adhesion[166,167]. Other interesting behaviors have been reported for droplets of dense active suspensions, where the interplay between active nematic flows and soft confinement results in wiggled propulsion or rotation[168]. Beyond extracting useful work for locomotion, active compartments usually need to guide themselves along specific paths to perform complex tasks. In biological systems, this is usually achieved by developing a functional asymmetry between the front and rear of the cell body[169]. Reproducing such properties artificially is very challenging and obtaining directed motion may require the combination of more than one guiding mechanism.

In this Chapter, we propose a new system in which active nematic droplets can develop enhanced directional self-locomotion when immersed inside a passive liquid crystal. Our system is inspired by a recent work by Guillamat et al.[170], where an active nematic droplet was embedded in a passive liquid crystal. As discussed in Chapter 1, the preferential molecular anchoring of the liquid crystal on the droplet surface induces the formation of one or several topological defects in the director field near the droplet. As the active flows transmit stresses to the surrounding LC medium, these external passive defects describe intriguing oscillations coupled to the trajectory of the internal active defects of the droplet. Unlike previous realizations dealing with bacterial droplets embedded in liquid crystals[65], the active flows on the surface of an active nematic droplet can be tuned experimentally, enabling to explore different dynamics, from chaotic to periodic flow regimes. Here we exploit this hybrid (active/passive) coupling to develop new ways of self-propulsion. We show how locally breaking the symmetry of the external environment of the droplet enhances directional motion.

4.1.2 Active nematic emulsions: an overview

Microtubule based active nematic emulsions were reported for the first time a few years ago by the group of Dogic at Brandeis University. In their experiments, aqueous droplets encapsulating bundled active networks (BANS) were emulsified in fluorinated oil and partially compressed between two treated surfaces[70]. Unlike typical aqueous emulsions devoid of any source of power, most of the MTs droplets moved along intriguing trajectories with no preferential orientation. According to the authors, the motion of the entire droplet was originated from the frictional coupling between the droplet active flows and the contacting hard surfaces. They concluded this by qualitatively correlating the behavior of the active flows with the displacement of the center of mass of the droplet. For small droplets (with diameters below $30\mu m$), the encapsulated MTs bundles were pushed against the water-oil interface, but they were not able to buckle, leading to a quasi-static state. As a consequence, the filaments remained dispersed and immobile throughout the space. Large droplets, on the other hand, exhibited coherent spontaneous flows at their surfaces that resulted in an autonomous, periodic displacement of the whole object.

These experiments were further taken up by P. Guillamat from the University of

Barcelona[139]. He produced the emulsions by mechanically mixing the active material with a low-viscosity fluorinated oil supplemented by a fluorinated surfactant. The experiments revealed that the flow jets generated by +1/2 defects when passing near a hard surface act as droplet propellers. The motion for medium sized droplets ($\sim 75\mu m$), in particular, was shown to be almost rotational and periodic in conformity with the defects trajectories, which exhibited repeated and regular patterns. Droplets with larger diameters ($\sim 100\mu m$), revealed, on the other hand, the presence of both positive and negative semi-integer defects, describing much more complex trajectories.

In a more ingenious approach, P. Guillamat produced the active emulsions using a nematic liquid crystal instead of the classical oily phase as the continuous medium, and confined the whole system in between two treated glass plates[170]. Because of the presence of the aqueous droplets, the anisotropic host medium was distorted and forced to adapt to the imposed anchoring conditions by creating topological defects in the vicinity of the droplets. In typical experiments, the anchoring at the plates was set to be uniformly planar while at the droplet surface it was set to be either homeotropic or conical. The first configuration resulted into a quadrupolar symmetry of the director field around the droplet, characterized by a single Saturn ring (SR) defect in a plane perpendicular to the far-field direction of alignment. The second configuration, on the other hand, led to an hexadecapolar symmetry in which not only a SR accommodates around the inclusion, but also two surface point defects occupy the two poles of the droplet. The authors also restricted their study to droplets whose diameters ranged from 60 to $120\mu m$ to suppress the excess of defects on the surface of the active droplet. Under these conditions, many of the SRs encircling the droplets were continuously dragged by the inner cortical flows to develop really regular oscillatory modes. These observations were supported by numerical simulations in which the trajectories of the defects on the active nematic shell were set to follow the classical periodic evolution from a tetrahedral to a planar arrangement. From the calculations, the authors determined that one period of the SR oscillations corresponded to multiple transitions between the two conformations of the active defects.

In the following part, we will show that this coupling is not only robust for quadrupoles and hexadecapoles, but that it can be also extended to other types of multipoles. For the particular case of the dipole, we will show that this coupling can be exploited to induce directional self-propulsion in the droplet.

4.1.3 Active nematic dipoles

4.1.3.1 Experimental setup

In our experiments, active nematic emulsions were produced by following a protocol similar to the one used by P. Guillamat *et al*[170]. Briefly, we prepare planar cells by spin coating a $3wt\%$ PVA solution at 3000 rpm for 30 s on two $1.5 \times 1.5\ cm^2$ glass slides. The treated plates are then heated at 150°C for over 30min, and rubbed unidirectionally using a soft velvet to induce parallel alignment. A sheet of double-sided tape corresponding to a thickness of $90\mu m$ is then bound to one of the plates to form an open cell. The latter is filled with $\approx 55\mu L$ of 5CB liquid crystal and stored at room temperature for over 30 min to allow unwanted defects to relax. The active droplets, supplemented with $3v\%$ of Tween-20 surfactant, are injected in a controlled way in the LC matrix by means of a Femtojet pressure pump following the procedure described in section 2.4.2.4. The second glass slide is finally placed on top of the cell in the same orientation as the rubbing

direction. A scheme of the final cell is shown in Fig. 4.1.

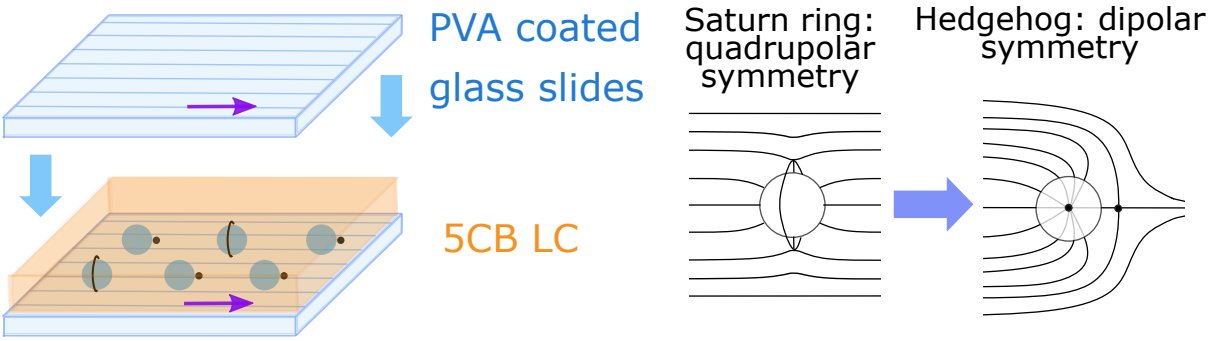

Figure 4.1: Scheme of the experimental setup. PVA coated uniform planar cells are filled with a dispersion of MTs/kinesin active droplets inside a 5CB nematic liquid crystal. The anchoring conditions imposed by the active droplets lead to the formation of Saturn ring (SR) defects which rapidly collapse into hedgehog point defects.

4.1.3.2 Results

Inside the active micro-droplets, fluorescently labeled MTs are pushed toward the water/5CB interface due to depletion forces caused by PEG polymer coils present in the droplet bulk. A few minutes later, most of the filaments attain the inner surface of the droplets and form a dense 2D active nematic film which is constantly supplied by energy from the droplet bulk. The structure of the active shell is visualized by means of a confocal fluorescence microscope whereas the external configuration of the passive material around is detected by polarizing and bright-field microscopy. The diameters of the produced droplets ranged between $30\mu m$ and $90\mu m$ to restrict the number of active defects on the droplet surface as much as possible. Compared to the system studied by Guillamat et al., the range of droplets size selected was slightly smaller. Nevertheless it was sufficient to observe both the four topologically required $s = +1/2$ defects in small droplets ($< 70\mu m$) and additional positive and negative defects in large ones ($\sim 80 - 90\mu m$).

Peiodic oscillating dipoles

At the surface of the droplets, the 5CB director field is locally distorted, giving rise to the formation of topological defects, see Fig. 4.1. Indeed, due to the non-ionic Tween-20 surfactant in the droplet aqueous phase, the 5CB molecules in the passive medium are forced to orient themselves perpendicular to the droplet surface, giving rise to the formation of a Saturn ring loop around the droplet equator, which attests for quadrupolar symmetry in the 5CB director field. Nevertheless, most of the SR defects are not stable in the presence of active flows and quickly collapse into a bulk point defect, referred to as a hedgehog, leading to a director field with dipolar symmetry. A typical sample contains $\sim 60\%$ of dipoles and $\sim 40\%$ of quadrupoles. Remarkably, Saturn rings are not the only defects displaying intriguing modes of oscillation, but hedgehogs also beat rhythmically along their symmetry axis because of the persistent drag exerted by the active flows on the droplet surface. In Fig. 4.2 (a), we show the evolution of the hedgehog conformation in the passive LC (bottom panel) and how it correlates with the trajectories of the active defects (top panel) over an entire period for small droplets ($D < 50\mu m$). Note that these snapshots correspond to the structure of the system 15 min after the emulsion

preparation. From the polarized-light optical microscopy (POM) images we observe that the hedgehogs oscillate about a central point, with a motion reminiscent of fish tail beating, while gradually opening and closing around the droplet symmetry axis. At the same time, the four topologically required +1/2 active defects in the inner shell travel all over the droplet surface following regular trajectories that oscillate in time. Fig. 4.1(a) shows fluorescence micrographs where one or two defects (red arrows) are visible, while the remaining ones are hidden either in the back-plane of the droplet or near the bright zones of the hemisphere. As expected, this oscillatory dynamics corresponds to the dynamical states previously observed on spherical active nematics[136]. For small droplets, the hedgehog oscillates with a typical period of approximately 50-55 s. This result is obtained by analyzing the time-series of the hedgehog oscillations and its corresponding power spectrum in Fig. 4.2(b)-(c). For time intervals of approximately 10 to 15 minutes, the dynamics of the hedgehog are very robust, with at least dozens of periodic cycles, at a single frequency of 18 mHz.

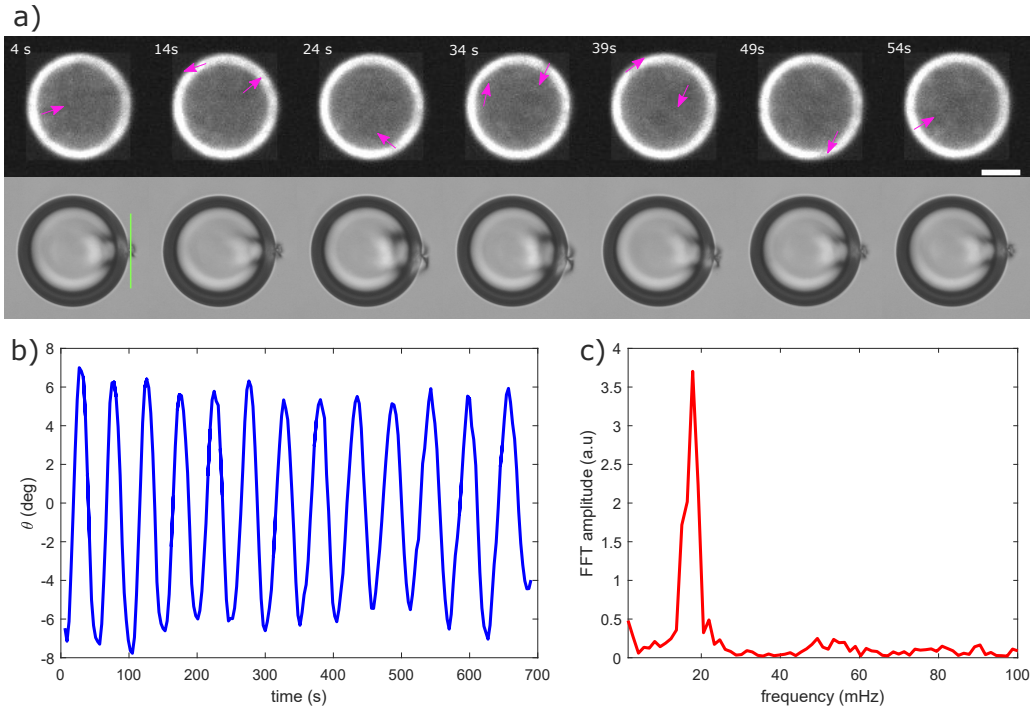

Figure 4.2: Single-mode oscillating dipole. (a) Top panel: Fluorescence images showing the dynamics of the active defects on the droplet surface over a single period of oscillation for small droplets. Scale bar is $20\mu m$. Bottom panel: Bright field images of the oscillating hedgehog for a droplet of similar dimensions. (b) Evolution of the hedgehog orientation along the green line in the bottom-left image of (a). (c) Fast Fourier transform (FFT) power spectrum of the signal in (b).

Interestingly, when the behavior of small active dipoles is analyzed at longer time intervals, we witness some variations in the hedgehog dynamics. In Fig. 4.3, we show the oscillations of a hedgehog over 30min, starting 5min after the emulsion preparation. At the beginning (t<350s) the dynamics is seemly chaotic, with wide fluctuations in amplitude and irregular oscillation periods. We attribute this behavior to the initial structure of the active layer which is not completely formed, and thus, imposes chaotic interfacial stresses to the external medium. Subsequently the hedgehog oscillates regularly at a frequency of $\sim 12mHz$, and then, decelerates to $\sim 11mHz$ with the gradual decay of activity in the droplet. In the power spectrum, the latter regular regimes (the one

at high frequencies and the one at lower frequencies) appear as two main peaks almost overlapping each other Fig. 4.3 (b).

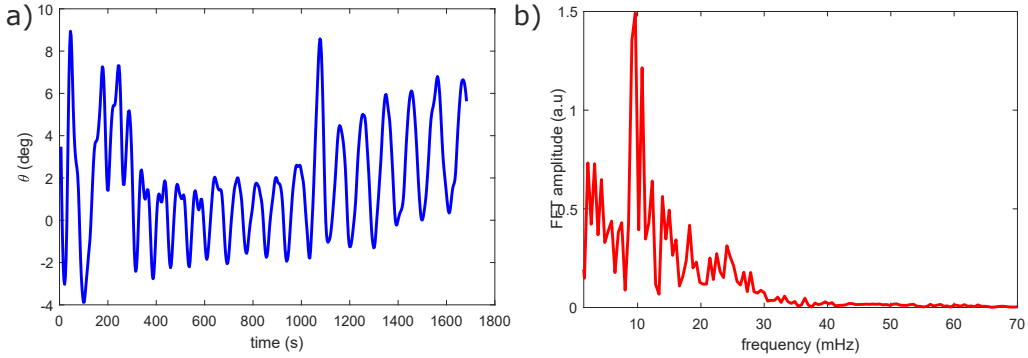

Figure 4.3: Oscillation of a Hedgehog defect for a small droplet ($\sim 40\mu m$) over a large time range. (a) Time-series of the hedgehog oscillations and (b) Fast Fourier transform (FFT) power spectrum of (a).

For middle size inclusions ($D \sim 50 - 70\mu m$), a multimode oscillatory behavior corresponding to three distinct regimes is clearly evidenced. Similar to the behavior of small droplets, there is an initial condensation regime in which the interfacial film is sparsely populated with MTs bundles, resulting in incoherent, persistent flows over the droplet surface. This phase is much longer than the one observed for small droplets, lasting about 12min, as it can be seen in Fig. 4.4(b). It is likely because the larger surface area of the droplet requires longer intervals of MTs condensation to achieve a well-organized active nematic phase. In a second regime, the hedgehog oscillations stabilize, with a regular up-down beating every 65s, Fig. 4.4(a)-(c). The activity decay progressively drives the system to the last regime, where the active defects move slowly over the surface, imposing a longer pulse of oscillations to the external defect. Contrary to the Fourier spectrum for small inclusions, the signal in Fig. 4.4(c) displays three independent peaks of periodic regimes at frequencies very distinct from each other.

For even bigger droplets ($D > 80\mu m$), the activity reservoir of the system is significantly larger, making defects in the inner shell accelerate or even proliferate by continuous cycles of annihilation and regeneration, see Fig. 4.5(a). This is translated by the loss or periodicity in the dynamics of the hedgehog, as illustrated in Fig. 4.5(b) and in the noisy spectrum in Fig. 4.5(c).

In this first Section, we have studied how the internal dynamics of the active nematic shell influences the oscillatory behavior of the external defect at the vicinity of the droplet. In small and middle size droplets ($D < 70$), active flows trigger a rhythmical beating of the hedgehog at frequencies of the order of tens of mHz, gradually decreasing along with the activity of the system. For large droplets, periodicity vanishes for both active and passive defects, with numerous active defect jets randomly pushing the external hedgehog to oscillate in a incoherent way. Remarkably, the physical impulse generated by the internal active material on the well-ordered anisotropic LC continous phase can have important physical effects on a larger scale. In the next Section, we will show that the active nematic flows transfer movement to the drop, which performs a directed migration within the passive LC medium.

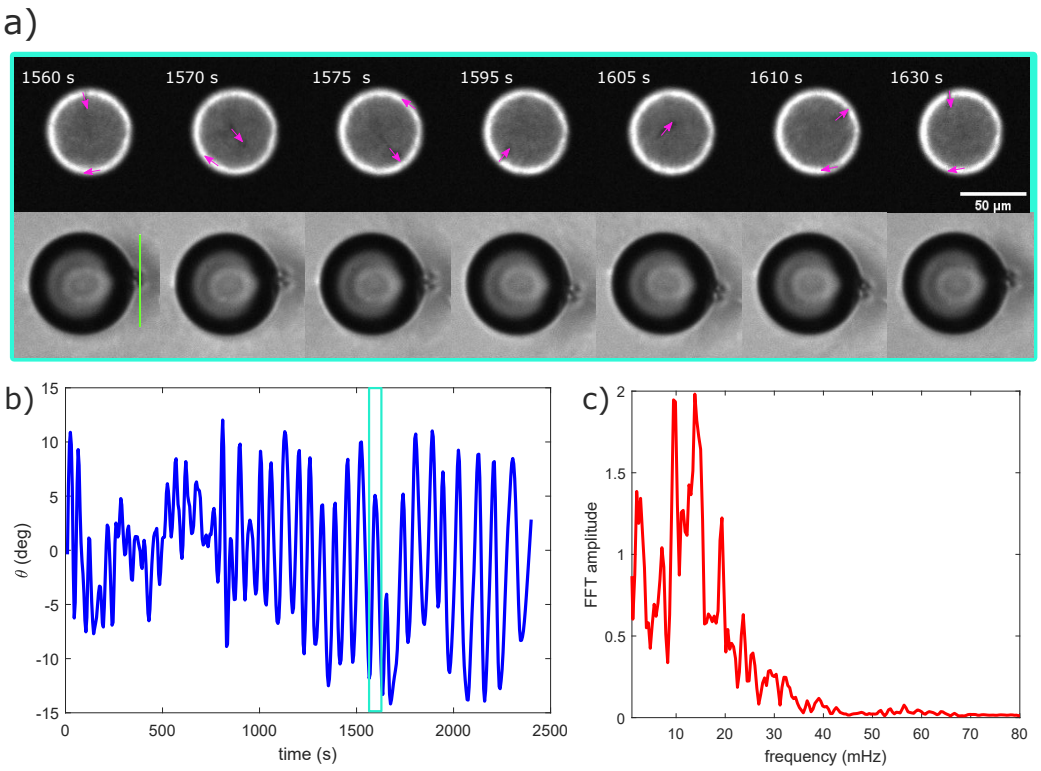

Figure 4.4: Multi-mode oscillating dipole. (a) Top panel: Fluorescence images of a droplet hemisphere over a single period of oscillation for middle size droplets. Bottom panel: Bright field images of the oscillating hedgehog. (b) Evolution of the hedgehog orientation along the green line in the bottom-left image of (a). (c) Fast Fourier transform (FFT) power spectrum of the signal in (b).

Directional transport: from micro-activity to macro-movement

As previously mentioned in section 1.1.9, when active particles are dispersed in an isotropic fluid, the thermal fluctuations of the medium are a source of randomness in the particle motion. Typically, this results in normal diffusion characterized by a linear growth of the mean squared displacement (MSD) with time. In our experiments, normal diffusion can be altered by the anisotropy of the dispersing medium and the polar director configuration around the droplets. The hedgehog structure is able to rectify the otherwise chaotic and circular motion reported in experiments by Sanchez et al.[70] and Guillamat et al.[139] and redirect the droplet along a preferred orientation. In Fig. 4.6(a) we observe that the top-left dipolar droplet exhibits almost rectilinear trajectories along the far field orientation (indicated by a white double arrow in the image). Moreover, the direction of locomotion at long times (>5min) is not random as for particles of non-polar fore-aft symmetry but rather imposed by the hedgehog, which steers the direction of self-propulsion. Note, however, that droplets don't move unidirectionally but rather perform small steps back and forward along the direction of the far field alignment, with displacement towards the hedgehog prevailing over that in the opposite direction as shown in the top panel in Fig. 4.6(b) and in Movie 10. The nature of the displacements along the x and y axes is determined by analysing the MSD of the inclusions. As it can be seen in Fig. 4.7 (a), regardless of their size, all droplets feature a super-diffusive behavior along the far field direction with exponents α ranging from 1.60 to 1.68. Motion in the transversal direction (Fig. 4.7(b)) attests, on the other hand, for normal diffusion with α values really close to the unit.

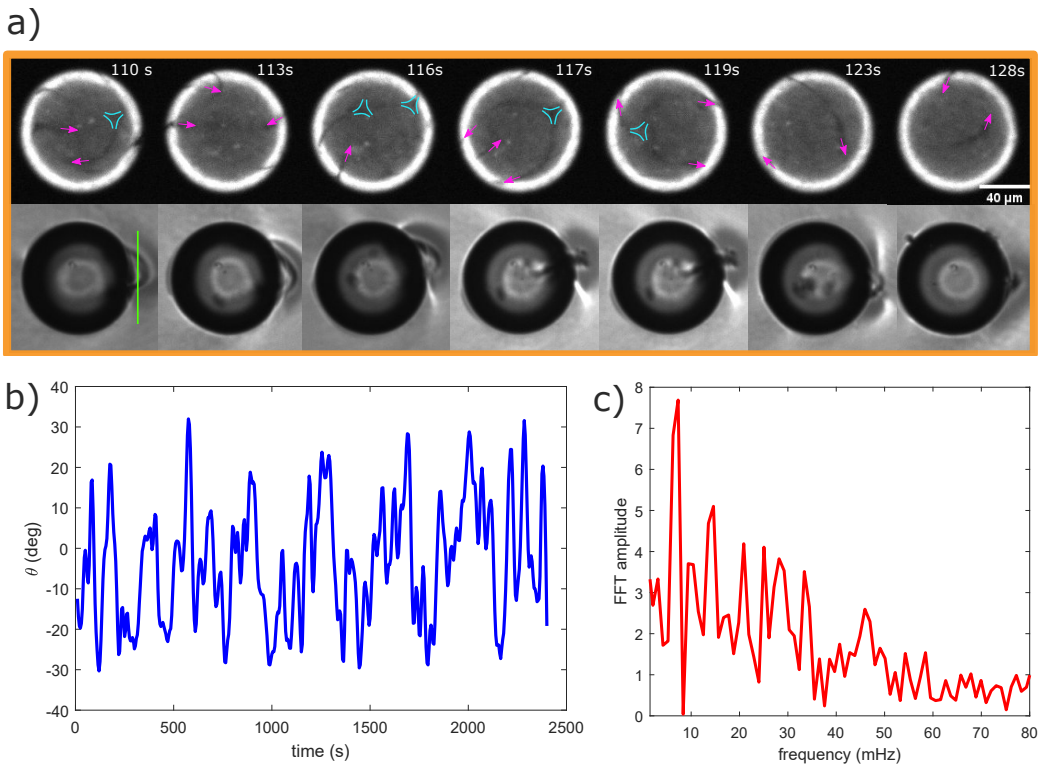

Figure 4.5: Oscillation signals of a Hedgehog defect in a big dipole. (a) Top panel: Fluorescence images of a droplet hemisphere over a single period of oscillation for large size droplets. Bottom panel: Bright field images of the oscillating hedgehog. (b) Evolution of the hedgehog orientation along the green line in the bottom-left image of (a). (c) Fast Fourier transform (FFT) power spectrum of the signal in (b).

Furthermore, the speed of motion of the active droplets depends on their size as shown in Fig. 4.8(a). Droplets with large diameters propel much faster, with an average velocity of $v > 0.15\mu m/s$, than smaller ones, with $v < 0.10\mu m/s$. The speed of locomotion is strongly connected to the speed of the active flows, and the defects guiding them, on the inner shell. In Fig. 4.8(b), we illustrate that defect speed also grows with respect to the droplet diameter, matching the general trend observed in Fig. 4.8(a). Additionally, we have analyzed the angular fluctuations of the hedgehog with respect to the dipole axis to detect an eventual correlation with the propulsion mechanism of the droplet. The mean amplitude of the deviation angle θ varies between 6° to 17° for droplets with different sizes, with typical values of around 12° for most droplets (Fig. 4.9). These values are much larger than those reported for equilibrium Hedgehog structures ($\pm 1°$)[40] or even for externally driven particles[53]. Conversely, they are rather comparable to the values obtained in active droplets made of bacterial solutions, $\pm(10-15)°$[65]. The increase of θ is strongly connected to the forces exerted by the active flows and transmitted through the interface.

With time, energy availability inside the droplets diminishes due to the persistent consumption of ATP. This causes active defects on the nematic layer to decrease their speed, as shown in Fig. 4.10 (b) for a typical droplet with a diameter of $\sim 50\mu m$. In parallel, the entire droplet decelerates before stopping (Fig. 4.10(a)) when defect speed reaches its minimum about 40 min from the beginning of the recording (Fig. 4.10(b)).

On the other hand, quadrupoles characterized by a Saturn ring loop along the equatorial plane do not exhibit directional migration along the director. Half of the quadrupo-

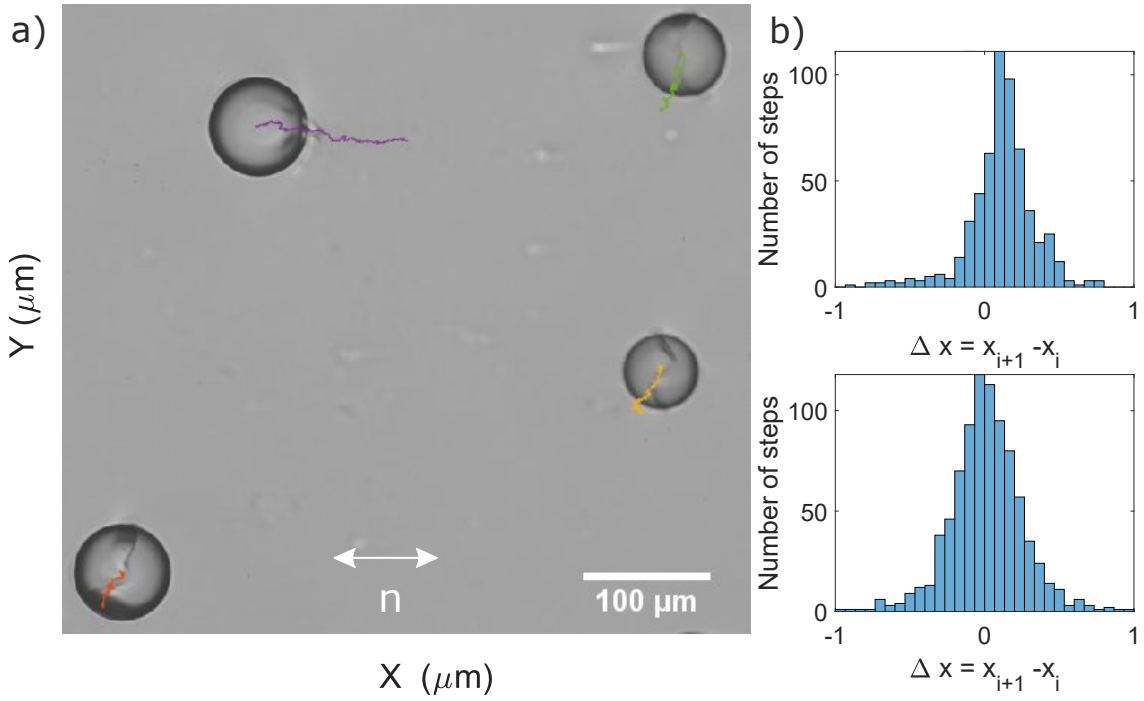

Figure 4.6: Motion of active nematic droplets in a nematic liquid crystal. a) Bright field image and trajectory of dipoles and quadrupoles over 40 min. b)Histogram of droplet displacements along the x axis, measured every 3s. In dipoles (top panel) positive steps are directed towards the hedgehog while in quadrupoles (bottom panel) the steps are symmetrically distributed on the x direction.

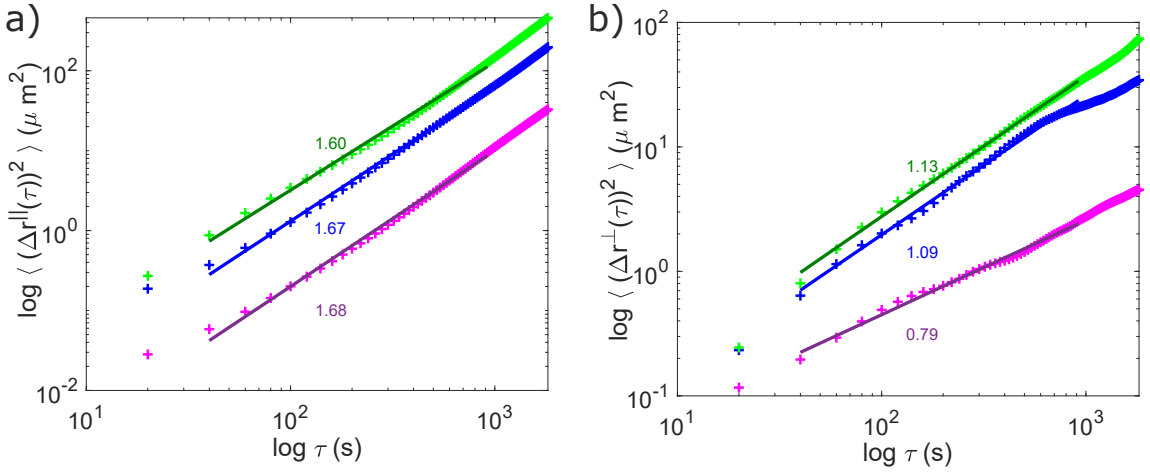

Figure 4.7: Average mean square displacement (MSD) versus time window for dipolar active droplets a) along the far field orientation and b) in the perpendicular direction. Pink, blue and green lines are the average MSD for droplets with diameters comprised between $31-50\mu m$, $51-70\mu m$ and $71-90\mu m$, respectively. The power law fit yields to exponents α between 1.6 and 1.68 along the rubbing direction and 0.79 to 1.13 transversal to it.

lar droplets studied walk randomly along diagonal paths, such as those represented in Fig. 4.6(a), performing an equivalent number of steps to one side and to the other of the ring (bottom panel in Fig. 4.6(b)). The other half, is seen to fluctuate around their center of mass following chaotic paths, Fig. 4.11.

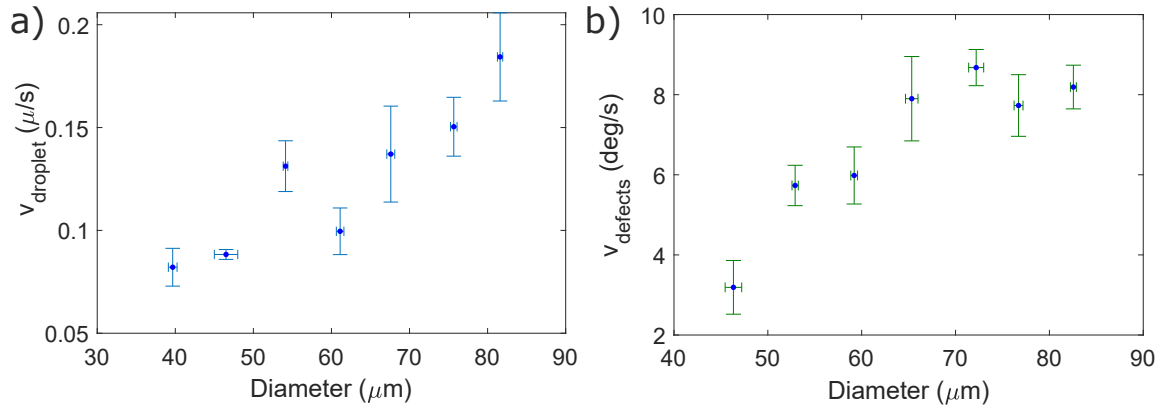

Figure 4.8: Velocity of (a) droplets and (b) defects as a function of the droplet diameter. Velocity has been calculated by averaging the data within 20 min since sample preparation for droplets with diameters in the range $38\mu m$ to 90 μm.

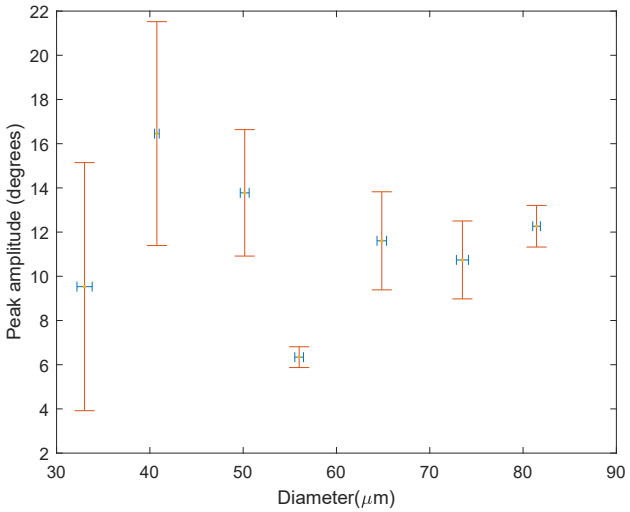

Figure 4.9: Mean peak amplitude of the hedgehog oscillations as a function of the droplet diameter.

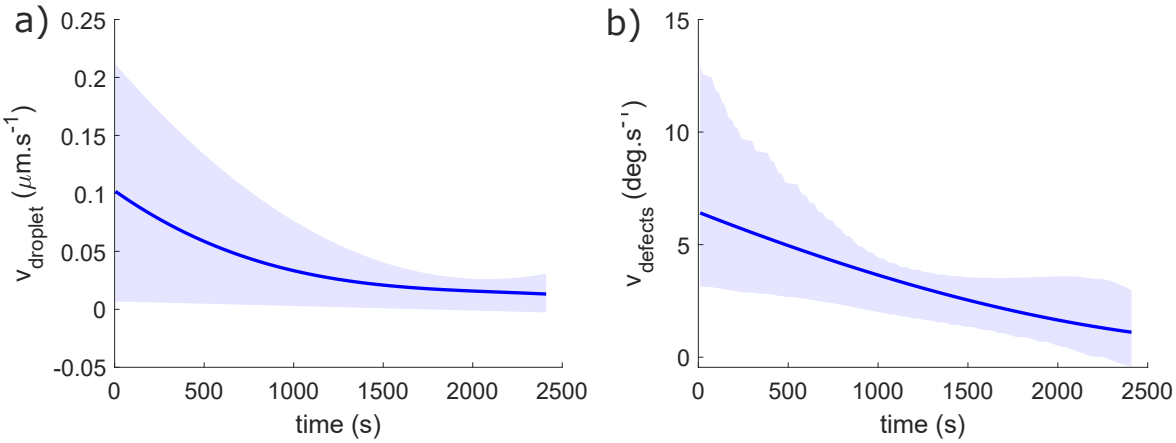

Figure 4.10: Evolution of the (a) droplet speed and (b) defect speed with time. Blue lines corresponds to the polynomial fits of the droplets and defects speeds of a droplet with diameter $\sim$ $50\mu m$. Blue shades represent the data dispersion around the lines.

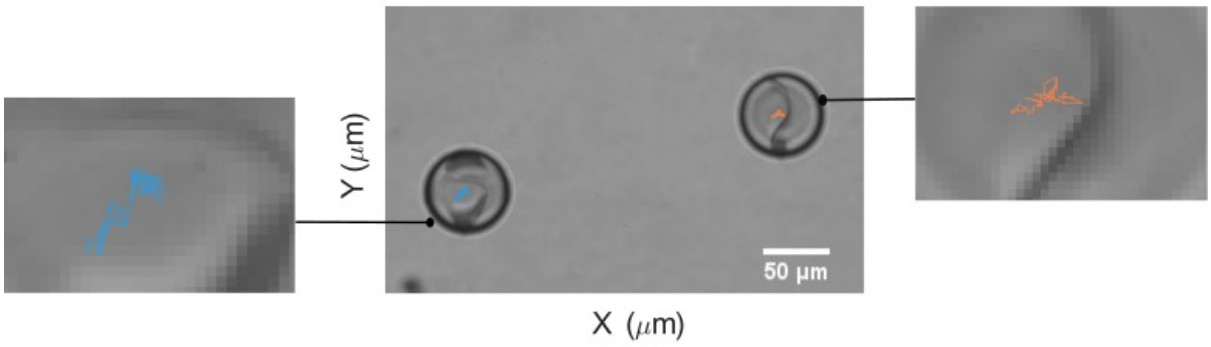

Figure 4.11: Trajectories of quadrupolar droplets

Conclusion

In this part, we have shown how the internal work of microscopic active agents can power the directional self-propulsion of the compartment that they inhabit. Our system, in particular, consisted of MT-based active droplets immersed in a uniform nematic 5CB liquid crystal. Unlike previous studies with bacteria encapsulated inside emulsion drops, the mechanical efforts are not generated everywhere in the three dimensional volume, but are rather localized at the water/5CB interface, where a well-ordered nematic layer results from the condensation of the MT filaments. The passive configuration around the droplets is customized by the presence of a T-20 surfactant in the aqueous phase, which forces the otherwise uniformly aligned mesogen molecules to adopt a radial orientation. In some cases, the ring structure around the droplets is sufficiently robust and supports the stimulus of the internal active flows, but in other cases, the ring gets unstable and collapses into a Hedgehog defect oriented along the far field. On one side, the active flows generated by the internal active nematic cortex are capable to drive robust, periodic oscillations of the external Hedgehog depending on the experimental details. On the other side, they can set into motion the entire droplet to perform unusual ways of self-propulsion. According to the dynamic analysis conducted in this part, we have shown that droplets encircled by a Saturn ring defect (quadrupoles) behave as "anchors" since they display little to no displacement from their initial position. Hedgehog defects in dipolar droplets, on the other, hand behave as "rudders", since they are capable to rectify the otherwise chaotic or rotational trajectories reported for isotropic fluids[70,139] and to steer the droplet along **n**.

So far, we have discussed about the dynamics of single active droplets, showing that they can display fascinating modes of oscillation and self-locomotion. In the next section, we will explore these properties at a larger level, by building complex active assemblies of droplets connected via topological defects.

4.2 Topologically linked active nematic emulsions

4.2.1 Motivation

The cooperative behavior of coupled oscillators is of great interest in a wide variety of domains, including physics, biology, or even social sciences. In finance, for example, networks of oscillators are used to explain how individual stock markets respond to

global market crashes[171]. Similarly, in biology, it is important to understand how cells, characterized by complicated dynamics, interact with each other to coordinate a general response at a higher organizational level. It is well-known, for instance, that pacemaker cells couple mechanically with each other to stimulate cardiac cells that synchronize cardiac beating[172]. Alternate ways of coordination can be seen in the pancreas, where synchronous waves propagate across insulin to produce pancreatic β-cells[173,174]. In some cases, however, the global reaction of a group of individuals is not perfectly coherent, leading to chaotic communication. The causes behind this behavior are diverse and can range from small perturbations in the dynamics of functional units to insufficient coupling strength between autonomous oscillators. In this regard, important questions have been raised, specially concerning the stability of a synchronized state against noise or a small physical mismatch of the interacting agents.

To address these points, recent studies have described synchronization beyond the traditional idea of two nonidentical systems which optimally adjust their behavior to oscillate with the same frequency and amplitude. In the late 1990's, Rosenblum et al. showed that even weakly coupled self-sustained chaotic oscillators can exhibit a sort of synchronization, where the frequencies are entrained, while the amplitude is unbounded[175]. In more real oscillatory systems, such as electronic and laser devices, or electrochemical reactors, coherence is neither persistent nor present everywhere. In fact, when three or more oscillators are driven to communicate, only partial synchronization is detected, in the sense that just a portion of the oscillators synchronize while the others do not[174]. This phenomenon, in which strong coordination coexists with chaos, is of particular importance for living organisms where the interacting entities cannot be assumed to be always identical and where the global message is continually regulated by external impulses of the fluctuating environment.

The urge for understanding these phenomena has inspired material scientists to develop new platforms for studying the interaction between oscillatory systems in a simple and controllable manner. One of the principal challenges in the design of such prototypes is to select appropriate parameters for achieving a consistent communication between two or more independent units. Some time ago, Kuramoto[176] suggested that at least two factors were essential for this aim: the connection topology and the coupling. The first term refers to how nearest neighbors are bounded to all other units in a network[177] while the second relates more to how power is transmitted between them. In macroscopic rigid systems, for example, coupling can be achieved by joining two rotating pieces with defined shafts (topologies) at their ends. Nevertheless, replicating a similar device in biological media is much more delicate, first because oscillators have to be created at the miscroscopic scale, and second because topological connectors have to be designed in soft or liquid media.

Because of their rich physical-chemical properties, liquid crystals are promising candidates to overcome these barriers. On the one hand, they are soft, viscous and well-structured, which allows them to easily transfer power via elastic distortions, and on the other hand, they display fascinating topological features that can be exploited to develop strong links among oscillators. Recently, these properties started to be exploited in colloidal sciences. In works by Lintuvuori et al., the interaction of passive colloidal dimers within cholesterics was simulated at different inter-particle distances[178,179]. The pair featured two dynamical modes in which rotations about the center of mass were either persistent (synchronized state) or alternated with freezing periods (desynchronised state) depending on the forcing magnitude. Although these great efforts provided an initial overview on

how well-ordered fields enhance partially coordinated interactions, there is no experimental evidence on how oscillatory particles communicate in liquid crystalline environments. More notably, there has been no work devoted on analyzing the collective dynamics of soft active oscillators topologically linked together in anisotropic media.

In this chapter, we study these questions experimentally for the first time. We develop a novel, robust platform in which active droplets embedded in a nematic liquid crystal are connected via different topological structures. Due to the continuous drag forces exerted by the active cortex of individual droplets, on the one hand, and the elastic nature of the passive liquid crystal, on the other hand, the topological point defects, loops and knots residing in the external passive medium develop oscillatory modes that attest for a cooperative behavior under certain conditions.

4.2.2 Entangled structures

Saturn Rings are one of the most common defects encountered around single particles embedded in a nematic liquid crystal. Specially, they are found in quadrupoles and hexadecapoles, surrounded respectively by four and eight sectors of attractive and repulsive inter-particle interactions, as explained in section 1.1.7. This means that, if two of these particles are placed in close vicinity, with attractive sectors facing each other, they will approach and form a stable dimer. The other case, in which particles meet by the zones of repulsion is rare and unstable because of higher energy requirements. This rare case can be better illustrated with pairs of quadrupoles placed side by side, i.e, with their Saturn Ring defects perfectly coplanar. Because the two rings are repulsive, the particles won't approach unless they move either above or below the plane, towards the regions of attraction. One of the open questions in this subject is what would happen if these repulsive rings are forced to be close together. Due to the experimental complexity it demands, this question was first addressed in theory by Guzman et al in 2003[180]. In their work, based on molecular simulations of colloidal spheres immersed in a nematic LC, the authors demonstrated that, at short separation distances, an additional disclination ring appears in between the spheres, in a plane normal to that of the Saturn rings, see Fig. 4.12. The presence of this unusual disclination was explained by the persistence of the local order between the inner hemispheres of each particle (those facing each other) that results in a "bridge" of director field lines connecting the spheres.

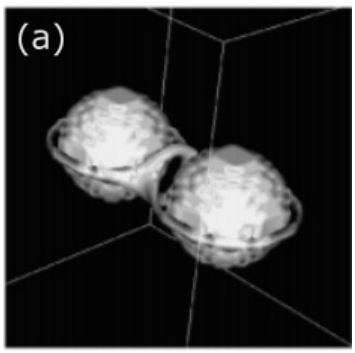

Figure 4.12: Contour plot of a three-ring topological structure. Extracted from[180]

This seminal study was followed by computational works of Araki and Tanaka[181] who found the formation of a single loop with the shape of a "figure of eight" closely encircling

the two particles. They suggested that this configuration was quasi-stable and resulted from a complex formation process in which the 3-ring defect structure shown in Fig. 4.12 was a transient structure. These results were almost simultaneously corroborated by Ravnik et al.[46], who performed the numerical quench of a pair of colloidal particles in a nematic phase. The rapid cooling from the isotropic to the nematic phase gave rise to various kinds of entanglements evolving with time. In real experiments, these results were reproduced by the groups of Muševic and Škarabot[15,46], using high-power laser tweezers. At the beginning, the laser is just used to place as close as possible two independent colloids, each of them decorated by a defect ring. Subsequently, the laser is focused in the region between the particles and its intensity is increased to locally melt the liquid crystal into the isotropic phase. When the laser is shut down and the liquid crystal gradually cools down, and a cloud of topological defects appears. These defects annihilate by pairs until a single loop surrounding the two particles is left. With this technique, three different defect configurations linking the pair of spherical particles can be obtained, each of them with a different probability of occurrence. The first loop is the one reported by Araki and Tanaka, with a shape reminiscent of that of the number 8, and hence called *figure of* 8, see Fig. 4.13 (a). It has a topological charge of $-1/2$ and it is the most common among all the defect structures, with a 36% of occurrence. The second one is the *figure of Omega*, because of its resemblance to the Greek letter Ω, see Fig. 4.13(b). This loop does not cross itself, as in the figure of eight, but describes a small loop in between the two spherical particles in the plane perpendicular to that of the cell. It is observed 13% of the times but is very unstable and evolves into the third and more rare configuration, the *entangled hyperbolic defect*, shown in Fig. 4.13(c). The latter was detected only in 3% of direct quench experiments and is composed of two topological structures. The most evident is a $-1/2$ defect encircling the two particles which are slightly apart from each other. This separation is caused by another inner smaller loop or even a point sitting in between the spheres. Note that the reported probabilities correspond to passive colloids with diameters of the order of $20\mu m$.

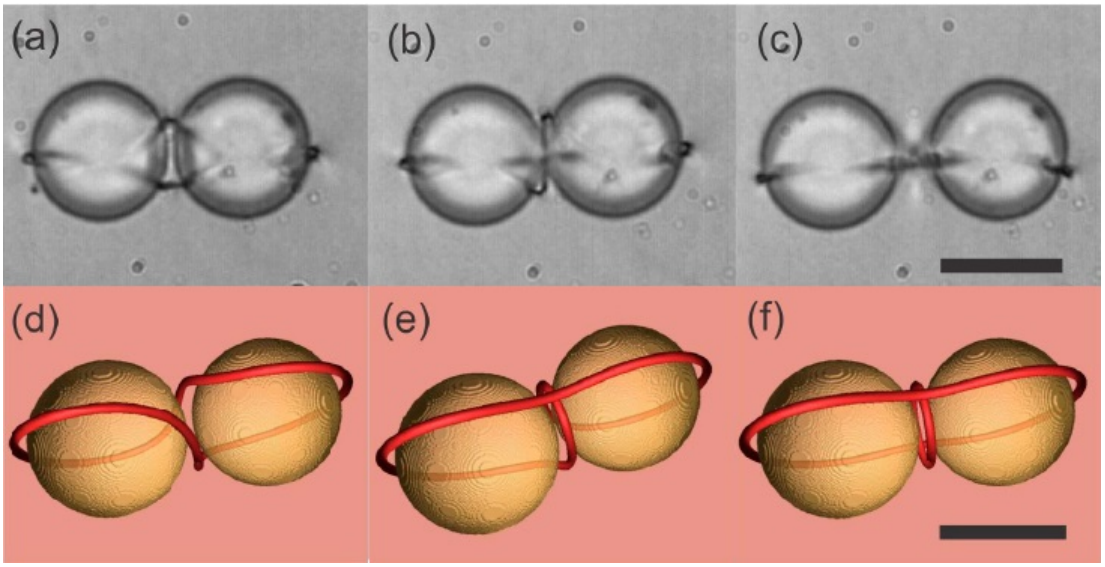

Figure 4.13: Entangled colloidal dimers. Bright field micrographs of (a) Figure of 8, (b) Figure of Omega and (c) Entangled hyperbolic defects. (d-f) Corresponding numerical representations of the defects. Adapted from[46,182].

An important feature of the final entanglements (figure of eight and entangled hyper-

bolic defect) is that they are very stable and that the attached particles do not separate unless an external force is applied on them. This is due to a structural force that pushes the two particles together to minimize the length of the loop and to reach a lower energy state. The associated binding potential is estimated to be of the order of 10 000 k_BT, which is much stronger than the potential generated by isolated point defects.

To further customize topological bounds between colloidal inclusions, optical trapping was complemented by several other strategies, including imposing complex boundary conditions or geometrical constraints. These advances resulted in a wide variety of 2D and 3D structures as well as many linked and knotted objects of fascinating topology. In a simple realization, anti-parallel dipoles are pushed together along the director to form an escaped defect known as the *bubble-gum*[183] (see appendix D). This meta-stable conformation is mostly observed in chiral nematic cells and, unlike the above mentioned structures, the attractive force that holds the particles together is almost independent of their mutual separation. Alternative assemblies made of elementary dipolar building blocks are linear chains, such as those reported by Poulin et al.[30], or even soft rails of colloids prospected for microscopic cargo in microfluidic devices[184].

4.2.3 Experimental setup

To build oligomers of active nematic droplets, we perform two types of experiments. The first one consists of binding several droplets together via complex knots and links with the help of optical traps, whereas the second one is based on the controlled fabrication of a disclination line that connects the droplets together to form active necklace structures.

Thermal fabrication of entangled active emulsions

As for classical active emulsions fabrication (section 4.1.3.1), the first step is the construction of the confining cell. One sheet of double-sided tape is stuck onto a rubbed PVA-coated glass slide to form an open chamber of 90 μm depth. The chamber is filled with a 5CB LC at room temperature and stored for over 30 min to allow undesirable defects to annihilate each other while the system relaxes. The aqueous droplets are produced by injecting small volumes of the active gel inside the LC matrix with a Femtojet. The droplets are stabilized via a surfactant contained inside the gel. A second rubbed, PVA coated glass slide is placed on top of the chamber, with its alignment direction perpendicular to the one of the bottom plate. This configuration ensures a 90° twist of the director between the confining plates, which is essential for the stability of the nematic knots and links.

Individual droplets in the chiral nematic cell acquire hexadecapolar symmetry when stabilized with the surfactant Tween-80. The latter imposes conical anchoring to 5CB molecules near the droplet interface yieding a SR defect around the mid-plane of the droplets and to two diametrically opposed surface point defects, named boojums. In this experiment, we produced hexadecapoles instead of quadrupoles since they display more stable SR defects due to the presence of the pair of quasi-immobile boojums[170].

Active droplets were brought together by gently pushing them with optical tweezers. When the droplets were close enough, the laser was focused on their topological defects, fusing them together. The LC material locally melts and rapidly cools down to form complex interlinked loops and defects such as those shown in Movie 11. Depending on

the regions of the SR that interact and the type of defects involved, various kinds of assemblies can be obtained (see appendix D).

Controlled fabrication of active necklace structures

The manufacturing protocol of the cells for the preparation of active necklace structures is described in detail in section 2.4.2.5. In brief, we produce polydimethylsiloxane (PDMS) channels of inner dimensions $4mm$ long and $300\mu m$ wide via standard soft lithography. In parallel, a clean microscope glass slide is spin-coated with a $3wt\%$ PVA solution at 2200 rpm for 30s and is subsequently rubbed unidirectionally using a soft velvet to induce parallel alignment. The PDMS channels are bonded to the glass substrate by, first, exposing them to oxygen plasma for 50s with the help of a plasma cleaner, and second, pressing them against the glass slide mechanically to ensure its adhesion. Note that the channels can be accommodated either parallel or orthogonal to the rubbing direction but, since we aimed to produce a disclination line along the channels, we chose to place them orthogonally. The system is stored at room temperature for at least 48 hours to allow PDMS channels to recover their original surface properties.

A 5CB liquid crystal in the nematic phase (room temperature) is introduced by capillarity in the channels with the help of a Femtotip. Because the 5CB molecules tend to match simultaneously the uniform planar anchoring imposed at the bottom plate, the perpendicular anchoring at the channel walls, and the perpendicular anchoring at the 5CB/air interface, a disclination line nucleates along the channels as shown in Fig. 4.14. Each disinclination on a channel displays a charge of $-1/2$. Sometimes the disclinations are not perfectly centered in the channel and tend to bend towards the PDMS walls with time. To prevent this, the experiments are conducted just after filling the channels with the nematic liquid crystal.

The active solution of MTs and kinesin motors, supplemented with a Tween-20 surfactant, is finally injected in the form of droplets along the disclination line with the help of a microinjector, following the protocol described in section 2.4.2.4. In order to perform this step as fast as possible, the microscope stage is slowly moved in the direction of the line after each injection, while keeping the position of the micromanipulator unchanged. The droplets are quickly attached to the disclination thus forming an active necklace. A sketch of the director profile around the droplets is represented in Fig. 4.14 (d),(e).

4.2.4 Sample characterization and dynamic analysis

Image acquisition and defects dynamics

To characterize the inner (active) and outer (passive) conformations of the entangled active emulsions, fluorescence and bright-field microscopies have been used, respectively. Bright-field microscopy was performed with a Nikon Ni-U microscope, whereas fluorescence imaging was done with a Nikon TI-E inverted microscope equipped with a Cy5 fluorescence filter.

Before analyzing the dynamics of defects in the external passive LC, the position of each droplet was stabilized via a home-made MATLAB program. The dynamics of the passive defects around each droplet were then extracted by using either the *stack radial profiler* plugin or the *reslice* command of the software ImageJ. The former computes a space-time plot from a ring-shaped selection, while the latter does it along a straight line.

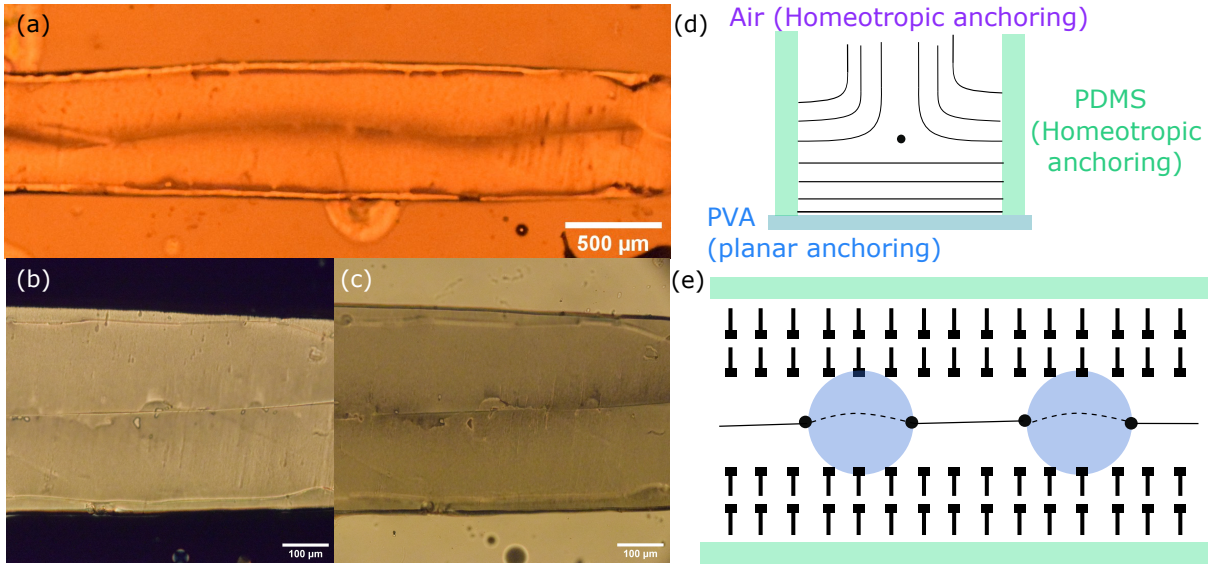

Figure 4.14: Director field configuration and necklace structure in a narrow channel. (a)Bright field image of a disclination line in a channel. (b-c) Cross-polarization images of the line defect when polarizers are crossed with respect to each other. d)Scheme of the director configuration around a -1/2 disinclination in the cross-section of the channel. e) Sketch of a final necklace structure along the channel.

Signal comparison: The wavelet transform

As many biological systems, our oscillators feature a non-stationary behavior, meaning that their properties evolve with time. To localize the events of interest or to predict common trends between oscillations of the droplets, we have performed a time-frequency analysis. The traditional way to do it is to consider the Short-Time Fourier Transform (STFT), where we compute the Fourier transform over short-time windows. Unfortunately, STFT has special limitations due to the Heisenberg's uncertainty principle, leading to either poor resolution in time when frequency resolution is improved or vice-versa. To overcome this problem we use the wavelet transform, which provides a better balance between time and frequency localization. In particular, we choose to work with a continuous *Morlet* wavelet ψ, which is useful for feature extraction purposes. The final continuous wavelet transform (CWT) takes the form[185]:

$$W_n^X(s) = \sqrt{\frac{\delta t}{s}} \sum_{n'=1}^{N} x_{n'} \psi[(n-n')\frac{\delta t}{s}] \tag{4.1}$$

where $x_{n'}$ is the time series $(n = 1, ..., N)$ with uniform time steps δt, and s the varying scale associated with the stretching of the wavelet in time. The principle behind the CWT is to apply the wavelet as a band pass filter to the signal with the scale s linearly related to the characteristic period of the filter. The wavelet power is given by $|W_n^X(s)|^2$ and the local phase by $arg(W_n^X(s))$.

To compare two signals, we compute at each step the Cross Wavelet Transform (XWT), which describes their common power. XWT can be calculated by multiplying the CWT of the first time series with the complex conjugate CWT of the second one: $W^{1,2} = W^1 W^{2}*$[185]. The relative phase between the two signals is determined by $arg(W^{1,2})$. Additionally we calculate the Wavelet Coherence (WTC) from two CWT, which corresponds to the significant coherence of the signals even at low common power.

From the definition[186], WTC can be expressed as:

$$R_n^2(s) = \frac{|S(s)W_n^{1,2}(s)|^2}{S(s^{-1}|W_n^1(s)|^2).S(s^{-1}|W_n^2(s)|^2)} \tag{4.2}$$

where S is an smoothing operator. This formula is close to that of a traditional correlation coefficient and the WTC can be thus though as a localized correlation coefficient in time-frequency space, varying from 0 to 1.

In general terms, the cross wavelet transform (XWT) exposes the areas of high common power between two signals, whereas the wavelet coherence (WTC) expresses the degree of linearity between them. If two sets of data are physically related, we would expect wavelet coherence values close to 1, denoting that signals are perfectly phase locked (perfect linear relation , i.e, phase synchronization) even if the XWT values are low. Phase locking should be validated by a consistent or slow variation of phase lag between the two signals. If also XWT values are high, this eventually indicates a strong synchronization both in phase and in amplitude.

In the generated XWT and WTC plots the phase difference between two signals 1 and 2 is deduced from the interpretation of arrow patterns[187] Fig. 4.15:

Direction	Meaning
Right →	Signals in phase
Left ←	Signals in anti-phase
Up ↑	*Signal 2 (S2)* leads *Signal 1 (S1)* by π/2 radians (or *(S1)* leads *(S2)* by 3π/2 radians)
Down ↓	*S1* leads *S2* by π/2 radians (or *S2* leads *S1* by 3π/2 radians)

Figure 4.15: Arrow patterns for basic phase lag interpretation

For the sake of clarity, we would like to explain the interpretation of the above mentioned concepts (XWT, WTC, phase lag) with a short, illustrative example, before moving to our results.

Example:

An example of two non stationary, interlinked, physical events occurring in nature are the state of the arctic atmosphere during winter and the ice conditions. In geophysics, the former event is usually accounted for by the Arctic Oscillation index (AO), measuring the degree at which Arctic air penetrates into middle latitudes. The latter event, on the other hand, can be analysed by means of the Baltic maximum sea ice extent record (BMI)[185]. These indices were tracked over several years by the end of the twentieth century giving rise to the time series in Fig. 4.16 (a). To find a connection between the two events, that seem at first glance completely uncorrelated, we can compare rigorously the two signals by analysing the XWT and the WTC diagrams in Fig. 4.16. In the XWT plot (Fig. 4.16 (b)), we observe a common feature (also found by eye in the time-series) in the 8–15 year band from 1940 to 1980. This gives us a first hint on the regions of eventual correlation between the signals, since a high common power can be attributed, but not necessarily, to a local overlap of the two signals. Before drawing any conclusion, we should look at the WTC. In the diagram of Fig. 4.16 (c), we notice that a larger significant section stands

out. This section overlaps the red regions of the XWT diagram, meaning that phase-locking is highly probable in this common region. It is possible for two series to show a significant degree of correlation at one specific scale, although the area of significant correlation is very low. In Fig. 4.16 (c), however, the significant region is so extensive that it is unlikely that this is merely due to chance. To get rid of doubts, we should check the phase-lag of the signals given by the orientation of the arrows in the diagrams. We see than in the section of significance of the coherogram, Fig. 4.16 (c), the arrows point on average to the left and also that variations in their orientation are smooth. This confirms that from 1920 to 1980, in the 8–16 year band, AO and BMI signals were anti phase-locked with also an eventual amplitude correlation between 1940 and 1980.

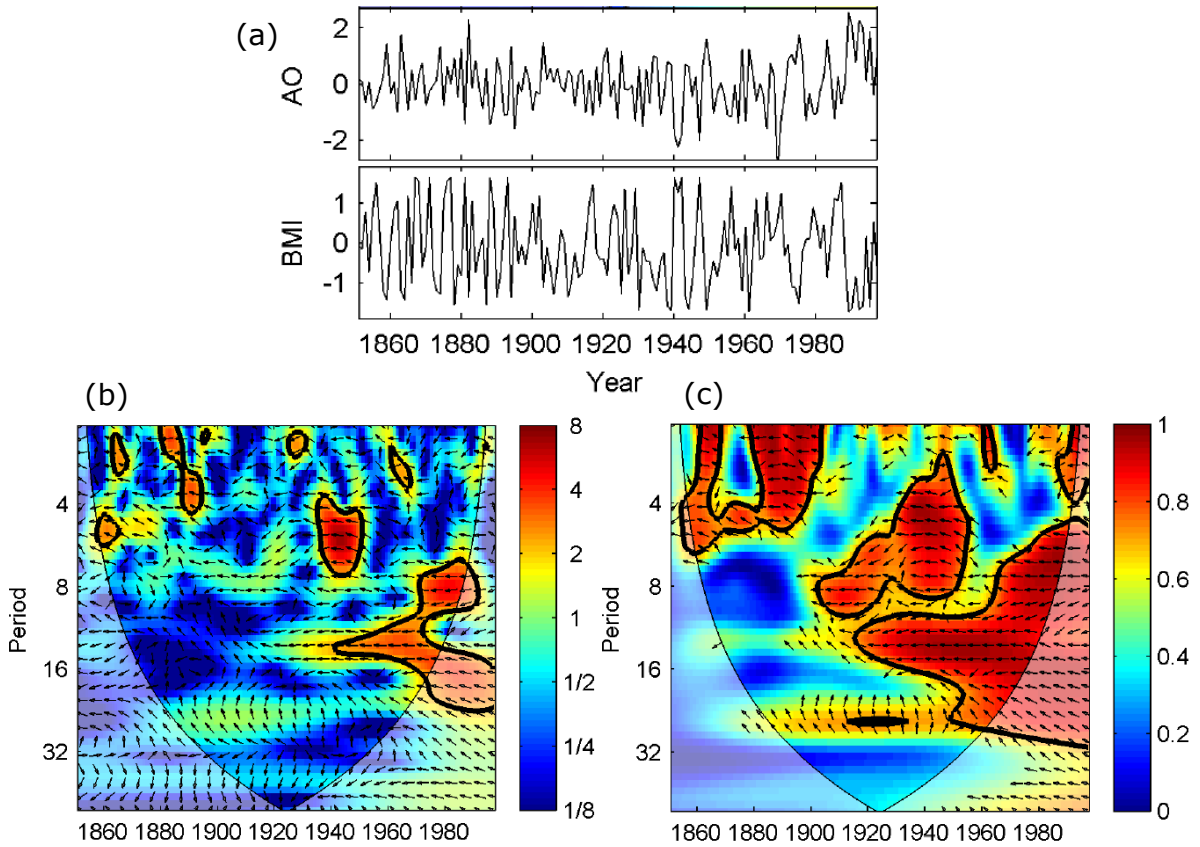

Figure 4.16: Example on the wevelet analysis. (a) standardized time series of AO and BMI. (b) Cross wavelet transform of the time series in (a). (c) squared wavelet coherence between the time series in (a). Adapted from[185]

4.2.5 Results

Linked, knotted and entangled structures

We first analyzed the dynamic behavior of active dimers connected via figure of eight defect loops. This type of entanglement is the most commonly obtained when heating the active hexadecapoles locally with the laser tweezers, with an occurrence of approximately 50%. Alternatively, $\approx 48\%$ of the times, the two independent SRs fuse, joining one of their ends together for a few seconds before detaching and stabilizing back towards its initial configuration. The remaining 2% corresponds to entangled hyperbolic defects reminiscent

to those observed in small passive structures, see Fig. 4.13(f). For the dynamic analysis, we focused specially on dimers composed of droplets with diameters between $30\mu m$ and $60\mu m$. Within this range, the probability that defects in the neighborhood of isolated droplets undergo regular oscillations is significant[170], and thus, we expect that active assemblies built under these conditions have more chance to organize periodic dynamic regimes.

When the sample monitoring begins (typically 15 min after the emulsion preparation), the figure of eight loop encircling the two droplets continually oscillates with its left and right ends freely moving up and down with respect to the mid-section (purple dotted line in Fig. 4.17(a)), showing dynamics similar to those of SRs around isolated active droplets. Near the crossing point (the region where the droplets almost meet), the visible right and left adjacent parts of the loop, numbered as 2 and 3 in Fig. 4.17(a), display similar oscillations but without crossing the equator, remaining apart from each other (see Movie 12). This dynamics are translated by the sequence of time-series shown in Fig. 4.17 (b), representing the angular evolution of the four different portions of the loop visible inside the dashed circumferences (yellow lines) Fig. 4.17(a). Note that in Fig. 4.17 (b) θ_n angles are normalized to ease the comparison between signals. Qualitatively, some of the signals seem to be really regular (S1) with only little changes in frequency and amplitude while others (S2, S3) exhibits low amplitude episodes interspersed between consistent modes of oscillation. Because these disruptions make visual comparison between pairs of signals misleading, we performed a complete wavelet analysis to extract the frequency and amplitude information of the oscillations. In Fig. 4.17 (c), we present the cross wavelet transform (XWT) resulting for the six different compared pairs.

In all the panels, a maximal common power is attained for periods comprised from $64s$ to $160s$ (resp. $15.6mHz$ to $6mHz$), meaning that all the considered portions of the loop oscillate at similar frequencies and with similar amplitudes despite the short perturbations detected. Interestingly, this does not necessarily imply that all the signals are well-synchronized with each other. Most WTC diagrams in Fig. 4.18 are noisy with only the top-left and bottom-right panels displaying significant coherence values in the frequency range described above. Strongly correlated pairs correspond to signals 1-2 (S1-S2) and 3-4 (S3-S4), i.e, to the signals of the diametrically opposed sides of each half of figure of eight. In other words, these are the signals otherwise belonging to the same SRs disclination loops. The coherence trend is consistent with phase angle variations represented by dark arrows patterns in the diagrams. In plots WTC S1-S2 and WTC S3-S4 the orientation of arrows inside the black contour varies slowly with time, with a maximal deviation of 45°. In the other plots (Fig. 4.18(c)) phase fluctuations in the same frequency domain are more abrupt and chaotic, as shown by arrows pointing in all directions of space. If we compare these results with those of a reference experiment in which SRs oscillate around isolated droplets far apart from each other (appendix A), no particular improvement in the coordination between oscillators is detected.

To understand the reasons behind this behavior, we analyzed the internal configuration of the entangled active droplets by means of confocal fluorescence microscopy. In Fig. 4.19, we illustrate a sequence of a hemisphere of the nematic shell in the 2D plane. We have localized the position of positive defects on the left and right droplets with red and yellow arrows respectively, pointing towards the direction of motion. The size of the analyzed droplets is of the same order than above to suppress the excess of defects and to enhance the regularity of the flowing active material. The images show how active defects travel along regular trajectories at the surface of each droplet but without coordinating

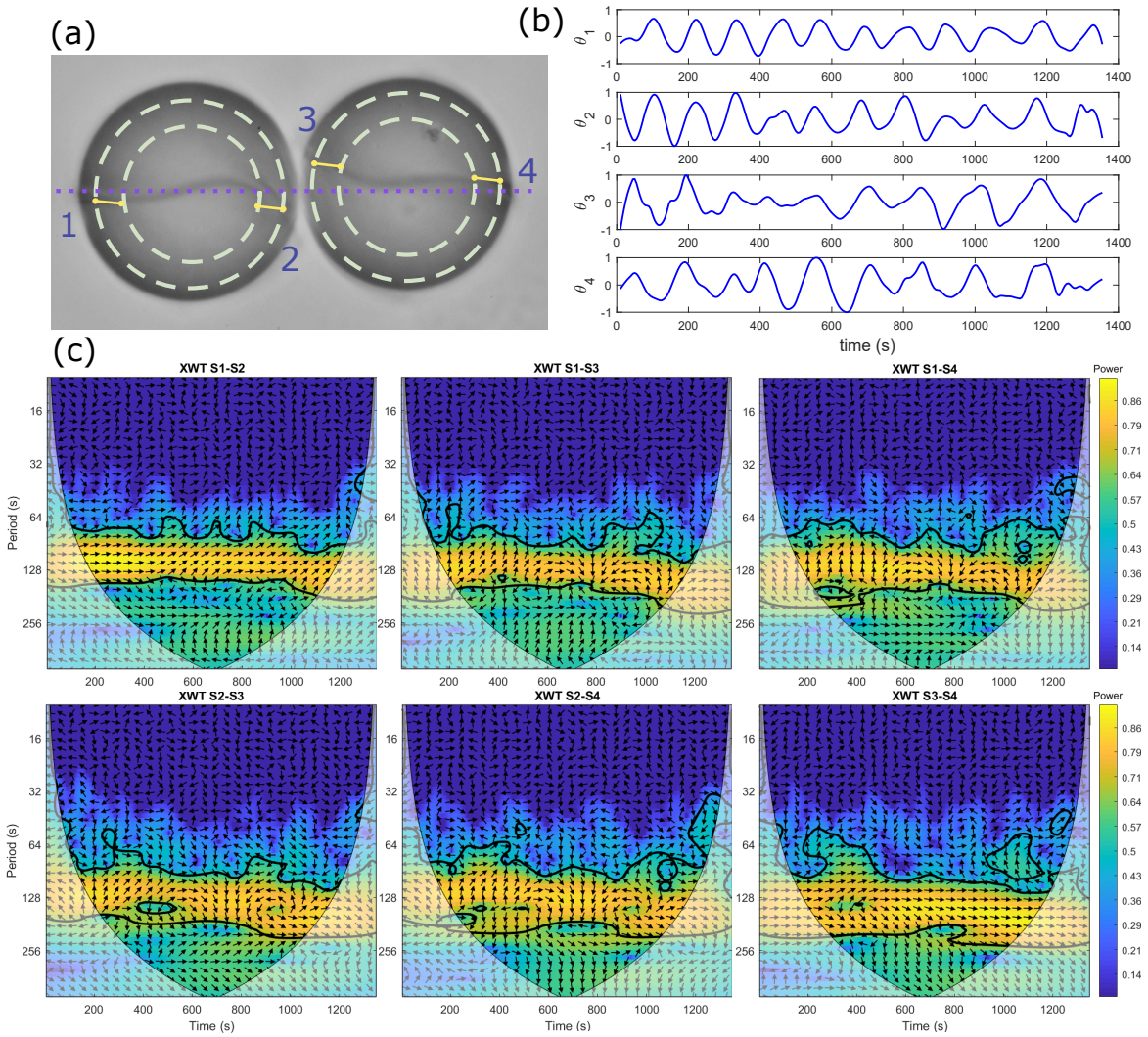

Figure 4.17: Dynamics of active hexadecapoles attached via a figure of eight loop. (a) Bright-field micrograph of the dimer surrounded by the figure of eight defect. Dashed circles limit the area analyzed for obtaining the space time plots in (b). Time series in (b) are numbered from 1 to 4 according to the position of the analyzed loop section. (c) Cross wavelet transform of the time series in (b). The phase lag between the signals is given by the orientation of the black arrows. The dark contour represents a significance level of 5% against noise. The opaque regions correspond to the cone of influence (COI [2]).

their positions with those of defects in the neighboring shell. This attests that at certain range of frequencies, active flows act individually at the surface of each droplet despite the global constraints imposed by the passive material. Consistently with the previous results, we believe that the active forces exerted at the surface of each droplet can be sensed only in the immediate passive LC environment of the droplet, but not far from it. As a result, each half of the eight loop oscillates coherently (S1-S2 and S3-S4), while the two halves between them do not (S1-S3, S1-S4, S2-S3, S2-S4).

We speculate that the coupling strength between the oscillators is not strong enough either to transfer the stress from one droplet to the other one or to achieve a regular steady state in the system. Even at intermediate frequencies such as those reported above, the

[2]COI: cone of influence where edge effects might affect the spectrogram. It corresponds to the area in which the wavelet power caused by a discontinuity at the edge has dropped to e^{-2} of the value at the edge.

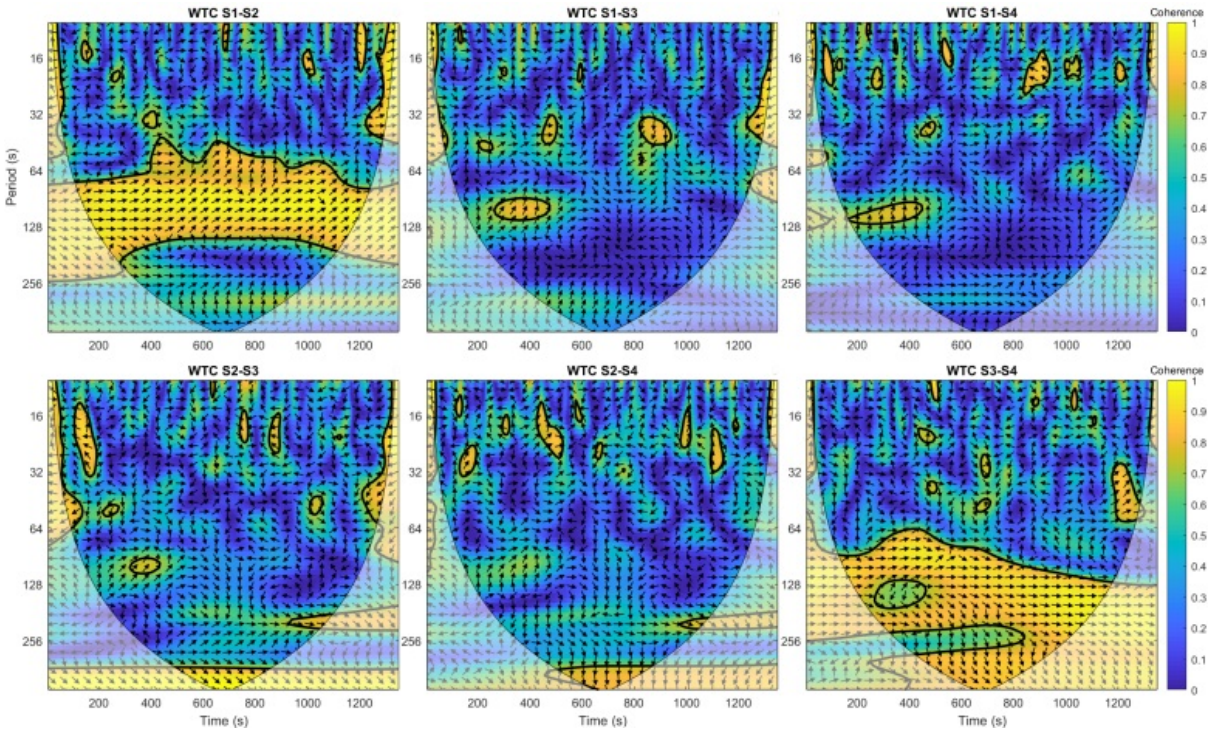

Figure 4.18: Wavelet coherence spectrums of signals in Fig. 4.17 (b) The phase lag between the signals is given by the orientation of the black arrows. The dark contour represents a significance level of 5% against noise. The opaque regions correspond to the cone of influence (COI).

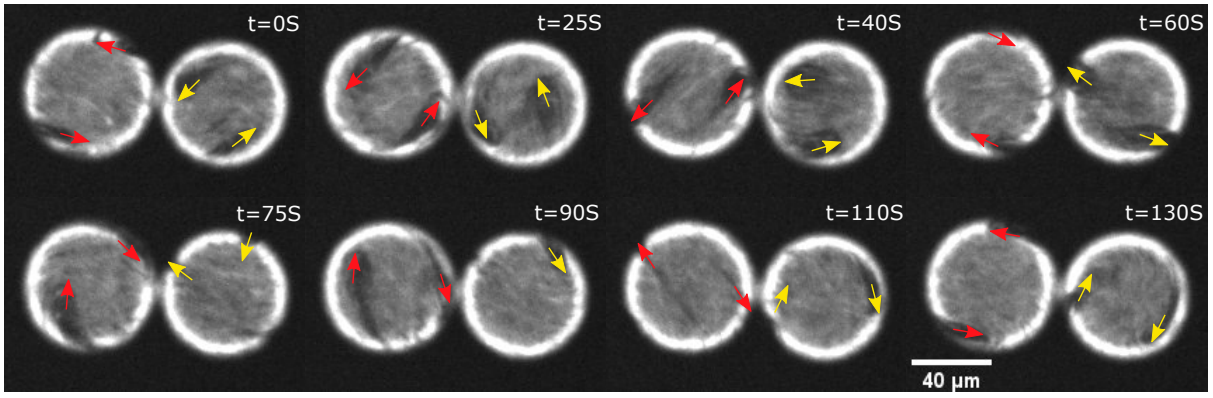

Figure 4.19: Evolution of the internal active nematic layer of two droplets connected via a figure of eight defect and oscillating at intermediate frequencies. Fluorescence images represent a droplet hemisphere over a single period of oscillation. Red and yellow arrows show the defects positions on the left and right droplets respectively.

active forces of the nematic shell seem to dominate over the elastic contributions of the passive material.

In order to investigate the effect of the activity of the individual droplets, we have analyzed dimers attached via the same loop and oscillating at lower frequencies. The data set Fig. 4.20 (b) and the Movie 13 clearly illustrate how the oscillations of the different loop sections of the new assembly occur slowly and extend over large periods of time. Similar than in the previous example, the XWT and the WTC are calculated to compare the common power and the coherence between two signals respectively. The cross spectra in Fig. 4.20 (c) reveal that the higher power occurs for all signals at typical periods (resp. frequencies) of $260s$ (resp. $4mHz$). Remarkably, at this frequency interesting features

also appear in the coherograms, see Fig. 4.21. Strong coherence is not only present in S1-S2 and S3-S4 pairs but also in otherwise uncorrelated signals S2-S3 and S2-S4. Moreover the phase lag for all these pairs is almost constant with time, as shown by the nearly uniformly aligned arrow patterns inside the black contours, validating the computed coherence data. It is worth noting that the arrows in the different plots do not point towards a unique average direction. In WTC S1-S2 and WTC S3-S4 arrows point right meaning that the compared signals are in phase whereas, in WTC S2-S3 and WTC S2-S4 arrows point left attesting for anti-phase oscillations.

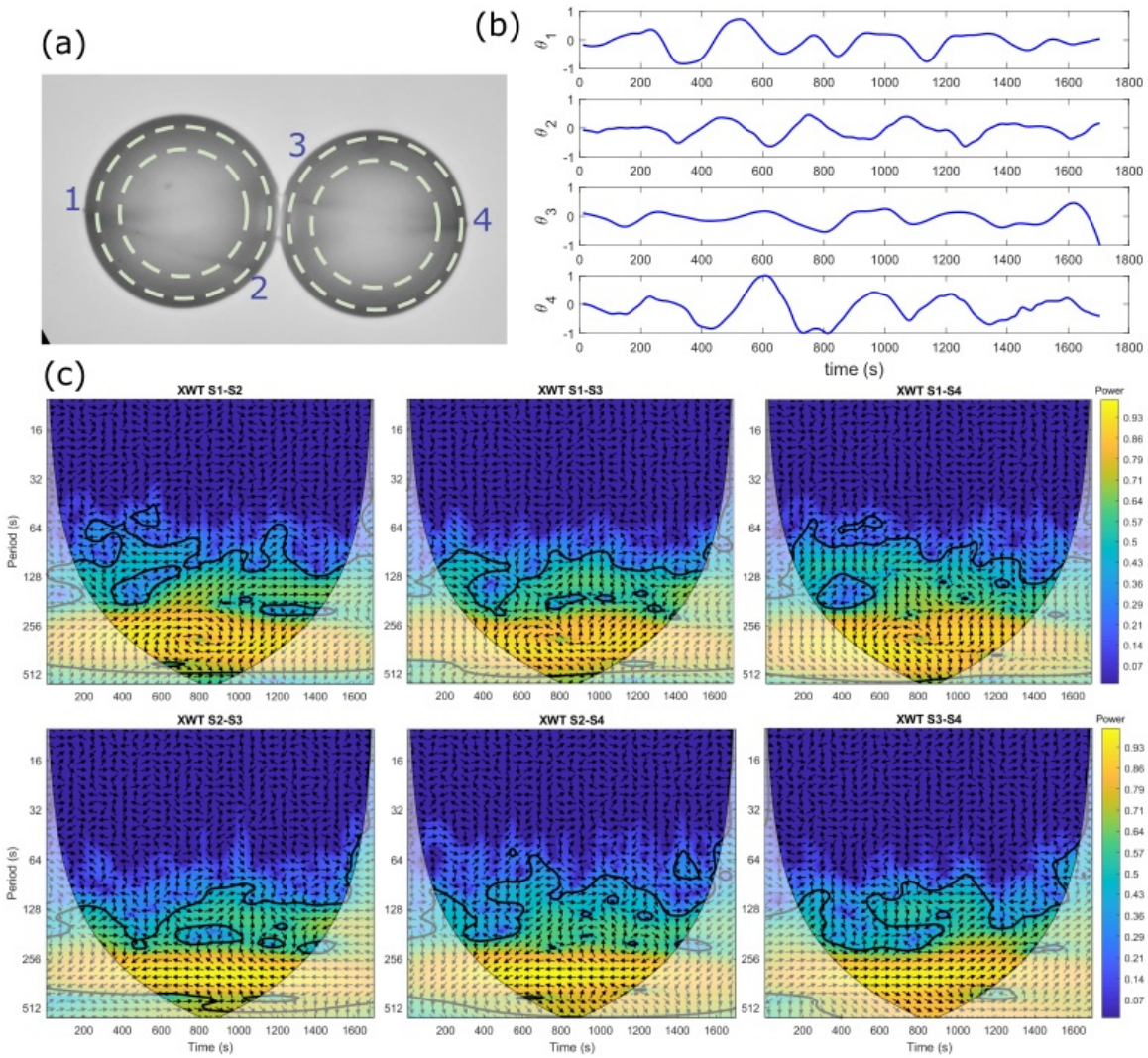

Figure 4.20: Dynamics of an active dimer oscillating at low frequencies. (a) Bright-field micrograph of the dimer surrounded by the figure of eight defect. Dashed circles limit the area analyzed to obtain the space time plots in (b). Time series in (b) are numbered from 1 to 4 according to the position of the analyzed loop section. (c) Cross wavelet transform of the time series in (b). The phase lag between the signals is given by the orientation of the black arrows. The dark contour represents a significance level of 5% against noise. The opaque regions correspond to the cone of influence (COI).

The evolution of the internal structure of the droplets corroborates the external dynamics of the figure of eight defect at low frequency regimes. Snapshots (Fig. 4.22) show how active defects move slowly guiding the flows of the different droplets along trajectories which are almost equivalent under reflection symmetry, the symmetry plane being the plane in between the droplets, perpendicular to the plane of the figure of eight loop.

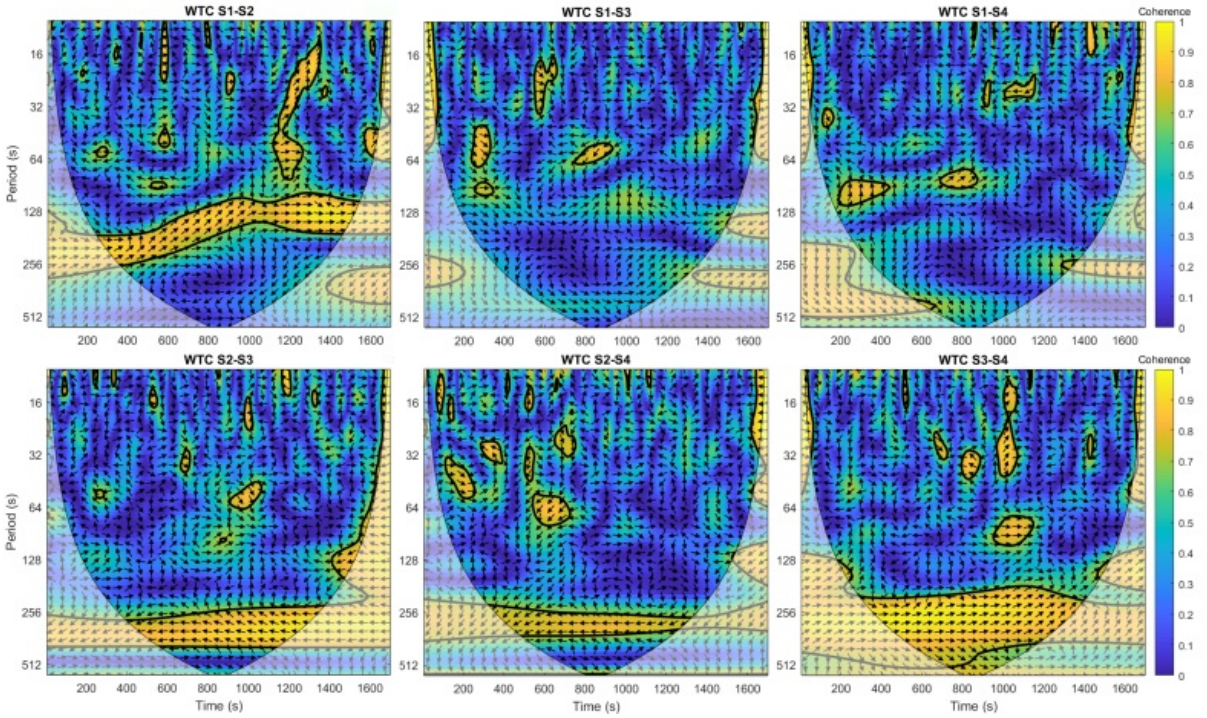

Figure 4.21: Wavelet coherence spectrums of signals Fig. 4.20 (b) The phase lag between the signals is given by the orientation of the black arrows. The dark contour represents a significance level of 5% against noise. The opaque regions correspond to the cone of influence (COI).

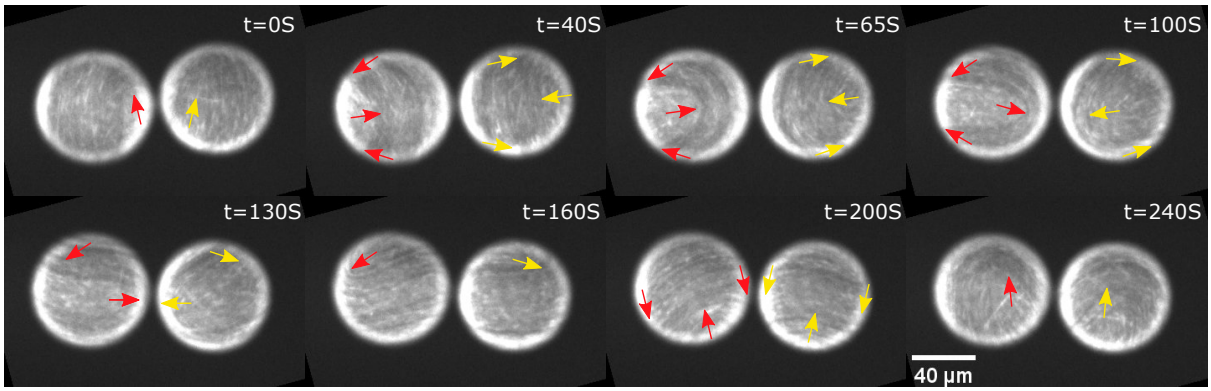

Figure 4.22: Evolution of the internal active nematic layer of two droplets connected via a figure of eight defect and oscillating at low frequencies. Fluorescence images represent a droplet hemisphere over a single period of oscillation. Red and yellow arrows show the defects positions on the left and right droplets respectively.

The concordance between the oscillations of the inner and outer conformations of the inclusions suggests that the active/passive coupling can also occur on a higher organizational level. We believe that, at low frequencies, the passive material is able to respond to the active stimulus by homogeneously regulating the active flows of the two droplets. In the following part, we will analyze linear assemblies of droplets, oligomers, linked together by other type of bounding defects to elucidate the importance of the connecting topology on the dynamics of active assemblies.

Active necklace structures

The fabrication of a colloidal liquid crystalline necklace is based on the insertion of two or more particles along a disinclination line. When the particles are aqueous droplets with diameters of the order of tens of microns, the process is not trivial, since the droplets can collapse because of levitation effects[188] aggravated by the presence of the supporting line defect, which bring the droplet in contact with air. To overcome this problem, the active droplets are stabilized with a Tween-20 surfactant (instead of the Tween-80), ensuring the robustness of the assembly for long periods. At the surface of the droplets, the surfactant imposes homeotropic anchoring, and thus, leads to the formation of either quadrupoles or dipoles. In the disclination line, quadrupoles are very unstable and quickly collapse, leading in all the cases to chains of dipoles such as the one represented in Fig. 4.23 (a). A typical mechanism of interaction between homeotropically anchored droplets and a disclination line is illustrated in the appendix B.

Contrary to assemblies bound by closed defect loops and knots, necklaces are open and linear structures. This impacts the whole dynamics of the system, specially regarding the way in which distortions propagate along the disclination line. Close to the droplet surface, the passive material undergoes important distortions reflected by the persistent up and down beating of the line defect (see Movie 14). At larger distances, the oscillations are progressively damped making the disclination fluctuate smoothly from its original position. Note however, that, in all situations, such a conformation restricts the amplitude of the movement of the line defect, preventing it from escaping far from the connection axis. For the dynamic analysis, we focused specially on the regions neighboring the droplets, as shown in Fig. 4.23 (a) and (b). The computed XWT spectra (Fig. 4.23 (c)) reveal a significant common power for periods close to 80s (12.5mHz in the frequency domain) for all the compared signals and during all the monitoring time. The trend is markedly different in the coherograms (Fig. 4.24), showing that only S2-S3 pair is anti-phase locked for periods ranging from 64s to 128s, while the other pairs are uncorrelated despite sporadic episodes of coincidence that we attribute to chance. We believe that the correlation between S2 and S3 is caused by the taut elastic configuration surrounding the disclination core. Along the channel, the line defect has associated a tension T growing with K, the average elastic constant of the LC and L the thickness of the confining cell[189,190]. In nematic cells with similar conditions than ours ($K \approx 12pN$ and $L \approx 100\mu m$), tension has been found to attain $85pN$[190], which is large enough to keep the line virtually straight over short distances. Between regions 2 and 3 of the necklace, the disclination is thus sufficiently taut to balance the deformations induced by the two active shells in the passive medium, making them oscillate at similar rates. At regions 3 and 4 however, the active stress at the cortex of the droplets is progressively dissipated through the passive material in an incoherent way, generating long wavelength undulations of the line vanishing far away from the droplets.

One of the advantages of the fabrication procedure of active necklace structures is that it does not involve heating, which affects the integrity of the aqueous droplets. Chains with more than two particles can be easily formed as long as the connecting disclination is sufficiently long and stable. In appendix C, we show for example two necklaces composed of three and five active droplets, respectively. For the sake of clarity, we will not go into the details of the dynamic behavior of such assemblies, but we would rather point out their most important features. Similar to short chains such as the one in Fig. 4.23 (a), the connecting disclination exhibits low amplitude oscillations because of the strong line

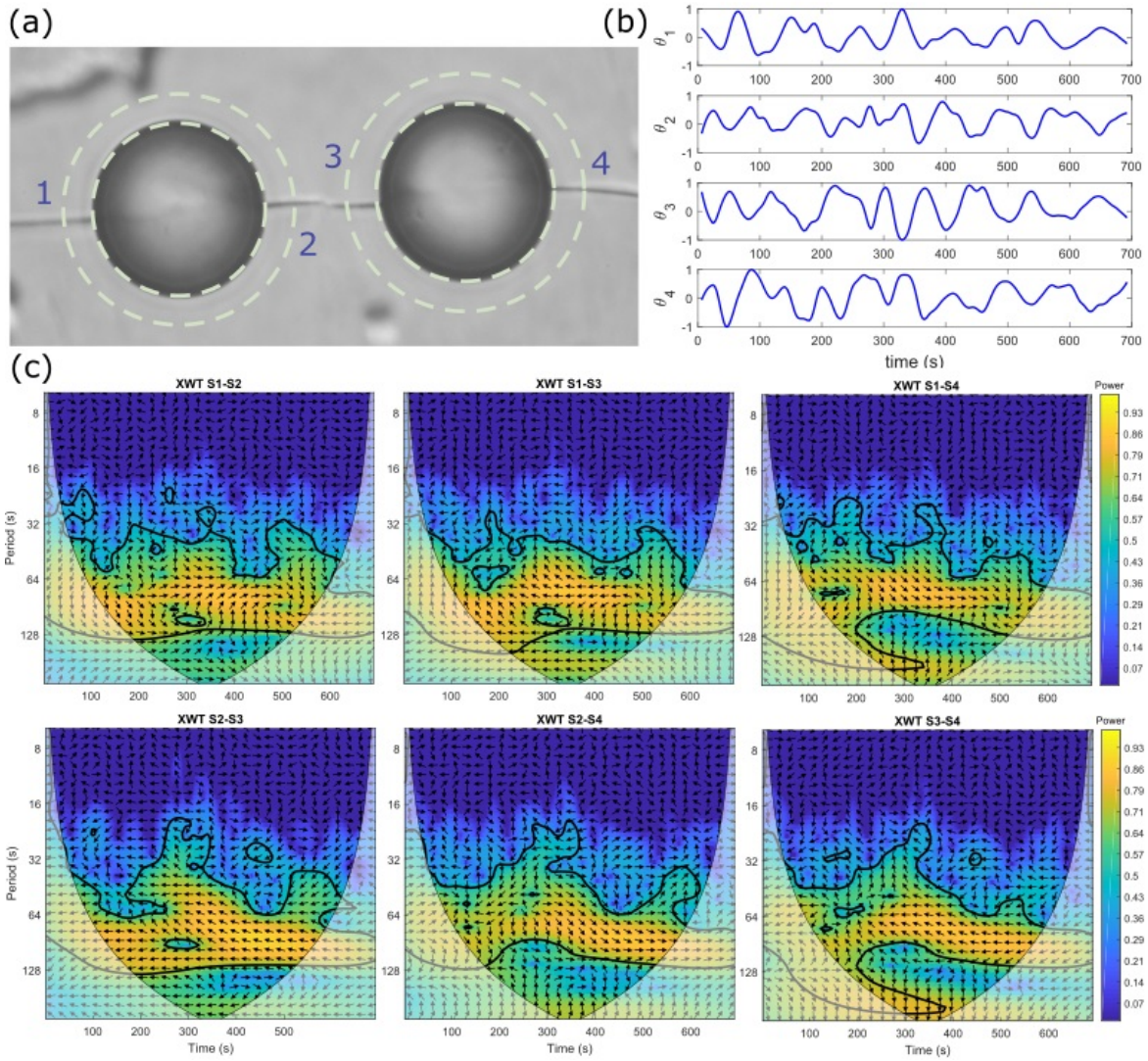

Figure 4.23: Dynamics of an active necklace structure. (a) Bright-field micrograph of a dimer connected through a disclination line. Dashed circles limit the area analyzed for obtaining the time series in (b). Time series in (b) are numbered from 1 to 4 according to the position of the analyzed section. (c) Cross wavelet transform of the time series in (b). The phase lag between the signals is given by the orientation of the black arrows. The dark contour represents a significance level of 5% against noise. The opaque regions correspond to the cone of influence (COI).

tension, which forces its stabilization to a fixed position along the channel. Furthermore, the incorporation of additional droplets seems to render the dynamics of the assembly even more chaotic. At frequencies between 8mHz (resp. periods of 128s) and 31mHz (resp. periods of 32s) the signals of the sections in between the droplets are mainly uncorrelated as shown by the noisy color distribution in the coherograms and the irregular arrow patterns in appendix C. This confirms that, at high oscillation frequencies, the tension of the line and the elastic counter-acting forces of the passive material are insufficient to couple two or more active droplets together. Unlike other assemblies where the topological defects are free to orbit around the particles, the dynamics of taut necklaces cannot be analysed in the low frequency domain. This is because the amplitude of the oscillations becomes extremely low at the point that the waving signals turn into noise. Nevertheless, an alternate necklace built from more flexible line defects can be used to explore this last

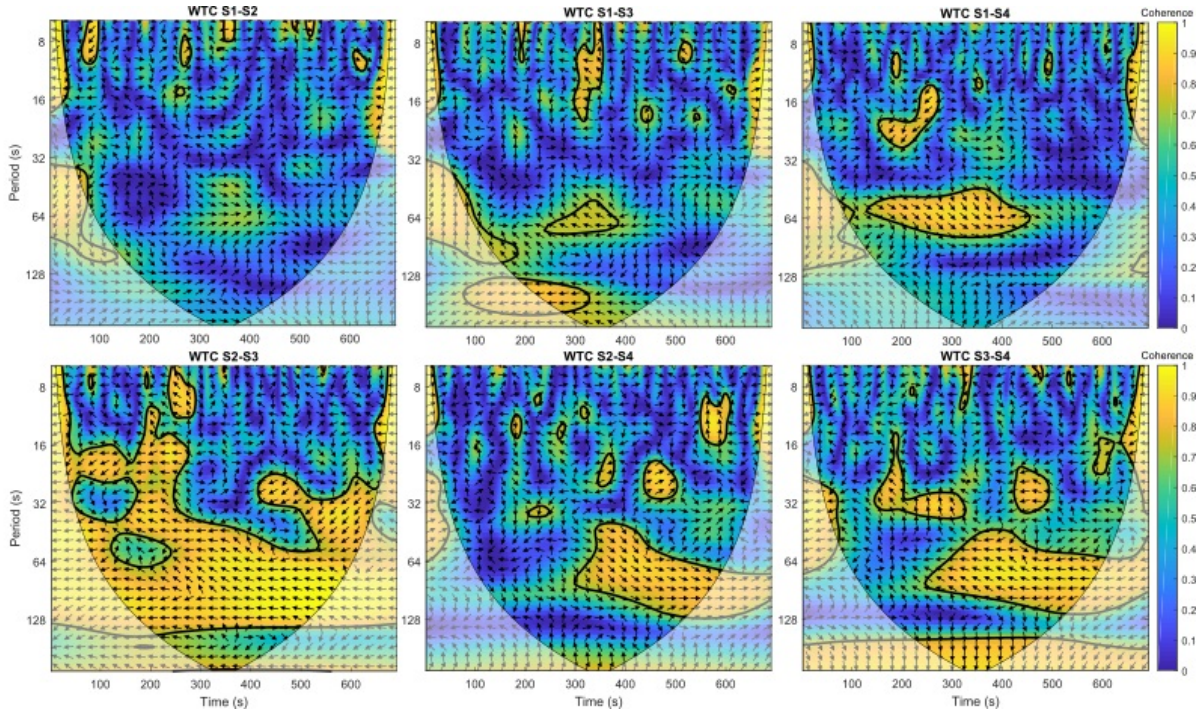

Figure 4.24: Wavelet coherence spectrums of signals Fig. 4.23(b) The phase lag between the signals is given by the orientation of the black arrows. The dark contour represents a significance level of 5% against noise. The opaque regions correspond to the cone of influence (COI).

scenario. The assembly in Fig. 4.25(a) was built in an open 5CB planar cell, by attaching tiny droplets of active solution with a disclination line simultaneously "drawn" by the injection capillary tip. Since the disclination was not confined to a narrow channel as in the previous cases but was rather free in the bulk, the tension of the line is supposed to be weaker, thus making the supporting line more flexible. This can be evidenced in Movie 15 where, despite the slow oscillations of the necklace, the amplitude remains sufficiently important to preserve the shape of the waving signals (Fig. 4.25 (b)). The highest common power occurs for periods comprised between 128s (8mHz) and 260s (4mHz) for all pairs of signals for over 30 min, as shown in the cross-spectrum (Fig. 4.25 (c)). For these period intervals (resp. frequencies), anti phase-locking is observed for pairs S2-S3 and S4-S5 (Fig. 4.26). Similar to the example in Fig. 4.23, these signals correspond to the regions in between two consecutive droplets. The other pairs are only partially synchronized for short intervals at the beginning and at the end of the monitored time.

Conclusion

In this Chapter, we have explored the dynamics of active nematic assemblies built from two different approaches. In the first one, MTs-kinesin active droplets, embedded in a passive liquid crystal, were attached together by fusing their external defects with the help of laser tweezers. This gave rise to dimers connected via complex links and knots orbiting around the droplets such as the figure of eight defect, or the entangled hyperbolic defect. The second approach consisted in producing the active droplets directly on a disclination line to form active necklace structures. In both situations, we explored several parameters, with particular emphasis in the oscillation frequency, which is directly related to the activity of the nematic droplets. Fast oscillating assemblies connected via a figure of eight defect revealed poor coordination between their constitutive droplets. This was first

evidenced by comparing the dynamic behavior of the external defect around each droplet via a wavelet analysis, and second, by a close inspection of the defect dynamics on the inner cortical active nematic layer. Slow oscillating dimers, on the other hand, revealed partial phase-synchronization with a portion of the topological connector oscillating coherently and the two neighboring inner shells describing symmetric flow trajectories. The second type of assemblies, namely, the active necklaces, display local anti phase-locking in the portion constrained in between the droplets and a disordered behavior away from it. Irregularities in the communication between the droplets are more notorious at high frequencies or by increasing the number of active constituents in the chain. Under low activity conditions, the oscillatory dynamics of the active defects on the droplet surface can adapt more easily to the oscillatory rhythm imposed by the assembly. First, because at low activity, the dynamics of the active defects are more regular, and second, because oscillations are also slower, and thus, the time that the passive medium has to transfer the elastic distortions between the two ends of the assembly is longer. Increasing activity, on the other hand, introduces certain degree of chaos in the active defect oscillations and decreases the time the LC has to relax elastic distortions, resulting in the loose of spatial correlation in the assembly. Although we believe that an ideal phase-amplitude synchronization is not reached in our systems because of the weak coupling strength between the active and the passive fluids, this should be confirmed by numerical calculations, which are currently being performed by the group of Slobodan Žumer, Miha Ravnik and Simon Copar at University of Ljubljana. Their work will be key not only to shed light on the origin of the coupling, but also to understand to which extent each of the parameters considered (size of the droplets, activity, elasticity of the passive LC, type of topological connector, etc..) contributes to achieve a consistent coordination between droplets. Finally, our investigation has raised many open questions that we propose to address in the near future: What type or forces (elastic/hydrodynamic) are involved in the coupling of active nematic oscillators? What are the relevant time or length scales involved in this process? How do perturbations induced by the active material propagate in the passive medium and vice-versa? What kind of experiments can we perform to determine the contribution of every parameter (distance between droplets, size of the droplets, elasticity of the liquid crystal, anchoring strength, activity)?

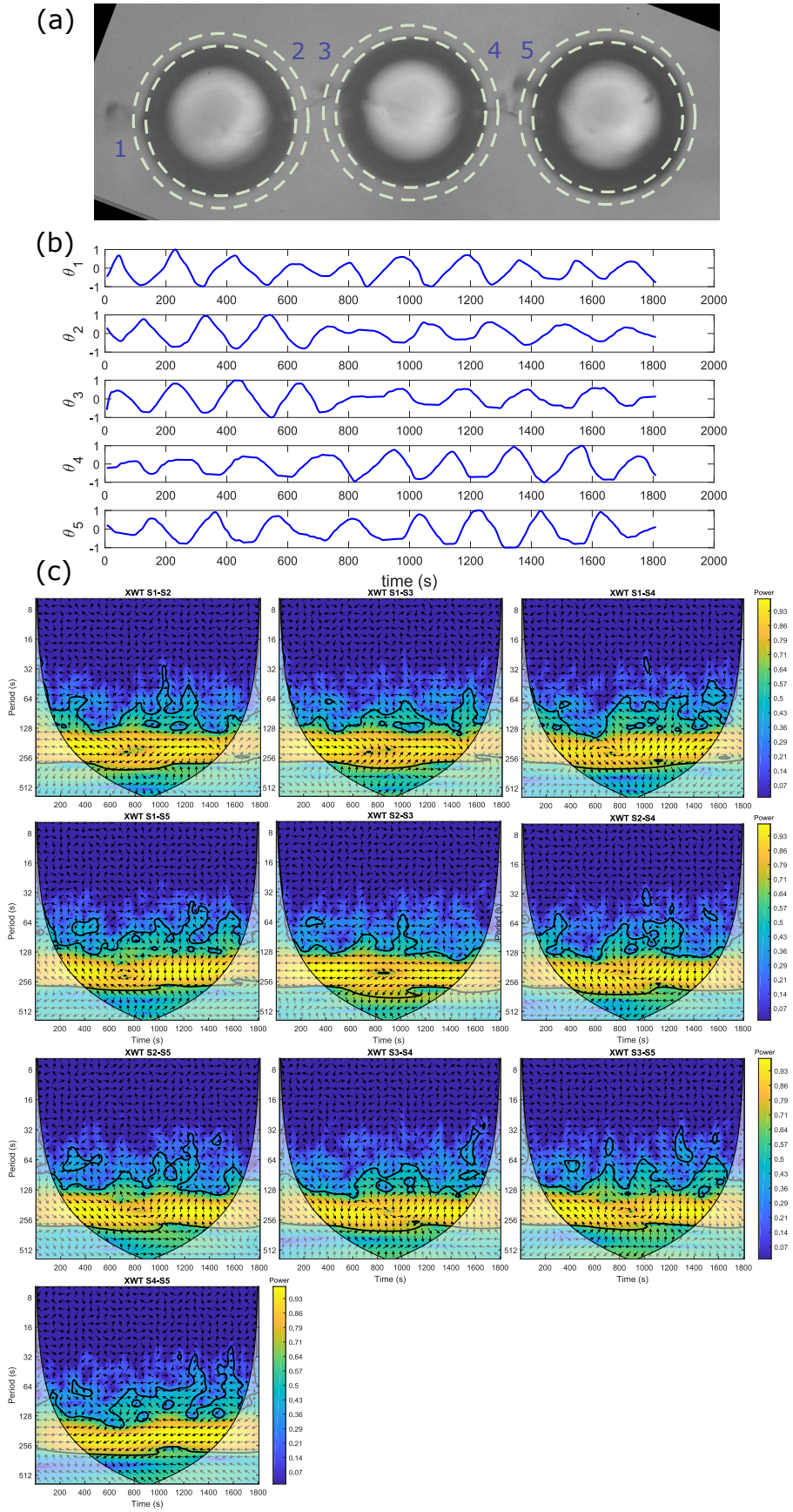

Figure 4.25: Dynamics of an active necklace structure. (a) Bright-field micrograph of a trimer connected through a disclination line. Dashed circles limit the area analyzed for obtaining the space time plots in (b). Time series in (b) are numbered from 1 to 5 according to the position of the analyzed section. (c) Cross wavelet transform of the time series in (b). The phase lag between the signals is given by the orientation of the black arrows. The dark contour represents a significance level of 5% against noise. The opaque regions correspond to the cone of influence (COI).

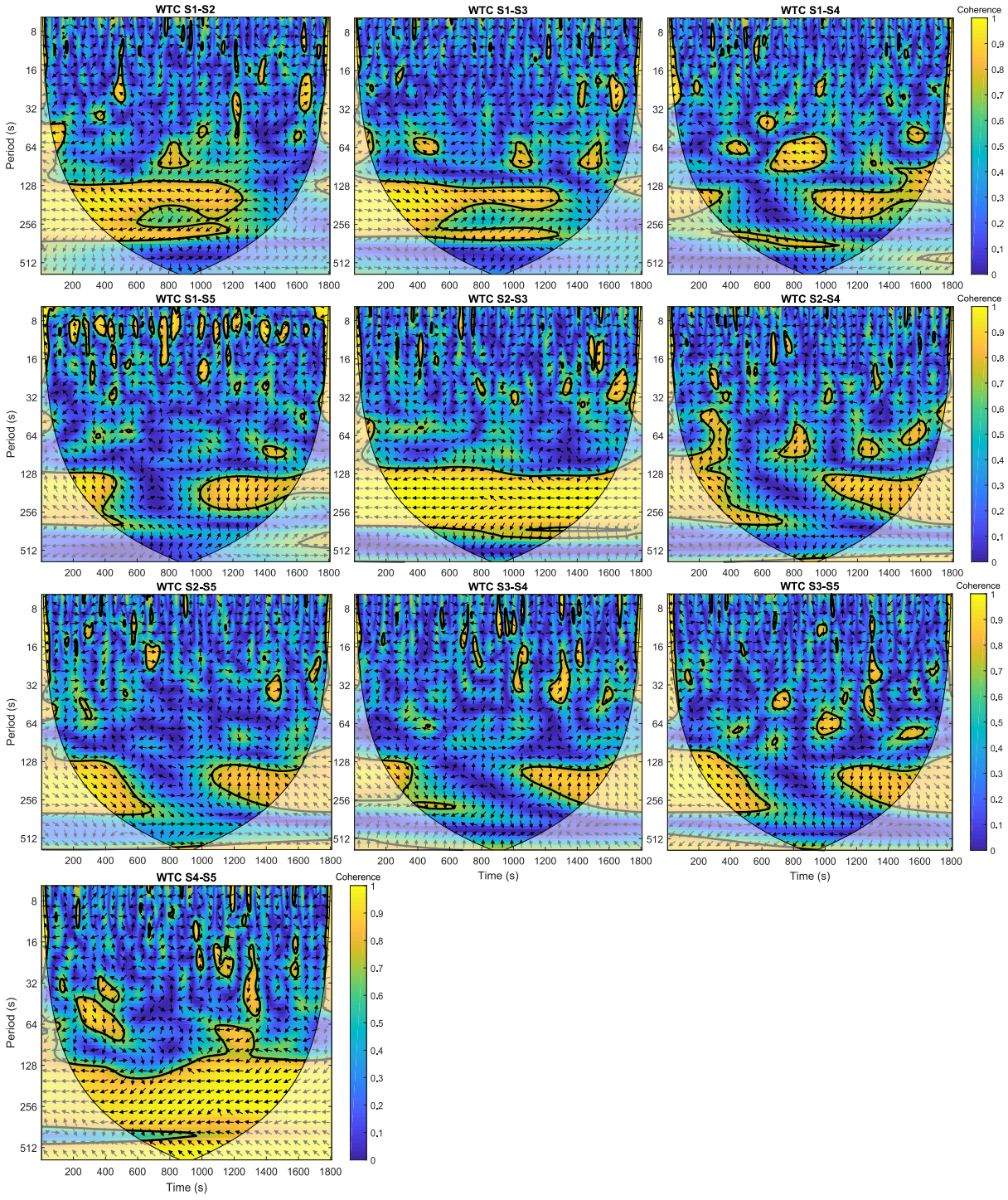

Figure 4.26: Wavelet coherence spectrums of the signals in Fig. 4.25(b). The phase lag between the signals is given by the orientation of the black arrows. The dark contour represents a significance level of 5% against noise. The opaque regions correspond to the cone of influence (COI).

CHAPTER

FIVE

PERSPECTIVES AND CONCLUSIONS

Perspectives

In this work, we have addressed several problems related to different areas of soft active matter physics, ranging from turbulence regulation in complex geometries to the design of autonomous self-propelled systems and topologically coupled oscillators. With time, as the spectrum of the findings broadened, new challenges and ideas emerged, quickly demanding more investigation. Some of these challenges required a deeper understanding of certain phenomena, while others appealed for the use of new experimental techniques and set-ups. Here we briefly present some ongoing research topics, as well as several guidelines for future investigation.

5.1 Probing the dynamics of active nematics on new geometries

In chapter 3, we studied the intricate dynamics of topological defects in active nematic shells of non-spherical shape. We demonstrated that small variations in the curvature, size and length of the droplets resulted in spatio-temporal patterns that shared common features, namely oscillations between a rotational and a translational regime. In this regard, it should be of particular interest to make such variations more pronounced in order to explore the potential emergence of essentially new dynamical states. For example, although it has not been reported in the document so far, very long droplets (with an aspect ratio beyond 3) can be produced with the same microfluidic protocol detailed in section 2.4.2.2.

To go even further in this subject, one could envisage to study active nematics confined to the surface of liquid crystalline fibers. In previous experiments, regarding smectic liquid crystals in contact with an aqueous solution of cetyl ammonium bromide (CTAB), it has been observed that instabilities at the LC surface trigger the formation of wrinkles and occasionally the ejection of tiny jets of LC material[191,192]. These jets subsequently re-organize into fibers, provided that the surfactant concentrations are much larger than the critical micellar concentration (Fig. 5.1). Regarding the fiber organization, it has been suggested that they are built from coaxial smectic layers, rolled-up into a hollow tube[192]. These cylindrical structures are an interesting support on which the active nematic could be condensed. Although Gaussian curvature is zero all along the tube (and positive at

the poles), the new smectic texture and shape of the tube are expected to induce new spatio-temporal behaviors in the active nematic. The main experimental challenge to overcome would be the identification of a suitable surfactant to simultaneously ensure the stability of the fibers and the compatibility with the active material.

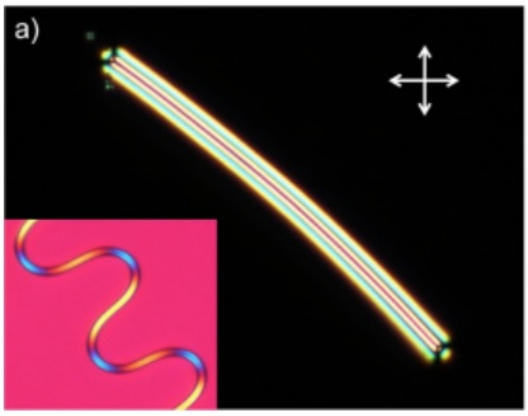

Figure 5.1: Polarizing microscopy image of a smectic-A 8CB microfiber (diameter $\approx 10\mu m$) doped with $0.01wt\%$ of Nile red in aqueous CTAB solution. The inset shows a thinner fiber (diameter $\approx 3\mu m$), displaying a bend S-like shape. The alternating yellow/blue bands indicate that messogen molecules are always aligned perpendicular to the surface of the fiber. Adapted from[193].

5.2 Improving the coupling strength in active nematic oscillators

In section 4.2.5, we discussed the parameters that influence the coupling strength between active nematic oscillators. We suggested that the active forces generated by the cortical layer are communicated to the passive liquid crystal by an elastic/hydrodynamic coupling. However, the importance of each of these two contributions is still uncertain. Several strategies could be envisaged to decouple hydrodynamic and elastic effects. For instance, we could evaluate the effect of elasticity by heating the LC to reach the isotropic phase, where the viscosity is almost maintained but the elasticity decays to zero. The problem with this approach is that the temperature required for attaining the isotropic phase would affect the integrity of the biological active gel. A better alternative for probing the viscous character of the coupling would be to study the dynamics of active nematic assemblies in a viscous oil. An important degree of correlation in this situation would indicate that the coupling results from hydrodynamic effects rather than from the elastic regulation. Similarly, we can probe the effect of elasticity by replacing the 5CB liquid crystal by another nematic material with high elastic constants, at room temperature. By implementing this change, one can expect to enhance the propagation of elastic distortions over all the active assemblies, thus improving the coupling strength.

Even if we are able to determine the main nature of the coupling (viscous or elastic), it is difficult to elucidate from experiments the extent to which each of the parameters is involved. This is still an open question. To complement our investigation, simulations evaluating the effect of viscous damping and elasticity on the regulation of the dynamics of active assemblies should be performed.

In chapter 4, we also discussed the dynamic behavior of active necklace structures. To increase the coherence of the oscillations in necklaces, we suggest to build closed circuits,

so that the disclination line connecting the droplets undergoes continual feedbacks that regulate the oscillatory behavior of the assembly. This idea stands on the fact that synchronization in many biological oscillators does not rely only on the periodic rhythm of individual units but also on internal feedback signals transmitted via messenger agents, such as hormones or neurotransmitters. In the simplest scenario, the active necklace described in appendix B can be built as a closed loop rather than as a linear chain. For this, we can think of an experimental setup where the closed disclination line is produced in an annular channel. Such a channel could be built by confining the 5CB liquid crystal between two concentric PDMS disks, sitting on a substrate treated to impose concentric planar alignment. A schematic representation of the proposed cell is shown in Fig. 5.2. The challenge in this project is to achieve a good precision in the design of the cell, which is hard to obtain because of the small dimensions required. We speculate that closing the necklace will provide the continual feedback required for correcting incoherence in the dynamics of the oscillators. To go even further, these cells of hybrid (planar/ homeotropic) anchoring can be customized in order to develop complex circuits of disinclination lines, acting as feedback paths for regulating locally the oscillatory behavior of single droplets.

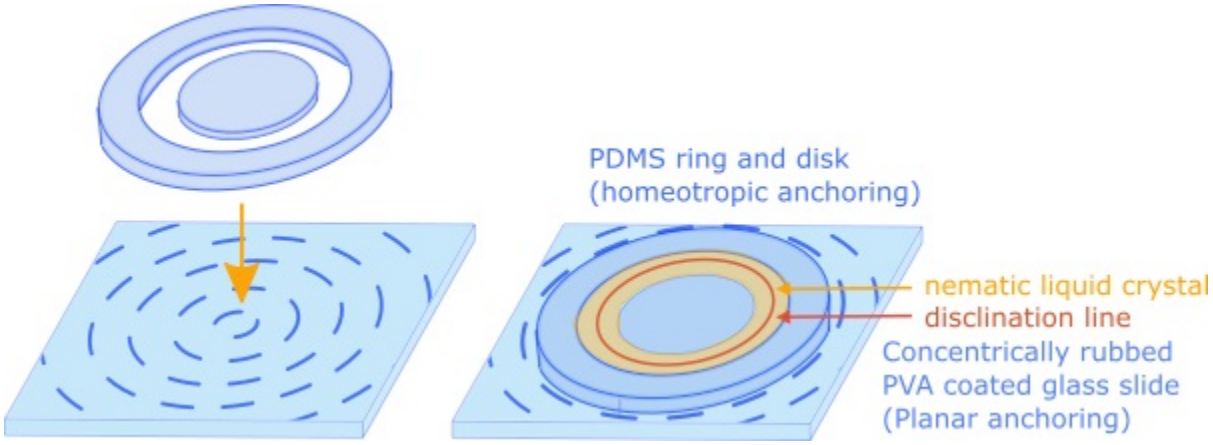

Figure 5.2: Cell design for the fabrication of a closed necklace circuit. Two PDMS pieces are stuck on a rubbed PVA coated glass slide. If the inner circuit is filled with a nematic liquid crystal, messogen molecules would orient perpendicular to the walls (homeotropic) and parallel to bottom plate (planar), leading to a disclination line encircling the small PDMS disk.

5.3 Large assemblies, complex knots and hierarchical structures

In section 4.2.5, we mainly focused on studying the oscillatory behavior of pairs of active droplets or small clusters made from no more than 3 identical droplets. The purpose of choosing a small number of similar droplets was to understand the fundamental forces and configurations that make the system communicate. In the future, we would like to explore more sophisticated dynamic structures. One can envisage for instance to build 2D and 3D active assemblies, analogue to those obtained with passive colloids (Fig. 5.3)[15,46].

In Fig. 5.3, the left and right lattices are built from unit blocks composed from dipoles (panel (a)) and quadrupoles (panel (b)), oriented along specific directions of attractive interaction, given by an angle γ. In the future, we could consider building 2D-structures made, not only from homogeneous elementary units, as in Fig. 5.3, but

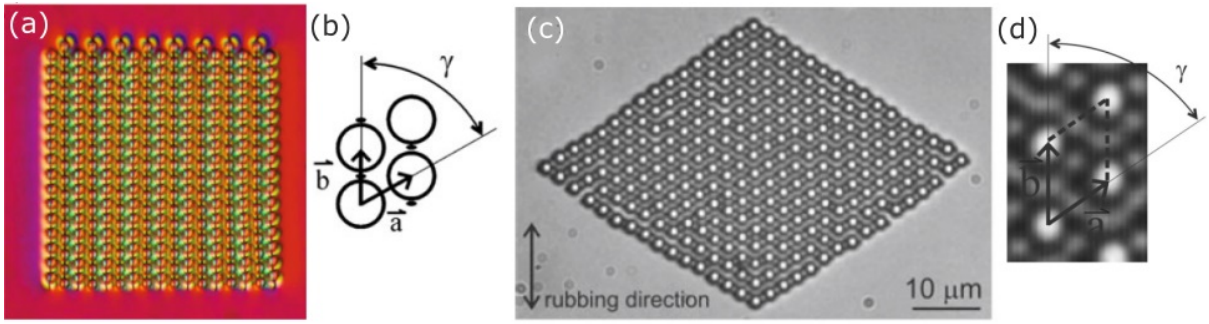

Figure 5.3: 2D nematic colloidal crystals. a) The lattice is made from antiparallel dipolar chains of silica particles. b) Unit cell of the dipolar colloidal crystal and lattice vectors separated by an angle $\gamma = 61° \pm 1°$. c) Quadrupolar nematic colloidal crystal, assembled by using the laser tweezers. d) Unit building block of the quadrupolar crystal is made from kinked chains ($\gamma = 56° \pm 1°$) where SR-SR interactions are repulsive. Unlike the dipolar colloidal crystal, the quadrupolar crystal is fragile and sometimes spontaneously desintegrates. Adapted from [192]

also from hybrid building blocks, such as those described in Fig. 5.4. There is a myriad of possible combinations that can be used to build robust 2D assemblies, where we can explore the effect of the topological connectors on the communication of interconnected active nematic emulsions.

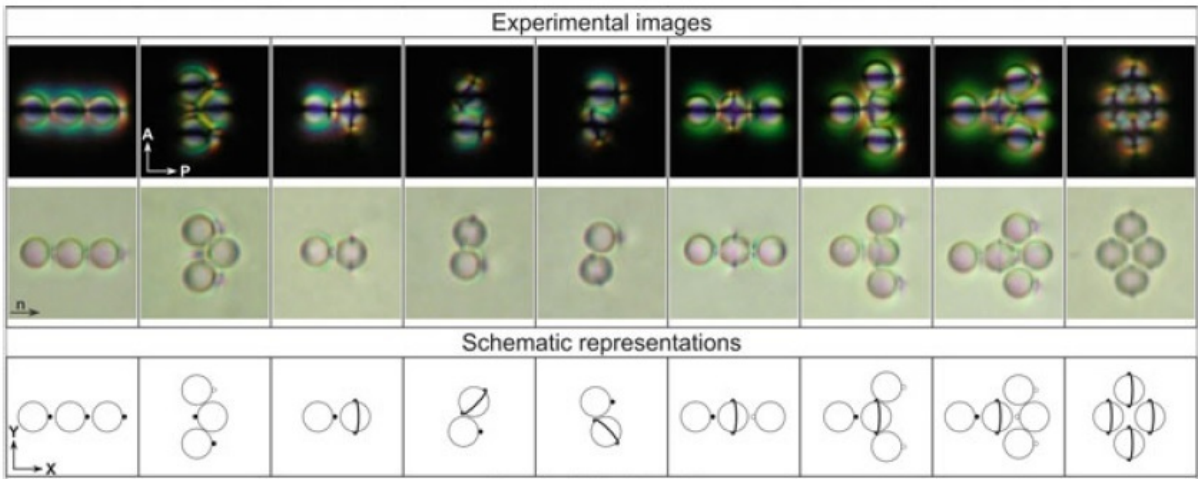

Figure 5.4: Microscopy images and schematic representation of possible dipole and quadrupole combinations. Adapted from [192]

The first goal in the near future will be thus to reproduce such structures, by replacing the hard colloids by AN droplets to bring the system out-of equilibrium. Second, we propose to study the dynamics of inter-particle defects to evaluate how droplets interact with each other within large assemblies. In this regard, we speculate that increasing the number of neighbor particles can have an important damping effect on the otherwise chaotic behavior observed for small dimers.

Additionally, we would like to study the oscillatory behavior of several active droplets woven into nematic braids. The latter consist of 1/2 disclination loops winding around several particles to form knotted crystallites, such as those represented in Fig. 5.5. Contrary to classical 2D or 3D assemblies, braids can contain more than one loop in multi-component links, as well as different crossing points between particles. Replicating these

patterns with active droplets will be thus interesting for probing the effect of the connectivity topology, as well the rotational symmetry in the oscillatory behavior of linked active emulsions. In fact, these parameters have been shown to be of paramount importance for modeling coupled oscillators and eventually achieving robust synchronized states[194].

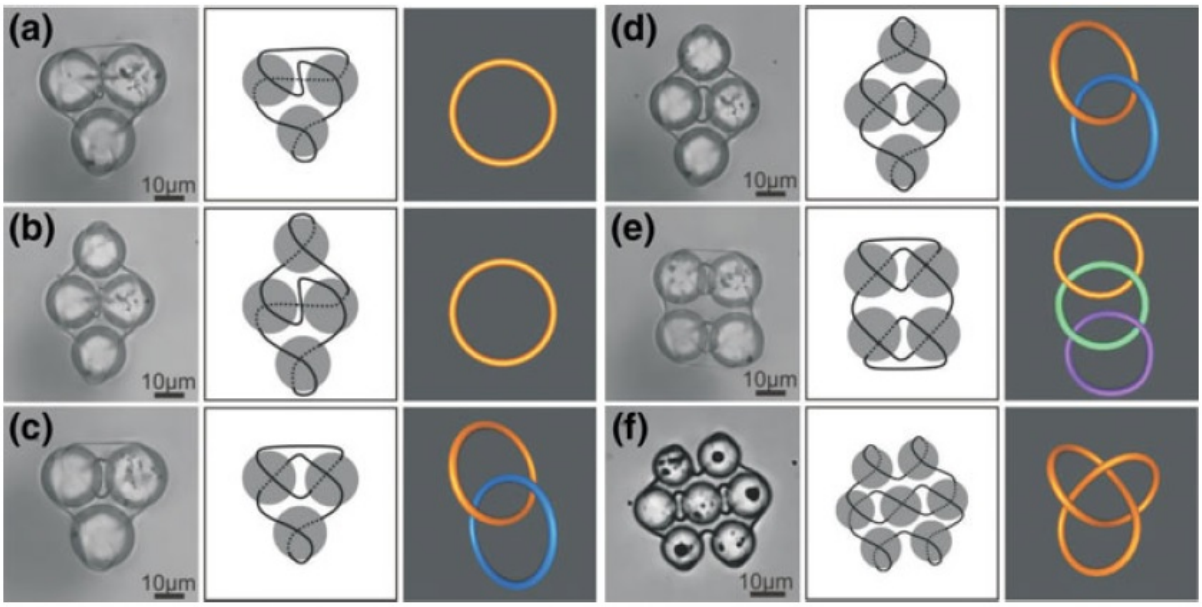

Figure 5.5: Entangled colloidal structures in a twisted cell. Cross-polarization images are shown on the left, their corresponding schematic representation in the middle and the minimized topological loop structure on the right. Adapted from[192]

A final suggestion in this topic would be the study of hierarchical active nematic assemblies. By this, we refer to the fabrication and characterization of networks or oligomers of active emulsions, such as those studied in section 4.2.5 , in which the droplets would not be monodisperse, but display significant size variations. One of our realizations is shown in Fig. 5.6. In this simple trimer, the diameter of the central droplet is almost twice larger than that of the lateral ones. Because of the difference in dimension, the encircling loops can oscillate at different amplitudes and, more importantly, at different frequencies. A promising direction for future work will thus be to deepen the understanding of the oscillatory behavior of these hierarchical assemblies and evaluate the effect of the droplet size on the coupling strength. Moreover, these results can inspire the design of a plethora of new structures involving complex combinations of droplets sizes, positions and topological connectors.

5.4 Active nematics on deformable geometries

The experiments described in section 3.4 have shown how active nematic flows adapt to the shape of the surface they inhabit. Notably, for fixed geometries such as spheres and ellipsoids, distinct regular dynamical patterns have been reported. Yet, much less is known on how active flows behave on deformable surfaces and on the way that shape distortions correlate with active stresses. In previous works by Kleber et al., these questions were explored for the first time by encapsulating the active material inside vesicles

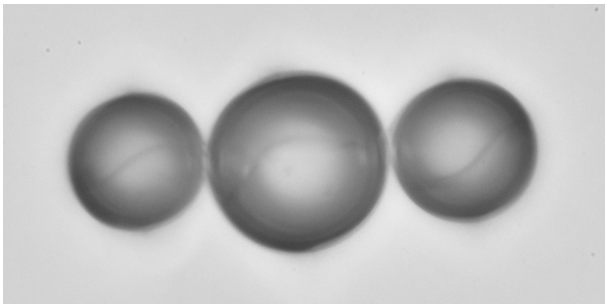

Figure 5.6: Polydisperse active nematic trimer. The diameter of the droplet in the center is twice larger than the one of the lateral droplets and dominates the motion of the assembly.

with diameters of the order of tens of microns. They demonstrated that due to the very low surface tension, the vesicle dramatically deforms under the active forces generated by the cortical active nematic flows. Specially, they highlighted the apparition of streaming filopodia-like protrusions tightly coupled to the dynamics of the underlying defects[136]. In parallel, simulations by Giomi et al. on active nematic droplets with low surface tension reported that the coupling between curvature and active stresses could result into more other types of deformation, motility and even to droplet division[195]. In 3D active nematic droplets, numerical investigations predicted an unprecedented range of complex morphologies, such as finger-like protrusions and surface wrinkles[196]. Lastly, the response of defects to changes in curvature for atypical spheroids has demonstrated significant deviations from the tetrahedral, minimal energy configuration[197].

We believe that an interesting strategy to explore the coupling between curvature and active stresses in vesicles could be using the method developed in chapter 3: instead of encapsulating the MTs mixture inside the vesicle, we suggest to immerse the vesicles inside the active solution. The advantage of this configuration is to have a higher availability of MTs around the sphere, so that they can form a denser nematic layer. Our intuition is that this density change can influence the active length scale of the active coating, modifying the way in which the spherical surface deforms. Eventually, this could lead to vesicle division and other dynamical states described by Giomi et al[195]. One of the principal challenges in this project is the preparation of giant vesicles of at least $30\mu m$ in diameter. In smaller vesicles, the surface curvature of surface bound MTs becomes too high as well as the energetic cost of confining the active material to the vesicle surface. As a consequence MTs may not be likely to adhere to the small surface, or if they do manage to, they may be unable to buckle or to move properly.
In the course of this PhD, we did many trials to produce and stabilize giant vesicles (GVs), with only partial success. For fabricating them, we employed a classical glass microfluidic device (Fig. 2.8) for oil-in-water (W/O/W) double emulsion production. The inner and outer phases were aqueous solutions containing surfactants, while the middle fluid was a $L-\alpha-phosphatidylcholine$ (Egg PC) lipid dissolved in a mixture of a highly volatile good solvent and a less volatile poor solvent. As shown in Movie 16, in the dripping regime, the middle phase wraps around the emulsion core to form the raw vesicle template. In a subsequent step, the bad solvent is supposed to gently de-wet from the double emulsions, forming the GVs. This last step usually occurs in a collection solution having the same osmolarity as the inner water core to prevent osmotic stress. Unfortunately, in our case it seemed that the dewetting mechanism was too abrupt and the vesicle membrane collapsed in less than 5 min after collection. Despite probing various surfactant solutions and oils in

the vesicle formulation, as well as many collection substances, we did not really manage to stabilize the giant emulsions long enough to be manipulated and mixed with the active material. To improve the stability of the vesicles, the composition and the nature of the membrane can be enhanced. For example, one can mix two or more lipids such as DOPC or other negatively charged lipids and cholesterol with specific functions in the middle phase[198]. The first compound provides faster monolayer assembly, while the second category controls membrane edge tension[199]. Other strategies include the use of block-copolymers instead of lipids to improve the permeability and flexibility of the vesicle membrane[200].

5.5 Conclusions

In this dissertation, we investigated the coupling between conventional passive liquid crystals (LCs) and active cytoskeletal nematics (ANs) in curved geometries. We explored two different scenarios: in the first one, droplets of passive LC were dispersed inside an aqueous phase containing the active material (LC/AN) (chapter 3), while in the second one, droplets of active nematic were dispersed inside a passive liquid crystal (AN/LC)(chapter 4).

The first configuration (LC/AN) was obtained from an original protocol involving: i) the fabrication of W/LC/W double emulsions by microfluidics, using a smectic LC as middle phase, ii) a thermally induced destabilisation of the double emulsions, which collapse into smectic LC droplets with non-spherical shapes, and iii) the dispersion of the smectic droplets inside the active solution, so that an AN layer forms on the surface of the droplets. Unlike traditional emulsions, the smectic droplets obtained with this process display a wide variety of polymorphic shapes with non-constant Gaussian curvature. In chapter 3, our main goal was to study how the presence of gradients of Gaussian curvature impacts the dynamics of active nematics. An extensive discussion was particularly dedicated to ellipsoidal systems, showing the existence of unprecedented spatio-temporal patterns: a transitory state with quadrupolar symmetry and a final state with dipolar symmetry. In both cases, the dynamics of the system are characterized by regular oscillations between a rotational and a translational regime, regulated by the motion of two pairs of topological defects. In the final state, during the rotational regime, a pair of $+1/2$ defects move on each pole of the ellipsoid, describing spiral trajectories. This regime is periodically interrupted by a bending instability that makes the defects migrate by pairs towards the opposite pole, what we have called the translational regime. By combining our experimental results with numerical simulations, we concluded that these new dynamical states stem from the cooperative action of several physico-chemical parameters. The main ones are the inhomogeneous Guassian curvature of the confining substrate, the viscous anisotropy imposed by the smectic structure of the droplet, and the hydrodynamic forces transmitted from the external medium. In an extension of this project, we considered ellipsoidal droplets with larger aspect-ratios, or droplets with more exotic shapes, such as sphero-cylinders and pear-shaped droplets. The more interesting behaviors were observed with the elongated ellipsoids, whose large surfaces enable to accommodate several rings of defect pairs at the equator in transient states, dividing the droplet surface into bands with alternating direction of rotation.

We used the second configuration (AN/LC) to investigate the dynamical solid-body behavior of both single AN droplets and groups of AN droplets connected via different topological links. In this case, the AN droplets were created *in-situ* by locally injecting small volumes of the active solution inside an aligned passive nematic liquid crystal (5CB). In the case of isolated droplets, we explored their diffusive behavior in the anisotropic environment provided by the liquid crystal. We showed that the symmetry of the director distortion around the particle determines the transport mode, as well as the direction and speed of the droplet motion. Elastic quadrupoles, characterized by an encircling SR disclination loop exhibited very slow displacement, mainly perpendicular to the far field orientation. Conversely, dipolar droplets, displaying a negatively charged point defect (hyperbolic hedgehog) near their surface, undergo rectilinear super-diffusion in the direction of the far-field director. Typical speeds of small self-propelled dipoles were of the order of $0.1\mu m/s$. Moreover, we analyzed the trajectories of the internal active defects and correlated them with the dynamics of the hyperbolic hedgehog sitting in the passive medium. We demonstrated that the typical oscillation period was of the same magnitude for both active and passive defects, meaning that the inner cortical flows regulated the oscillatory rhythms of the hedgehog in a similar way than in hexadecapolar active emulsions[170].

Finally, we developed robust experimental techniques to build a plethora of active oligomers in the LC, that is, chains of AN droplets linked by topological defects. The first strategy, inspired by previous works on passive nematic colloids, consists on quenching from the isotropic phase two or more neighboring droplets to form binding loops and knots between them. The second strategy relies on the fabrication of a disclination line running along a channel and acting as the backbone for the fabrication of an active necklace. The pearls of the necklace, *i.e.* the AN droplets, were added using high-precision injection techniques. With this technique, we can link together a larger number of droplets: the number of linked droplets is only limited by the length and stability of the disclination line. The active droplets, powered by their inner energy reservoir drove intriguing modes of oscillation in the external LC material, reflected by the persistent beating of the otherwise passive defects. Regardless of the type of entanglement, large oscillation frequencies in the active material led to uncorrelated oscillatory regimes. In contrast, for lower frequency oscillations, we observed consistent modes of local phase-synchronization. In particular, partial phase locking was observed in the regions of the loop facing each other: in the case of two droplets linked by defect line with the shape of a figure of eight, these regions were those close to the crossing point of the eight; in the case of the necklace, it corresponded to those parts of the line at the right and left regions of two consecutive droplets, respectively. A robust phase-amplitude synchronization could not be achieved everywhere in the active assemblies, or for many oscillation cycles because of an insufficient coupling strength. These results pave the way further studies in this new field of "active nematic colloids". More research needs to be done to elucidate the exact origin of the LC-mediated partial synchronisation that we observed between AN droplets in order to increase the coupling between the active and passive liquid crystals.

As the popular saying goes "a picture is worth a thousand words", we would like to summarize the main research work performed during these last years by the following figure, representing in a simple manner the principal protocols and results described in this dissertation.

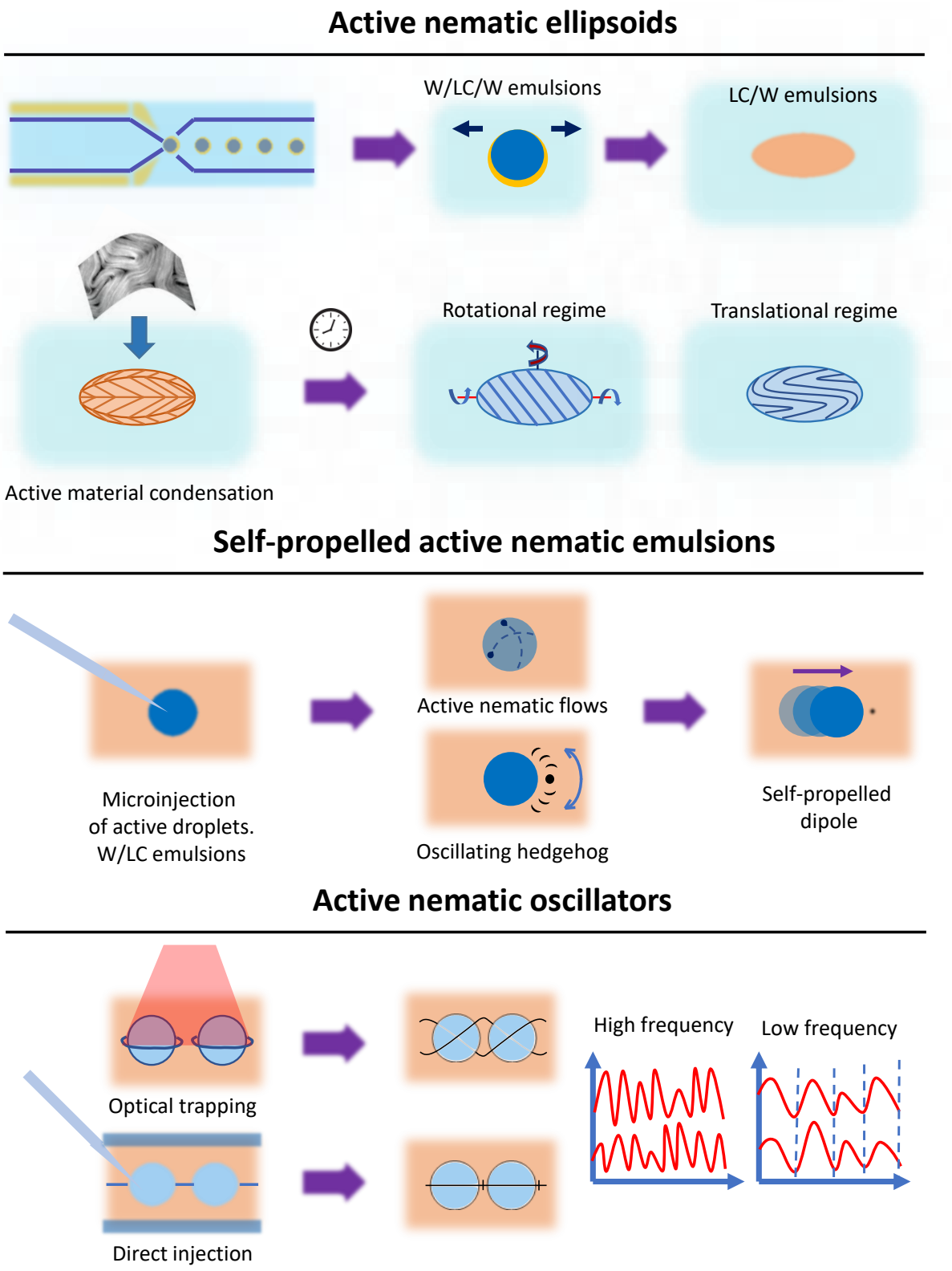
Active nematic ellipsoids
W/LC/W emulsions
LC/W emulsions
Rotational regime
Translational regime
Active material condensation
Self-propelled active nematic emulsions
Active nematic flows
Microinjection
of active droplets.
W/LC emulsions
Oscillating hedgehog
Self-propelled
dipole
Active nematic oscillators
High frequency
Low frequency
Optical trapping
Direct injection

BIBLIOGRAPHY

[1] Patrick Oswald and Pawel Pieranski. *Nematic and Cholesteric Liquid Crystals: Concepts and Physical Properties Illustrated by Experiments*. CRC Press, Boca Raton, February 2005. ISBN 978-0-429-21574-2. doi: 10.1201/9780203023013.

[2] Guillaume Durey. *Stripes, Fingers and Skyrmions: Taming Cholesteric Liquid Crystal Shells under Perpendicular Anchoring*. PhD thesis, 2018.

[3] Lin Lei. Bowlic Liquid Crystalsl. *Molecular Crystals and Liquid Crystals*, 146(1): 41–54, May 1987. ISSN 0026-8941. doi: 10.1080/00268948708071801.

[4] Dipti Sharma. Non-isothermal kinetics of melting and nematic to isotropic phase transitions of 5CB liquid crystal. *J Therm Anal Calorim*, 102(2):627–632, November 2010. ISSN 1572-8943. doi: 10.1007/s10973-010-0837-2.

[5] P. G. de Gennes and J. Prost. *The Physics of Liquid Crystals*. International Series of Monographs on Physics. Oxford University Press, Oxford, New York, second edition edition, April 1995. ISBN 978-0-19-851785-6.

[6] B. Jerome. Surface effects and anchoring in liquid crystals. *Rep. Prog. Phys.*, 54 (3):391–451, March 1991. ISSN 0034-4885. doi: 10.1088/0034-4885/54/3/002.

[7] Elasticity of Mesomorphic Phases. In Maurice Kleman and Oleg D. Lavrentovich, editors, *Soft Matter Physics: An Introduction*, pages 135–183. Springer, New York, NY, 2003. ISBN 978-0-387-21759-8. doi: 10.1007/978-0-387-21759-8_5.

[8] P. M. Chaikin and T. C. Lubensky. Principles of Condensed Matter Physics, June 1995.

[9] F. C. Frank. I. Liquid crystals. On the theory of liquid crystals. *Discuss. Faraday Soc.*, 25(0):19–28, January 1958. ISSN 0366-9033. doi: 10.1039/DF9582500019.

[10] Oleg Lavrentovich, Paolo Pasini, Claudio Zannoni, and Slobodan Zumer, editors. *Defects in Liquid Crystals: Computer Simulations, Theory and Experiments*. Nato Science Series II:. Springer Netherlands, 2001. ISBN 978-1-4020-0169-7. doi: 10.1007/978-94-010-0512-8.

[11] Mikhail V. Kurik and O. D. Lavrentovich. Defects in liquid crystals: Homotopy theory and experimental studies. *Sov. Phys. Usp.*, 31(3):196, March 1988. ISSN 0038-5670. doi: 10.1070/PU1988v031n03ABEH005710.

[12] O. D. Lavrentovich. Nematic Liquid Crystals: Defects. In K. H. Jürgen Buschow, Robert W. Cahn, Merton C. Flemings, Bernhard Ilschner, Edward J. Kramer, Subhash Mahajan, and Patrick Veyssière, editors, *Encyclopedia of Materials: Science and Technology*, pages 6071–6075. Elsevier, Oxford, January 2001. ISBN 978-0-08-043152-9. doi: 10.1016/B0-08-043152-6/01072-X.

[13] Fumito Araoka, Khoa V. Le, Shuji Fujii, Hiroshi Orihara, and Yuji Sasaki. Polymer-stabilized liquid crystalline topological defect network for micro-pixelated optical devices. In *Emerging Liquid Crystal Technologies XIII*, volume 10555, page 1055504. International Society for Optics and Photonics, February 2018. doi: 10.1117/12.2299505.

[14] Anja Pusovnik, Jure Aplinc, and Miha Ravnik. Optical properties of metamaterial split ring nematic colloids. *Scientific Reports*, 9(1):7025, May 2019. ISSN 2045-2322. doi: 10.1038/s41598-019-43470-6.

[15] Igor Muševič, Miha Škarabot, Uroš Tkalec, Miha Ravnik, and Slobodan Žumer. Two-Dimensional Nematic Colloidal Crystals Self-Assembled by Topological Defects. *Science*, 313(5789):954–958, August 2006. ISSN 0036-8075, 1095-9203. doi: 10.1126/science.1129660.

[16] S. Trickey, editor. *Quantum Fluids and Solids*. Springer US, 1977. ISBN 978-1-4684-2420-1. doi: 10.1007/978-1-4684-2418-8.

[17] O. D. LAVRENTOVICH. Topological defects in dispersed words and worlds around liquid crystals, or liquid crystal drops. *Liquid Crystals*, 24(1):117–126, January 1998. ISSN 0267-8292. doi: 10.1080/026782998207640.

[18] Igor Muševič. *Liquid Crystal Colloids*. Soft and Biological Matter. Springer International Publishing, 2017. ISBN 978-3-319-54914-9. doi: 10.1007/978-3-319-54916-3.

[19] Jürgen Nehring and Alfred Saupe. On the schlieren texture in nematic and smectic liquid crystals. *J. Chem. Soc., Faraday Trans. 2*, 68(0):1–15, January 1972. ISSN 0300-9238. doi: 10.1039/F29726800001.

[20] V. S. U. FAZIO, L. KOMITOV, and S. T. LAGERWALL. Alignment and alignment dynamics of nematic liquid crystals on Langmuir-Blodgett mono-layers. *Liquid Crystals*, 24(3):427–433, March 1998. ISSN 0267-8292. doi: 10.1080/026782998207253.

[21] Núria Petit-Garrido, Rahul P. Trivedi, Jordi Ignés-Mullol, Josep Claret, Clayton Lapointe, Francesc Sagués, and Ivan I. Smalyukh. Healing of defects at the interface of nematic liquid crystals and structured Langmuir-Blodgett monolayers. *Phys Rev Lett*, 107(17):177801, October 2011. ISSN 1079-7114. doi: 10.1103/PhysRevLett.107.177801.

[22] Mengfei Wang, Yannian Li, and Hiroshi Yokoyama. Artificial web of disclination lines in nematic liquid crystals. *Nature Communications*, 8(1):388, August 2017. ISSN 2041-1723. doi: 10.1038/s41467-017-00548-x.

[23] Pau Guillamat, Francesc Sagués, and Jordi Ignés-Mullol. Electric-field modulation of liquid crystal structures in contact with structured surfactant monolayers. *Phys Rev E Stat Nonlin Soft Matter Phys*, 89(5):052510, May 2014. ISSN 1550-2376. doi: 10.1103/PhysRevE.89.052510.

[24] John J. Sandford O'Neill, Patrick S. Salter, Martin J. Booth, Steve J. Elston, and Stephen M. Morris. Electrically-tunable positioning of topological defects in liquid crystals. *Nature Communications*, 11(1):2203, May 2020. ISSN 2041-1723. doi: 10.1038/s41467-020-16059-1.

[25] S Hyde, Z Blum, T Landh, S Lidin, B.W Ninham, S Andersson, and K Larsson. *The Language of Shape: The Role of Curvature in Condensed Matter Physics*. Elsevier Science, first edition, 1996.

[26] Mark J. Bowick and Luca Giomi. Two-dimensional matter: Order, curvature and defects. *Advances in Physics*, 58(5):449–563, September 2009. ISSN 0001-8732. doi: 10.1080/00018730903043166.

[27] T. Maquart. Disk-sphere field duality theorem. 2018.

[28] Jérôme Hardoüin, Francesc Sagués, and Jordi Ignés. *Active Liquid Crystals in Confinement*. PhD thesis, Universitat de Barcelona, 2019.

[29] Oleg D. Lavrentovich. Transport of particles in liquid crystals. *Soft Matter*, 10(9): 1264–1283, February 2014. ISSN 1744-6848. doi: 10.1039/C3SM51628H.

[30] null Poulin, null Stark, null Lubensky, and null Weitz. Novel Colloidal Interactions in Anisotropic Fluids. *Science*, 275(5307):1770–1773, March 1997. ISSN 1095-9203. doi: 10.1126/science.275.5307.1770.

[31] E. M. Terentjev. Disclination loops, standing alone and around solid particles, in nematic liquid crystals. *Phys. Rev. E*, 51(2):1330–1337, February 1995. doi: 10.1103/PhysRevE.51.1330.

[32] H. Stark. Director field configurations around a spherical particle in a nematic liquid crystal. *Eur. Phys. J. B*, 10(2):311–321, May 1999. ISSN 1434-6036. doi: 10.1007/s100510050860.

[33] H. Stark and D. Ventzki. Non-linear Stokes drag of spherical particles in a nematic solvent. 2002. doi: 10.1209/EPL/I2002-00541-0.

[34] O. Mondain-Monval, J.C. Dedieu, T. Gulik-Krzywicki, and P. Poulin. Weak surface energy in nematic dispersions: Saturn ring defects and quadrupolar interactions. *Eur. Phys. J. B*, 12(2):167–170, November 1999. ISSN 1434-6036. doi: 10.1007/s100510050992.

[35] Yuedong Gu and Nicholas L. Abbott. Observation of Saturn-Ring Defects around Solid Microspheres in Nematic Liquid Crystals. *Phys. Rev. Lett.*, 85(22):4719–4722, November 2000. doi: 10.1103/PhysRevLett.85.4719.

[36] C. Völtz, Y. Maeda, Y. Tabe, and H. Yokoyama. Director-Configurational Transitions around Microbubbles of Hydrostatically Regulated Size in Liquid Crystals. *Phys. Rev. Lett.*, 97(22):227801, November 2006. doi: 10.1103/PhysRevLett.97.227801.

[37] Bohdan Senyuk, Jure Aplinc, Miha Ravnik, and Ivan I. Smalyukh. High-order elastic multipoles as colloidal atoms. *Nature Communications*, 10(1):1825, April 2019. ISSN 2041-1723. doi: 10.1038/s41467-019-09777-8.

[38] Ye Zhou, Bohdan Senyuk, Rui Zhang, Ivan I. Smalyukh, and Juan J. de Pablo. Degenerate conic anchoring and colloidal elastic dipole-hexadecapole transformations. *Nature Communications*, 10(1):1000, March 2019. ISSN 2041-1723. doi: 10.1038/s41467-019-08645-9.

[39] Bohdan Senyuk, Owen Puls, Oleh M. Tovkach, Stanislav B. Chernyshuk, and Ivan I. Smalyukh. Hexadecapolar colloids. *Nature Communications*, 7(1):10659, February 2016. ISSN 2041-1723. doi: 10.1038/ncomms10659.

[40] T. C. Lubensky, David Pettey, Nathan Currier, and Holger Stark. Topological defects and interactions in nematic emulsions. *Phys. Rev. E*, 57(1):610–625, January 1998. doi: 10.1103/PhysRevE.57.610.

[41] F. Brochard and P. G. de Gennes. Theory of magnetic suspensions in liquid crystals. *J. Phys. France*, 31(7):691–708, July 1970. ISSN 0302-0738. doi: 10.1051/jphys:01970003107069100.

[42] Markus Kreuzer, Theo Tschudi, and Rudolf Eidenschink. Erasable Optical Storage in Bistable Liquid Crystal Cells. *Molecular Crystals and Liquid Crystals Science and Technology. Section A. Molecular Crystals and Liquid Crystals*, 223(1):219–227, January 1992. ISSN 1058-725X. doi: 10.1080/15421409208048253.

[43] Jurij Kotar, Mojca Vilfan, Natan Osterman, Dušan Babič, Martin Čopič, and Igor Poberaj. Interparticle Potential and Drag Coefficient in Nematic Colloids. *Phys. Rev. Lett.*, 96(20):207801, May 2006. doi: 10.1103/PhysRevLett.96.207801.

[44] R. W. Ruhwandl and E. M. Terentjev. Monte Carlo simulation of topological defects in the nematic liquid crystal matrix around a spherical colloid particle. *Phys. Rev. E*, 56(5):5561–5565, November 1997. doi: 10.1103/PhysRevE.56.5561.

[45] M. Škarabot, M. Ravnik, S. Žumer, U. Tkalec, I. Poberaj, D. Babič, N. Osterman, and I. Muševič. Interactions of quadrupolar nematic colloids. *Phys. Rev. E*, 77(3):031705, March 2008. doi: 10.1103/PhysRevE.77.031705.

[46] M. Ravnik, M. Skarabot, S. Zumer, U. Tkalec, I. Poberaj, D. Babic, N. Osterman, and I. Musevic. Entangled nematic colloidal dimers and wires. *Phys Rev Lett*, 99(24):247801, December 2007. ISSN 0031-9007. doi: 10.1103/PhysRevLett.99.247801.

[47] R. W. Ruhwandl and E. M. Terentjev. Friction drag on a particle moving in a nematic liquid crystal. *Phys. Rev. E*, 54(5):5204–5210, November 1996. doi: 10.1103/PhysRevE.54.5204.

[48] Holger Stark and Dieter Ventzki. Stokes drag of spherical particles in a nematic environment at low Ericksen numbers. *Phys. Rev. E*, 64(3):031711, August 2001. doi: 10.1103/PhysRevE.64.031711.

[49] J. C. Loudet, P. Hanusse, and P. Poulin. Stokes Drag on a Sphere in a Nematic Liquid Crystal. *Science*, 306(5701):1525–1525, November 2004. ISSN 0036-8075, 1095-9203. doi: 10.1126/science.1102864.

[50] Mohammad Mydul Alam and Raffaele Mezzenga. Particle Tracking Microrheology of Lyotropic Liquid Crystals. *Langmuir*, 27(10):6171–6178, May 2011. ISSN 0743-7463. doi: 10.1021/la200116e.

[51] I. I. Smalyukh, S. Chernyshuk, B. I. Lev, A. B. Nych, U. Ognysta, V. G. Nazarenko, and O. D. Lavrentovich. Ordered Droplet Structures at the Liquid Crystal Surface and Elastic-Capillary Colloidal Interactions. *Phys. Rev. Lett.*, 93(11):117801, September 2004. doi: 10.1103/PhysRevLett.93.117801.

[52] R. Ganapathy, A. K. Sood, and S. Ramaswamy. Superdiffusion of concentration in wormlike-micelle solutions. *EPL*, 77(1):18007, January 2007. ISSN 0295-5075. doi: 10.1209/0295-5075/77/18007.

[53] Josep M. Pagès, Jordi Ignés-Mullol, and Francesc Sagués. Anomalous Diffusion of Motile Colloids Dispersed in Liquid Crystals. *Phys. Rev. Lett.*, 122(19):198001, May 2019. doi: 10.1103/PhysRevLett.122.198001.

[54] Jaime Ortega Arroyo. Anomalous Diffusion Due to Interleaflet Coupling and Molecular Pinning. In Jaime Ortega Arroyo, editor, *Investigation of Nanoscopic Dynamics and Potentials by Interferometric Scattering Microscopy*, Springer Theses, pages 59–79. Springer International Publishing, Cham, 2018. ISBN 978-3-319-77095-6. doi: 10.1007/978-3-319-77095-6_4.

[55] T. Turiv, I. Lazo, A. Brodin, B. I. Lev, V. Reiffenrath, V. G. Nazarenko, and O. D. Lavrentovich. Effect of Collective Molecular Reorientations on Brownian Motion of Colloids in Nematic Liquid Crystal. *Science*, 342(6164):1351–1354, December 2013. ISSN 0036-8075, 1095-9203. doi: 10.1126/science.1240591.

[56] Rui Zhang, Ali Mozaffari, and Juan J. de Pablo. Autonomous materials systems from active liquid crystals. *Nature Reviews Materials*, 6(5):437–453, May 2021. ISSN 2058-8437. doi: 10.1038/s41578-020-00272-x.

[57] Oleg D. Lavrentovich. Active colloids in liquid crystals. *Current Opinion in Colloid & Interface Science*, 21:97–109, February 2016. ISSN 1359-0294. doi: 10.1016/j.cocis.2015.11.008.

[58] Dinesh Kumar Sahu, Swapnil Kole, Sriram Ramaswamy, and Surajit Dhara. Omnidirectional transport and navigation of Janus particles through a nematic liquid crystal film. *Phys. Rev. Research*, 2(3):032009, July 2020. doi: 10.1103/PhysRevResearch.2.032009.

[59] Sergi Hernàndez-Navarro, Pietro Tierno, Jordi Ignés-Mullol, and Francesc Sagués. AC electrophoresis of microdroplets in anisotropic liquids: Transport, assembling and reaction. *Soft Matter*, 9(33):7999–8004, July 2013. ISSN 1744-6848. doi: 10.1039/C3SM51705E.

[60] Ivan I. Smalyukh, John Butler, Joshua D. Shrout, Matthew R. Parsek, and Gerard C. L. Wong. Elasticity-mediated nematiclike bacterial organization in model extracellular DNA matrix. *Phys Rev E Stat Nonlin Soft Matter Phys*, 78(3 Pt 1): 030701, September 2008. ISSN 1539-3755. doi: 10.1103/PhysRevE.78.030701.

[61] Anil Kumar, Tigran Galstian, Sudip K. Pattanayek, and Simon Rainville. The Motility of Bacteria in an Anisotropic Liquid Environment. *Molecular Crystals and Liquid Crystals*, 574(1):33–39, May 2013. ISSN 1542-1406. doi: 10.1080/15421406.2012.762493.

[62] Shuang Zhou, Andrey Sokolov, Oleg D. Lavrentovich, and Igor S. Aranson. Living liquid crystals. *PNAS*, 111(4):1265–1270, January 2014. ISSN 0027-8424, 1091-6490. doi: 10.1073/pnas.1321926111.

[63] John Toner, Hartmut Löwen, and Henricus H. Wensink. Following fluctuating signs: Anomalous active superdiffusion of swimmers in anisotropic media. *Phys. Rev. E*, 93(6):062610, June 2016. doi: 10.1103/PhysRevE.93.062610.

[64] Gabriel Ramos, María Luisa Cordero, and Rodrigo Soto. Bacteria driving droplets. *Soft Matter*, 16(5):1359–1365, February 2020. ISSN 1744-6848. doi: 10.1039/c9sm01839e.

[65] Mojtaba Rajabi, Hend Baza, Taras Turiv, and Oleg D. Lavrentovich. Directional self-locomotion of active droplets enabled by nematic environment. *Nat. Phys.*, 17(2):260–266, February 2021. ISSN 1745-2473, 1745-2481. doi: 10.1038/s41567-020-01055-5.

[66] J. S. Lintuvuori, A. Würger, and K. Stratford. Hydrodynamics Defines the Stable Swimming Direction of Spherical Squirmers in a Nematic Liquid Crystal. *Phys Rev Lett*, 119(6):068001, August 2017. ISSN 1079-7114. doi: 10.1103/PhysRevLett.119.068001.

[67] Abdallah Daddi-Moussa-Ider and Andreas M. Menzel. Dynamics of a simple model microswimmer in an anisotropic fluid: Implications for alignment behavior and active transport in a nematic liquid crystal. *Phys. Rev. Fluids*, 3(9):094102, September 2018. doi: 10.1103/PhysRevFluids.3.094102.

[68] Hai Chi, Mykhailo Potomkin, Lei Zhang, Leonid Berlyand, and Igor S. Aranson. Surface anchoring controls orientation of a microswimmer in nematic liquid crystal. *Communications Physics*, 3(1):162, December 2020. doi: 10.1038/s42005-020-00432-z.

[69] Stephan Herminghaus, Corinna C. Maass, Carsten Krüger, Shashi Thutupalli, Lucas Goehring, and Christian Bahr. Interfacial mechanisms in active emulsions. *Soft Matter*, 10(36):7008–7022, August 2014. ISSN 1744-6848. doi: 10.1039/C4SM00550C.

[70] Tim Sanchez, Daniel T. N. Chen, Stephen J. DeCamp, Michael Heymann, and Zvonimir Dogic. Spontaneous motion in hierarchically assembled active matter. *Nature*, 491(7424):431–434, November 2012. ISSN 1476-4687. doi: 10.1038/nature11591.

[71] X. L. Wu and A. Libchaber. Particle diffusion in a quasi-two-dimensional bacterial bath. *Phys Rev Lett*, 84(13):3017–3020, March 2000. ISSN 0031-9007. doi: 10.1103/PhysRevLett.84.3017.

[72] Tamás Vicsek, András Czirók, Eshel Ben-Jacob, Inon Cohen, and Ofer Shochet. Novel Type of Phase Transition in a System of Self-Driven Particles. *Phys. Rev. Lett.*, 75(6):1226–1229, August 1995. doi: 10.1103/PhysRevLett.75.1226.

[73] Chenhui Peng, Taras Turiv, Yubing Guo, Qi-Huo Wei, and Oleg D. Lavrentovich. Command of active matter by topological defects and patterns. *Science*, 354(6314):882–885, November 2016. ISSN 0036-8075, 1095-9203. doi: 10.1126/science.aah6936.

[74] Christopher Dombrowski, Luis Cisneros, Sunita Chatkaew, Raymond E. Goldstein, and John O. Kessler. Self-Concentration and Large-Scale Coherence in Bacterial Dynamics. *Phys. Rev. Lett.*, 93(9):098103, August 2004. doi: 10.1103/PhysRevLett.93.098103.

[75] Matthias Mussler, Salima Rafai, Philippe Peyla, and Christian Wagner. Effective viscosity of non-gravitactic Chlamydomonas Reinhardtii microswimmer suspensions. *EPL*, 101(5):54004, March 2013. ISSN 0295-5075, 1286-4854. doi: 10.1209/0295-5075/101/54004.

[76] D. Marenduzzo, E. Orlandini, and J. M. Yeomans. Hydrodynamics and Rheology of Active Liquid Crystals: A Numerical Investigation. *Phys. Rev. Lett.*, 98(11):118102, March 2007. doi: 10.1103/PhysRevLett.98.118102.

[77] Shape oscillations of non-adhering fibroblast cells - IOPscience. https://iopscience.iop.org/article/10.1088/1478-3975/4/4/004/pdf.

[78] M. C. Marchetti, J.-F. Joanny, S. Ramaswamy, T. B. Liverpool, J. Prost, Madan Rao, and R. Aditi Simha. Soft Active Matter. http://arxiv.org/abs/1207.2929, July 2012.

[79] Peng Liu, Hongwei Zhu, Ying Zeng, Guangle Du, Luhui Ning, Dunyou Wang, Ke Chen, Ying Lu, Ning Zheng, Fangfu Ye, and Mingcheng Yang. Oscillating collective motion of active rotors in confinement. *PNAS*, 117(22):11901–11907, June 2020. ISSN 0027-8424, 1091-6490. doi: 10.1073/pnas.1922633117.

[80] Vijay Narayan, Sriram Ramaswamy, and Narayanan Menon. Long-lived giant number fluctuations in a swarming granular nematic. *Science*, 317(5834):105–108, July 2007. ISSN 1095-9203. doi: 10.1126/science.1140414.

[81] Walter F. Paxton, Kevin C. Kistler, Christine C. Olmeda, Ayusman Sen, Sarah K. St. Angelo, Yanyan Cao, Thomas E. Mallouk, Paul E. Lammert, and Vincent H. Crespi. Catalytic Nanomotors: Autonomous Movement of Striped Nanorods. *J. Am. Chem. Soc.*, 126(41):13424–13431, October 2004. ISSN 0002-7863. doi: 10.1021/ja047697z.

[82] Antoine Bricard, Jean-Baptiste Caussin, Nicolas Desreumaux, Olivier Dauchot, and Denis Bartolo. Emergence of macroscopic directed motion in populations of motile colloids. *Nature*, 503(7474):95–98, November 2013. ISSN 1476-4687. doi: 10.1038/nature12673.

[83] John Toner, Yuhai Tu, and Sriram Ramaswamy. Hydrodynamics and phases of flocks. *Annals of Physics*, 318(1):170–244, July 2005. ISSN 0003-4916. doi: 10.1016/j.aop.2005.04.011.

[84] Tamás Vicsek, András Czirók, Eshel Ben-Jacob, Inon Cohen, and Ofer Shochet. Novel Type of Phase Transition in a System of Self-Driven Particles. *Phys. Rev. Lett.*, 75(6):1226–1229, August 1995. doi: 10.1103/PhysRevLett.75.1226.

[85] Michael Rubenstein, Alejandro Cornejo, and Radhika Nagpal. Programmable self-assembly in a thousand-robot swarm. *Science*, 345(6198):795–799, August 2014. ISSN 0036-8075, 1095-9203. doi: 10.1126/science.1254295.

[86] Christian Scholz, Michael Engel, and Thorsten Pöschel. Rotating robots move collectively and self-organize. *Nature Communications*, 9(1):931, March 2018. ISSN 2041-1723. doi: 10.1038/s41467-018-03154-7.

[87] J. Buhl, D. J. T. Sumpter, I. D. Couzin, J. J. Hale, E. Despland, E. R. Miller, and S. J. Simpson. From disorder to order in marching locusts. *Science*, 312(5778):1402–1406, June 2006. ISSN 1095-9203. doi: 10.1126/science.1125142.

[88] John Toner and Yuhai Tu. Long-Range Order in a Two-Dimensional Dynamical XY Model: How Birds Fly Together. *Phys. Rev. Lett.*, 75(23):4326–4329, December 1995. doi: 10.1103/PhysRevLett.75.4326.

[89] M. Ballerini, N. Cabibbo, R. Candelier, A. Cavagna, E. Cisbani, I. Giardina, V. Lecomte, A. Orlandi, G. Parisi, A. Procaccini, M. Viale, and V. Zdravkovic. Interaction ruling animal collective behavior depends on topological rather than metric distance: Evidence from a field study. *PNAS*, 105(4):1232–1237, January 2008. ISSN 0027-8424, 1091-6490. doi: 10.1073/pnas.0711437105.

[90] Gerhard Gompper, Roland G. Winkler, Thomas Speck, Alexandre Solon, Cesare Nardini, Fernando Peruani, Hartmut Löwen, Ramin Golestanian, U. Benjamin Kaupp, Luis Alvarez, Thomas Kiørboe, Eric Lauga, Wilson C. K. Poon, Antonio DeSimone, Santiago Muiños-Landin, Alexander Fischer, Nicola A. Söker, Frank Cichos, Raymond Kapral, Pierre Gaspard, Marisol Ripoll, Francesc Sagues, Amin Doostmohammadi, Julia M. Yeomans, Igor S. Aranson, Clemens Bechinger, Holger Stark, Charlotte K. Hemelrijk, François J. Nedelec, Trinish Sarkar, Thibault Aryaksama, Mathilde Lacroix, Guillaume Duclos, Victor Yashunsky, Pascal Silberzan, Marino Arroyo, and Sohan Kale. The 2020 motile active matter roadmap. *J. Phys.: Condens. Matter*, 32(19):193001, February 2020. ISSN 0953-8984. doi: 10.1088/1361-648X/ab6348.

[91] Stephen J. DeCamp, Gabriel S. Redner, Aparna Baskaran, Michael F. Hagan, and Zvonimir Dogic. Orientational Order of Motile Defects in Active Nematics. *Nat Mater*, 14(11):1110–1115, November 2015. ISSN 1476-1122. doi: 10.1038/nmat4387.

[92] Song Liu, Suraj Shankar, M. Cristina Marchetti, and Yilin Wu. Viscoelastic control of spatiotemporal order in bacterial active matter. *Nature*, 590(7844):80–84, February 2021. ISSN 1476-4687. doi: 10.1038/s41586-020-03168-6.

[93] D. Dell'Arciprete, M. L. Blow, A. T. Brown, F. D. C. Farrell, J. S. Lintuvuori, A. F. McVey, D. Marenduzzo, and W. C. K. Poon. A growing bacterial colony in two dimensions as an active nematic. *Nature Communications*, 9(1):1–9, October 2018. ISSN 2041-1723. doi: 10.1038/s41467-018-06370-3.

[94] R. Kemkemer, V. Teichgräber, S. Schrank-Kaufmann, D. Kaufmann, and H. Gruler. Nematic order-disorder state transition in a liquid crystal analogue formed by oriented and migrating amoeboid cells. *Eur. Phys. J. E*, 3(2):101–110, October 2000. ISSN 1292-8941. doi: 10.1007/s101890070023.

[95] Kyogo Kawaguchi, Ryoichiro Kageyama, and Masaki Sano. Topological defects control collective dynamics in neural progenitor cell cultures. *Nature*, 545(7654): 327–331, May 2017. ISSN 1476-4687. doi: 10.1038/nature22321.

[96] Robert Blackwell, Oliver Sweezy-Schindler, Christopher Baldwin, Loren E. Hough, Matthew A. Glaser, and M. D. Betterton. Microscopic origins of anistropic active stress in motor-driven nematic liquid crystals. *Soft Matter*, 12(10):2676–2687, March 2016. ISSN 1744-683X. doi: 10.1039/c5sm02506k.

[97] Apala Majumdar, Marchetti M. Cristina, and Epifanio G. Virga. Perspectives in active liquid crystals. *Philos Trans A Math Phys Eng Sci*, 372(2029), November 2014. ISSN 1364-503X. doi: 10.1098/rsta.2013.0373.

[98] Luca Giomi, Mark J Bowick, Prashant Mishra, Rastko Sknepnek, and M Cristina Marchetti. Defect dynamics in active nematics. *Philos Trans A Math Phys Eng Sci*, 372(2029), November 2014. ISSN 1364-503X. doi: 10.1098/rsta.2013.0365.

[99] Laura R. Serbus, Byeong-Jik Cha, William E. Theurkauf, and William M. Saxton. Dynein and the actin cytoskeleton control kinesin-driven cytoplasmic streaming in Drosophila oocytes. *Development*, 132(16):3743–3752, August 2005. ISSN 0950-1991, 1477-9129. doi: 10.1242/dev.01956.

[100] Peter D. Olmsted. Perspectives on shear banding in complex fluids. *Rheol Acta*, 47 (3):283–300, April 2008. ISSN 1435-1528. doi: 10.1007/s00397-008-0260-9.

[101] Buddhapriya Chakrabarti, Moumita Das, Chandan Dasgupta, Sriram Ramaswamy, and A. K. Sood. Spatiotemporal Rheochaos in Nematic Hydrodynamics. *Phys. Rev. Lett.*, 92(5):055501, February 2004. doi: 10.1103/PhysRevLett.92.055501.

[102] R. Voituriez, J. F. Joanny, and J. Prost. Spontaneous flow transition in active polar gels. *EPL*, 70(3):404, April 2005. ISSN 0295-5075. doi: 10.1209/epl/i2004-10501-2.

[103] S. A. Edwards and J. M. Yeomans. Spontaneous flow states in active nematics: A unified picture. *EPL*, 85(1):18008, January 2009. ISSN 0295-5075. doi: 10.1209/0295-5075/85/18008.

[104] Luca Giomi, M. Cristina Marchetti, and Tanniemola B. Liverpool. Complex Spontaneous Flows and Concentration Banding in Active Polar Films. *Phys. Rev. Lett.*, 101(19):198101, November 2008. doi: 10.1103/PhysRevLett.101.198101.

[105] Sumesh P. Thampi, Ramin Golestanian, and Julia M. Yeomans. Instabilities and topological defects in active nematics. *EPL*, 105(1):18001, January 2014. ISSN 0295-5075. doi: 10.1209/0295-5075/105/18001.

[106] Berta Martínez-Prat, Jordi Ignés-Mullol, Jaume Casademunt, and Francesc Sagués. Selection mechanism at the onset of active turbulence. *Nature Physics*, 15(4): 362–366, April 2019. ISSN 1745-2481. doi: 10.1038/s41567-018-0411-6.

[107] Jörn Dunkel, Sebastian Heidenreich, Knut Drescher, Henricus H. Wensink, Markus Bär, and Raymond E. Goldstein. Fluid Dynamics of Bacterial Turbulence. *Phys. Rev. Lett.*, 110(22):228102, May 2013. doi: 10.1103/PhysRevLett.110.228102.

[108] Luca Giomi. Geometry and Topology of Turbulence in Active Nematics. *Phys. Rev. X*, 5(3):031003, July 2015. doi: 10.1103/PhysRevX.5.031003.

[109] P. Guillamat, J. Ignés-Mullol, and F. Sagués. Taming active turbulence with patterned soft interfaces. *Nature Communications*, 8(1):564, September 2017. ISSN 2041-1723. doi: 10.1038/s41467-017-00617-1.

[110] M. C. Marchetti, J. F. Joanny, S. Ramaswamy, T. B. Liverpool, J. Prost, Madan Rao, and R. Aditi Simha. Hydrodynamics of soft active matter. *Rev. Mod. Phys.*, 85(3):1143–1189, July 2013. doi: 10.1103/RevModPhys.85.1143.

[111] Ewan J. Hemingway, Prashant Mishra, M. Cristina Marchetti, and Suzanne M. Fielding. Correlation lengths in hydrodynamic models of active nematics. *Soft Matter*, 12(38):7943–7952, September 2016. ISSN 1744-6848. doi: 10.1039/C6SM00812G.

[112] Amin Doostmohammadi and Julia M. Yeomans. Coherent motion of dense active matter. *Eur. Phys. J. Spec. Top.*, 227(17):2401–2411, March 2019. ISSN 1951-6401. doi: 10.1140/epjst/e2019-700109-x.

[113] F. J. Ndlec, T. Surrey, A. C. Maggs, and S. Leibler. Self-organization of microtubules and motors. *Nature*, 389(6648):305–308, September 1997. ISSN 1476-4687. doi: 10.1038/38532.

[114] Apala Majumdar, Marchetti M. Cristina, and Epifanio G. Virga. Perspectives in active liquid crystals. *Philos Trans A Math Phys Eng Sci*, 372(2029), November 2014. ISSN 1364-503X. doi: 10.1098/rsta.2013.0373.

[115] Amin Doostmohammadi, Sumesh P. Thampi, and Julia M. Yeomans. Defect-Mediated Morphologies in Growing Cell Colonies. *Phys. Rev. Lett.*, 117(4):048102, July 2016. doi: 10.1103/PhysRevLett.117.048102.

[116] Thuan Beng Saw, Amin Doostmohammadi, Vincent Nier, Leyla Kocgozlu, Sumesh Thampi, Yusuke Toyama, Philippe Marcq, Chwee Teck Lim, Julia M. Yeomans, and Benoit Ladoux. Topological defects in epithelia govern cell death and extrusion. *Nature*, 544(7649):212–216, April 2017. ISSN 1476-4687. doi: 10.1038/nature21718.

[117] Kyogo Kawaguchi, Ryoichiro Kageyama, and Masaki Sano. Topological defects control collective dynamics in neural progenitor cell cultures. *Nature*, 545(7654): 327–331, April 2017. ISSN 1476-4687. doi: 10.1038/nature22321.

[118] Guillaume Duclos, Christoph Erlenkämper, Jean-François Joanny, and Pascal Silberzan. Topological defects in confined populations of spindle-shaped cells. *Nature Physics*, 13(1):58–62, January 2017. ISSN 1745-2481. doi: 10.1038/nphys3876.

[119] Amin Doostmohammadi, Jordi Ignés-Mullol, Julia M. Yeomans, and Francesc Sagués. Active nematics. *Nature Communications*, 9(1):3246, August 2018. ISSN 2041-1723. doi: 10.1038/s41467-018-05666-8.

[120] Mirco Castoldi and Andrei V. Popov. Purification of brain tubulin through two cycles of polymerization-depolymerization in a high-molarity buffer. *Protein Expr Purif*, 32(1):83–88, November 2003. ISSN 1046-5928. doi: 10.1016/S1046-5928(03)00218-3.

[121] Radhika Subramanian and Jeff Gelles. Two distinct modes of processive kinesin movement in mixtures of ATP and AMP-PNP. *J Gen Physiol*, 130(5):445–455, November 2007. ISSN 0022-1295. doi: 10.1085/jgp.200709866.

[122] G. Pelzl and A. Hauser. Birefringence and phase transitions in liquid crystals. *Phase Transitions*, 37(1):33–62, December 1991. ISSN 0141-1594. doi: 10.1080/01411599108203447.

[123] Jerneja Pavlin, Nataša Vaupotič, and Mojca Čepič. Direction dependence of the extraordinary refraction index in uniaxial nematic liquid crystals. *Eur. J. Phys.*, 34(2):331–344, January 2013. ISSN 0143-0807. doi: 10.1088/0143-0807/34/2/331.

[124] Olympus FluoView Resource Center: Introduction to Confocal Microscopy. http://www.olympusconfocal.com/theory/confocalintro.html.

[125] ZEISS Microscopy Online Campus | Introduction to Spinning Disk Microscopy. http://zeiss-campus.magnet.fsu.edu/articles/spinningdisk/introduction.html.

[126] Optical tweezers: Where physics meets biology. https://physicsworld.com/a/optical-tweezers-where-physics-meets-biology/, November 2008.

[127] J. Bibette, F. Leal Calderon, and P. Poulin. Emulsions: Basic principles. *Rep. Prog. Phys.*, 62(6):969–1033, January 1999. ISSN 0034-4885. doi: 10.1088/0034-4885/62/6/203.

[128] Liangzhi Hong, Guanqing Sun, Jinge Cai, and To Ngai. One-Step Formation of W/O/W Multiple Emulsions Stabilized by Single Amphiphilic Block Copolymers. *Langmuir*, 28(5):2332–2336, February 2012. ISSN 0743-7463. doi: 10.1021/la205108w.

[129] Jinhye Bae, Thomas P. Russell, and Ryan C. Hayward. Osmotically Driven Formation of Double Emulsions Stabilized by Amphiphilic Block Copolymers. *Angewandte Chemie International Edition*, 53(31):8240–8245, 2014. ISSN 1521-3773. doi: 10.1002/anie.201405229.

[130] Heng-Dong Xi, Hao Zheng, Wei Guo, Alfonso M. Gañán-Calvo, Ye Ai, Chia-Wen Tsao, Jun Zhou, Weihua Li, Yanyi Huang, Nam-Trung Nguyen, and Say Hwa Tan. Active droplet sorting in microfluidics: A review. *Lab Chip*, 17(5):751–771, February 2017. ISSN 1473-0189. doi: 10.1039/C6LC01435F.

[131] Jessamine Ng Lee, Cheolmin Park, and George M. Whitesides. Solvent Compatibility of Poly(dimethylsiloxane)-Based Microfluidic Devices. *Anal. Chem.*, 75(23): 6544–6554, December 2003. ISSN 0003-2700. doi: 10.1021/ac0346712.

[132] Michael W. Toepke and David J. Beebe. PDMS absorption of small molecules and consequences in microfluidic applications. *Lab Chip*, 6(12):1484–1486, December 2006. ISSN 1473-0197. doi: 10.1039/b612140c.

[133] J. Clerk Maxwell. Statique expérimentale et théorique des Liquides soumis aux seules Forces moléculaires. *Nature*, 10(242):119–121, June 1874. ISSN 1476-4687. doi: 10.1038/010119a0.

[134] Lord Rayleigh. On The Instability Of Jets. *Proceedings of the London Mathematical Society*, s1-10(1):4–13, 1878. ISSN 1460-244X. doi: 10.1112/plms/s1-10.1.4.

[135] A. S. Utada, E. Lorenceau, D. R. Link, P. D. Kaplan, H. A. Stone, and D. A. Weitz. Monodisperse double emulsions generated from a microcapillary device. *Science*, 308(5721):537–541, April 2005. ISSN 1095-9203. doi: 10.1126/science.1109164.

[136] Felix C. Keber, Etienne Loiseau, Tim Sanchez, Stephen J. DeCamp, Luca Giomi, Mark J. Bowick, M. Cristina Marchetti, Zvonimir Dogic, and Andreas R. Bausch. Topology and dynamics of active nematic vesicles. *Science*, 345(6201):1135–1139, September 2014. ISSN 0036-8075, 1095-9203. doi: 10.1126/science.1254784.

[137] Perry W. Ellis, Daniel J. G. Pearce, Ya-Wen Chang, Guillermo Goldsztein, Luca Giomi, and Alberto Fernandez-Nieves. Curvature-induced defect unbinding and dynamics in active nematic toroids. *Nature Physics*, 14(1):85–90, January 2018. ISSN 1745-2481. doi: 10.1038/nphys4276.

[138] Pau Guillamat, Jordi Ignés-Mullol, Suraj Shankar, M. Cristina Marchetti, and Francesc Sagués. Probing the shear viscosity of an active nematic film. *Phys. Rev. E*, 94(6):060602, December 2016. doi: 10.1103/PhysRevE.94.060602.

[139] Pau Guillamat. *Control of Active Flows through Soft Interfaces*. PhD thesis, Universitat de Barcelona, 2017.

[140] Christophe Blanc and Maurice Kleman. Tiling the plane with noncongruent toric focal conic domains. *Phys. Rev. E*, 62(5):6739–6748, November 2000. doi: 10.1103/PhysRevE.62.6739.

[141] Gil Henkin, Stephen J. DeCamp, Daniel T. N. Chen, Tim Sanchez, and Zvonimir Dogic. Tunable dynamics of microtubule-based active isotropic gels. *Philosophical Transactions of the Royal Society A: Mathematical, Physical and Engineering Sciences*, 372(2029):20140142, November 2014. doi: 10.1098/rsta.2014.0142.

[142] Silke Henkes, M. Cristina Marchetti, and Rastko Sknepnek. Dynamical patterns in nematic active matter on a sphere. *Phys. Rev. E*, 97(4):042605, April 2018. doi: 10.1103/PhysRevE.97.042605.

[143] Rui Zhang, Ye Zhou, Mohammad Rahimi, and Juan J. de Pablo. Dynamic structure of active nematic shells. *Nature Communications*, 7(1):1–9, November 2016. ISSN 2041-1723. doi: 10.1038/ncomms13483.

[144] Rastko Sknepnek and Silke Henkes. Active swarms on a sphere. *Phys. Rev. E*, 91 (2):022306, February 2015. doi: 10.1103/PhysRevE.91.022306.

[145] Diana Khoromskaia and Gareth P. Alexander. Vortex formation and dynamics of defects in active nematic shells. *New J. Phys.*, 19(10):103043, November 2017. ISSN 1367-2630. doi: 10.1088/1367-2630/aa89aa.

[146] Liesbeth M. C. Janssen, Andreas Kaiser, and Hartmut Löwen. Aging and rejuvenation of active matter under topological constraints. *Scientific Reports*, 7(1):1–13, July 2017. ISSN 2045-2322. doi: 10.1038/s41598-017-05569-6.

[147] Hugo Wioland, Francis G. Woodhouse, Jörn Dunkel, John O. Kessler, and Raymond E. Goldstein. Confinement Stabilizes a Bacterial Suspension into a Spiral Vortex. *Phys. Rev. Lett.*, 110(26):268102, June 2013. doi: 10.1103/PhysRevLett.110.268102.

[148] Pavel Castro-Villarreal and Francisco J. Sevilla. Active motion on curved surfaces. *Phys. Rev. E*, 97(5):052605, May 2018. doi: 10.1103/PhysRevE.97.052605.

[149] Dalija Jesenek, Samo Kralj, Riccardo Rosso, and Epifanio G. Virga. Defect unbinding on a toroidal nematic shell. *Soft Matter*, 11(12):2434–2444, March 2015. ISSN 1744-6848. doi: 10.1039/C4SM02540G.

[150] D. J. G. Pearce, Perry W. Ellis, Alberto Fernandez-Nieves, and L. Giomi. Geometrical Control of Active Turbulence in Curved Topographies. *Phys. Rev. Lett.*, 122 (16):168002, April 2019. doi: 10.1103/PhysRevLett.122.168002.

[151] Teresa Lopez-Leon, Alberto Fernandez-Nieves, Maurizio Nobili, and Christophe Blanc. Smectic shells. *J. Phys.: Condens. Matter*, 24(28):284122, June 2012. ISSN 0953-8984. doi: 10.1088/0953-8984/24/28/284122.

[152] Teresa Lopez-Leon, Alberto Fernandez-Nieves, Maurizio Nobili, and Christophe Blanc. Nematic-smectic transition in spherical shells. *Phys. Rev. Lett.*, 106(24): 247802, June 2011. ISSN 1079-7114. doi: 10.1103/PhysRevLett.106.247802.

[153] C. Blanc and M. Kléman. Curvature walls and focal conic domains in a lyotropic lamellar phase. *Eur. Phys. J. B*, 10(1):53–60, May 1999. ISSN 1434-6036. doi: 10.1007/s100510050829.

[154] Christophe Blanc, Guillaume Durey, Randall D. Kamien, Teresa Lopez-Leon, Maxim O. Lavrentovich, and Lisa Tran. Helfrich-Hurault elastic instabilities driven by geometrical frustration. *arXiv:2109.14668 [cond-mat]*, September 2021.

[155] O. V. Manyuhina and M. J. Bowick. Thick smectic shells. *International Journal of Non-Linear Mechanics*, 75:87–91, October 2015. ISSN 0020-7462. doi: 10.1016/j.ijnonlinmec.2015.04.003.

[156] I. Andrade-Silva, M. G. Clerc, and V. Odent. Zig-zag wall lattice in a nematic liquid crystal with an in-plane switching configuration. *Phys. Rev. E*, 90(2):022504, August 2014. doi: 10.1103/PhysRevE.90.022504.

[157] Pau Guillamat, Jordi Ignés-Mullol, and Francesc Sagués. Control of active liquid crystals with a magnetic field. *PNAS*, 113(20):5498–5502, May 2016. ISSN 0027-8424, 1091-6490. doi: 10.1073/pnas.1600339113.

[158] H. Poincaré. Sur les courbes définies par les équations différentielles (III). *Journal de Mathématiques Pures et Appliquées*, 1:167–244, 1885. ISSN 0021-7874.

[159] Benoît Jubin. A generalized Poincar\'e-Hopf index theorem. *arXiv:0903.0697 [math]*, September 2009.

[160] Semjon Stepanow. Adsorption of a semiflexible polymer onto interfaces and surfaces. *J. Chem. Phys.*, 115(3):1565–1568, July 2001. ISSN 0021-9606. doi: 10.1063/1.1379533.

[161] Daniel Claxton. Surface curvature. MATLAB Central File Exchange.

[162] O. T. Dyer and R. C. Ball. Influence of thermal fluctuations on active diffusion at large Péclet numbers. *Physics of Fluids*, 33(5):051904, May 2021. ISSN 1070-6631. doi: 10.1063/5.0049386.

[163] Michael F. Staddon, Dapeng Bi, A. Pasha Tabatabai, Visar Ajeti, Michael P. Murrell, and Shiladitya Banerjee. Cooperation of dual modes of cell motility promotes epithelial stress relaxation to accelerate wound healing. *PLOS Computational Biology*, 14(10):e1006502, October 2018. ISSN 1553-7358. doi: 10.1371/journal.pcbi.1006502.

[164] Arpita Upadhyaya. Mechanosensing in the immune response. *Semin Cell Dev Biol*, 71:137–145, November 2017. ISSN 1084-9521. doi: 10.1016/j.semcdb.2017.08.031.

[165] Priti Agarwal and Ronen Zaidel-Bar. Mechanosensing in embryogenesis. *Curr Opin Cell Biol*, 68:1–9, February 2021. ISSN 1879-0410. doi: 10.1016/j.ceb.2020.08.007.

[166] A. E. Carlsson. Mechanisms of Cell Propulsion by Active Stresses. *New J Phys*, 13, July 2011. ISSN 1367-2630. doi: 10.1088/1367-2630/13/7/073009.

[167] Juliet Lee, Akira Ishihara, Julie A. Theriot, and Ken Jacobson. Principles of locomotion for simple-shaped cells. *Nature*, 362(6416):167–171, March 1993. ISSN 1476-4687. doi: 10.1038/362167a0.

[168] Tong Gao and Zhaorui Li. Self-Driven Droplet Powered By Active Nematics. *Physical Review Letters*, 119:108002, September 2017. ISSN 0031-9007. doi: 10.1103/PhysRevLett.119.108002.

[169] Alexander B. Verkhovsky, Tatyana M. Svitkina, and Gary G. Borisy. Self-polarization and directional motility of cytoplasm. *Current Biology*, 9(1):11–S1, January 1999. ISSN 0960-9822. doi: 10.1016/S0960-9822(99)80042-6.

[170] Pau Guillamat, Žiga Kos, Jérôme Hardoüin, Jordi Ignés-Mullol, Miha Ravnik, and Francesc Sagués. Active nematic emulsions. *Science Advances*, 4(4):eaao1470, April 2018. ISSN 2375-2548. doi: 10.1126/sciadv.aao1470.

[171] Leonidas Sandoval Junior and Italo De Paula Franca. Shocks in financial markets, price expectation, and damped harmonic oscillators. *arXiv:1103.1992 [q-fin]*, September 2011.

[172] Ido Nitsan, Stavit Drori, Yair E. Lewis, Shlomi Cohen, and Shelly Tzlil. Mechanical communication in cardiac cell synchronized beating. *Nature Phys*, 12(5):472–477, May 2016. ISSN 1745-2481. doi: 10.1038/nphys3619.

[173] Brian Lading, Erik Mosekilde, Sergiy Yanchuk, and Yuri Maistrenko. Chaotic Synchronization between Coupled Pancreatic β-Cells. *Progress of Theoretical Physics Supplement*, 139:164–177, May 2000. ISSN 0375-9687. doi: 10.1143/PTPS.139.164.

[174] Erik Mosekilde, Yuri Maistrenko, and Dmitry Postnov. *Chaotic Synchronization: Applications to Living Systems*, volume 42 of *World Scientific Series on Nonlinear Science Series A*. WORLD SCIENTIFIC, March 2002. ISBN 978-981-02-4789-8 978-981-277-826-0. doi: 10.1142/4845.

[175] Michael G. Rosenblum, Arkady S. Pikovsky, and Jürgen Kurths. Phase Synchronization of Chaotic Oscillators. *Phys. Rev. Lett.*, 76(11):1804–1807, March 1996. doi: 10.1103/PhysRevLett.76.1804.

[176] Yoshiki Kuramoto. Cooperative Dynamics of Oscillator Community: A Study Based on Lattice of Rings. *Progress of Theoretical Physics Supplement*, 79:223–240, February 1984. ISSN 0375-9687. doi: 10.1143/PTPS.79.223.

[177] Fatihcan M. Atay, Jürgen Jost, and Andreas Wende. Delays, Connection Topology, and Synchronization of Coupled Chaotic Maps. *Phys. Rev. Lett.*, 92(14):144101, April 2004. doi: 10.1103/PhysRevLett.92.144101.

[178] J. S. Lintuvuori, K. Stratford, M. E. Cates, and D. Marenduzzo. Self-assembly and nonlinear dynamics of dimeric colloidal rotors in cholesterics. *Phys Rev Lett*, 107(26):267802, December 2011. ISSN 1079-7114. doi: 10.1103/PhysRevLett.107.267802.

[179] G. Foffano, J. S. Lintuvuori, A. Tiribocchi, and D. Marenduzzo. The dynamics of colloidal intrusions in liquid crystals: A simulation perspective. *Liquid Crystals Reviews*, 2(1):1–27, January 2014. ISSN 2168-0396. doi: 10.1080/21680396.2013.878672.

[180] O. Guzmán, E. B. Kim, S. Grollau, N. L. Abbott, and J. J. de Pablo. Defect Structure around Two Colloids in a Liquid Crystal. *Phys. Rev. Lett.*, 91(23):235507, December 2003. doi: 10.1103/PhysRevLett.91.235507.

[181] Takeaki Araki and Hajime Tanaka. Colloidal Aggregation in a Nematic Liquid Crystal: Topological Arrest of Particles by a Single-Stroke Disclination Line. *Phys. Rev. Lett.*, 97(12):127801, September 2006. doi: 10.1103/PhysRevLett.97.127801.

[182] Igor Muševič. Nematic Liquid-Crystal Colloids. *Materials (Basel)*, 11(1), December 2017. ISSN 1996-1944. doi: 10.3390/ma11010024.

[183] Uroš Tkalec and Igor Muševič. Topology of nematic liquid crystal colloids confined to two dimensions. *Soft Matter*, 9(34):8140–8150, August 2013. ISSN 1744-6848. doi: 10.1039/C3SM50713K.

[184] Anupam Sengupta, Christian Bahr, and Stephan Herminghaus. Topological microfluidics for flexible micro-cargo concepts. *Soft Matter*, 9(30):7251–7260, July 2013. ISSN 1744-6848. doi: 10.1039/C3SM50677K.

[185] A. Grinsted, J. C. Moore, and S. Jevrejeva. Application of the cross wavelet transform and wavelet coherence to geophysical time series. *Nonlinear Processes in Geophysics*, 11(5/6):561–566, November 2004. ISSN 1023-5809. doi: 10.5194/npg-11-561-2004.

[186] Christopher Torrence and Peter J. Webster. Interdecadal Changes in the ENSO–Monsoon System. *Journal of Climate*, 12(8):2679–2690, August 1999. ISSN 0894-8755, 1520-0442. doi: 10.1175/1520-0442(1999)012<2679:ICITEM>2.0.CO;2.

[187] Congsheng Fu, April L. James, and Mark P. Wachowiak. Analyzing the combined influence of solar activity and El Niño on streamflow across southern Canada. *Water Resources Research*, 48(5), 2012. ISSN 1944-7973. doi: 10.1029/2011WR011507.

[188] O. P. Pishnyak, S. Tang, J. R. Kelly, S. V. Shiyanovskii, and O. D. Lavrentovich. Levitation, Lift, and Bidirectional Motion of Colloidal Particles in an Electrically Driven Nematic Liquid Crystal. *Phys. Rev. Lett.*, 99(12):127802, September 2007. doi: 10.1103/PhysRevLett.99.127802.

[189] Mengfei Wang, Yannian Li, and Hiroshi Yokoyama. Artificial web of disclination lines in nematic liquid crystals. *Nat Commun*, 8(1):388, August 2017. ISSN 2041-1723. doi: 10.1038/s41467-017-00548-x.

[190] Ivan I. Smalyukh, Bohdan I. Senyuk, Sergij V. Shiyanovskii, Oleg D. Lavrentovich, Andrey N. Kuzmin, Alexander V. Kachynski, and Paras N. Prasad. Optical Trapping, Manipulation, and 3D Imaging of Disclinations in Liquid Crystals and Measurement of their Line Tension. *Molecular Crystals and Liquid Crystals*, 450(1): 79/[279]–95/[295], July 2006. ISSN 1542-1406. doi: 10.1080/15421400600587787.

[191] Karthik Peddireddy, Pramoda Kumar, Shashi Thutupalli, Stephan Herminghaus, and Christian Bahr. Solubilization of Thermotropic Liquid Crystal Compounds in Aqueous Surfactant Solutions. *Langmuir*, 28(34):12426–12431, August 2012. ISSN 0743-7463. doi: 10.1021/la3015817.

[192] Igor Muševič. *Liquid Crystal Colloids*. Soft and Biological Matter. Springer International Publishing, 2017. ISBN 978-3-319-54914-9. doi: 10.1007/978-3-319-54916-3.

[193] Karthik Peddireddy, V. S. R. Jampani, Shashi Thutupalli, Stephan Herminghaus, Christian Bahr, and Igor Muševič. Lasing and waveguiding in smectic A liquid crystal optical fibers. *Opt Express*, 21(25):30233–30242, December 2013. ISSN 1094-4087. doi: 10.1364/OE.21.030233.

[194] A. Isakov and L. Mahadevan. Synchronization in a stochastic Hebbian network of phase oscillators. *arXiv:1404.2328 [cond-mat, physics:nlin]*, April 2014.

[195] Luca Giomi and Antonio DeSimone. Spontaneous Division and Motility in Active Nematic Droplets. *Phys. Rev. Lett.*, 112(14):147802, April 2014. doi: 10.1103/PhysRevLett.112.147802.

[196] Liam J. Ruske and Julia M. Yeomans. Morphology of Active Deformable 3D Droplets. *Phys. Rev. X*, 11(2):021001, April 2021. ISSN 2160-3308. doi: 10.1103/PhysRevX.11.021001.

[197] Ingo Nitschke, Sebastian Reuther, and Axel Voigt. Liquid crystals on deformable surfaces. *Proceedings of the Royal Society A*, September 2020. doi: 10.1098/rspa.2020.0313.

[198] Aurore Dupin and Friedrich C. Simmel. Signalling and differentiation in emulsion-based multi-compartmentalized in vitro gene circuits. *Nature Chem*, 11(1):32–39, January 2019. ISSN 1755-4349. doi: 10.1038/s41557-018-0174-9.

[199] Rafael B. Lira, Fernanda S. C. Leomil, Renan J. Melo, Karin A. Riske, and Rumiana Dimova. To Close or to Collapse: The Role of Charges on Membrane Stability upon Pore Formation. *Advanced Science*, 8(11):2004068, 2021. ISSN 2198-3844. doi: 10.1002/advs.202004068.

[200] Ruddi Rodríguez-García, Michael Mell, Ivan López-Montero, Jeanette Netzel, Thomas Hellweg, and Francisco Monroy. Polymersomes: Smart vesicles of tunable rigidity and permeability. *Soft Matter*, 7(4):1532–1542, February 2011. ISSN 1744-6848. doi: 10.1039/C0SM00823K.

Appendices

APPENDIX

ONE

OSCILLATIONS OF ISOLATED SRS DEFECTS

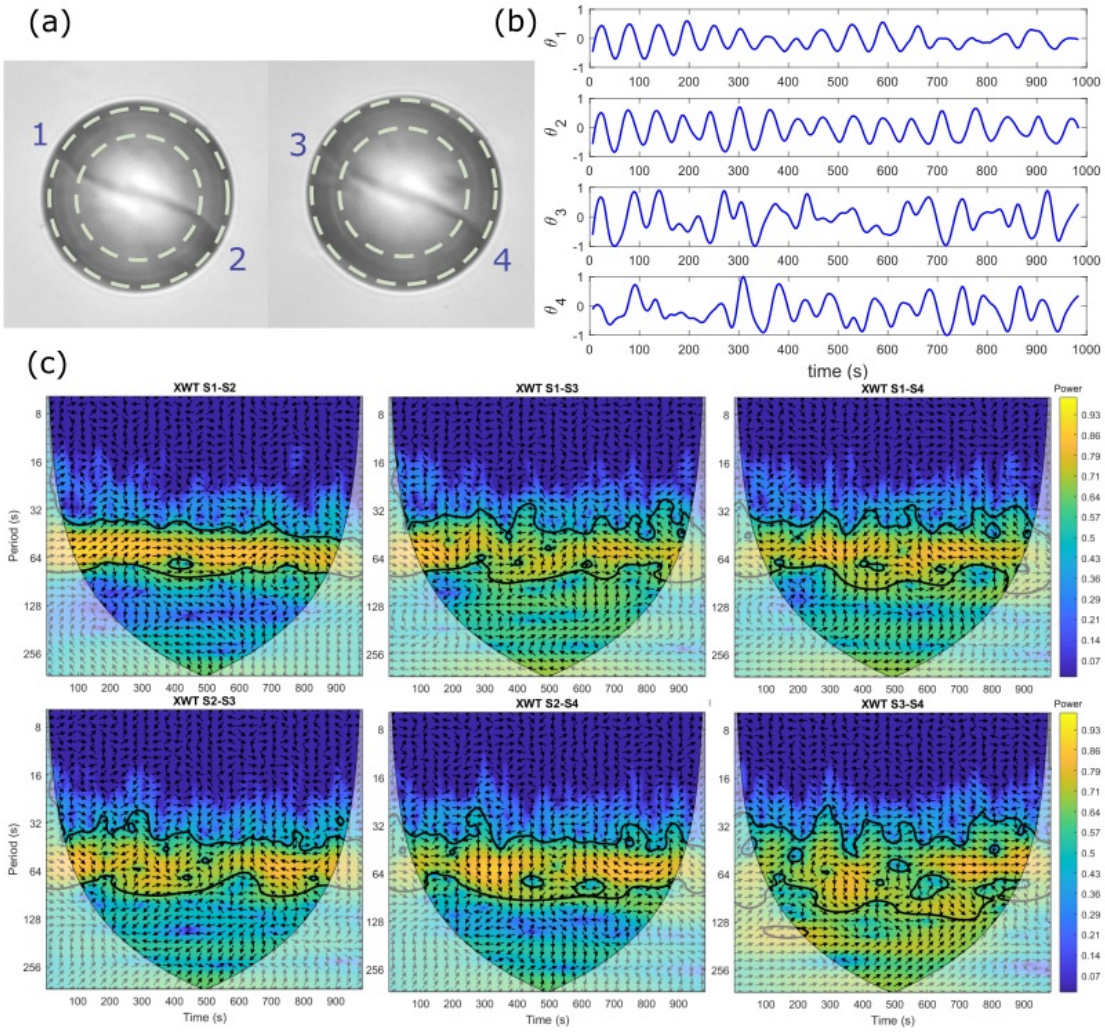

Figure A.1: Dynamics of SRs defects in isolated droplets. (a) Bright-field micrograph of a dimer connected through a disclination line. Dashed circles limit the area analyzed for obtaining the space time plots in (b). Time series in (b) are numbered from 1 to 4 according to the position of the analyzed section. (c) Cross wavelet transform of the time series in (b). The phase lag between the signals is given by the orientation of the black arrows. The dark contour represents a significance level of 5% against noise. The opaque regions correspond to the cone of influence (COI).

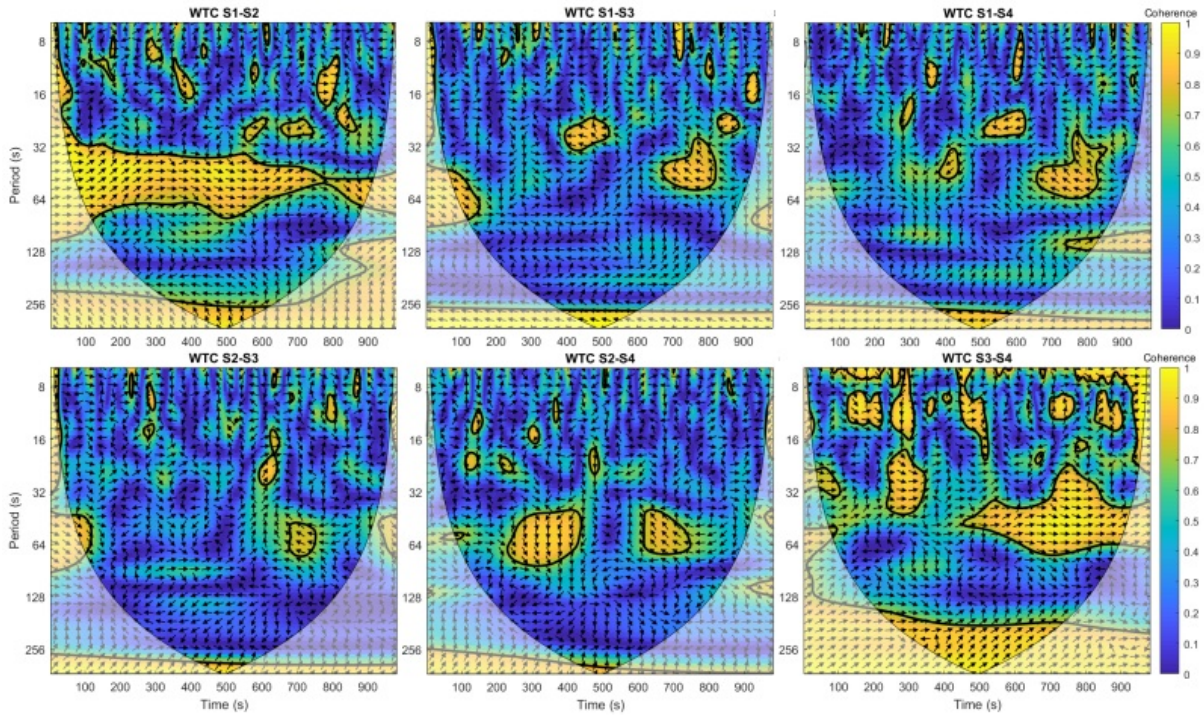

Figure A.2: Wavelet coherence spectrums of signals Fig. A.1 (b) The phase lag between the signals is given by the orientation of the black arrows. The dark contour represents a significance level of 5% against noise. The opaque regions correspond to the cone of influence (COI)

APPENDIX

TWO

ENTANGLEMENT OF ACTIVE NEMATIC DROPLETS IN A DISCLINATION LINE

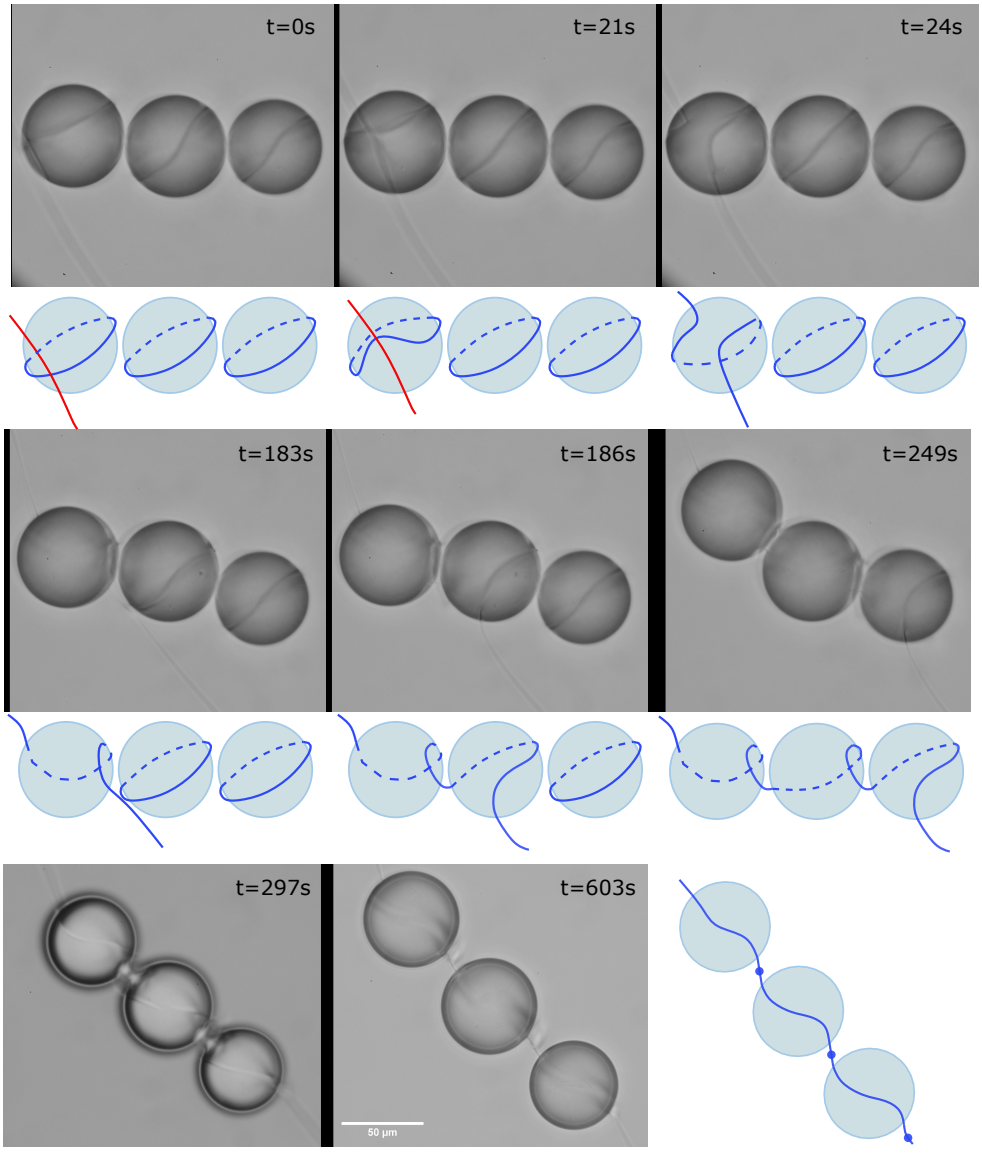

Figure B.1: Mechanism of formation of an active necklace structure. Image sequence shows the bright field images and the schematic representation of the disclination line wrapping around quadrupoles.

APPENDIX

THREE

DYNAMICS OF AN ACTIVE NECKLACE STRUCTURE

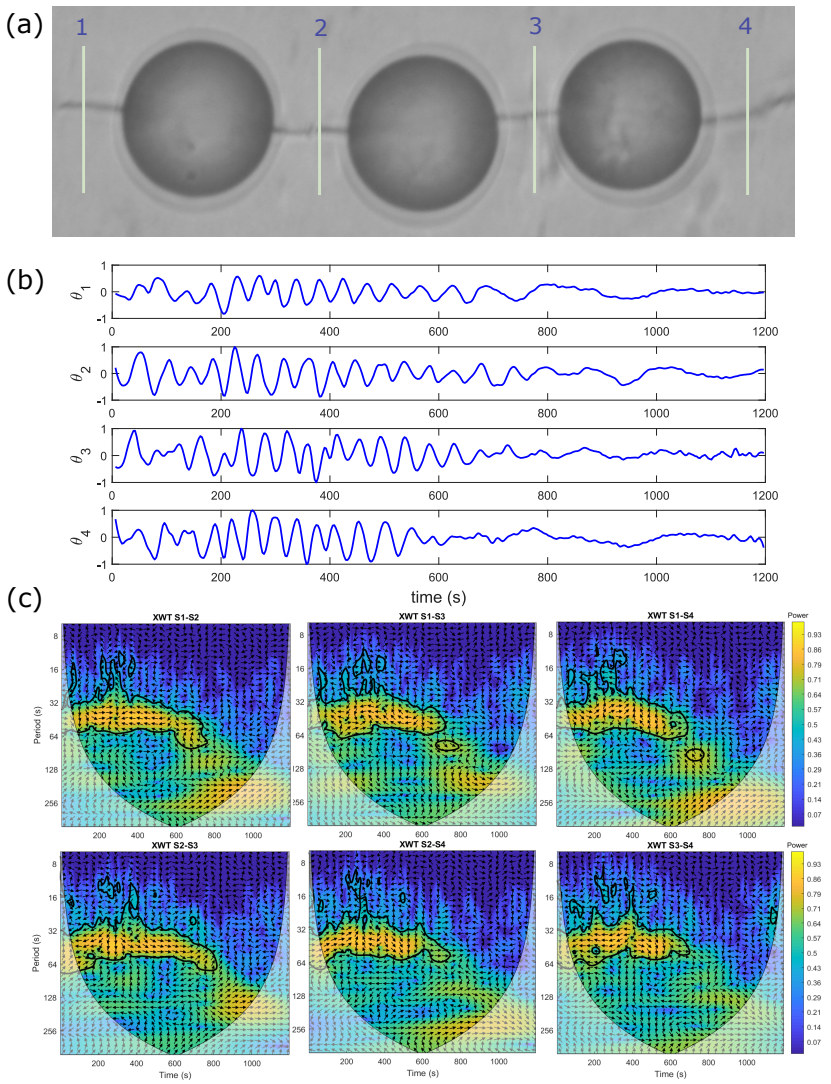

Figure C.1: Dynamics of an active necklace structure. (a) Bright-field micrograph of a trimer connected through a disclination line. White lines correspond to the analyzed sections for obtaining the space time plots in (b). Time series in (b) are numbered from 1 to 4 according to the position of the analyzed section. (c) Cross wavelet transform of the time series in (b). The phase lag between the signals is given by the orientation of the black arrows. The dark contour represents a significance level of 5% against noise. The opaque regions correspond to the cone of influence (COI).

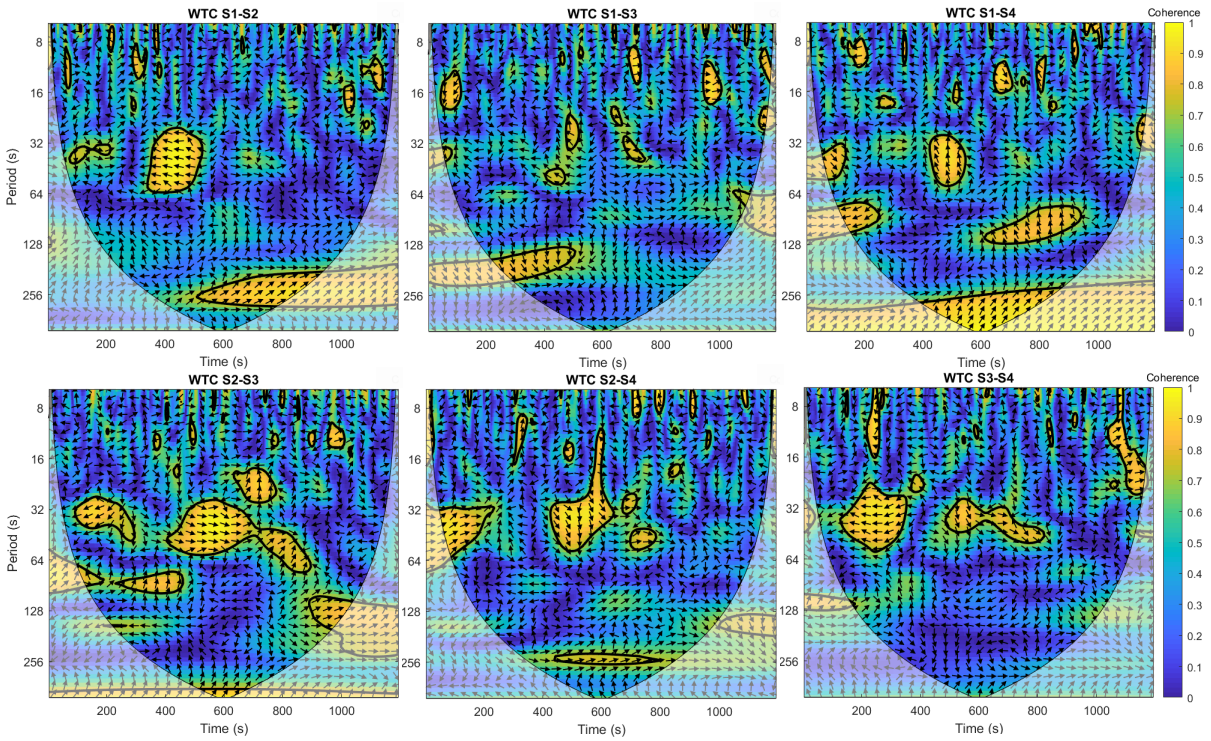

Figure C.2: Wavelet coherence spectrums of the signals in Fig. C.1(b). The phase lag between the signals is given by the orientation of the black arrows. The dark contour represents a significance level of 5% against noise. The opaque regions correspond to the cone of influence (COI).

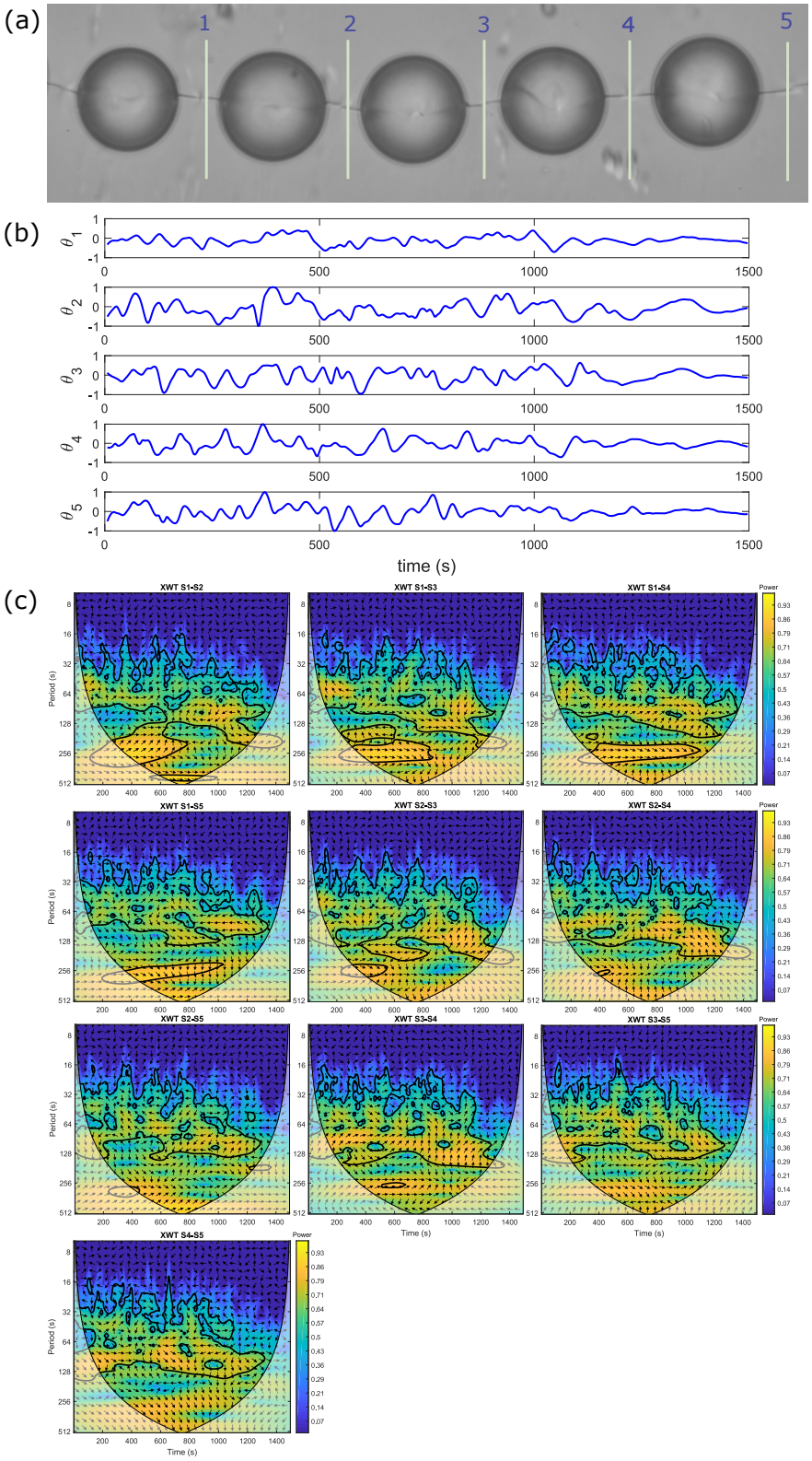

Figure C.3: Dynamics of an active necklace structure. (a) Bright-field micrograph of 5 droplets connected through a disclination line. White lines correspond to the analyzed sections for obtaining the space time plots in (b). Time series in (b) are numbered from 1 to 5 according to the position of the analyzed section. (c) Cross wavelet transform of the time series in (b). The phase lag between the signals is given by the orientation of the black arrows. The dark contour represents a significance level of 5% against noise. The opaque regions correspond to the cone of influence (COI).

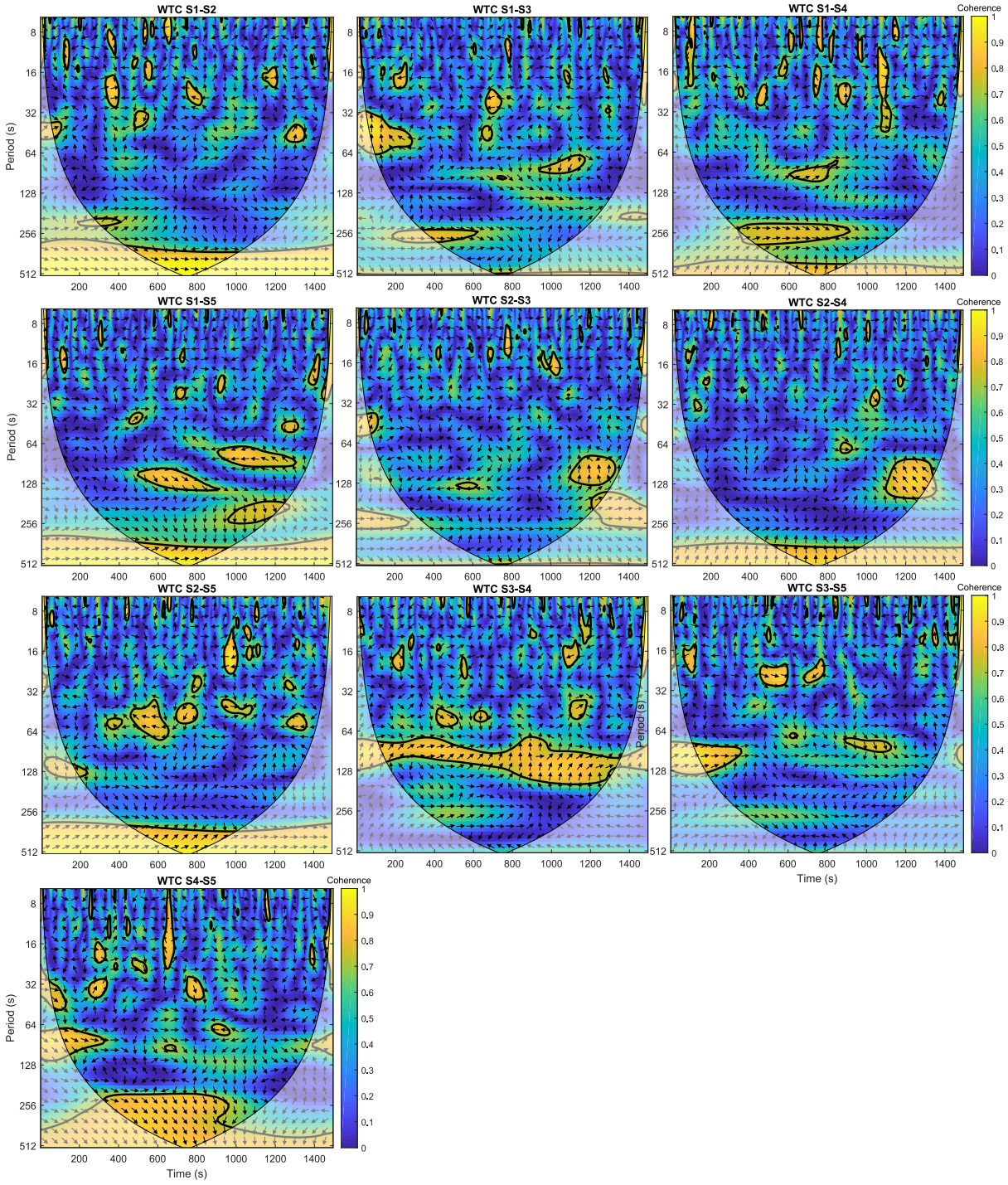

Figure C.4: Wavelet coherence spectrums of the signals in Fig. C.3(b). The phase lag between the signals is given by the orientation of the black arrows. The dark contour represents a significance level of 5% against noise. The opaque regions correspond to the cone of influence (COI).

APPENDIX

FOUR

TOPOLOGICALLY LINKED ACTIVE NEMATIC EMULSIONS

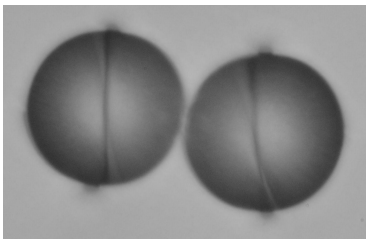

Hexadecapoles connected via a boojum-boojum interaction

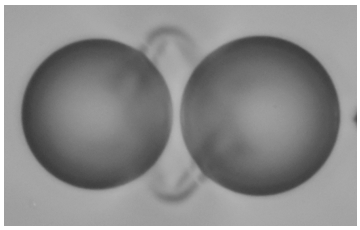

Dipoless connected via a bubble gum defect

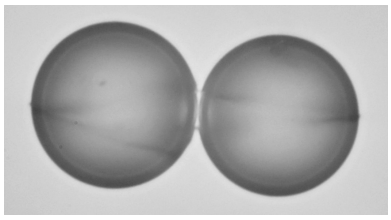

Hexadecapoles connected via a figure of eight defect

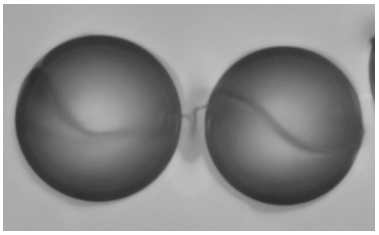

Hexadecapoles connected via a entangled hyperbolic defect

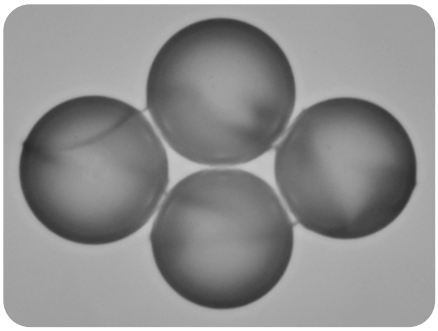

Hexadecapoles connected via a twisted loop defect

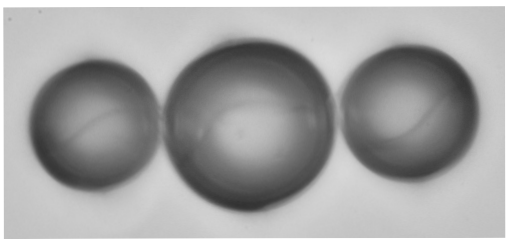

Hexadecapoles of different sizes connected via a figure of eight defect

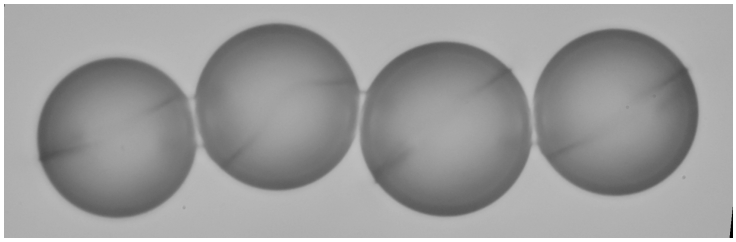

Necklace of hexadecapoles connected via figure of eight defects

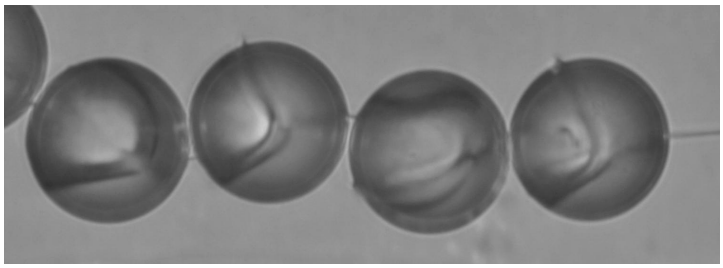

Necklace of quadrupolar droplets

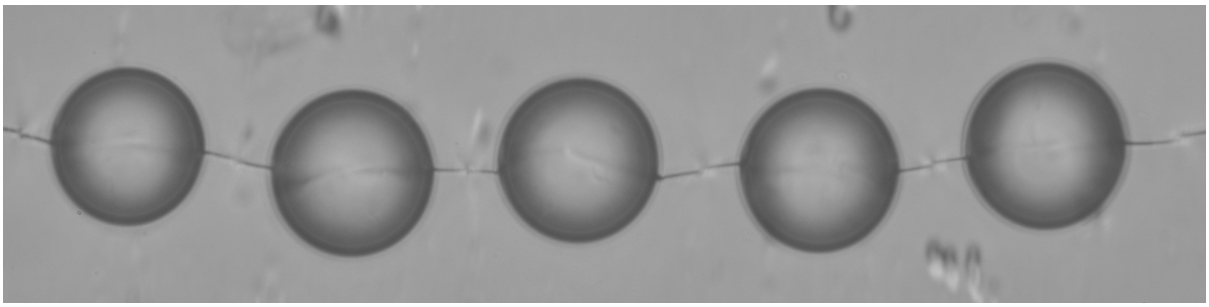

Necklace of dipolar droplets

RÉSUMÉ

De nombreux processus physiologiques, tels que la division ou la migration cellulaire, reposent sur la capacité de la machinerie cellulaire à s'adapter aux signaux mécaniques de son environnement, tels que les contraintes hydrodynamiques. Un réseau interne de polymères filamenteux et de protéines régulatrices, le cytosquelette, se réorganise pour surmonter les perturbations externes, influençant à son tour les propriétés du milieu extracellulaire. Le besoin de comprendre simultanément comment les structures actives internes répondent aux contraintes externes et vice-versa a encouragé la communauté scientifique à développer de nouveaux micro-environnements pour étudier ces questions de manière contrôlable. Dans cette thèse, nous avons construit une plateforme in vitro, inspirée de travaux antérieurs, en interfaçant un fluide biomimétique constitué de composants du cytosquelette cellulaire avec un cristal liquide (CL). Lorsque le matériau actif se condense à l'interface eau-CL, il développe un état dynamique, appelé nématique actif, dans lequel l'ordre d'orientation à longue portée coexiste avec des flux chaotiques persistants. L'objectif de cette recherche est d'étudier le couplage dynamique entre les nématiques actifs et les cristaux liquides passifs en ajoutant deux nouvelles variables au problème : le confinement géométrique et la courbure. L'interaction entre le couplage actif/passif et les paramètres géométriques sont d'abord mis en évidence sur des gouttelettes smectiques ellipsoïdales recouvertes d'une fine couche nématique active. L'anisotropie inhérente de l'ellipsoïde met en évidence des comportements dynamiques sans précédent, notamment des oscillations périodiques entre un régime de rotation et un régime de translation, où la dynamique du système est contrôlée par le mouvement de deux paires de défauts topologiquement requis. Nous avons également étudié une configuration inverse, dans laquelle des gouttes actives sphériques sont incorporées dans une phase cristal liquide, produisant autour d'elles un défaut topologique associé. Dans cette configuration, le couplage entre les fluides actif et passif entraîne le battement du défaut externe, induit par le mouvement des défauts actifs à la surface de la goutte. La brisure de symétrie et les dynamiques associées au défaut externe entraînent en outre l'auto-locomotion dirigée de la goutte. Enfin, le couplage est étudié à un niveau organisationnel plus large en analysant la dynamique d'émulsions nématiques actives topologiquement liées, montrant l'apparition d'une synchronisation partielle de phase dans certaines conditions. Ces résultats offrent de nouvelles perspectives pour la compréhension des processus biologiques et pour la conception de micro-machines bio-inspirées.

MOTS CLÉS

Nématiques actifs, cristaux liquides, couplage actif/passif, confinement géometrique, défauts topologiques, matériaux bio-inspirés

ABSTRACT

Many physiological processes such as cell division or migration rely on the ability of the cellular machinery to adapt to the mechanical cues of its surrounding environment such as hydrodynamic stresses and strains. To achieve this, an internal network of filamentous polymers and regulatory proteins, the cytoskeleton, rearranges to overcome the external perturbations, influencing in turn the properties of the extracellular matrix. In recent years, the urge for understanding simultaneously, how the internal active structures respond to the stimulus of external constraints and vice-versa has inspired the scientific community to develop new microenvironments to study these questions in a controllable manner. In this thesis, we have built an in vitro platform, inspired from previous works, by interfacing a biomimetic fluid made of cytoskeletal components with a liquid crystal (LC). When the active material condenses to a water–LC interface it develops a dynamical state, referred to as active nematic, in which long range orientational order coexists with persistent chaotic flows. The goal of this research is to investigate the dynamic coupling between active nematics and passive liquid crystals by incorporating two new variables to the problem: geometrical confinement and curvature. The interplay between the active/passive coupling and the former parameters is first evidenced on ellipsoidal smectic droplets coated with a thin active nematic layer. The inherent anisotropy of the ellipsoid brings under the spotlight unforeseen dynamical behaviors, including periodical oscillations between a rotational and a translational regime, where the system dynamics is controlled by the motion of two pairs of topologically required defects. We have also investigated a reverse configuration, in which spherical active droplets are embedded inside a liquid crystalline phase, producing, each of them, an associated topological defect in the liquid crystal. In this configuration, the crosstalk between the active and passive fluids results in the beating of the external passive defect, induced by the motion of the active defects on the droplet surface. The symmetry breaking and dynamics associated to the external defect further result in the directed self locomotion of the droplet. Finally, the coupling is probed at a larger organizational level by analyzing the dynamics of topologically linked active nematic emulsions, showing the apparition of partial phase-synchronization under certain conditions. These results provide new insights for the understanding of biological processes and perspectives for the design of bio-inspired micro-machines.

KEYWORDS

Active nematics, liquid crystals, active/passive coupling, geometrical confinement, topological defects, bio-inspired materials